

**SYNTHESIS
OF MOLECULAR AND POLYMERIC
ORGANO-METALLIC SYSTEMS:
TOWARDS NEW MATERIALS**

The cover shows a view of the molecular structure of the metal organic framework $[\text{Co}(\text{tdca})(\text{H}_2\text{O})\cdot(\text{H}_2\text{O})_{0.5}]_\infty$ described in Chapter 3 of this PhD Thesis.



UNIVERSITA' DEGLI STUDI DI FIRENZE

Dottorato di Ricerca in Scienze Chimiche - Ciclo XXII
Settore CHIM / 03 – Chimica generale e inorganica
Settore CHIM / 06 – Chimica organica

**SYNTHESIS
OF MOLECULAR AND POLYMERIC
ORGANO-METALLIC SYSTEMS:
TOWARDS NEW MATERIALS**

Doctoral Thesis

Submitted by

BARBARA DI CREDICO

Coordinator:

Prof. Gianni Cardini

Tutor:

Dr. Maurizio Peruzzini

Abstract

This thesis work describes results on the design of new metal organic frameworks (MOFs) and metal organic macrocycles (MOMs), to obtain new functional materials with tailored chemico-physical properties and potential applications in both host-guest chemistry and gas storage materials. The organic component of such materials is fundamental for the ultimate topology of the product, tethering the metal centres and propagating the structural information expressed in metal coordination preferences along the extended structure. In this regard, we identified carboxylic acids and phosphines as attractive building blocks for the synthesis of coordination compounds.

Chapter 2 describes the reactivity of very simple flexible ligands, such as the formate anion. Solvothermal syntheses afforded new 3D metallorganic magnesium frameworks existing in different crystalline polymorphs. A detailed analysis of their thermal behavior is reported. The microporous materials were tested in host-guest experiments with water, CO₂ and H₂. The potential application of these compounds as gas storage materials were also investigated by Raman spectroscopy, integrated by computational studies.

A series of thiazolidines, thiazoles or oxazoles scaffolds containing functional pyridyl and/or carboxylic groups, symmetrical or non-symmetrical, are investigated in Chapter 3. A new large-scale synthesis of such organic spacers has been developed starting from the naturally-occurring amino acids serine and cysteine. The heteroaromatic ligands obtained from the synthetic work were then tested with a variety of metal ions and led to a series of coordination complexes with interesting supramolecular structures. The chapter ends pointing up the synthesis of a chiral three-dimensional MOF of cobalt(II) with *syn*-thiazolidine-2,4-dicarboxylic acid.

The final Chapter is dedicated to deals with a new class of polydentate alkynyl phosphine ligands whose coordination properties were explored to develop new MOMs. The bi- and tridentate phosphine ligands, 1,4-(Ph₂PC≡C)₂C₆H₄ e 1,3,5-(Ph₂PC≡C)₃C₆H₃, were obtained *via* a novel synthetic approach and studied in reactions with half-sandwich cyclopentadienyl precursors of Ru(II). By appropriately varying the reaction conditions, a variety of bi- and tri-metallic complexes, with

interesting stereochemical features, and two MOMs, a dinuclear complex and a tetranuclear square, have been synthesized. Detailed characterization of the phosphine complexes by electrochemical methods and ESR spectroscopy, for the electrogenerated paramagnetic species, are also presented.

Keywords

Metal organic frameworks, macrocycles, supramolecular chemistry.

Riassunto

Questo lavoro di tesi si basa sulla progettazione di nuovi *frameworks* (MOFs) e macrocicli (MOMs) metallo-organici, al fine di ottenere nuovi materiali funzionalizzati, aventi specifiche e ben definite proprietà chimico-fisiche, con possibili applicazioni nel campo della chimica *host-guest* e dei materiali per l'immagazzinamento di gas. Il legante organico presente in questi complessi svolge un ruolo fondamentale nel determinare la topologia finale dei composti di coordinazione, in quanto stabilisce la modalità primaria di coordinazione tra i centri metallici e trasmette quindi l'informazione strutturale in base alle sue proprietà steriche ed elettroniche. Sono state così individuate per lo svolgimento di questo lavoro di tesi due principali classi di molecole organiche di rilevanza per la chimica dei materiali, quali i leganti carbossilici e quelli fosfinici.

Il Capitolo 2 descrive la reattività dell'anione formiato, un legante alifatico semplice e flessibile, verso specifici ioni metallici. La sintesi solvotermica ha permesso di ottenere nuovi formiati polimerici di magnesio, esistenti in differenti polimorfi cristallini. È stata effettuata un'attenta analisi del comportamento termico e in seguito le specie microporose sono state impiegate in esperimenti *host-guest* di adsorbimento di molecole di solvente e di gas, quali CO₂ e H₂. Lo studio mediante spettroscopia Raman, implementato con calcoli teorici computazionali, ha permesso di fornire un'analisi ed una valutazione preliminare di questi formiati metallici come possibili materiali per applicazioni nello *storage* di molecole gassose.

Una serie di leganti eterociclici, quali tiazoli, tiazolidine e ossazoli, decorati con gruppi funzionali piridinici e/o carbossilici, di tipo simmetrico e non simmetrico, sono stati studiati nel Capitolo 3. Una nuova metodologia per la sintesi su larga scala di tali composti è stata messa a punto a partire da due aminoacidi naturali, la serina e la cisteina. I leganti così ottenuti sono stati fatti reagire con un certo numero di ioni metallici ed hanno portato alla sintesi di una serie di strutture supramolecolari, con interessanti geometrie di coordinazione. Il capitolo si conclude mostrando la sintesi di un nuovo MOF chirale tridimensionale di cobalto bivalente, contenente l'acido *syn*-tiazolidin-2,4-dicarbossilico come legante.

Il Capitolo finale è dedicato alla sintesi di una nuova classe di leganti alchilfosfinici le cui proprietà strutturali sono state studiate per lo sviluppo di nuove architetture MOM. I leganti fosfinici, bi- e tridentati, 1,4-(Ph₂PC≡C)₂C₆H₄ e 1,3,5-(Ph₂PC≡C)₃C₆H₃, sono stati ottenuti mediante un nuovo approccio sintetico e quindi studiati in reazioni con precursori ciclopentadienilici di Ru(II). Variando opportunamente le condizioni di reazione, sono stati sintetizzati complessi sia monomolecolari che bi- e tri-metallici, con interessanti caratteristiche stereochimiche, e due MOMs, un complesso dinucleare e uno quadrato tetranucleare. Tutti i nuovi complessi sono stati caratterizzati per via elettrochimica e, le specie paramagnetiche elettrogenerate, mediante spettroscopia ESR.

Parole chiave

Frameworks metallo-organici, macrocicli, chimica supramolecolare.

Table of contents

Abstract	I
Riassunto	II
Frequently used abbreviations	IV
Chapter 1: Introduction and scope	1
1.1 Overview	1
1.2 Metal-organic systems	2
1.2.1 Factors controlling the supramolecular architecture in MOSs	6
1.3 Metal-organic macrocycles MOMs	9
1.3.1 MOM applications	12
1.4 Metal-organic frameworks MOFs	14
1.4.1 Principles in MOF synthesis: connectors, linkers, design	16
1.4.2 Porous properties of MOFs	20
1.4.3 MOF applications	23
1.5 Scope and aims of the thesis work	27
1.6 References	31
Chapter 2: Polymeric magnesium formates	35
2.1 Overview	35
2.2 Introduction	36
2.3 Results and discussion	37
2.3.1 Syntheses	37
2.3.2 Structures description	40
2.3.3 Infrared spectral analysis	42
2.3.4 Thermal behaviour	43
2.3.5 De-hydration and re-hydration of 2: a phase transition	45
2.3.6 Gas-sorption studies: the adsorption behaviour of $\text{Mg}(\text{HCOO})_2(\text{HCOOH}) \supset (\text{CH}_3)_2\text{NH}$	47
2.3.7 Gas sorption studies: the adsorption behaviour of $[\text{Mg}(\text{HCOO})_2 \cdot 2\text{H}_2\text{O}]$	55
2.4 Conclusions and outlook	57
2.5 Experimental section	58

2.6 References and notes	61
Chapter 3: Supramolecular architectures with thiazole and thiazolidine ligands	65
3.1 Overview	65
3.2 Introduction	66
3.3 Synthesis of oxazoles, thiazoles and thiazolidines	68
3.3.1 Results and discussion	68
3.4 Coordination chemistry of thiazole-based ligands	72
3.4.1 Introduction	72
3.4.2 Ligand thermal stability	73
3.4.3 Synthesis of supramolecular networks <i>via</i> multiple intermolecular hydrogen bonds	76
3.5 A new chiral metal organic framework	86
3.6 Conclusions and outlook	89
3.7 Experimental section	90
3.8 References and notes	108
Chapter 4: Phosphine ligands and ruthenium(II) complexes	111
4.1 Overview	111
4.2 Introduction	112
4.3 Results and discussion	114
4.3.1 Alkynylphosphine ligands: synthesis and characterisation	114
4.3.2 Neutral ruthenium complexes with dppab	115
4.3.3 Cationic ruthenium complexes with dppab	118
4.3.4 Crystallographic studies	123
4.3.5 Coordination chemistry of tppab towards [CpRuCl(PPh ₃) ₂]	126
4.3.6 Electrochemistry and spectroelectrochemistry	127
4.4 Conclusions and outlook	134
4.5 Experimental section	135
4.6 References and notes	144
Chapter 5: Appendix	147

Curriculum Vitae	183
Ringraziamenti	189

Note: The numbering scheme adopted to classify each compound within the different chapters is independent.

Frequently used abbreviations

AcOEt	Ethyl acetate
Cp	cyclopentadienyl
CGMC	grand canonical monte carlo
DBU	1,8-diazabicyclo[5.4.0]undec-7-ene
DDQ	2,3-dichloro-5,6-dicyanobenzoquinone
DMSO	dimethyl sulfoxide
dppa	diphenylphosphinoacetylene
dppab	1,4-bis[(diphenylphosphino)ethynyl]benzene
DTA	differential thermal analysis
EDC	<i>N</i> -(3-dimethylaminopropyl)- <i>N</i> '-ethylcarbodiimide
ESI-MS	electrospray ionisation mass spectrometry
ESR	electron spin resonance
FT-IR	infrared spectroscopy
H ₂ tdca	thiazolidine-2,4-dicarboxylic acid
Htzc	thiazole-carboxylic acid
Htzc-py	2-(pyridin-4-yl)thiazole-4-carboxylic acid
2,4-H ₂ tzdc	thiazole-2,4-dicarboxylic acid
<i>J</i>	coupling constant
MOF	metal-organic framework
MOM	metal-organic macrocycle
MOS	metal-organic system
MS	mass spectrometry
MW	microwave
NMR	nuclear magnetic resonance
PSD	pore size distribution
rt	room temperature
TGA	thermogravimetric analysis
THF	tetrahydrofuran
tppab	1,3,5-tris[(diphenylphosphino)ethynyl]benzene
XRD	single-crystal X-ray diffraction
XRPD	powder X-ray diffraction

A mia madre e a mio padre

Elvira e Tommaso

Introduction and scope

1.1 Overview

This chapter provides a general background for the concepts and the related chemistry described in this thesis work. The emphasis of this overview is on the synthesis of metal-organic systems (MOS), supramolecular metallamacrocycles and metal-organic coordination polymers together with fundamental features of organic ligands synthesis and choice of metal ions in the design of new materials. A brief overview will be given also on the potential applications of metal organic frameworks to a number of fields, including magnetism (long-range ordering, spin cross-over), porosity (gas storage, ion and guest exchange), non-linear optical activity, chiral networks, catalysis, luminescence, sensors and others.

1.2 Metal-organic systems

The tailored design and the synthesis of **new materials** has long been recognized as the most essential feature of advancing technology. In the last century, the discovery of new compounds has been frequently driven by serendipity and has been generally considered closer to an art than to a science. However, it is becoming increasingly urgent to produce materials purposely designed to perform highly specific and cooperative functions. In attempting to fulfil this strategic goal, it was soon clear that the design of suitable architectures is pivotal via proper choice of molecular building blocks to obtain a material with the desired properties.¹ In this respect, a “material” can be considered as a molecular object whose properties arise from co-operative interactions between the components of bulk assembly and are not exhibited by the individual molecules.²

In this context, coordination chemistry has played a key role over the years, and its role in materials chemistry is currently growing at an enormous rate. The highly tunable interaction between a metal and a ligand gives access to an unlimited number of combinations, generating new structures and materials with infinite potential applications. Over the past few decades a myriad of inorganic solids has been described that contain metal ions linked by molecular species. While in the past the discovery of these solids was mostly related to empirical methods defined “*shake and bake*” or “*mix and wait*”, the modern research is based on the coherent design of the material with properly tailored functional features and structural requirements that drive the selection of building blocks to its continuous implementation. The study of the supramolecular “structure-functions” relationship guides the rational design and synthesis of self-assembling functional metallo-supramolecular complexes displaying interesting physical and chemical properties. Many examples of materials based on discrete molecules are available, in which the bulk properties depend, more than on the nature of the building units, on the precise ordering of such molecules in the condensed phase with respect to each another. Other examples of coordination complexes as materials are based, rather than on molecular structures, on infinite one-, two- or three-dimensional polymeric networks whose modular construction can be geared to address very specific tasks.

Metal-organic macrocycles (MOMs) and **metal-organic frameworks (MOFs)** are **metal-organic systems (MOSs)** that consist of two main building blocks, *i.e.* the selected inorganic metal ions (Lewis acids) and the designed organic ligands (Lewis bases), held together by coordination bonds and/or weak interactions to form 1-D, 2-D, and 3-D structures.

Generally the use of a convergent building block gives a metallo-supramolecular cycle whereas a divergent one will generate a metal-organic framework (Figure 1-1).³ Therefore, a tight prerequisite for cyclic structure formation is the use of at least one building block with bent geometry.⁴

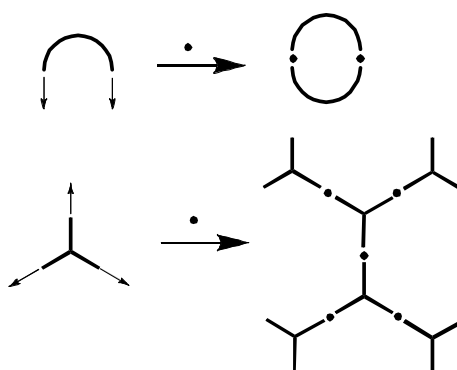


Figure 1-1. Formation of metallasupramolecules (top) and coordination polymers (bottom) through use of convergent and divergent ligands, respectively. Adapted from ref 3.

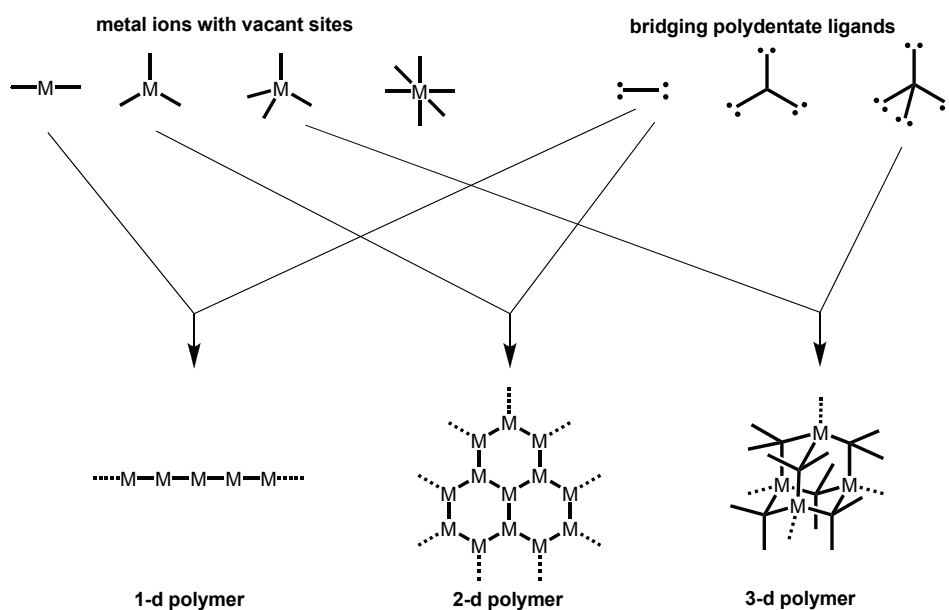


Figure 1-2. 1-3D polymers can be obtained using the building block principle.⁵

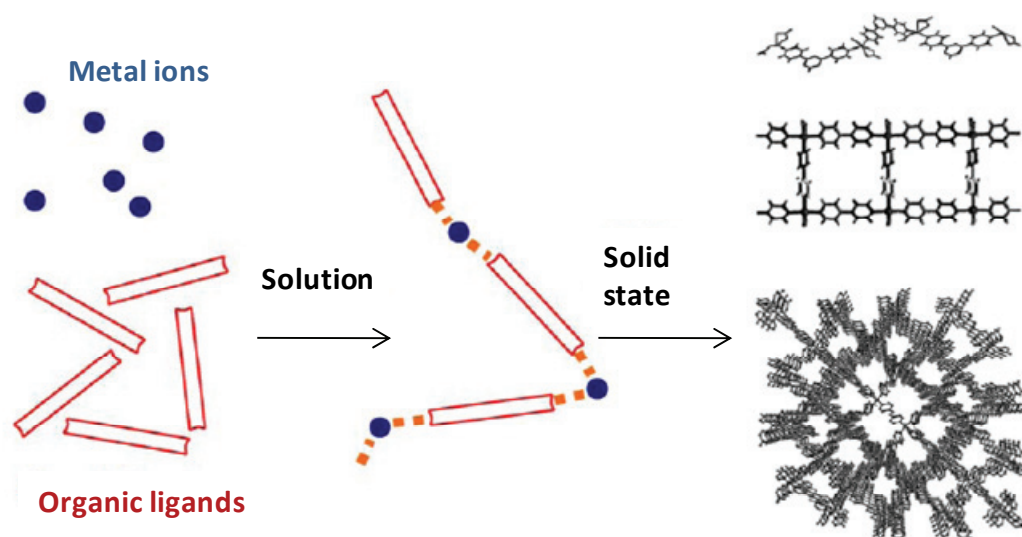
In order to obtain a MOF, it is compulsory to have two integrated molecular ingredients: *i.e.* a metal ion with one or more vacant or labile coordination sites and a ligand having at least two independent sites of coordination. Thus, either infinitely extended polymeric or discrete closed oligomeric structures can arise, depending on the nature of the system used. In particular, extended polymers may result whenever “divergent” metal or ligand sites are coordinated.

The interaction distance between the metal and the ligand in a MOS is typically the **coordination bond** whose energy value may be roughly estimated around 50 KJ mol⁻¹. The coordination bond strength is less than the conventional covalent bond but larger than weak interactions such as hydrogen bonds, dipole-dipole, van der Waals and π - π bonds. This intermediate value allows to control the self-assembly of the metal-ligand bond in a more predictable way, thus allowing the chemists for the rational design of MOSs. As the metal orbitals involved in the coordination bond are spatially oriented, the coordination bond itself is a directional bond, with generally predictable geometries around the metal centre, and strong enough to provide robust materials and, in the presence of suitable ligands, good electronic and magnetic communication between metal centres. On the other hand, the strength-lability and reversibility of metal-ligand coordination interaction affords ordered materials by controlling the structure growth. In this respect, when the metal-ligand combination is labile enough, the initially formed (kinetic) product(s) have the opportunity to rearrange yielding the thermodynamically favoured product(s). Although the main structure is determined by coordination bonds, weaker interactions can influence (sometimes quite significantly) the assembling process. Among these interactions, relevant for this purpose are hydrogen bonds and π - π , metal-metal, and metal-aromatic interactions. Aromatic-aromatic interactions are π - π stacking forces which involve either face-to-face (with or without offset) and edge-to-face (C-H \cdots π interactions) alignments. In the assembly of a solid material the aromatic rings stack in a way to minimize all the repulsive interactions and maximize attraction. Metal-aromatic interactions are possible when metal cations may accept π -electrons from unsaturated organic molecules.⁶

Table 1-1 Typical interactions in MOS and their characteristics. Adapted from ref 6.

Interaction type	Energy (kJ mol ⁻¹)	Approximate distance range (Å)
Coordination bond M-L (M = transition metal, L = organic ligand)	50 - 200	d(M-O,N) = 1.7-3.5 variable, depending on transition metal and donor element
Dipole-Dipole	5 - 50	variable
Hydrogen bond A...H-D (A = acceptor, D = donor)	4 - 120	d(A...D) = 2.2-4.0
π - π stacking	< 50	d(face-to-face) = 2.8-3.5 d(edge-to-face) = 2.9-3.8
van der Waals	< 5	ca. sum of van der Waals radii
Metal-metal interaction	~ 5	variable

Moreover, by taking advantage from the systematic variations of metals and ligands, it is possible to modulate the structure and properties of MOSs. A tailored change of the nodality and geometry of the building bricks as well as the self-assembly of metals and ligands, can produce either MOMs, which exist in solution as individual species, or MOFs, in the form of insoluble polymeric materials.⁷

**Figure 1-3.** Self-assembly of MOSs. Adapted from ref 7.

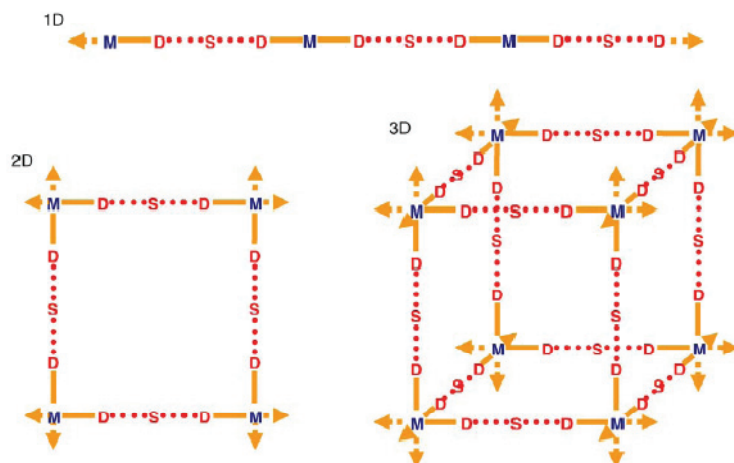


Figure 1-4. Dimensionality of a MOF (M, metal ions; D donor groups of the ligands; S, spacer in the ligand backbone). Adapted from ref 7.

1.2.1 Factors controlling the supramolecular architecture in MOSs

The synthesis or self-organization of MOSs depends on the choice of four different molecular elements: the metal ion, the organic ligand, the counter ion and the solvent. While the first two elements are the true building blocks, the other two ingredients also play a fundamental role in tuning the ultimate molecular architecture. The MOSs topology is indeed controlled by a combination of the coordination geometry of the metal ion, the chemical structure and the electronic properties of the chosen organic ligand, the solvent, the nature of the counterion and the metal-to-ligand ratio.

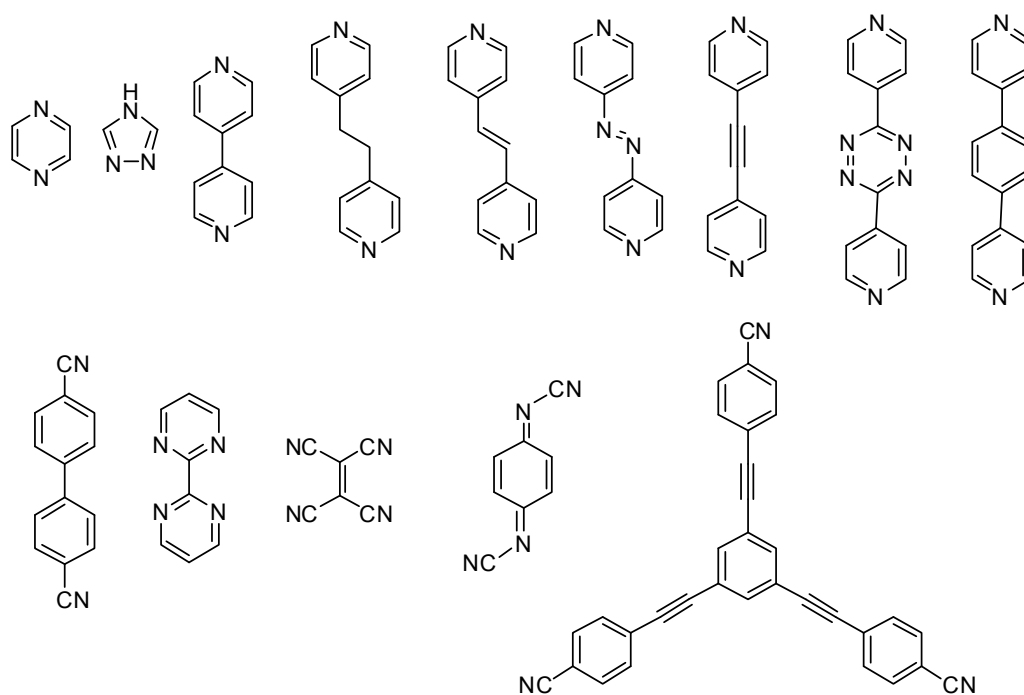
The **metal ion** is chosen according to the assessment of a number of features: size, oxidation state, hardness/softness, ligand-field stabilization energy and coordination geometry which may span a large number of possibilities, ranging, for 3d metal ions, from linear, to trigonal-planar, T-shaped, tetrahedral, square-planar, square-pyramidal, octahedral, trigonal prismatic, or trigonal bipyramidal. The choice of a metal over the others and the proper selection of its oxidation state determines the final coordination geometry and therefore not only the structure of the future material, but also its chemical and physical properties. Most metals have coordination preferences that depend on the chemical behaviour and the specific oxidation state; as a consequence, the coordination environment around the metal ion is rather predictable.

The metal ions mostly widely used are transition metal ions and lanthanides. The most popular are the 3d-transition elements, but also d-block elements with complete d-shell, such as Zn, Cd, Hg, or 4d- and 5d-transition ions such as Ag, Au, Ru, Pd, Pt have received an increased attention probably due to their kinetic lability, availability and stability. There are also examples of MOSs containing light main group metal cations such as Mg(II)⁸ and Al(III),⁹ whose large polarizing power gives rise to relatively strong coordination bonds. Although several lanthanides have interesting luminescence properties, their use in MOS systems is limited,¹⁰ as they present the drawback of higher connectivities with coordination numbers that can vary from 7 to 10 making difficult to predict the behaviour of these metals toward MOF formation.

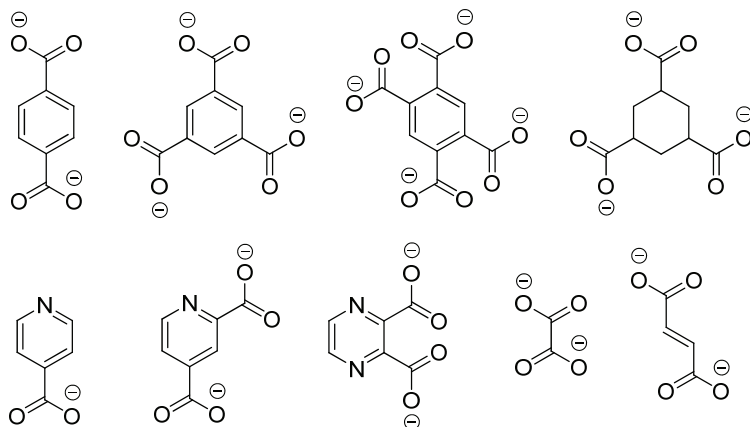
Although the choice of the metal precursor is important, the infinite variability and creativity of **organic ligand** design is the greatest discriminating factor establishing the ultimate topology of the product and the real variations in the coordination compounds. The organic ligands act as bridging groups between the metal centres thus forming the architrave of the whole molecular structure. In MOMs the ligands generally used are bridging (bidentate), whereas in MOFs they have to be multidentate with at least two donor atoms, mostly N-, O-, and S-donors. Coordination ability, shape (rigid or flexible, symmetric or asymmetric), length (distance between the coordination functions), orientation of the donor groups, geometry and presence of other special features like heteroatoms, polar groups, aromatic rings, alkyl chains and chiral centers in the organic ligand all play a very important role in the MOS synthesis. Examples of some popular ligands¹¹ in MOS-oriented coordination chemistry are shown in Figure 1-5.

For these reasons the synthesis of new ligands is currently one of the main goal of the research in coordination chemistry and particularly in the research for new materials.

Neutral ligands



Anionic ligands



Cationic ligands

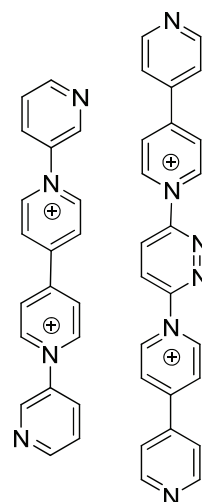


Figure 1-5. Organic molecules typically used as linkers in MOS-oriented coordination chemistry. Adapted from ref 11.

Counter ions are always present in the structures when the ligands used are neutral, unless zerovalent metal complexes are considered. Either in the solid state or in solution, the counter ion can influence the properties of the overall system, being involved in weak interactions or acting as guest molecule in the macrocycle cavity or in the void spaces left over in the solid state packing. Hence, the presence

of anions not only involves a change in the volume and shape of the structure, but also contributes to sustain the molecular framework *via* specific chemical interactions (templating effect). In the case of MOFs, **solvent molecules** can co-crystallize, acting as guests, in the vacant spaces into the 3D-polymer. The solvent molecules can play an important role when highly porous materials are built up. In fact, they may be present in a first synthetic step as fillers which can be removed once the final network is formed and stabilized in the solid state. Furthermore, the solvent, although present in the solid state, may be removed by thermal activation to allow sometime sites to accommodate small molecules such as hydrogen or methane.

1.3 Metal-organic macrocycles MOMs

Metallo-organic species are defined by the endocyclic role, *i.e.* the connection of organic ligands and metal centres to form a closed structure. The pioneering works of Fujita¹² and Stang¹³ have clearly demonstrated the possibility to synthesize molecular cycles based on metal-ligand coordination with appropriate rigid and directional building blocks. These first examples have shown that a pre-requisite for cyclic structure formation is the use of at least one building component with bent geometry. Two types of building blocks are required: linear units (L) of two-fold symmetry, which contain reactive sites oriented at 180° with respect to each other and angular units (A), possessing reactive sites with other desirable angles which may contain either two-fold or higher symmetry axes. The final shapes and symmetries of the resulting assemblies will exclusively depend on the type and stoichiometry of linear and angular building units.¹⁴ The structure of the desired coordination polygon can be readily rationalized based on such simple symmetry and geometric arguments.

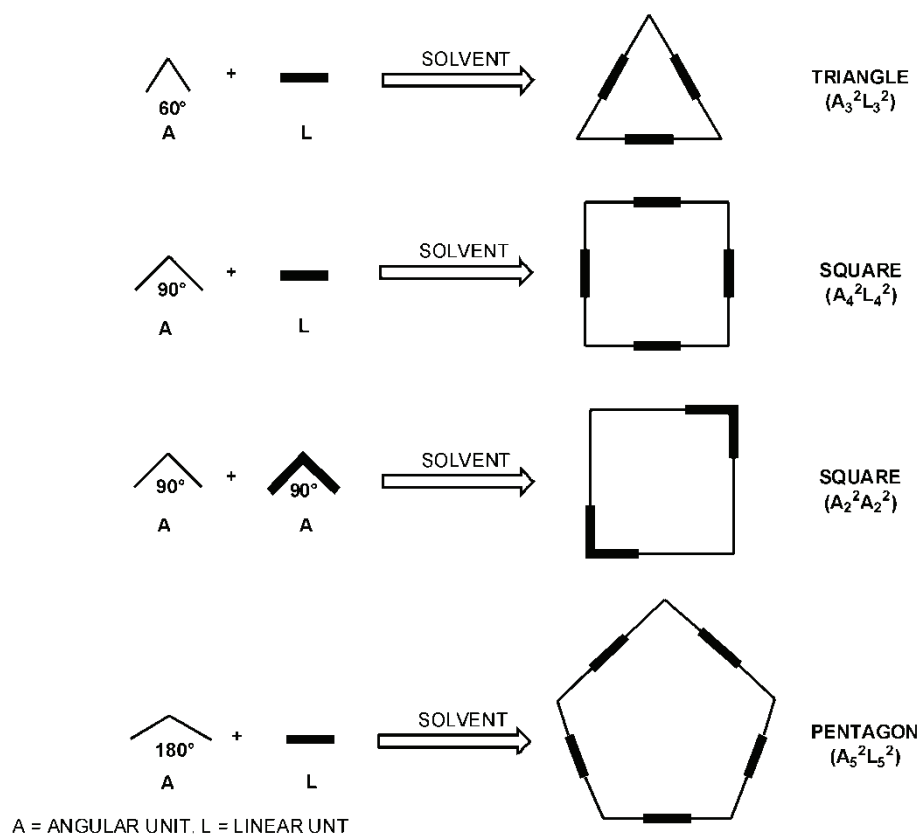


Figure 1-6. Rational design of geometrically shaped metallacycles. Adapted from ref 13a.

Generally, by increasing the angle of the building blocks, the number of components in the cyclic ring system increase and the size of MOMs can be expanded. The highly directional formation of coordination bonds can generate a variety of either polygonal (triangles, squares, hexagons) or polyhedral (triangular prisms, octahedra, cubes) structural motifs. For instance (Figure 1-6), combining three linear plus three 60°-angular building subunits together one will generate a planar triangle. The combination of a square planar metal ion having two vacant *cis*-coordination sites (*i.e.* an acceptor unit enclosing a 90° angle) with a rigidly linear ditopic ligand (*i.e.* a donor unit enclosing an angle of 180°) may lead to the formation of a molecular square. Finally, the assembly of a molecular pentagon can be achieved by combining five linear subunits with five angular ones that possess a 180° angle between their binding sites.

Alternatively, the MOM size can be regulated through the variation of the ditopic ligand length: the longer the spacer, the larger the size of the resulting assembly (Figure 1-7).

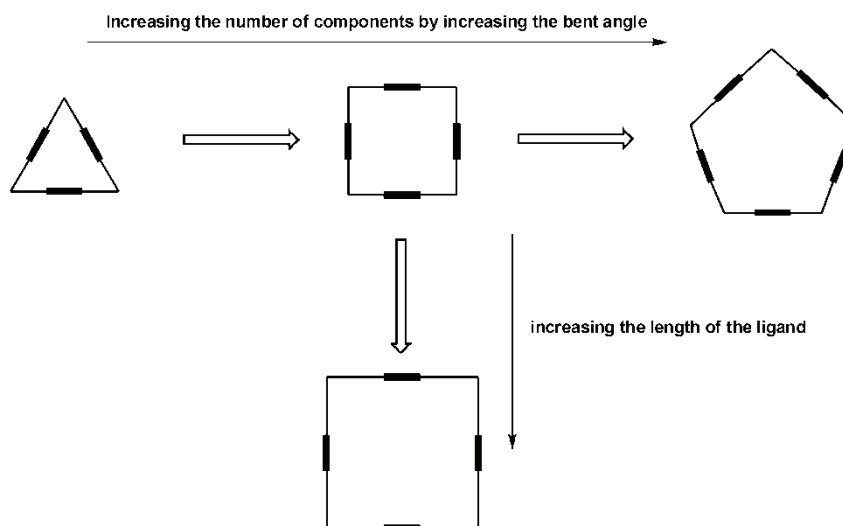


Figure 1-7. Size control of MOMs. Adapted from ref 4.

These predictions of metallacycle sizes assume total conformational rigidity of subunits, but deviations from the ideal binding angles can occur. Metallacycles of different shapes from those predicted by these simple geometrical considerations can therefore occasionally result because of conformational flexibility of the building units.

The MOM synthesis is usually a thermodynamically controlled process; thus the preferred assembly must be thermodynamically more favourable than any other conceivable structure. Several studies¹⁵ on the role of thermodynamic factors in the self-assembly of metallacyclic compounds demonstrated that cyclic structures are preferred over linear ones for enthalpic reasons, because of an increase in the number of bonds is possible per subunit in a cyclic arrangement than to a linear one. Although a cyclic oligomer may polymerize to increase the number of bonds formed, the donor and acceptor sites at each end of the polymer will always remain uncoordinated. When cyclization is unfavourable, the oligomers will likely polymerize until higher oligomers precipitate as kinetic reaction products. Generally, small cycles are favoured over large ones (at low concentrations) for entropic reasons. The greater population of small cycles leads to an increase of the

entropy ($\Delta S > 0$) and thus a decrease of the free energy ($\Delta G < 0$), assuming negligible steric effects and ring strain, (it means $\Delta G \approx -T \Delta S$). On the other hand, larger metallacycles can be obtained under kinetically controlled conditions (at high dilution).

1.3.1 MOM applications

Various applications have been developed for MOM systems. Molecular polygons are known to participate in hydrophobic-hydrophilic molecular recognition and to form host-guest complexes involving electron-rich or anionic guests.¹³ One of the first supramolecular metallacycles by Maverick *et al.*¹⁶ (Figure 1-8) was reported to act as a host for various nitrogen heteroaromatic bases such as pyrazine, pyridine, quinolidine, showing in some cases a remarkable selectivity.

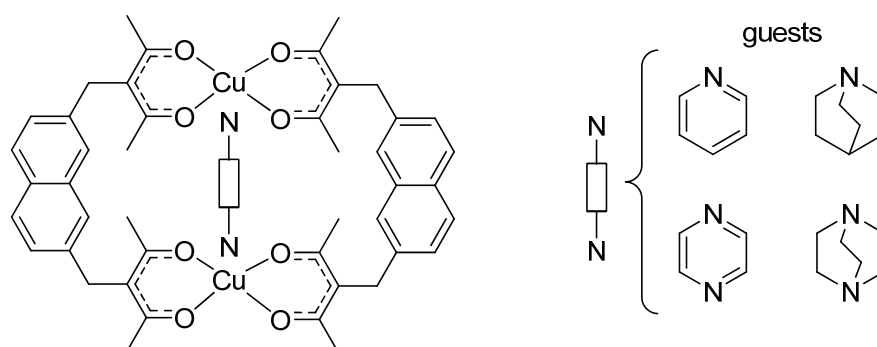


Figure 1-8. The Maverick's dicopper metallacycle as host towards heteroaromatic bases. Adapted from ref 16.

Soon thereafter, Fujita reported the preparation of a macrocyclic palladium complex, $[(en)Pd(4,4'\text{-bpy})]_4(NO_3)_8$ (*en* = ethylenediamine, *bpy* = bipyridine), which is capable of recognizing an organic molecule in aqueous media.¹⁷ Metalla-squares have been used for the transportation of salts over organic phases,¹³ while other square-shaped cycles are potentially useful as artificial receptors.¹⁸ Some MOMs show selective recognition towards anions such as fluoride¹⁹ and nitrate.²⁰ In this respect, Severin *et al.* have described an organometallic metallacyclic complex $[Cp^*Ir(C_5H_3NO_2)]_3$ (Cp^* = pentamethylcyclopentadienyl, C_5Me_5) which acts as a receptor for LiF (Figure 1-9).¹⁹ Cyclic systems have been proven to act as small alkali-metal ions carriers, and in some cases to accommodate reaction intermediates.²¹

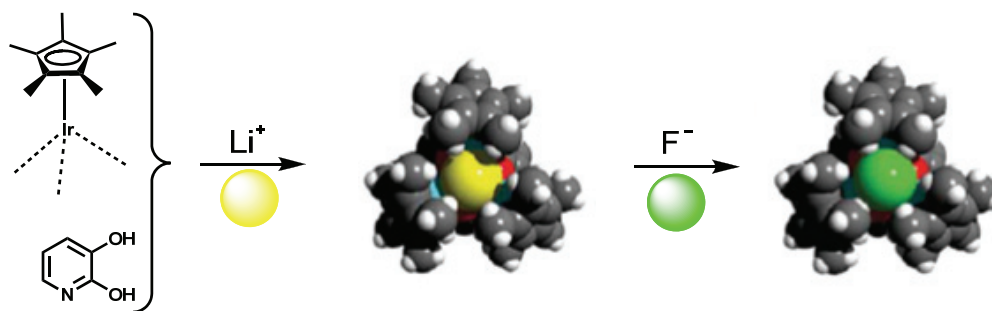


Figure 1-9. A lithium ion, coordinated to a receptor containing three Cp*Ir moieties with bridging 2,3-dihydroxypyridine ligands, is acting as a highly specific binding site for fluoride anion. Adapted from ref 19.

A variety of macrocycles were synthesized in view of a potential application in technological devices²² due to the growing interest in this field. Once embedded into a macrocycle, the metal centres into MOMs have shown photoluminescence or photoelectron transfer properties, as well as highly modified redox and magnetic properties.²³ An example of a photoluminescent metallacyclophane was reported by Hupp *et al.* who synthesised the tetranuclear metallamacrocycle,²⁴ $[\{\text{Pd}(\text{en})\}\{4,4'\text{-bpy}\}\{\text{Re}(\text{CO})_3\text{Cl}\}]_2$ (en = ethylenediamine, bpy = bipyridine), which contains redox active rhenium and cationic palladium centres. The photoluminescence of the compound arises from metal to ligand charge transfer within the π^* -acceptor orbital of the 4,4'-bpy ligand. The use of paramagnetic metal centres in metallacycles construction not only provides access to paramagnetic potential host molecules, but also allows for intramolecular magnetic interactions to be studied within large molecular arrays.²³ Moreover, in many cyclic systems the inclusion of a guest molecule leads to a variation of the host-guest adduct chemical and physical properties with respect to the isolated components.

Finally, MOMs have been also used in catalysis although their potential in this area is far from being exploited. Lin and co-workers²⁵ developed chiral MOM systems having applications in chiral sensing and asymmetric catalysis (Figure1-10). The chiral organometallic triangular complex $[\text{cis}-(\text{PEt}_3)_2\text{Pt}(\text{L4})]_3$, where L4 is the enantiopure [6,6'-dichloro-2,2'-dihydroxy-1,1'-binaphthyl-4,4'-bis(acetylene)] ligand, was successfully used for highly enantioselective catalytic diethylzinc additions to aromatic aldehydes.

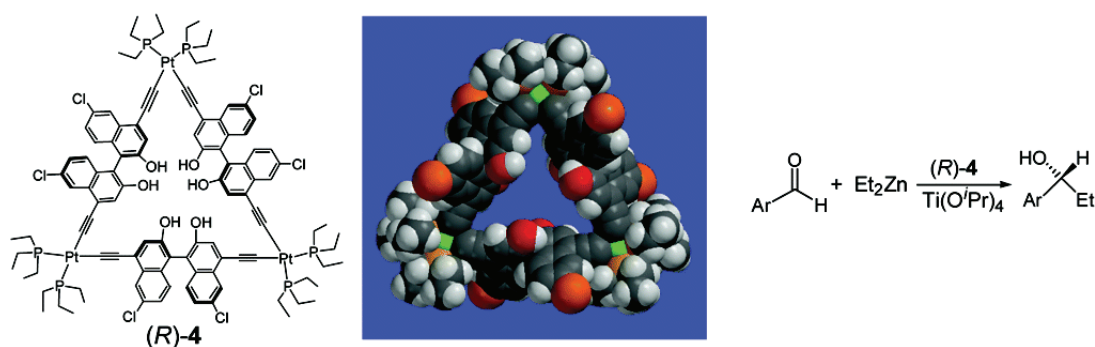


Figure 1-10. A chiral triangular macrocycle and its application in asymmetric catalysis. Adapted from ref 25.

Raymond *et al.* described a highly charged, water-soluble, supramolecular assembly, Ga_4L_6 with $\text{L} = N,N'$ -bis(2,3-dihydroxybenzoyl)-1,5-diaminonaphthalene), with a hydrophobic interior cavity that thermodynamically stabilizes protonated substrates. Consequently, it catalyzes the normally acidic hydrolysis of orthoformates in basic solution, with rate accelerations of up to 890-fold.²⁶ Fujita and co-workers described an aqueous organopalladium cage which induces highly unusual regioselectivity in the Diels-Alder coupling of anthracene and phthalimide guests, promoting reactivity at a terminal rather than the central anthracene ring, with significantly faster rate.²⁷

It was noticed that cyclic squares have the tendency to stack uniformly upon crystallization so that their internal cavities align to form a pore in the structure. This interesting zeolite-like arrangement may find application in solid-state catalysis, especially in cases where the exact dimensions of the absorbing channel are of importance.^{13a} Many square MOMs, reported in the literature,²⁸ form open channels not only in the macroscopic single crystals but also in the microcrystalline thin film. These materials are exceptionally porous with cavities tailored to match the proper size of small molecules while blocking larger molecules. This size-selective materials may consequently find interesting applications in both chemical sensing and catalysis.

1.4 Metal-organic frameworks MOFs

Metal-organic frameworks, MOFs, are crystalline solids that are assembled by connection of metal ions or clusters through molecular bridges.²⁹ Yaghi first

introduced the term **MOF** for the newly synthesized copper 4,4'-bipyridyl complex that exhibited extended metal-organic coordination interaction. According to him: *“for a solid to be labeled a metal-organic framework, it should display the inherent attributes that this term implies: strong bonding providing robustness, linking units that are available for modification by organic synthesis, and a geometrically well-defined structure”*. Although in the literature the term coordination polymers and metal-organic frameworks are often used indiscriminately, *“the term coordination polymers is undoubtedly the most nebulous, as it simply signifies the extended connection of metal and ligand monomers through coordination bonds with no regard towards the final structure or morphology”*.^{29a} Thus, the term “coordination polymer” very broadly includes all the extended structures based on metal ions linked into infinite chains, sheets, or three-dimensional architectures by bridging ligands, usually, but not exclusively, containing carbon atoms.³⁰ The term MOF identifies a class of crystalline porous materials with extraordinary surface areas exceeding those of state-of-art materials, stable in air at room temperature and withstanding temperatures up to 450 °C, made using simple, inexpensive and high yielding solution synthetic methods. The topic search using SciFinder Scholar[®] for the term MOF has increased extraordinarily during the years 2001-2008 along with the exceptional development of this new area of research at the borderline of inorganic, organic, organometallic and materials chemistry.

Table 1-2. Hits for “coordination polymers” and “metal-organic frameworks” in the scientific literature using SciFinder[®] database.

Years	Coordination polymers	Metal-organic frameworks
Up to 1950	1	0
1951-1960	12	0
1961-1970	175	0
1971-1980	130	0
1981-1990	154	0
1991-2000	531	0
2001-2008	3348	687

The first coordination wide-ranging network containing organic bridging ligands was reported in 1952 by Kinoshita *et al.*³¹ who described the polymer $[\text{Cu}(\text{NO}_3)(\text{adiponitrile})_2]_n$ exhibiting a diamond net. This seminal discovery was later followed by a series of milestones in the area which include Werner-type complexes,³² Prussian blue compounds³³ and Hofmann clathrates which first exhibited reversible adsorption properties towards small molecules.³⁴ In 1990, Robson and co-workers described a MOF capable of an anion exchange,³⁵ while in 1994, Fujita *et al.* reported the synthesis of a bipyridine cadmium MOF endowed with catalytic properties.³⁶ Since then, remarkable progress has been made in the MOF area and many research groups have looked into this extraordinary research field contributing to assess it as one of the fundamental research area of modern inorganic and materials chemistry.

1.4.1 Principles in MOF synthesis: connectors, linkers, design

The design of a metal-organic framework is based on the approach defined by Yaghi as **reticular synthesis**, meaning the chemistry of linking molecular building blocks, by strong bonds, into predetermined structures. In the process of structure prediction, it is important to determine the secondary building unit (**SBU**). The SBU are structural entities or simple geometric polygons and/or polyhedra, representing the coordination spheres that are linked together by the typically linear organic components to form the product network. The optimization of the one-step reaction conditions that reproducibly lead to such a particular secondary building unit, allows a tight control of the vertex geometry in the resulting MOF. An illustrative example is MOF-5 originally described by Yaghi in 1999, which consists of Zn_4O units connected by linear 1,4-benzenedicarboxylate linkers to form a cubic network. In MOF-5 the metal-carboxylate structure **a** is an octahedral SBU linked by benzene units to generate a primitive cubic network, **b** (Figure 1-11).³⁷

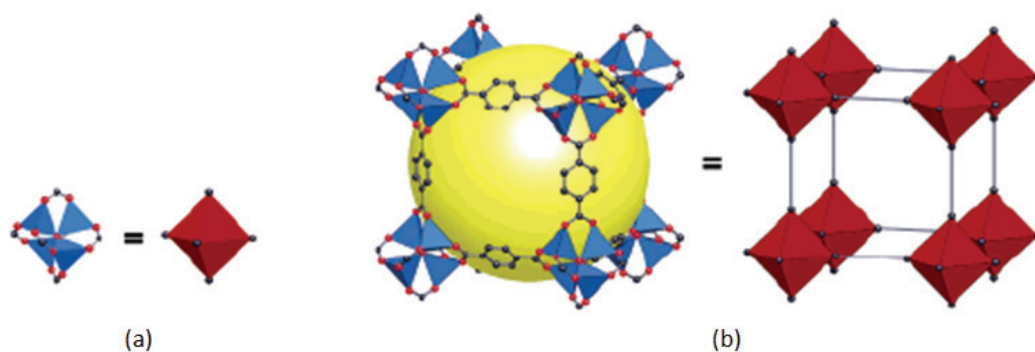


Figure 1-11. Schematic representation of MOF-5.³⁸ Adapted from ref 38.

Since the organic linkers remain intact and their geometry preserved throughout the assembly process, one should also be able to predict the underlying topology of the resulting MOF structure. However, the number of topologies that could, in principle, result from linking molecular shapes into extended MOF structures is so vast that it is difficult to develop a method that can lead to the rationalization and prediction of extended structures.

In spite of this, in some simple cases the synthesis of metal-organic frameworks has led to design porous structures in which functionalities and pore size could be varied systematically. For example, starting from MOF-5 (example **1** in Figure 1-12), it was possible to develop a family of frameworks structurally based on the skeleton of MOF-5, but with pore functionality and size significantly varied without changing the original cubic topology. These structures were called IRMOFs (= isorecticular MOFs). Several members of this series have pore sizes in the mesoporous range ($> 20 \text{ \AA}$) as well as the lowest crystal density of any material reported to date.³⁹

One of the requirements for MOF synthesis and full characterization is to obtain high quality single crystal for structural analysis. Thus, it is often necessary to modify synthetic conditions such as concentration, solvent, pH, temperature within a large range before getting the desired result. Different techniques can be employed, which generally involve the very slow reaction of the building blocks to reduce the rate of crystallite nucleation. These methods include evaporation of a solution of the precursors, layering of solutions, or slow diffusion of one component into another through a membrane or an immobilizing gel (Figure 1-13).

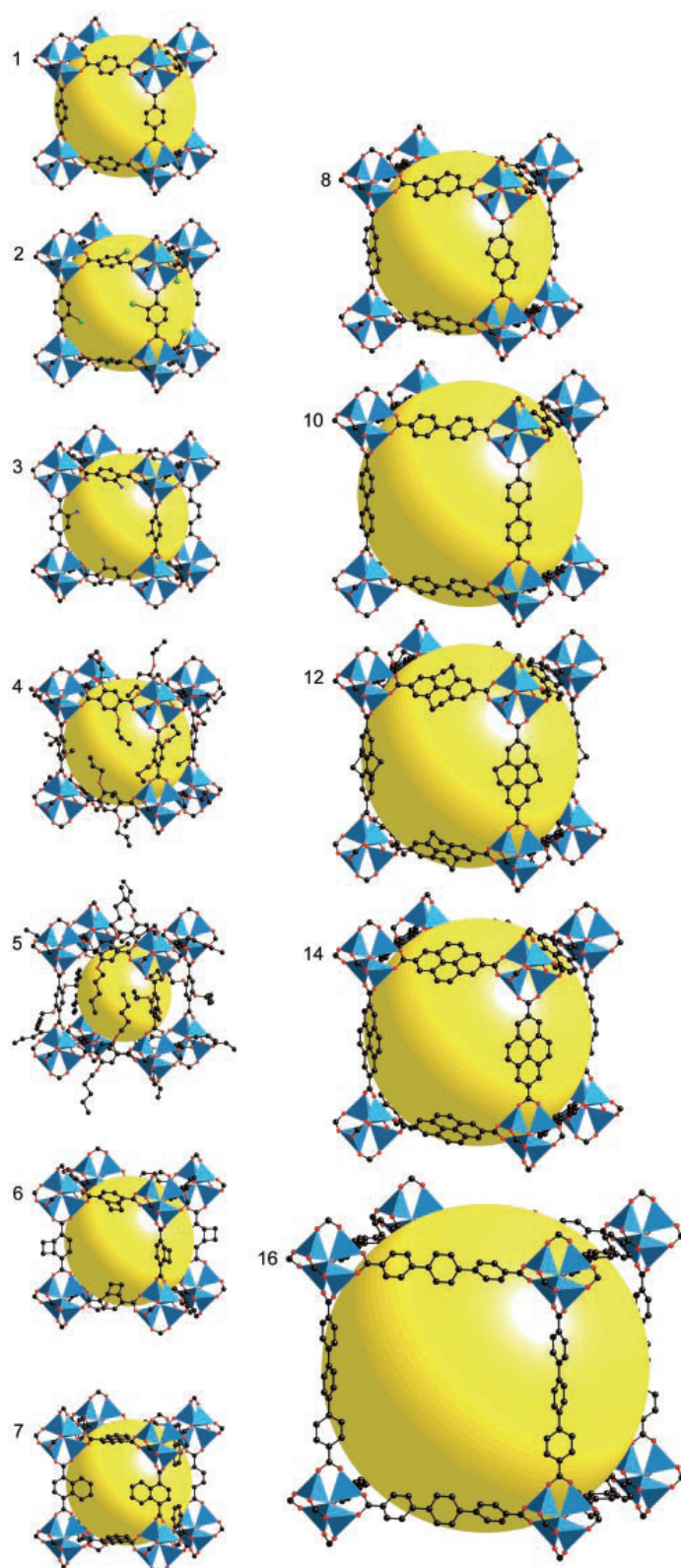


Figure 1-12. Single crystal X-ray structures of MOF $[Zn_4O(R_x-BDC)_3]_n$ obtained with 1,4-benzenedicarboxylate (BDC) as ligand and functionalized with different expanded molecular spacers biphenyl, pyrene, tetrahydropyrene, terphenyl, indicated with R. The large yellow spheres represent the largest van der Waals spheres that would fit in the cavities without touching the frameworks. Adapted from ref 29a.

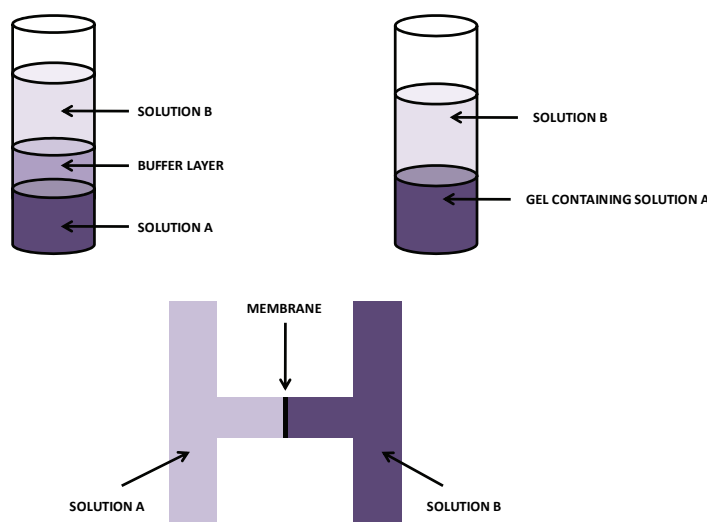


Figure 1-13. Different methods used for the growth of crystalline MOFs. Adapted from ref 3.

Good results were obtained also using microwave and ultrasonic methods,⁴⁰ although both methodologies have not been completely explored yet. The method which seems to be the most efficient is the hydro(solvo)thermal synthesis,⁴¹ originally used for the synthesis of zeolites. The precursors are combined as dilute solutions in polar solvents such as water, alcohols, acetone and acetonitrile and heated in sealed vessels such as Teflon-lined stainless steel autoclaves or glass tubes, under autogenous pressure. The running temperature ranges from 120 to 260 °C. Under these severe conditions the reduced viscosity of water or other solvents enhances the diffusion process and thus extraction of solids and crystal growth from solution are favoured. Mixed solvent systems are often used to tune the solution polarity and the kinetics of solvent-ligand exchange, resulting in the effective enhancement of crystal growth.³

An important aspect of MOF crystallization is the possible formation of various solid species from the same starting materials, irrespectively from the stoichiometry ratio used. Supramolecular isomerism is defined as the capability of a substance to exist in more than one type of network superstructure for the same molecular building units and the same formal stoichiometry. When flexible molecular components are used, *i.e.* ligands with different conformations, this phenomenon is termed conformational supramolecular isomerism. Structural isomers are structures with different metal coordination spheres. The polymorphism is the existence of the same compound in more than one crystalline

modification; it means materials with different lattice and/or molecular conformation. In particular, the pseudo-polymorphs or solvates are crystalline forms that differ for the nature or the stoichiometry of solvent molecules. Different solids can be generated under different reaction conditions or may be assembled at the same time as a mixture in the same batch, and also in the same crystal with concomitant motifs

1.4.2 Porous properties of MOFs

High porosity is surely one of the essential characteristics of MOFs for many applications such as gas storage, catalysis and molecular sieving, exploiting the reversible passage of the guest molecules through the host. The adsorption process depends on the interaction between guests and surface and ultimately on the host's pore size and shape. Pores can be classified according to their size as shown in Table 1-3.⁴² Obviously the ideal pore size for maximal attraction of an adsorbate is the same as its diameter.

Table 1-3. Classification of pores in porous materials.

Pore type	Pore size (Å)
Ultramicropore	< 5
Micropore	5 - 20
Mesopore	20 - 500
Macropore	> 500

In order to define a porous material, the pores must exist independently from the presence of a guest. Since the holes of the MOF are usually occupied by solvent molecules, it is necessary to remove or exchange them with other species and then to verify the integrity of the framework after the *activation* process. The term *open framework* defines a material containing highly disordered unbonded solvent molecules that appear to flow freely through the void spaces of the well-defined frameworks.^{29b} The XRPD and thermogravimetric analysis (TGA) are usually very useful techniques to investigate the structural stability of a MOF. Powder X-ray

diffraction (XPRD) is a unique and effective tool to establish the purity of the crystalline MOF.⁴³ In fact, the various phases present in a solid mixture can be identified by indexing of the diffractogram peaks followed by comparison with tabulated data. TGA reveals the temperature of guest removal as well as the temperature of framework decomposition, but it does not provide any information on the framework stability. By heating above the guest removal temperature, the XRPD pattern of the guest-free bulk material is obtained. The structural analysis thus affords direct information about both robustness and flexibility and also gives some indications whether the crystalline phase is maintained or an amorphous material is produced upon heating. Other important preliminary characterisation data come from the elemental analysis (EA), and the standard spectroscopic methods, like solid-state or solution infrared (IR) and/or nuclear magnetic resonance (NMR) spectroscopies which can indicate the occurrence of structural changes during guest desorption.

Subsequently, to establish the attainment of permanent porosity the measurement of gas isotherms are indispensable. There are six representative adsorption isotherms according to IUPAC classification, which correlate the sorption type with the porous structure (Figure 1-14).⁴⁴

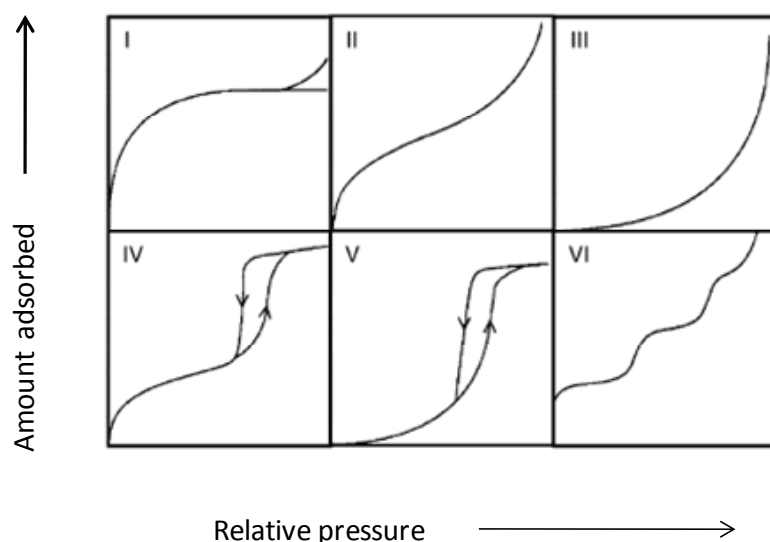


Figure 1-14. IUPAC classification of adsorption isotherms.

The type I isotherm is characteristic of microporous materials, while types II, III and VI are typical of non-porous and macroporous solids. Types IV and V are associated with mesoporosity. The presence of the hysteresis loop in these isotherms is a direct proof of evidence of the presence of mesopores. This is due to different adsorption and desorption rates at high P/P° values. The physisorption on a mesoporous sample is regulated by capillary condensation, which determines a sharp adsorption rise around the mid relative-pressure region. The gas sorption on microporous cavities occurs on the nanoscale level (*i.e.* holes with the same order of magnitude of the adsorbent used); so, the isotherm shows a steep rise at very low pressures and a rapid reach of the saturation limit even at very low relative pressures.

The measurement of gas (nitrogen and argon) isotherms, performed at the adsorptive condensation temperature (77 K or 87 K, respectively) provides an estimation of the MOF apparent surface area, that is a very important parameter together with the pore size distribution. Type I isotherms can be described by the Langmuir model,⁴⁵ which assumes that a homogenous monolayer of the adsorbate is formed on the walls of the adsorbent. Sorption isotherms of organic vapours (such as chloroform, benzene, or cyclohexane) aid in the estimation of MOF morphology and stability. The gas and vapour sorption isotherms for the desolvated sample can be measured using an electromicrogravimetric balance to evaluate the pore volume and the apparent surface area of frameworks.⁴⁶ Ion,^{47,42e} solvent⁴⁸ and guest molecule exchanges are studied to provide evidence of the accessibility of these void regions.

Many of the known MOFs possess surface areas greater than $2000 \text{ m}^2 \text{ g}^{-1}$, which is a much higher value than that normally found in zeolites (around $700\text{--}800 \text{ m}^2 \text{ g}^{-1}$). The surface area calculated from the nitrogen isotherm of MOF-177, $[\text{Zn}_4\text{O}(\text{benzene-1,2,3-tribenzoate})_2]_n$, is particularly notable, $4500 \text{ m}^2 \text{ g}^{-1}$. This MOF exhibits pores of 0.69 mL g^{-1} volume and cavities of $10.9 - 11.8 \text{ \AA}$ diameter.^{29b}

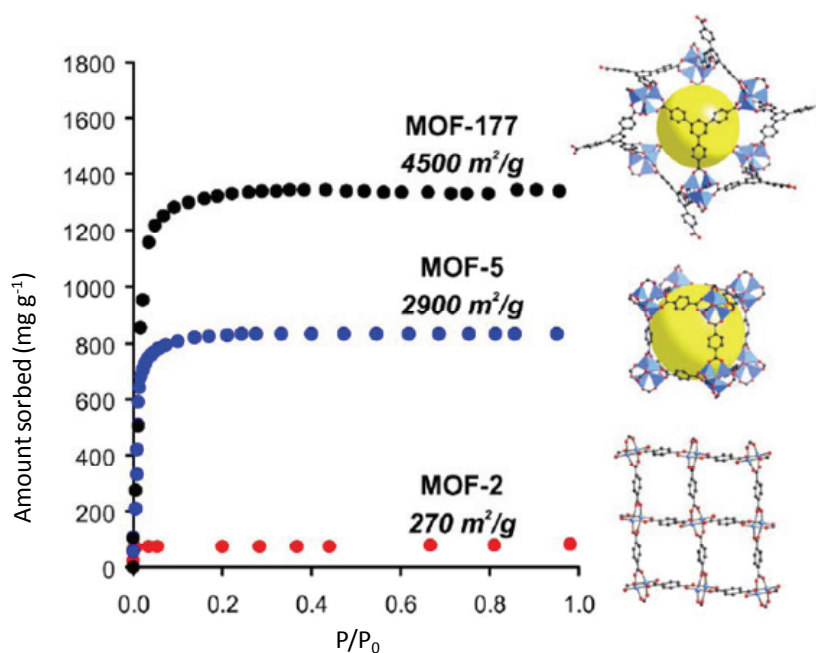


Figure 1-15. The nitrogen sorption isotherms in various MOFs, measured at 77 K, display hydrogen sorption capacity, as expected for compounds with uniform micropores. Adapted from ref 29b.

Currently, the largest surface area is $5900 \text{ m}^2 \text{ g}^{-1}$, value reported by Férey *et al.*⁴⁹ for a chromium(III) terephthalate-based solid $\{\text{Cr}_3\text{F}(\text{H}_2\text{O})_2\text{O}[(\text{O}_2\text{C})\text{-C}_6\text{H}_4\text{-(CO}_2)_2]_3 \cdot n\text{H}_2\text{O}\}_2$ showing large pore size (30 - 34 Å) and giant cell volume ($702,000 \text{ Å}^3$).

The adsorption isotherms of small molecules can be modelled by using Monte Carlo (MC) simulations.⁵⁰ This is an approach based on the known crystallographic and adsorption data of MOFs, reported in the literature. The MC simulations are carried out using formal HF-based and B3LYP-based charge densities. In these simulations it is not necessary to make any assumption about the host structures because of the well-characterized regular structure exhibited by porous networks. Consequently, this predictive approach gives good results often in nice agreement with experimental data, as it has been shown for the frameworks $[\text{Zn}(1,4\text{-benzdicarboxylate})]_n$ and $[\text{Cu}_3(1,3,5\text{-benzdicarboxylate})_2]_n$.⁵¹

1.4.3 MOF applications

The porosity of a material is a feature of considerable value, which has aroused great interest in both the scientific community and the industrial field.

Specifically, porous coordination polymers are good candidates to be used as adsorbents for the storage of different gaseous molecules such as hydrogen, methane, nitrogen, carbon dioxide and argon.

Hydrogen is currently considered a promising green energy source alternative to fossil fuels, whose availability is strongly influenced by political-economic factors and limited natural reserves.⁵² Hydrogen is not a primary energy source but an energy carrier, since it cannot be found in natural reservoirs like oil, but must be generated before use. It may be employed as a fuel in a combustion engine or in a fuel cell giving electricity without emission of greenhouse gases and related air pollution. One of the most important challenges for the development of the “hydrogen economy”⁵³ is the availability of a safe and efficient system for hydrogen storage and transportation for automobile applications. A possible idea behind this concept is to find the way to compress H₂ inside a porous material at moderate pressure and at nearly ambient temperature. Materials suitable for fulfilling this goal must satisfy a series of criteria. They should be light to reduce the weight associated with the on-board technology; they should have small volumes and exhibit fast kinetics for hydrogen reloading at an easily accessible temperatures. Finally, hydrogen should be easily released, possibly by moderately heating the storage tool.

During the last decades, metal hydride systems, zeolites and various carbon-based adsorbents, including carbon nanotubes and nanofibers, have been investigated as possible candidates to store H₂.⁵⁴ Recently, MOFs have been tested for this purpose. Having a large quantity of chemically stored hydrogen would solve the problem of carrying pressurized or liquefied gas in heavy metal cylinders, and in turn would allow for a constant low-pressure supply of hydrogen for fuel cells which could replace the traditional engine in cars and other mobile applications. The US Department of Energy (DOE) target for hydrogen to be used in automobile fuelling is 6.0 wt% , that is about 45 grams of hydrogen per liter. Yaghi and co-workers have demonstrated that it is possible to store hydrogen in MOF-177 at 7.5 wt% at 77 K. It means it is possible to store sufficient hydrogen in MOFs to be useful for storage and automotive application, but at 77 K. Currently, MOF-177 provides the best H₂-storage result obtained so far,⁵⁵ with 62 grams of hydrogen per liter at 77 K, which

is more than two thirds than that obtained from liquid hydrogen at 20 K. The next goal is to obtain similar hydrogen uptake numbers at (nearly) ambient temperatures.

The current hydrogen adsorption record for a metal-organic framework at room temperature is indeed still far from DOE target being that of the compound $[\text{Mn}_3\{(\text{Mn}_4\text{Cl})_3(\text{BTT})_8\}_2]$ [H_3BTT = benzene-1,3,5-*tris*(1H-tetrazole)],⁵⁶ which is capable of storing 12.1 g L^{-1} of hydrogen at $9 \times 10^6 \text{ Pa}$ and 298 K, corresponding to 1.6 wt% (Figure1-16).

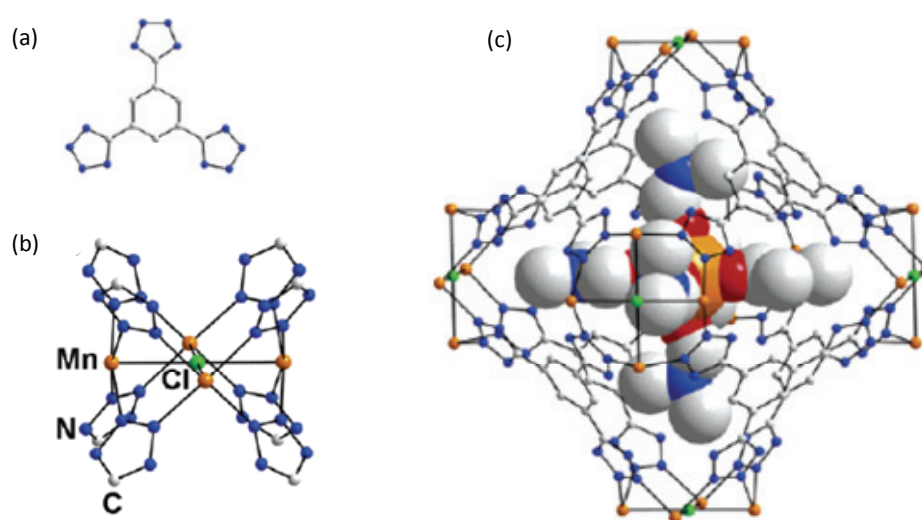


Figure 1-16. Portions of the crystal structure of $[\text{Mn}_3\{(\text{Mn}_4\text{Cl})_3(\text{BTT})_8\}_2]$: (a) molecular structure of the tritopic ligand H_3BTT ; (b) a square-planar Mn_4Cl cluster surrounded by eight tetrazolate rings, (c) a sodalite cage-like unit encasing a $[\text{Mn}(\text{DMF})_6]^{2+}$ complex. Adapted from ref 56.

The metal-organic frameworks are good materials for the storage of methane and carbon dioxide too, with important implications for the environment. Unlike hydrogen, a high uptake is currently possible at room temperature for both molecules and intriguing perspectives are opened for the development of MOFs-based tanks for methane in automobile industry.^{57, 39}

Methane, as well as hydrogen, is a cleaner fuel than petrol or coal, and it represents two-thirds of our global natural energy resources.^{57a} So the methane is an important candidate for clean transportation fuels. The conventional adsorbents with macro- or mesopores are unable to trap the methane molecules because the holes are too big. Instead, it has been demonstrated that in microporous materials,

such as MOFs, whose pore size is suited for methane, the gas is homogeneously and thickly distributed in the solid. The IRMOF-6, $[\text{Zn}_4\text{O}(\text{cyclobutyl-1,4-dibenzoate})_3 \cdot (\text{CHCl}_3)_7]$ (IRMOF-n is a MOF-5 $[\text{Zn}_4\text{O}(\text{R}_n\text{-1,4-dibenzoate})_3]$ with different R_n functional groups) exhibits an uptake of $240 \text{ cm}^3 \cdot \text{g}^{-1}$ of CH_4 at 298 K and 36 atm. It means the methane adsorbed is about 70% of the amount stored in gas cylinders where much higher pressure (205 atm) are used.

MOFs can find applications in areas related to an important environmental issue such as the control of **carbon dioxide** emissions and greenhouse effect. The world produces more than four tons of carbon dioxide *pro capite* each year which are considered the main responsible the global warming.⁴⁶ In order to control the emission levels of carbon dioxide, it has been proposed to use a porous material capable of trapping the flue gas from power sources, thus reducing the cost for CCS procedures generally based on the application of aqueous amine solutions as CO_2 scavengers. For example, MOF-177 gave good results even in carbon dioxide storage. About 33.5 mmol g^{-1} of CO_2 can be stored in MOF-177 at room temperature at very acceptable pressures.

The porous nature of MOFs may provide significant advantages for applications in **heterogeneous catalysis**. The implementation of MOFs in catalysis represents a promising field of “industrially-oriented” research. However, catalytic tests have been reported only in a few instances and this area deserves much more attention. There are two distinct possibilities to account for MOF application in catalysis: the coordination networks themselves can be catalytically active or they can act as hosts for other metallic nanoparticles that catalyze specific transformations. In this context, a dimensional microporous polymer of Rh fumarate or terephthalate complexes, synthesized by Saito and co-workers, exhibited high catalytic activity for hydrogen exchange and hydrogenation of olefins at 200 K.⁵⁸ The hydrogen exchange reaction takes place only inside the nanopores of the complexes without complete scission of the alkene C–H bond. Rosseinsky *et al.* reported the rational, post-synthetic modification of an homochiral MOF leading to a functional Brønsted acidic material that is active as asymmetric catalyst in the methanolysis of *cis*-2,3-epoxybutane.⁵⁹ Corma *et al.* reported a palladium-containing metal–organic framework (Pd-MOF) which behaves as an active catalyst

for alcohol oxidation, Suzuki coupling, and olefin hydrogenation.⁶⁰ The MOF structure is preserved throughout the catalytic reaction and the material is reusable. The Pd-MOF demonstrates remarkable shape-selectivity for olefin hydrogenation.

Chiral metal organic frameworks have been synthesized and used for asymmetric catalysis. These materials have catalytic pocket cavities with chiral environment for enantioselective control. Kim *et al.* reported the synthesis of a homochiral metal-organic porous material that allows the enantioselective inclusion of metal complexes into the pores and catalyses the asymmetric transesterification of 2,4-dinitrophenyl acetate with bulky alcohols such as isobutanol, neopentanol and 3,3,3-triphenyl-1-propanol.⁶¹ Finally, Sasai *et al.* have reported chiral MOFs containing two binaphthol units coordinated by Ti(II) which catalyze the asymmetric carbonyl-ene reactions.⁶²

As a final consideration, it is worth mentioning that MOF may be also used for applications not strictly related to porosity. Metallorganic polymers have been indeed studied for their luminescence properties and investigated for their potential applications as light-emitting diodes (LEDs).⁶³ Magnetic studies of MOFs have been also undertaken and are related to the area of molecular magnetism and the design of light-molecular-based magnets.⁶⁴ MOFs containing luminescent lanthanides⁶⁵ or paramagnetic transition metals⁶⁶ proved to have excellent sensor capabilities when the optical, electronic or magnetic properties are altered by guest interactions.

1.5 Scope and aims of the thesis work

In this PhD thesis work, our attention has mostly focused on the design of new MOF- and MOM-type materials, applying the general “*complex-as-ligand approach*” for the rational design of metallasupramolecular assemblies. Focusing mainly on this point, our approach was that of suggesting some new ligands to be applied in this area. Namely, ligands belonging to two classes of compounds have been investigated: carboxylic acids and phosphines. A short summary of each thesis chapter is given below.

Chapter 2. Di-, tri-, and tetra-carboxylate molecules are typical anionic linkers used in MOF synthesis. Multidentate linkers such as carboxylates allow for the formation of more rigid frameworks due to their ability to aggregate metal ions into M-O-C clusters/secondary building units (SBUs, Figure 1-17).⁶⁷

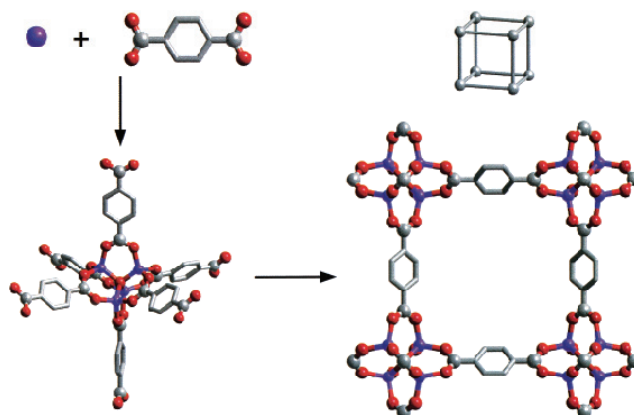


Figure 1-17. Assembly of metal-organic frameworks (MOFs) by the copolymerization of metal ions with organic linkers to give rigid metal-carboxylate clusters that can be linked by benzene to form rigid extended frameworks in which the M-O-C core (SBU) of each cluster acts as a large octahedron decorating a 6-connected cube (M, purple; O, red; C, gray). Adapted from ref 67.

Since rigid linkers with aromatic groups have been widely used in the synthesis of MOFs, we were interested in exploring this chemistry by using some aliphatic carboxylic ligands whose flexibility might increase the degree of structural diversity of the resulting networks. Solvothermal syntheses afforded new 3D magnesium formates existing in different crystalline polymorphs, $\text{H}[\text{Mg}(\mu\text{-HCOO})_3] \supset \text{NHMe}_2$ (**a** in Figure 1-18) and $\text{Mg}(\mu\text{-HCOO})_2 \cdot 2\text{H}_2\text{O}$ (**b** and **c** in Figure 1-18), depending on the initial concentration of the solution (Figure 1-18).⁶⁸ The $\text{H}[\text{Mg}(\mu\text{-HCOO})_3] \supset \text{NHMe}_2$ microporous species was tested in host-guest experiments with water, CO_2 and H_2 . GCMC (Grand Canonical Monte Carlo) simulations of H_2 absorption isotherms pointed to the existence of two different adsorption sites at high pressures of H_2 and estimate a theoretical maximum loading of H_2 corresponding to 12 molecules per unit cell, that is 4.2 mg g^{-1} . Raman studies of physisorbed H_2 confirmed the theoretical data.

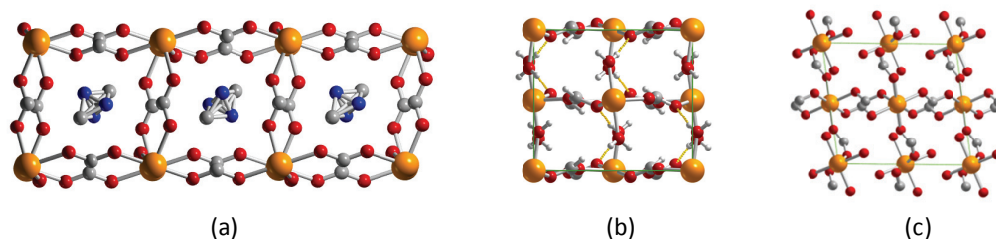


Figure 1-18. Crystal structures of MOFs $\text{H}[\text{Mg}(\mu\text{-HCOO})_3] \cdot \text{NHMe}_2$ (a) e two $\text{Mg}(\mu\text{-HCOO})_2 \cdot 2\text{H}_2\text{O}$ (b, c) (C, grey; O, red; Mg, orange; N, blue).

Chapter 3. A series of molecules containing functional pyridyl and/or carboxylic groups, either symmetrical, $^-\text{OOC-X-COO}^-$ ($X = \text{spacer}$), or non-symmetrical, $^-\text{OOC-X-pyridine}$, based on thiazolidine, thiazole or oxazole spacers were considered as possible ligands in coordination chemistry. A new large-scale synthesis of the organic spacers has been developed starting from the naturally-occurring amino acids serine and cysteine.⁶⁹ The coordination properties of the new heteroaromatic ligands were inspected with a variety of metal ions and led to a series of coordination complexes with interesting supramolecular structures.⁷⁰ Finally, the aliphatic cycle *syn*-(2*R*,4*R*)-tdca [tdca = thiazolidine-2,4-dicarboxylate] formed a three-dimensional MOF with cobalt salts (Figure 1-19), whose structure shows an alternation of hydrophobic and hydrophilic channels, with cross sections of about 16 \AA^2 .

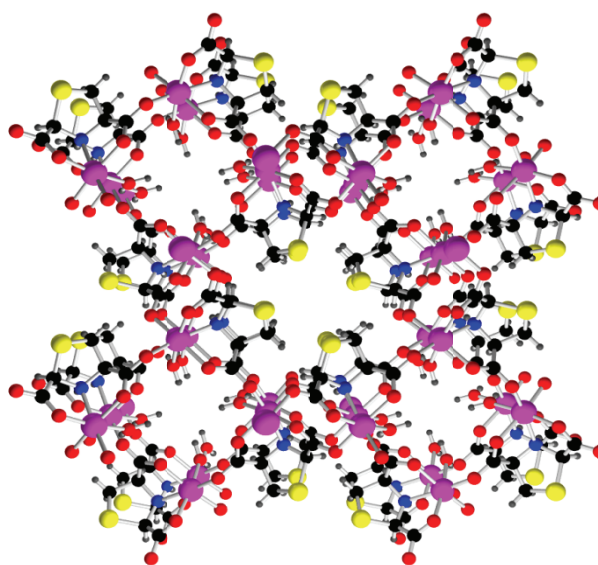


Figure 1-19. Crystal structure of the MOF $[\text{Co}(\text{tdca})(\text{H}_2\text{O}) \cdot (\text{H}_2\text{O})_{0.5}]_\infty$ with tdca = (2*R*,4*R*)-thiazolidine-2,4-dicarboxylate (C, black; O, red; S, yellow; N, blue; Co, magenta).

The intrinsic chirality present in this system (the ligand is enantiomerically pure) may be of interest in possible applications in the field of enantioselective catalysis.

Chapter 4. Phosphines are very popular ligands in supramolecular chemistry. The pyramidal geometry at phosphorus and the relatively free P-C rotation allow for a range of accessible orientations of the lone pairs. The softer character of the P donor in phosphines *versus* the O-donor in carboxylic acids can in principle be an advantage and give access to very stable structures containing softer Lewis acids. Based on these considerations, a new class of bi- and tridentate alkynyl phosphine ligands was synthesized and their coordination properties explored to develop new metallorganic macrocycles MOMs.⁷¹ The phosphine ligands, 1,4-(Ph₂PC≡C)₂C₆H₄ e 1,3,5-(Ph₂PC≡C)₃C₆H₃, were obtained using a novel synthetic approach and studied in reactions with half-sandwich cyclopentadienyl complexes of Ru(II). By appropriately varying the reaction conditions, monomolecular bi- and trimetallic complexes, with interesting stereochemical features, and two MOMs, a dinuclear complex and a tetranuclear square, have been synthesized (Figure 1-20).

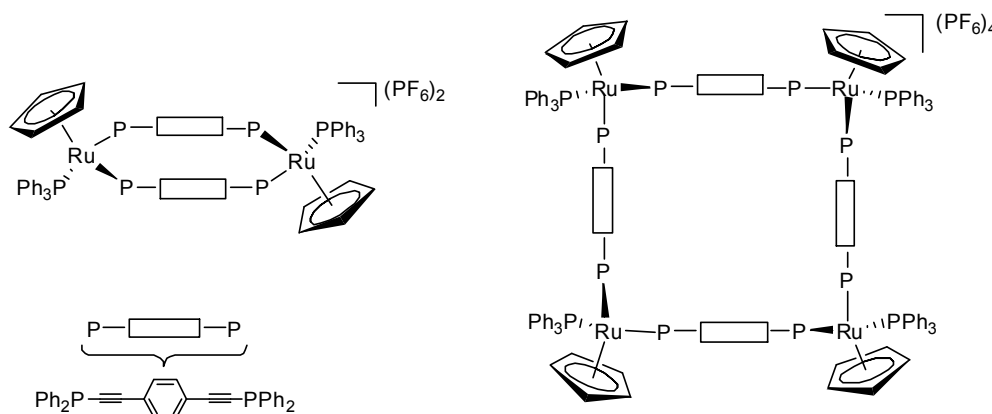


Figure 1-20. Dinuclear and tetranuclear ruthenium MOMs based on the dppab alkynylphosphine ligand.

All complexes were characterized by electrochemical methods and, for the electrogenerated paramagnetic species, by ESR spectroscopy. Using an ITO electrode (Indium Tin Oxide), the growth of a polymer film was observed for the tetranuclear complex.

1.6 References

- 1 Yaghi, O. M.; O'Keeffe, M.; Ockwing, N. W.; Eddaoudi, M.; Kim, J. *Nature* **2003**, *423*, 705.
- 2 Elsevier, C. J.; Reedijk, J.; Walton, P. H.; Ward, M. D. *Dalton Trans.* **2003**, 1869.
- 3 Batten, S. R.; Neville, S. M.; Turner, D. R. *Coordination Polymers Design, Analysis and Application*, The Royal Society of Chemistry, Cambridge, UK, **2009**.
- 4 Prakash, M. J.; Lah, M. S. *Chem. Commun.* **2009**, 3326.
- 5 James, S. L. *Chem. Soc. Rev.* **2003**, *32*, 276.
- 6 Janiak, C. J. *Chem. Soc. Dalton Trans.* **2000**, 3885.
- 7 Robin, A. Y.; Fromm, K. M. *Coord. Chem. Rev.* **2006**, *250*, 2127.
- 8 Fèrey, G.; Latroche, M.; Serre, C.; Millange, F.; Loiseau, T.; Percheron-Guègan, A. *Chem. Commun.* **2003**, 2976.
- 9 Côtè, A. P.; Shimizu, G. H. K. *Chem. Eur. J.* **2003**, *9*, 5361.
- 10 a) Chen, B.; Wang, L.; Zapata, F.; Qian, G.; Lobkovsky E. B. *J. Am. Chem. Soc.* **2008**, *130*, 6718; b) Liu, W. S.; Jiao, T. Q.; Li, Y. Z.; Liu, Q. Z.; Tan, M. Y.; Wang, H.; Wang, L. F. *J. Am. Chem. Soc.* **2004**, *126*, 2280; c) Zhao, B.; Chen, X.-Y.; Cheng, P.; Liao, D.-Z.; Yan, S.-P.; Jiang, Z.-H. *J. Am. Chem. Soc.* **2004**, *126*, 15394.
- 11 Kitagawa, S.; Noro, S. *Comp. Coord. Chem.* **2004**, *7*, 231.
- 12 a) Fujita, M.; Ogura, K. *Coord. Chem. Rev.* **1996**, *148*, 249; b) Fujita, M. *Chem. Soc. Rev.* **1998**, *27*, 417.
- 13 a) Stang, P. J.; Olenyuk, B. *Acc. Chem. Res.* **1997**, *30*, 502 and references therein; b) Leininger, S.; Olenyuk, B.; Stang, P. J. *Chem. Rev.* **2000**, *100*, 853; c) Olenyuk, B.; Fechtenkötter, A.; Stang, P. J. *J. Chem. Soc., Dalton Trans.* **1998**, 1707.
- 14 Swiegers, G. F.; Malefetse, J. *Chem. Rev.* **2000**, *100*, 3483.
- 15 a) Chi, X.; Guerin, A. J.; Haycock, R. A.; Hunter, C. A.; Sarson, L. D. *J. Chem. Soc., Chem. Commun.* **1995**, 2563; b) Chi, X.; Guerin, A. J.; Haycock, R. A.; Hunter, C. A.; Sarson, L. D. *J. Chem. Soc., Chem. Commun.* **1995**, 2567; c) Lawrence, D. S.; Jiang, T.; Levett, M. *Chem. Rev.* **1995**, *95*, 2229.
- 16 Maverick, A. W.; Buckingham, S. C.; Yao, Q.; Bradbury, J. R.; Stanley, G. G. *J. Am. Chem. Soc.* **1986**, *108*, 7430.
- 17 Fujita, M.; Yakazi, J.; Ogura, K. *J. Am. Chem. Soc.* **1990**, *112*, 5645.
- 18 Linton, B.; Hamilton, A. D. *Chem. Rev.* **1997**, *97*, 1669.
- 19 Leherain, M.-L.; Scoppeliti, R.; Piotrowski, H.; Severin, K. *Angew. Chem., Int. Ed.* **2002**, *41*, 1419.
- 20 Cutland, A. D.; Malkani, R. G.; Kamft, J. W.; Pecoraro, V. L. *Angew. Chem., Int. Ed.* **2000**, *39*, 2689.
- 21 Jung, M.; Kim, H.; Baek, K.; Kim, K. *Angew. Chem., Int. Ed.* **2008**, *47*, 5755.
- 22 Tasiopoulos, A. J.; Vinslava, A.; Wernsdorfer, W.; Abboud, K. A.; Christou, G. *Angew. Chem., Int. Ed.* **2004**, *43*, 2117.
- 23 Jones, C. J. *Chem. Soc. Rev.* **1998**, *27*, 289 and references therein.
- 24 Slone, R. V.; Yoon, D. I.; Calhoun, R. M.; Hupp, J. T. *J. Am. Chem. Soc.* **1995**, *117*, 11813.
- 25 a) Wu, C.-D.; Lin, W. *Angew. Chem., Int. Ed.* **2006**, *46*, 1075; b) Lee, S. J.; Lin, W. *Acc. Chem. Res.* **2008**, *41*, 521.
- 26 Pluth, M. D.; Bergman, R. G.; Raymond, K. N. *Science* **2007**, *316*, 85.
- 27 Yoshizawa, M.; Tamura, M.; Fujita, M. *Science* **2006**, *312*, 251.
- 28 Kumar, A.; Sun, S.-S.; Lees, A. J. *Coord. Chem. Rev.* **2008**, *252*, 922.

- 29 a) Yaghi, O. M.; Li, H. L. *J. Am. Chem. Soc.* **1995**, *117*, 10401; b) Roswell, J. L. C.; Yaghi, O. M. *Microporous Mesoporous Mater.* **2004**, *73*, 3; c) Kitagawa, S.; Kitaura, R.; Noro, S.-I. *Angew. Chem., Int. Ed.* **2004**, *116*, 2388; d) *Chem. Soc. Rev.* **2009**, *38*, 1201.
- 30 Biradha, K.; Ramanan, A.; Vittal, J. J. *Cryst. Growth Des.* **2009**, *9*, 2969.
- 31 Kinoshita, Y.; Matsubara, I.; Higuchi, T.; Saito, Y. *Bull. Chem. Soc. Jpn.* **1959**, *32*, 1221.
- 32 Barre, R. M. *Molecular Sieves*, American Chemical Society, Washington, USA, **1974**.
- 33 Wilde, R. E.; Ghosh, S. N.; Marshall, B. J. *Inorg. Chem.* **1970**, *9*, 2512.
- 34 a) Iwamoto, T. *Inclusion Compd.* **1984**, *1*, 29; b) Iwamoto, T. *Inclusion Compd.* **1991**, *5*, 172.
- 35 Hoshins, B. F.; Robson R. *J. Am. Chem. Soc.* **1990**, *112*, 1546.
- 36 Fujita, M.; Kwon, Y. J.; Washizu, S.; Ogura, K. *J. Am. Chem. Soc.* **1994**, *116*, 1151.
- 37 Li, H.; Eddaoudi, M.; O'Keeffe, M.; Yaghi, O. M. *Nature* **1999**, *402*, 276.
- 38 Rosi, N. L.; Kim, J.; Eddaoudi, M.; Chen, B.; O'Keeffe, M.; Yaghi, O. M. *J. Am. Chem. Soc.* **2005**, *127*, 1504.
- 39 Eddaoudi, M.; Kim, J.; Rosi, N.; Vodak, D.; Watcher J.; O'Keeffe, M.; Yaghi, O. M. *Science* **2002**, *295*, 469.
- 40 Some early examples of microwave and ultrasonic syntheses applied to MOFs are the following:
a) Jhung, S. H.; Lee, J.-H.; Forster, P. M.; Ferey, G.; Cheetham, A. K.; Chang, J.-S. *Chem. Eur. J.* **2006**, *12*, 7699; b) Hwang, Y. K.; Chang, J. S.; Park, S. E.; Kim, D. S.; Kwon, Y. U.; Jhung, S. H.; Hwang, J. S.; Park, M. S. *Angew. Chem. Int. Ed.* **2005**, *44*, 556; c) Qiu, L.-G.; Li, Z.-Q.; Wu, Y.; Wang, W.; Xu, T.; Jiang, X. *Chem. Commun.* **2008**, 3642.
- 41 Some early examples of solvothermal (or hydrothermal) syntheses applied to MOFs are the following: a) Yaghi, O. M.; Li, H. *J. Am. Chem. Soc.* **1995**, *117*, 10401; b) Yaghi, O. M.; Li, G.; Groy, T. L. *J. Solid State Chem.* **1995**, *117*, 256; c) Yaghi, O. M.; Li, G.; Li, H. *Nature* **1995**, *378*, 703; d) Yaghi, O. M.; Li, H.; Groy, T. L. *J. Am. Chem. Soc.* **1996**, *118*, 9096.
- 42 IUPAC Manual of symbols and terminology, Appendix 2, Pt. 1, Colloid and Surface Chemistry [*Pure Appl. Chem.* **1972**, *31*, 578].
- 43 An interesting review on the last advances in the XRPD technique is available, see: Harris, K. D. M.; Cheung, E. Y. *Chem. Soc. Rev.* **2004**, *33*, 526
- 44 Gregg, S. J.; Sing, K. S. W. *Adsorption, Surface Area, and Porosity*, Academic Press, London, UK, **1984**.
- 45 Rouquerol, F.; Rouquerol, J.; Sing, K. *Adsorption by Powders and Porous Solids*, Academic Press, London, UK, **1999**.
- 46 Li, H.; Eddaoudi, M.; Groy, T. L.; Yaghi, O. M. *J. Am. Chem. Soc.* **1998**, *120*, 8571.
- 47 a) Hoshins, B. F.; Robson R. *J. Am. Chem. Soc.* **1989**, *111*, 5962.
- 48 a) Gardner, G. B.; Venkataraman, D.; Moore, J. S.; Lee, S. *Nature* **1995**, *374*, 792; b) Gardner, G. B.; Kiang, Y.-H.; Lee, S.; Asgaonkar, A.; Venkataraman, D. *J. Am. Chem. Soc.* **1996**, *118*, 6946.
- 49 Férey, G.; Mellot-Draznieks, C.; Serre, C.; Millange, F.; Dutour, J.; Surblé, S.; Margiolaki, I. *Science* **2005**, *309*, 2040.
- 50 Frenkel, D.; Smit, B. *Understanding Molecular Simulations: From Algorithms to Applications*. 2nd ed.; Academic Press: San Diego, USA, **2002**.
- 51 *Organometallic conjugation: Structures, Reactions and Functions of d-d and d-p Conjugated Systems* (Eds.: Nakamura, A.; Ueyama, N.; Yamaguchi, K.), Kadansha-Springer, Tokio, JP, **2002**.

- 52 a) Dresselhaus, M. S.; Thomas, I. L. *Nature* **2001**, *414*, 332; b) Dorian, J. P.; Franssen, H. P.; Simbeck, D. R. *Energy Policy* **2006**, *34*, 1986.
- 53 See for example: **Di Credico, B.**; Rossin, A.; Peruzzini, M. *Biocombustibili e Biocarburanti – Soluzioni, strumenti, agevolazioni*. Edizioni IPSOA Wolters Kluwer S.r.l. **2007**, and reference therein.
- 54 a) Schlapbach, L.; Züttel, A. *Nature* **2001**, *414*, 353; b) Weitkamp, J.; Fritz, M.; Ernst, S. *Int. J. Hydrogen Energy* **1995**, *20*, 967; c) Dillon, A. C.; Jones, K. M.; Bekkedahl, T. A.; Kiang, C. H.; Bethune, D. S.; Heben, M. J. *Nature* **1997**, *386*, 377; d) Ye, Y.; Ahn, C. C.; Witham, C.; Fultz, B. *Appl. Phys. Lett.* **1999**, *74*, 2307; e) Liu, C.; Fan, Y. Y.; Liu, M.; Cong, H. T.; Cheng, H. M.; Dresselhaus, M. S. *Science* **1999**, *285*, 1127; f) Brown, C. M.; Yildirim, T.; Neumann, D. A.; Heben, M. J.; Gennett, T.; Dillon, A. C.; Alleman, J. L.; Fischer, J. E. *Chem. Phys. Lett.* **2000**, *329*, 311; g) Meregalli, V.; Parrinello, M. *Appl. Phys. A* **2001**, *72*, 143; h) Cao, A.; Zhu, H.; Zhang, X.; Li, X.; Ruan, D.; Xu, C.; Wei, B.; Liang, J.; Wu, D. *Chem. Phys. Lett.* **2001**, *342*, 510.
- 55 a) Wong-Foy, A. G.; Matzger, A. J.; Yaghi, O. M. *J. Am. Chem. Soc.* **2006**, *128*, 3494; b) Furukawa, H.; Miller, M. A.; Yaghi, M. O. *J. Mater. Chem.* **2007**, *17*, 3197.
- 56 Dinca, M.; Dailly, A.; Liu, Y.; Brown, C. M.; Neumann, D. A.; Long, J. R. *J. Am. Chem. Soc.* **2006**, *128*, 16876.
- 57 a) Furukawa, H.; Yaghi, O. M. *J. Am. Chem. Soc.* **2009**, *131*, 8875; b) Ma, S.; Sun, D.; Simmons, J. M.; Collier, C. D.; Yuan, D.; Zhou, H.-C. *J. Am. Chem. Soc.* **2008**, *130*, 1012; c) Senkowska, I.; Kaskel, S. *Microporous Mesoporous Mater.* **2008**, *112*, 108.
- 58 Naito, S.; Tanibe, T.; Saito, E.; Miyao, T.; Mori, W. *Chem. Lett.* **2001**, *30*, 1178.
- 59 Ingleson, M. J.; Perez Barrio, J.; Bacsá, J.; Dickinson, K.; Park, K.; Rosseinsky, M. J. *Chem. Comm.* **2008**, 1287.
- 60 Llabrés i Xamena, F. X.; Abad, A.; Corma, A.; Garcia, H. *Journal of Catalysis* **2007**, *250*, 294.
- 61 Seo, J. S.; Whang, D.; Lee, H.; Jun, S. I.; Oh, J.; Jeon, Y. J.; Kim, K. *Nature* **2004**, *404*, 982.
- 62 Takizawa, S.; Somei, H.; Jayaprakash, D.; Sasai, H. *Angew. Chem, Int. Ed.* **2003**, *42*, 5711.
- 63 a) Shi, J.-M.; Xu, W.; Liu, Q.-Y.; Huang, Z.-L.; Lei, H.; Yu, W.-T.; Fang, Q. *Chem. Commun.* **2002**, 756; b) Dong, Y.-B.; Jin, G.-X.; Smith, M. D.; Huang, R.-Q.; Tang, B.; Loye, H.-C. *Inorg. Chem.* **2002**, *41*, 4909.
- 64 a) Kahn, O. *Molecular Magnetism*, VCH, Weinheim, D, **1993**; b) Batten, S. R.; Murray, K. S. *Coord. Chem. Rev.* **2003**, *246*, 103.
- 65 Reineke, T. M.; Eddaoudi, M.; Fehr, M.; Kelley, D.; Yaghi, O. M. *J. Am. Chem. Soc.* **1999**, *121*, 1651.
- 66 a) Halder, G. J.; Kepert, C. G.; Moubaraki, B.; Murray, K. S.; Cashion, J. D. *Science* **2002**, *298*, 1762; b) MasPOCH, D.; Ruiz-Molina, D.; Wurst, K.; Domingo, N.; Cavallini, M.; Biscarini, F.; Tejada, J.; Rovira, C.; Veciana, J. *Nature Mater.* **2003**, *3*, 190.
- 67 Eddaoudi, M.; Moler, D. B.; Li, H.; Chen, B.; Reineke, T. M.; O'Keeffe, M.; Yaghi, O. M. *Acc. Chem. Res.* **2001**, *34*, 319.
- 68 Rossin, A.; Ienco, A.; Costantino, F.; Montini, F.; **Di Credico, B.**; Caporali, M.; Gonsalvi, L.; Fornasiero, P.; Peruzzini, M. *Cryst. Growth Des.* **2008**, *8*, 3302.
- 69 "Synthesis of 2-Substituted 4-Carboxy Oxazoles, Thiazoles and Thiazolidines from Serine or Cysteine Amino Acids" **Di Credico, B.**; Gonsalvi, L.; Peruzzini, M., Reginato, G.; Rossin, A., submitted.

- 70 "Coordination chemistry of thiazole-based ligands: novel hydrogen-bonded architectures" Rossin, A., **Di Credico, B.**; Giambastiani, G.; Gonsalvi, L.; Peruzzini, M.; Reginato, G. *manuscript in preparation*.
- 71 **Di Credico, B.**; Fabrizi de Biani, F.; Gonsalvi, L.; Guerri, A.; Ienco, A.; Laschi, F.; Peruzzini, M.; Reginato, G.; Rossin, A.; Zanello, P. *Chem. Eur. J.* **2009**, 15, 11985.

Polymeric magnesium formates

2.1 Overview

This chapter presents work related to the synthesis of different polymeric magnesium(II) formates,¹ followed by an investigation of their thermal behaviour. A careful analysis of the dehydration-rehydration cycle of magnesium formate dehydrate is also reported and discussed. The chapter concludes with a study of these compounds as potential gas storage materials.

2.2 Introduction

The rational design of supramolecular metal-organic frameworks upon preselected building units has provided an increasing number of novel compounds since the early 1990's. In this respect, the use of flexible linkers or spacers is still not widely developed. Indeed, a quick inspection of the Cambridge Data Base² shows that the number of registered metal-organic structures, which contain only rigid aromatic groups, is much higher (*ca.* 15 times) than the number of the corresponding compounds with flexible aliphatic ligands. Our interest in flexible connectors is also supported by considering that these derivatives should offer a greater degree of structural diversity and therefore open new possibilities for practical use.

In the last years, a boost on the study of polymeric metal formates has followed the discovery of a wide variety of crystalline phases that can be obtained with this simple and small organic linker.³ Even if molecular formates are known since a long time,⁴ the technical applications, explored recently in the MOF area,⁵ along with the necessity of finding new stable, cheap and ready-to-use materials, prompted many research groups to re-examine the chemistry of these "classical" species. Occurrence of polymorphism (see Chapter 1) is not a rare event in crystal engineering;⁶ the appearance of such a phenomenon is particularly likely when dealing with compounds that can be synthesised under different experimental conditions. In the field of metallorganic chemistry, very few examples are known⁷ where, after solvent or guest removal and re-adsorption in a coordination network, a crystal-to-crystal phase transition between polymorphs can take place. Retention of crystallinity during the process is usually only observed for systems displaying relatively subtle variations in the packing of molecules or in rigid 3D framework materials.⁸ Crystal-to-crystal phase transitions are particularly common among inorganic materials and organic polymers,⁹ but they are much more unusual in the case of coordination compounds. In this context, the formate anion is an efficient flexible linker, as evidenced by the diversity of its coordination modes to metals (Figure 2-1).

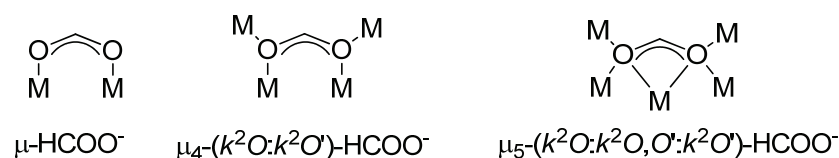


Figure 2-1. Coordination arrangements of formate ion (HCOO^-) whose flexibility facilitates the formation of polymorphs.

In this thesis work, a novel 3D framework is presented, deriving from **anhydrous magnesium formate**, isomorphous to the known zinc analogue $[(\text{CH}_3)_2\text{NH}_2][\text{Zn}(\mu\text{-HCOO})_3]$.¹⁰ In addition, a crystal-to-crystal phase transition of **magnesium formate dihydrate** $[\text{Mg}(\text{HCOO})_2 \cdot 2\text{H}_2\text{O}]$ has been discovered during the analysis of its dehydration-rehydration cycle carried out as host-guest experiment using water as guest molecule. Starting from an orthorhombic 2D lamellar material, water removal followed by re-hydration of the anhydrous phase so obtained, led to different 3D monoclinic micro-crystals of the same compound. The overall process has been followed by single-crystal (XRD) and powder (XRPD) X-ray diffraction,¹¹ infrared spectroscopy (FT-IR) and thermogravimetric analysis (TG-DTA).¹²

Finally, these compounds were tested as potential storage materials for use in the field of reduction of greenhouse gas emissions. CO_2 adsorption isotherms of the activated phase derived from $\text{Mg}(\text{HCOO})_2 \cdot 2\text{H}_2\text{O}$ have been recorded, to understand whether it could have permanent porosity and therefore application as an efficient “ CO_2 sponge”. The availability of materials of this kind containing s- or p-block metals is particularly sought for, owing to their low molecular weights, making them more appealing for practical applications. Preliminary experiments were performed on hydrogen physisorption and the process was followed by Raman spectroscopy and integrated by GCMC (Grand Canonical Monte Carlo) simulations of the adsorption isotherms and pore size distribution.

2.3 Results and discussion

2.3.1 Syntheses

Both compounds $\text{Mg}(\text{HCOO})_2(\text{HCOOH}) \supset (\text{CH}_3)_2\text{NH}$ (**1**) and $[\text{Mg}(\text{HCOO})_2 \cdot 2\text{H}_2\text{O}]$ (**2**) were prepared using solvothermal methods, in home-made stainless steel autoclaves with inner Teflon beaker (see Chapter 5). Originally, this methodology

was applied to the synthesis of “fully-inorganic” silicate materials (zeolites) and phosphates,¹³ but later it was successfully used to synthesize porous metal-organic materials.¹⁴ Traditional solution methods proved to be unsuccessful for the synthesis of the formate species, in particular if high yields of good-quality single crystals are desired. Several trials were made using different reaction conditions. For example, slow diffusion at ambient temperature through a G4 sintered glass filter of a toluene solution of triethylamine into a toluene/DMF solution containing HCOOH and magnesium perchlorate only led to few plate-like small crystals after 2 days, not suitable for XRD. Layering of a methanolic magnesium perchlorate solution over a water HCOOH solution led to white powdery products, both at ambient and low (4 °C) temperature. The protonated form of the acid is better than the carboxylate salts as starting material. Thus, when sodium formate is employed instead of formic acid, immediate formation of a white insoluble non-crystalline precipitate occurs. The solvent influence was also examined. Solvothermal attempts made either with DMF only or with a mixture of DMF/water as solvents under the same conditions led to poorer quality crystals, thus confirming that the presence of DMF is essential to get a crystalline product and to dissolve the inorganic salts thoroughly. At the temperatures chosen, DMF partially decomposes to give dimethylamine, which is eventually “trapped” inside the pores of **1**.

The reaction course seems to be driven by the concentration of the resulting solution. With dilute solutions (*i.e.* using 8 mmol of HCOOH in 10.0 mL of DMF), preferred formation of the 3D network **1** is observed, while, increasing the relative water content (*i.e.* by halving the amount of DMF to 5.0 mL), lead to a more concentrated solution in both reagents and water, and consequently the dihydrate 2D species **2** is the final product.

Changes in the stoichiometry of the reagents does not affect the composition of the final product which is always the same, no matter the metal-to-ligand ratio.

In order to investigate the role taken by the nature of the counter-anion, different magnesium inorganic salts were considered. $\text{Mg}(\text{ClO}_4)_2 \cdot 6\text{H}_2\text{O}$ or $\text{Mg}(\text{NO}_3)_2 \cdot 6\text{H}_2\text{O}$, afforded the same product with no significant differences for either yields or phase purity, as confirmed by the XRPD spectra of the two samples prepared from the two different magnesium salts (Figure 2-2).

The simulated powder diffraction patterns calculated from the single-crystal data show that the most intense peaks for **1** appear at $2\theta = 15^\circ$, 20° and 25° , respectively, while those of **2** fall at $2\theta = 19^\circ$, 24° and 29° , in close agreement with the experimental spectra shown above. As already mentioned, a small amount of impurities in the $9^\circ < 2\theta < 11^\circ$ range are also present in **1**.

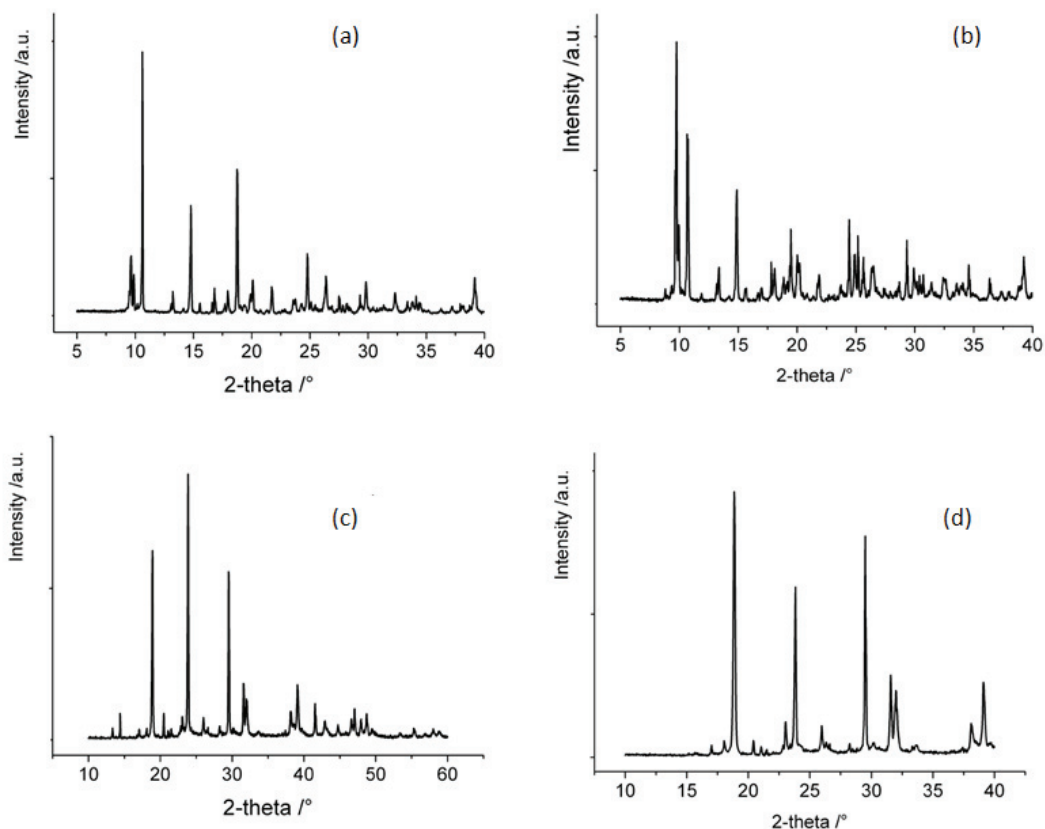


Figure 2-2. XRPD patterns of: (a) **1** prepared from magnesium nitrate hexahydrate; (b) **1** prepared from magnesium perchlorate hexahydrate; (c) **2** prepared from magnesium perchlorate hexahydrate; (d) **2** prepared from magnesium nitrate hexahydrate.

When we used the described reaction conditions (*i.e.* HCOOH in DMF), phase **1** is never obtained pure, the impurity being unknown.¹⁵ In contrast, phase **2** is pure, as checked through repeated syntheses under the same conditions. Successive efforts to optimize the synthesis process of **1** has allowed to understand the reaction mechanism.

A new synthetic pathway to prepare ultra-pure **1** was developed, using a medium-strength carboxylic acid, instead of using HCOOH as reagent directly. In

fact, the formation of polymeric formates is due to hydrolysis of the solvent DMF in an acidic medium. When the reaction was repeated with cyclobutan-1,1'-dicarboxylic acid, ($pK_{a1} = 2.92$; $pK_{a2} = 5.45$), pure **1** could be obtained as a result of the controlled hydrolysis process (Figure 2-3).

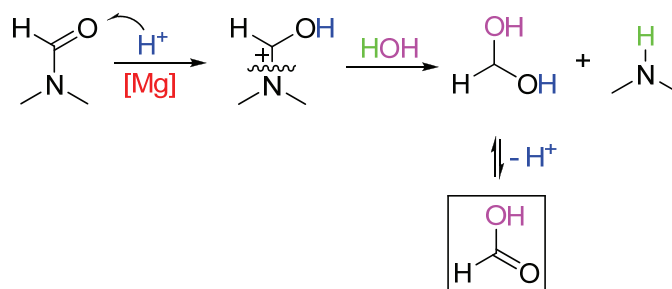


Figure 2-3. Possible mechanism of the *in situ* formation of the formate ligand.

2.3.2 Structures description

Figure 2-4 shows the XRD structure of **1**. A complete list of the crystallographic data are collected in the Appendix (Chapter 5).

The molecular framework of **1** does not differ from that of other known transition metal formates such as Mn, Co, Ni,¹⁶ Zn¹⁰ formates; nonetheless, it represents a new polymeric arrangement for a non transition metal such as (anhydrous) magnesium formate. The polymeric structure consists of a cubic polymeric network with the eight vertices of each cube occupied by Mg atoms. Each Mg(II) ion features a undistorted and practically perfect octahedral coordination polyhedron. Following the nomenclature proposed by Gao *et al.*,¹⁶ each formate ligand is sitting as a bridge between adjacent metal centres in an *anti-anti* coordination mode. Each cubic cavity is occupied by a dimethylamine molecule which is crystallographically disordered. The presence of such inclusion molecule is not unexpected and certainly is originated from the decomposition of DMF solvent under the solvothermal reaction conditions employed. The metrical parameters involving both Mg and C atoms, Mg-O [2.0901(1) Å], O-C [1.237(2) Å], Mg-O-C [129.3(1)°] and O-C-O [127.1(2)°], are in agreement with the corresponding distances and angles of other reported magnesium formate systems.³ⁱ

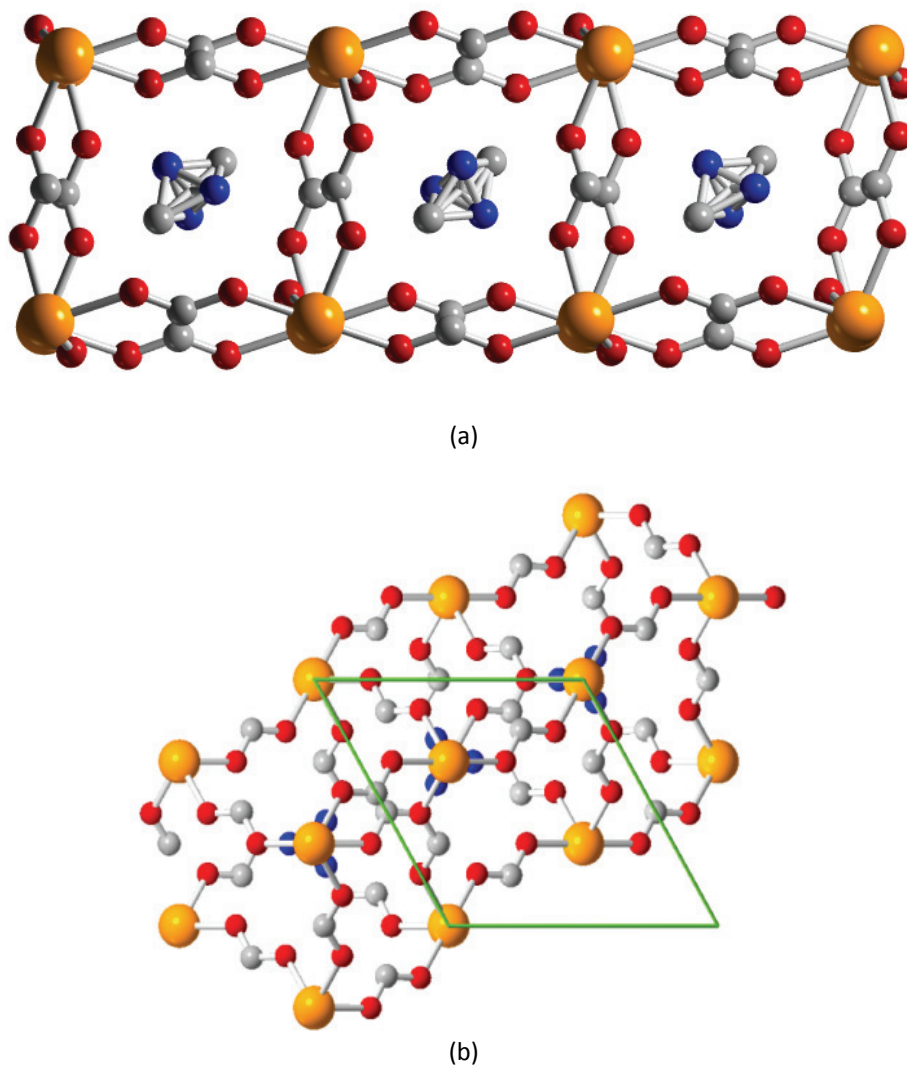


Figure 2-4. X-Ray crystal structure of **1**: (a) view of the cubic cavities with Mg atoms at the corners, containing (disordered) dimethylamine molecules (view along the [011] Miller planes); (b) view along the [001] Miller planes. Atom colour code: orange, magnesium; light gray, carbon; red, oxygen; blue, nitrogen. Hydrogen atoms omitted for clarity. Cell borders draw in light green.

Two-dimensional structure of **2** is reported in the Figure 2-5. Planes made of polymeric $\text{Mg}(\text{HCOO})_2$ moieties are inter-connected through hydrogen bonding between the two axial aquo ligands on magnesium and the formate ligands of the neighbouring (upper and lower) sheets (for further structural details refer to the cited article¹⁷).

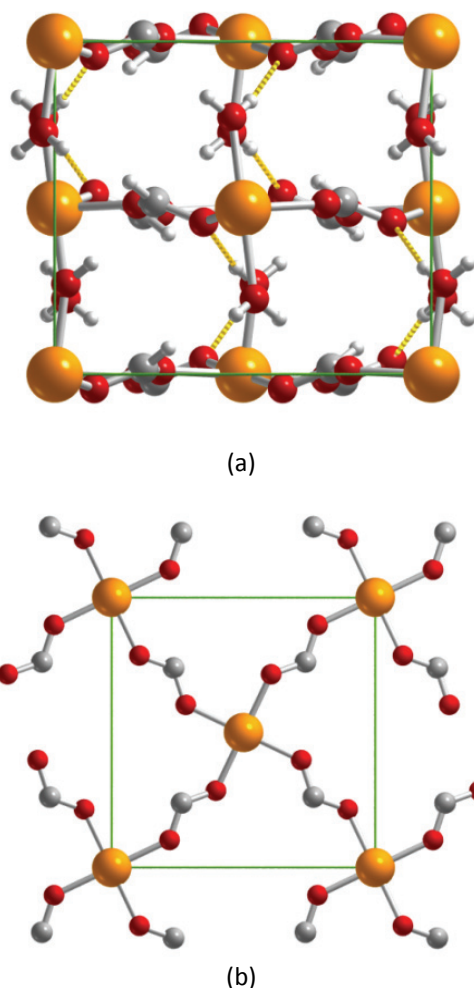


Figure 2-5. X-Ray crystal structure of **2**: (a) view of the 2D network made of infinite $\text{Mg}(\text{HCOO})_2$ sheets (view along the [001] Miller planes, axial aquo ligands and hydrogen atom on formate removed for clarity); (b) view along the [010] Miller planes, showing the complex hydrogen bonding between the axial aquo ligands and the formate ions on the adjacent planes. Atom colour code: orange, magnesium; light gray, carbon; red, oxygen. Cell borders drawn in light green. Hydrogen bonding drawn in yellow.

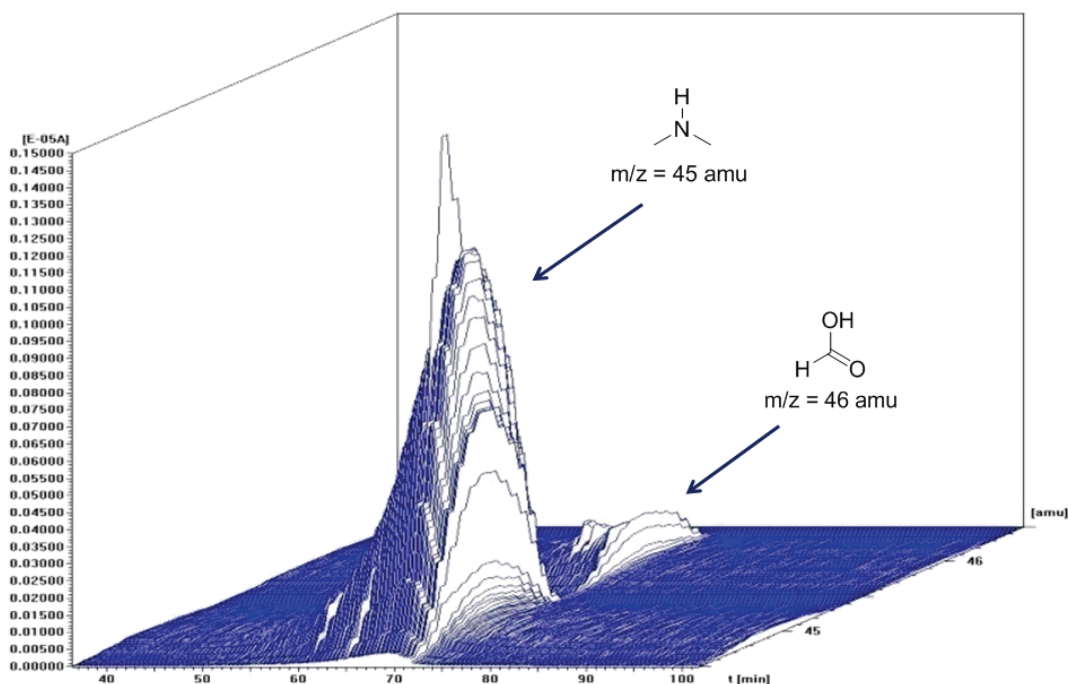
2.3.3 Infrared spectral analysis

Infrared spectra of formates **1** and **2** (KBr pellets) showed the characteristic stretching, bending and rocking modes of the formate molecule: $\nu_{\text{asym}}(\text{O-C-O})$ at 1681-1611 (**1**) / 1604 (**2**) cm^{-1} , $\nu_{\text{sym}}(\text{O-C-O}) + \delta_{\text{asym}}(\text{H-C-O})$ at 1374 (**1**) / 1378 (**2**) cm^{-1} , $\gamma(\text{HCOO}^-)$ at 1026 (**1**) / 1089 (**2**) cm^{-1} and $\delta_{\text{sym}}(\text{O-C-O})$ at 807 (**1**) / 819 (**2**) cm^{-1} . Tentative assignment of the normal modes is made referring to previous spectroscopic work present in the literature.¹⁸ The wave number shift in passing from free to metal-coordinated formate mirrors the trend already observed for molecular formates:¹⁹ in particular, both $\nu_{\text{sym}}(\text{O-C-O})$ and $\nu_{\text{asym}}(\text{O-C-O})$ are expected to increase upon carboxylate coordination to Mg(II). In the case of **1**, $\nu_{\text{sym}}(\text{O-C-O})$

shifts from 1361 [in Na(HCOO)] to 1374 cm^{-1} , while $\nu_{\text{asym}}(\text{O-C-O})$ moves from 1617 to 1681 cm^{-1} .

2.3.4 Thermal behaviour

The thermogravimetric analysis TG-MS for **1** are shown in Figure 2-6. No weight loss is observed for **1** up to 200 °C. The first weight change (45%) is found between 200 and 250 °C and corresponds to the loss of dimethylamine and formic acid, mostly detected as CO_2 . A plateau can then be observed up to 430 °C, before a weight loss of 34% occurs, which can be ascribed to the $\beta\text{-Mg}(\text{HCOO})_2 \rightarrow \text{MgO}$ transformation. In agreement with the plateau in the thermogravimetric curve, the diffraction pattern collected at 325 °C (Figure 2-7) shows the existence of a crystalline phase, whose calculated formula from TG measurement is consistent with the formula $\beta\text{-Mg}(\text{HCOO})_2$. The structure of this allotropic magnesium formate was determined and confirmed through PXRD fitting of the experimental peaks with those coming from database spectra.²⁰ On increasing the temperature above 400 - 450 °C, loss of water and carbon monoxide leaves MgO as the last phase at the end of the analysis.



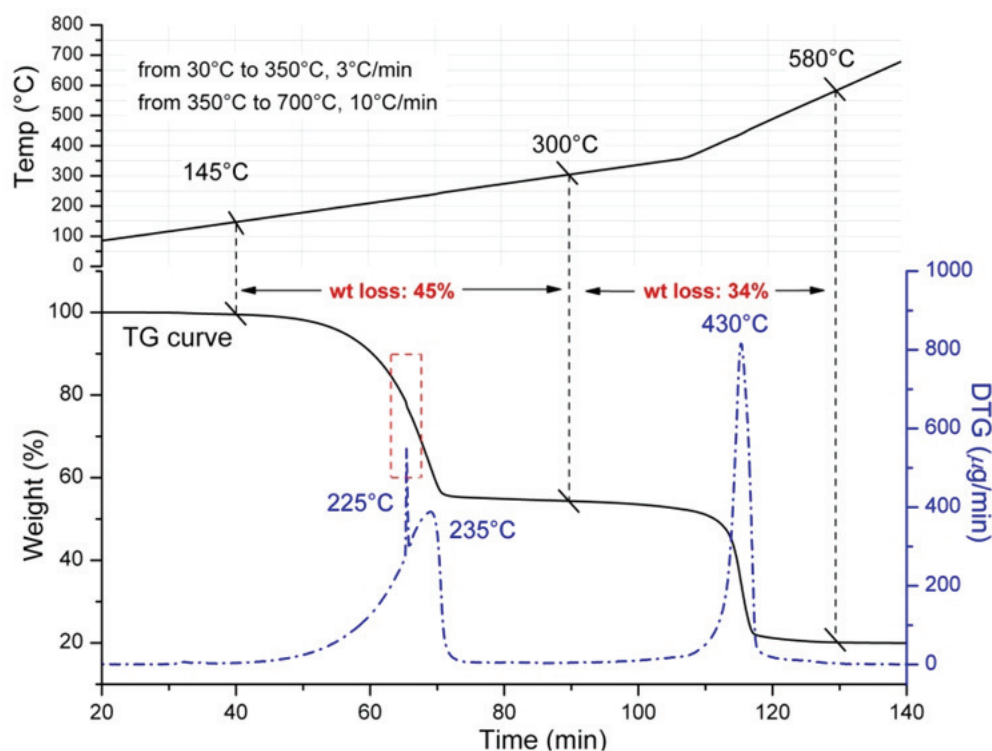


Figure 2-6. TG-MS characterisation of **1**.

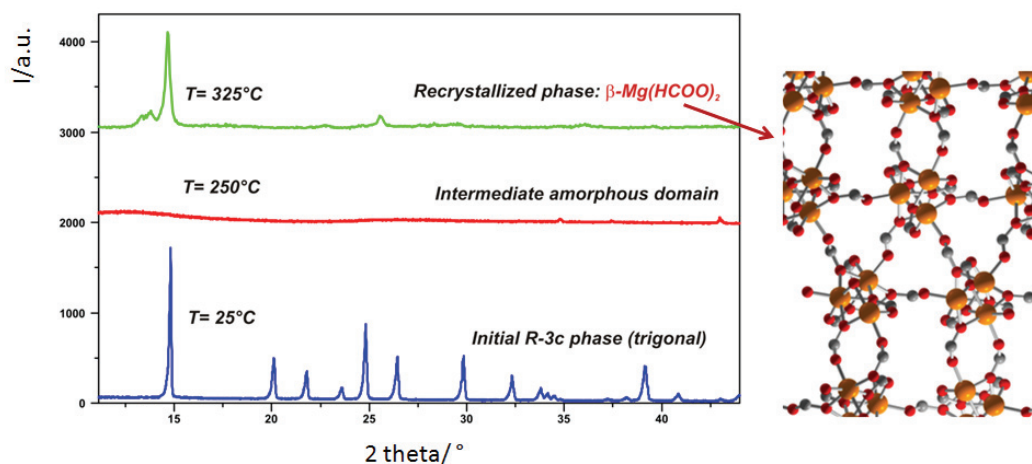


Figure 2-7. Temperature dependent XRPD patterns for **1** and crystal structure of β - $\text{Mg}(\text{HCOO})_2$ reported in the literature from Viertelhaus *et al.*²⁰

A similar thermal behaviour was observed for formate **2**, as shown in the X-ray diffraction patterns in Figure 2-8.

As already observed by Malard and co-workers,¹⁷ no weight loss is observed for **2** up in the TG-DTA analysis up to 120 °C. The first weight change (24%) is found between 120 and 140 °C and corresponds to the loss of two water molecules (calcd

24%). Thus, in a similar manner to **2**, is observed the crystalline phase $\text{Mg}(\text{HCOO})_2$ and MgO at the end of the analysis. The high thermal stability of **1** and **2** mirrors that observed in similar compounds previously synthesized.^{21,3i}

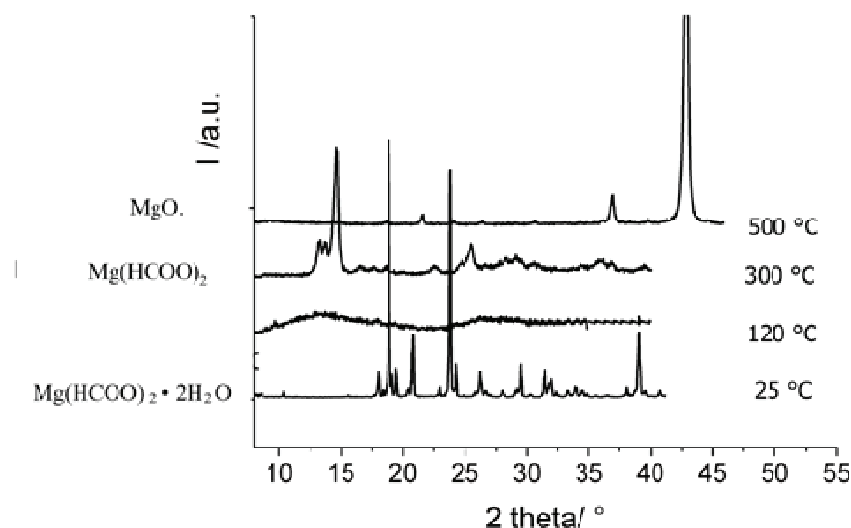


Figure 2-8. Temperature dependent XRPD patterns for **2**. The temperatures and the corresponding products are also indicated in the graphs.

2.3.5 De-hydration and re-hydration of **2**: a phase transition

In order to determine if anhydrous magnesium formate coming from thermal activation of **2** could interact again with water to form a guest-inclusion species after guest vapour diffusion into the hosting framework, the activated phase was put into a closed dessiccator, and exposed to vapours of H_2O under reduced pressure and at ambient temperature. The experiment was successful, but, instead of re-generating compound **2**, a different 3D dihydrate species (**2a**) was produced. Activation of **2** was achieved at 300 °C, yielding an activated phase **2_{act}** with very poor crystallinity degree (b in Figure 2-9), which could not be indexed. As observed from the TGA measurements, in this case the activated phase should correspond to the $\text{Mg}(\text{HCOO})_2$ “anhydrous” open framework. The hydrate **2a** was also obtained after soaking **2_{act}** into liquid water for 1 h, and its diffraction pattern is shown in Figure 2-9 (c). Its structure was successfully indexed, finding the following cell parameters: $a = 8.6528$, $b = 7.163$, $c = 9.4067$ Å, $\beta = 98.012$, space group = $P2_1/c$,

$M(20) = 23$. Additional experimental evidence, inferred from independent measurements on zinc formates,²² suggested that this species could be isostructural to Lipton's zinc formate dihydrate.^{3a} Thus, the structure of **2a** was refined using the Rietveld method implemented in the program GSAS,²³ starting from Lipton's phase and replacing magnesium with zinc in the framework.

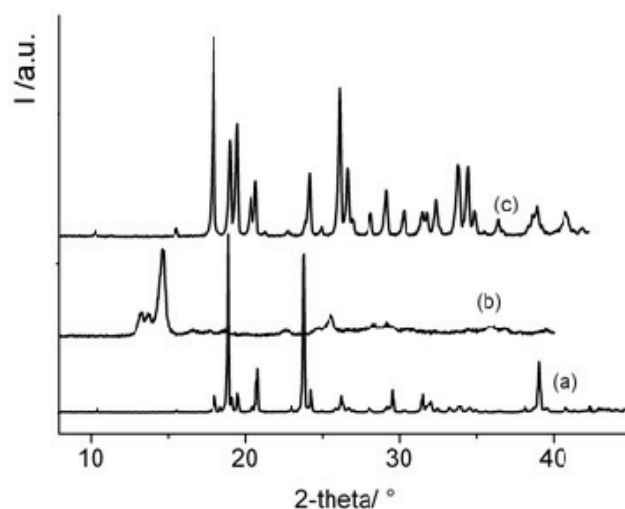


Figure 2-9. XRPD patterns of **2** (a), **2_{act}** (activated at 300 °C) (b) and water-regenerated phase **2a** (c).

The final Rietveld plot and the resulting structure are shown in Figure 2-10. Structural refinement confirmed the perfect crystal system analogy between **2a** and zinc(II) formate dihydrate.^{3a} The network is constituted by two different magnesium sites: in the first one the metal centre is coordinated to six different (bridging) formates, while the second one shows four aquo ligands occupying the equatorial positions and only two (bridging) formates on the axial positions. Thus, the overall formula could also be written as $[\text{Mg}(\text{HCOO})_2 \cdot \text{Mg}(\text{H}_2\text{O})_4(\text{HCOO})_2] \equiv 2 [\text{Mg}(\text{HCOO})_2 \cdot 2\text{H}_2\text{O}]$.

2D to 3D phase transitions similar to the present one are not very common among coordination compounds, and that occurring in our system represents, to the best of our knowledge, the very first transition of this kind observed. The process is “quasi-reversible”, in the sense that the de-hydration/re-hydration process is feasible, but the initial and final products are not structurally identical. They indeed represent two polymorphs of the same compound.

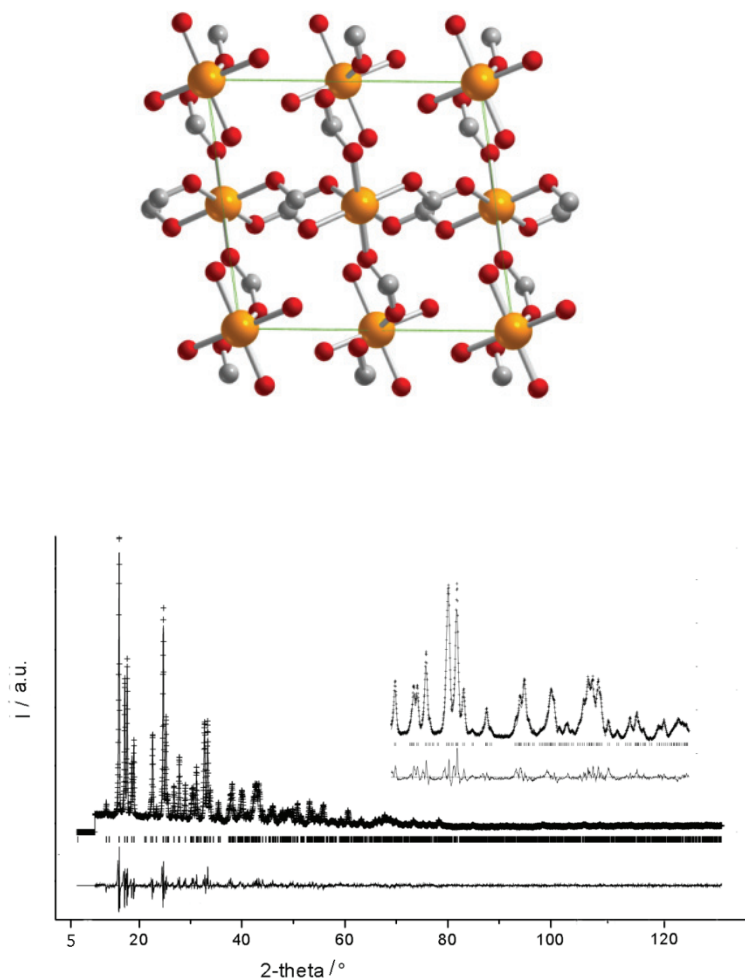


Figure 2-10. Structure representation and final Rietveld plot for **2a**. The inset shows a zoom on the 30-50° 2θ region. Atom colour code: orange, magnesium; light gray, carbon; red, oxygen. Hydrogen atoms omitted for clarity. Cell borders draw in light green.

2.3.6 Gas sorption studies: the adsorption behaviour of $\text{Mg}(\text{HCOO})_2(\text{HCOOH}) \supset (\text{CH}_3)_2\text{NH}$

The removal of dimethylamine nested into the cavities of magnesium formate **1** was obtained by activation at 140 °C for 48 h which afforded $[\text{Mg}(\text{HCOO})_2 \cdot \text{HCOOH}]$ (**1_{act}**). The effect of the “activation” process on the compound surface area and pore volume was investigated through nitrogen adsorption at 77 K (Figure 2-11). The activated phase shows a type I isotherm, with ultra-micropores and 244 m² g⁻¹ of Langmuir surface area.

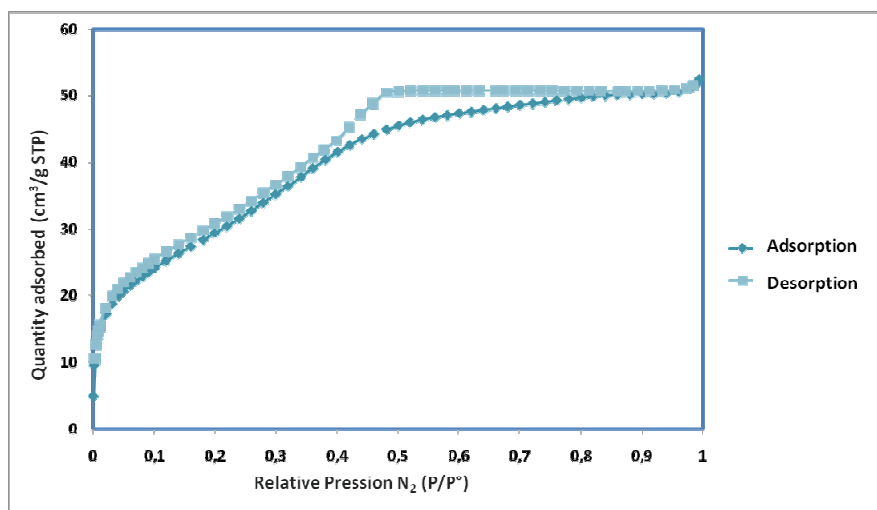


Figure 2-11. N_2 adsorption isotherm of $[Mg(HCOO)_2 \cdot HCOOH]$ (1_{act}).

The hysteresis loop is very narrow, indicating an homogeneous and well-defined pore shape of the micropores. Moreover, in order to collect more detailed information on pore structure, pore size distribution (PSD) curves were determined by the application of the Barrett–Joyner–Halenda (BJH) method.²⁴ The PSD curve shows an homogeneous distribution centered around the average value of 3.2 nm pore diameter (Figure 2-12).

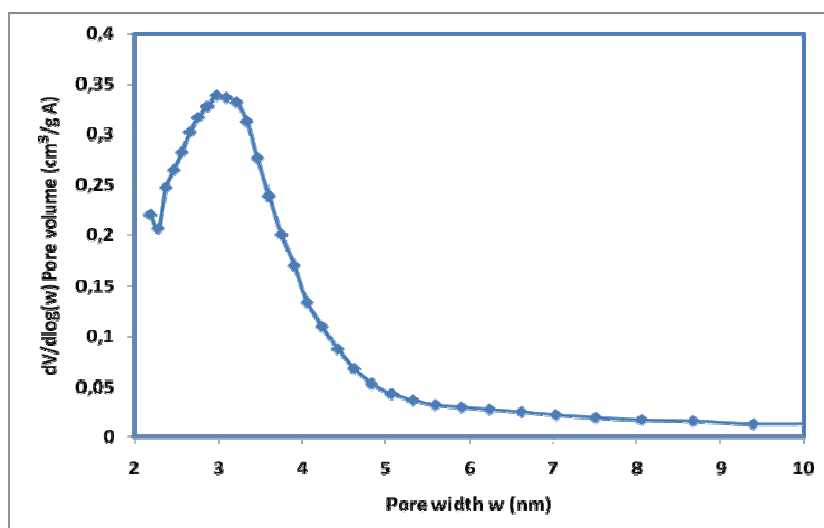


Figure 2-12. PSD of $[Mg(HCOO)_2 \cdot HCOOH]$ (1_{act}) calculated by BJH method along the desorption branch of the isotherm.

Finally, 1_{act} was tested as hydrogen storage material at very low temperature (down to 15 K) and low pressure (100 mbar), following the adsorption process *via*

Raman spectroscopy.²⁵ The Raman spectra, performed with three different excitation wavelengths, were coincident and showed two different vibrational peaks $\nu(\text{H-H})_{\text{ads}}$ ascribable to vibrational modes of the hydrogen molecule (Figure 2-13).

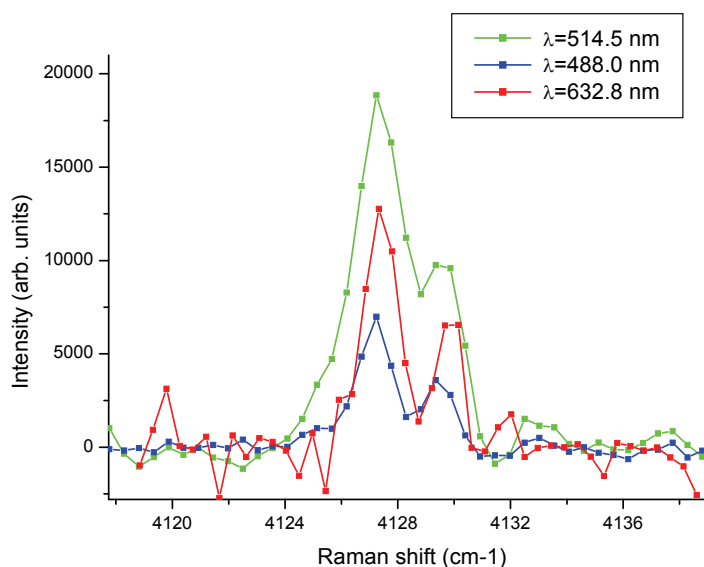


Figure 2-13. Raman spectra of H_2 physisorbed on $\mathbf{1}_{\text{act}}$ with three different excitation wavelengths.

The occurrence of these peaks suggests the existence of two different adsorption sites with similar energy at $\nu(\text{H-H})_{\text{ads}} = 4127 / 4129 \text{ cm}^{-1}$, about 2.3 cm^{-1} apart from each other. As the vibrational stretching frequency of free hydrogen molecule is $4155 / 4161 \text{ cm}^{-1}$, the measured vibrational frequency shifts falls at 30 cm^{-1} lower than that in free H_2 which are in perfect agreement with other literature cases.²⁶ Kong *et al.* evaluated that the $\nu(\text{H-H})$ shift of adsorbed dihydrogen in $[\text{Zn}_2(\text{terephthalate})_2(\text{triethylenediamine})]$ is about -28 cm^{-1} , mainly due to van der Waals interactions. Furthermore, they observed two different hydrogen binding orientations, corresponding at two different vibration frequencies with a minor energy difference of about 3 cm^{-1} .

Figure 2-14 shows the lattice vibrational modes between 100 and 300 cm^{-1} , a spectral region where the rotational $\delta(\text{H-H})_{\text{ads}}$ bands fall. The comparison between the spectrum of the “pure” formate sample and that with physisorbed hydrogen, highlights the appearance of the sole $S(0) (\text{H}_2)_{\text{ads}}$ rotational mode at $340 / 394 \text{ cm}^{-1}$,

again confirming the presence of two different adsorption sites. No band related to S(1) is observable.

Preliminary H₂ adsorption/desorption experiments on **1_{act}** were also performed. The weight percentage of adsorbed H₂ is found to be between 0.25 and 2.5 wt% which represent potentially interesting values.

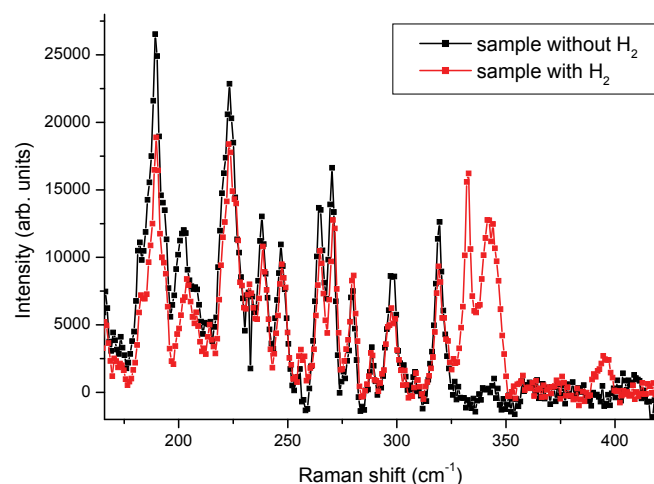


Figure 2-14. Raman spectra of MOF **1_{act}** (spectrum black) and MOF **1_{act}** with physisorbed hydrogen molecules (spectrum red).

Experiments of Powder Neutron Diffraction at the ISIS synchrotron center in Oxford (UK) are currently underway on a fully deuterated sample of **1_{act}**, with the aim of identifying experimentally the adsorption sites of D₂ on **1_{act}** and to compare the experimental results with the theoretical simulations (see next paragraph).

2.3.6.1 Molecular simulations on [Mg(HCOO)₂•HCOOH] (**1_{act}**)²⁷

Methane and hydrogen adsorption in the [Mg(HCOO)₂•HCOOH] (**1_{act}**) species were investigated using GCMC simulations¹² implemented in the multipurpose simulation code.²⁸ In the grand canonical ensemble, the chemical potential, both the volume and the temperature are kept fixed like in adsorption experiments. The chemical potential is related to the system pressure by the Peng-Robinson equation of state. In the simulation, molecules are randomly moved, inserted and deleted which allows the number of molecules in the framework to fluctuate.

An atomistic model for the MOFs was employed, where the framework atoms were kept fixed at the crystallographic positions. The standard Lennard-Jones (LJ)

potential was chosen to model the dispersive interatomic interactions. The parameters for the framework atoms were obtained from the universal force field (UFF).²⁹ In the LJ potential, the model used for methane and hydrogen uses a united-atom description, *i.e.* one molecule is represented by a single sphere ($\sigma_{\text{CH}_4} = 3.73 \text{ \AA}$, $\varepsilon_{\text{CH}_4} / k_B = 148 \text{ K}$ and $\sigma_{\text{H}_2} = 2.96 \text{ \AA}$, $\varepsilon_{\text{H}_2} / k_B = 34.2 \text{ K}$). The Lorentz-Berthelot mixing rules were employed to calculate fluid / framework parameters. Interactions beyond $5 \cdot \sigma_{\text{fluid-fluid}}$ were neglected for the simulations.

For the simulations of hydrogen at 77 K we implemented quantum effects during the molecular simulations since its thermodynamic properties divert from those of the corresponding classical fluid. We used the Feynman-Hibbs effective potential method³⁰ to enlarge the effective diameter of the hydrogen molecule due to the Heisenberg uncertainty.

The PSD was calculated with the method developed by Gelb and Gubbins which determines the diameter of the largest sphere that can fit into the cavities without overlapping with any of the framework atoms.³¹ The PSD for **1_{act}** (Figure 2-15) shows a single peak with a pore diameter of 3.35 Å, in agreement with the experimental data.

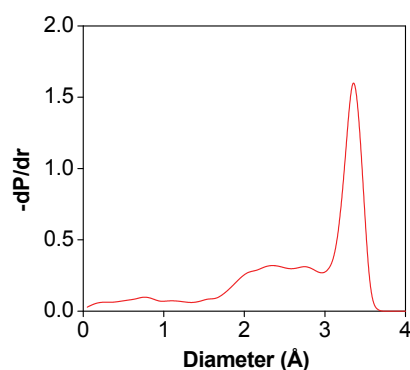


Figure 2-15. Pore sizes distribution (PSD) for the **1_{act}**.

Thus, we studied the methane and hydrogen absorption of **1_{act}**. Figure 2-16 shows the methane adsorption isotherms at 125 K, 200 K and 300 K on the **1_{act}** derivative (log scale), showing type I shapes typical for microporous materials.

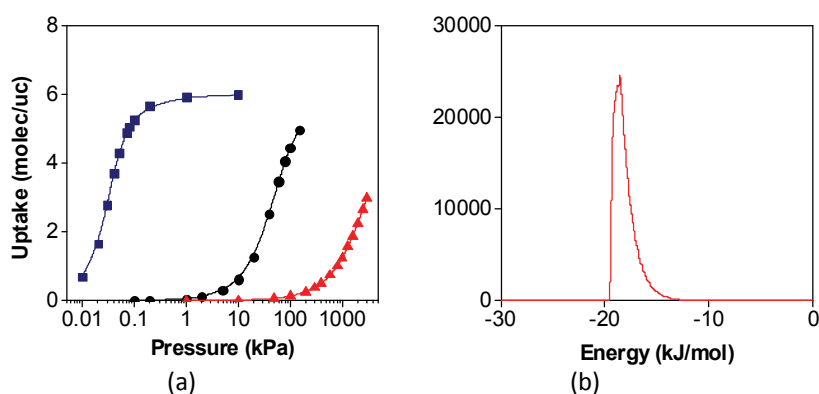


Figure 2-16. (a) Simulated adsorption isotherms of methane on $\mathbf{1}_{\text{act}}$ at 125 K, blue squares; 200 K, black circles and 300 K, red triangles. (b) Energy histograms of methane on $\mathbf{1}_{\text{act}}$ at 10 kPa and 125 K.

The maximum methane uptake for this structure is around 6 molecules per unit cell, *i.e.* 100.4 mg g^{-1} . In order to quantify the solid-methane interaction energy, we calculated the energy histograms for the maximum uptake (at 10 kPa and 125 K) of the $\mathbf{1}_{\text{act}}$ methane isotherm obtained before (b in Figure 2-16), *i.e.* we determined the potential energy for each methane molecule with the solid. Note that, the lower the energy, the higher the interaction between methane and the framework. We found a single peak in the histograms centered at $-18.5 \text{ kJ mol}^{-1}$ related to the filling of the porosity. The narrow peak is a strong confirmatory evidence that the molecules are very localised due to the narrow pores.

Figure 2-17 shows the density distribution of the methane in $\mathbf{1}_{\text{act}}$ unit cell framework, *i.e.* the different possible configurations of the methane molecules inside the structure. For these density distributions, the positions of the methane molecules in the simulation are marked by a black dot. They give not only information about the possible positions of the molecules inside the porosity, but also about the disorder of such molecules during the adsorption process. Methane molecules density distribution at maximum uptake shows that the adsorbed molecules are not localized at fixed regions, indicating that they are freely moving inside the pore cavities. Thus, methane molecules are adsorbed and distributed along the small pores found in the framework.

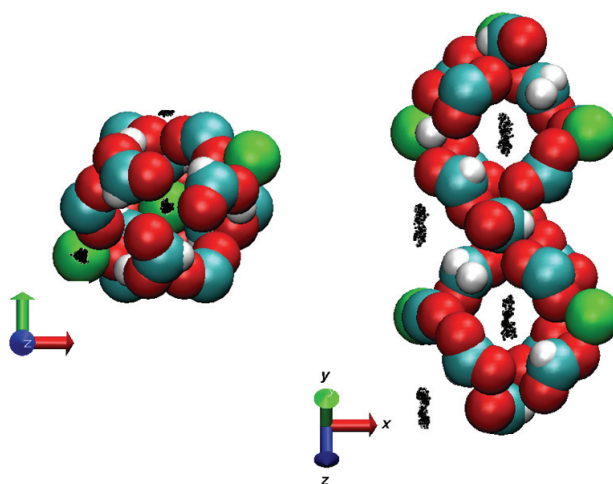


Figure 2-17. Density distributions of methane on $\mathbf{1}_{act}$ unit cell at 10 kPa and 125 K.

Figure 2-18 shows the calculated location of the methane molecules in the framework. These snapshots show the location of a single configuration in the molecular simulation and give an impression of how full the pores are and where the molecules sit. Snapshots reveal that the framework can be filled by a maximum of one methane molecule per cavity.

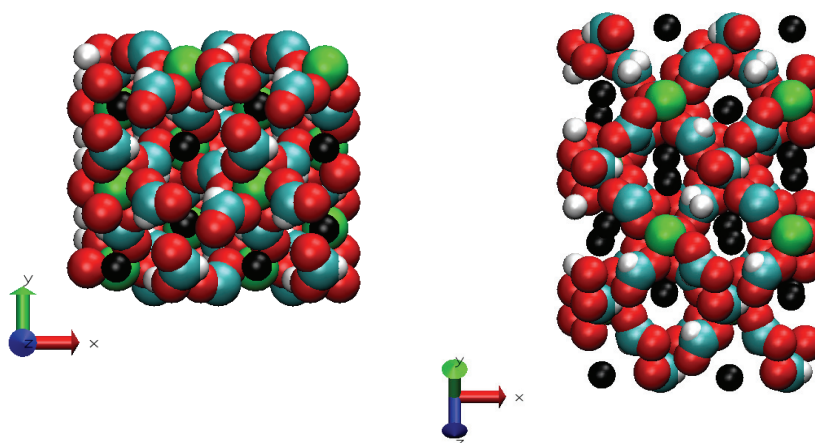


Figure 2-18. Snapshots of the calculated methane adsorption on $\mathbf{1}_{act}$ at 10 kPa and 125 K. Each black sphere represents one methane molecule.

Then, we turned our attention to model the hydrogen absorption issue, by carrying out the simulation for the adsorption isotherm of hydrogen at 77 K on $\mathbf{1}_{act}$. The isotherm presents a small step around 100 kPa which can be interpreted as due to the filling of two different sites in the framework although the PSD showed just one single kind of porosity (Figure 2-19).

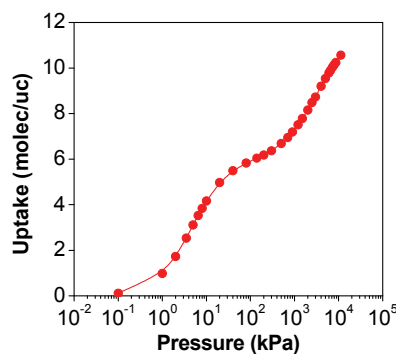


Figure 2-19. Simulated adsorption isotherms of hydrogen on 1_{act} at 77 K, red circles.

Figure 2-20 (a) shows the computed density distribution of the hydrogen molecules in the framework before (20 kPa) and after the step (11,300 kPa), which are likely related to different possible configurations of the hydrogen molecules inside the structure.

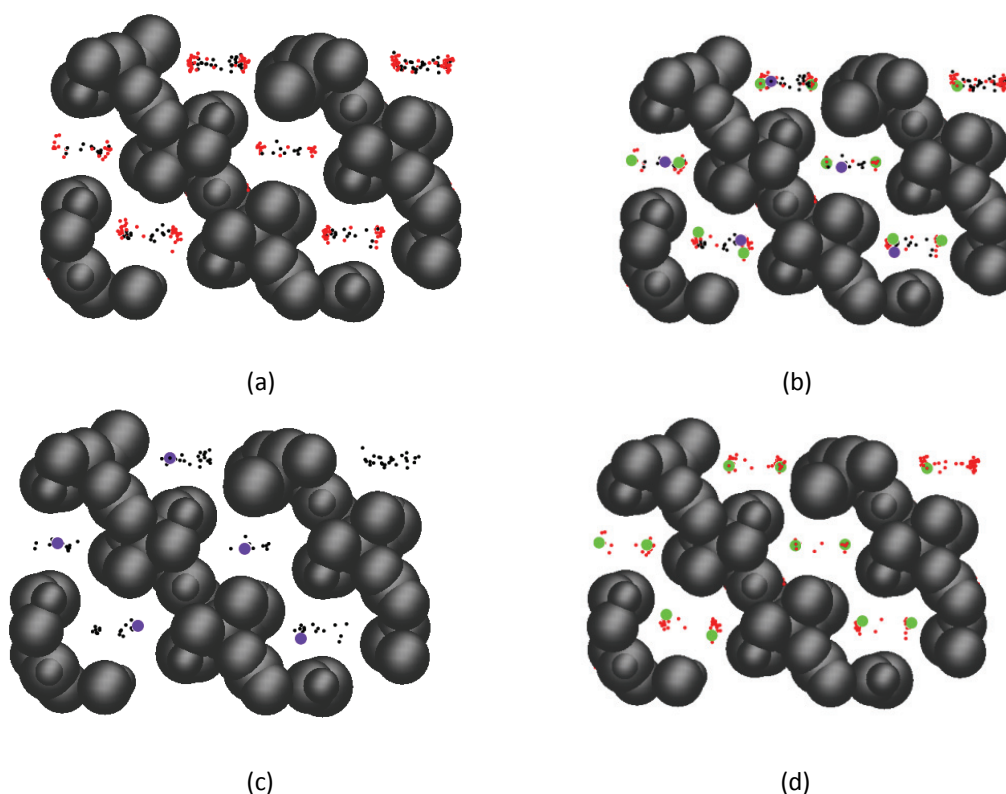


Figure 2-20. Hydrogen adsorption on 1_{act} at 77K. (a) Density distributions at 20 kPa, black dots and 11,300 KPa, red dots; (b) density distributions and snapshots at 20 kPa, purple spheres and 11,300 KPa, green spheres. (c) and (d) represent separately the density distributions and snapshots at 20 kPa and 11,300 kPa, respectively.

Here, black dots are related to the density distributions before the step whereas red dots are related to density distributions after the step, at higher

uptakes. The density distribution for the lower uptake is fairly wide rather than localised at discrete points meaning that the molecules are free to move inside the pore cavities without any further space limitation or hydrogen-hydrogen packing effects. This could present a dilution in the scattering density in neutron scattering experiments, resulting in difficulties when trying to refine the neutron scattering pattern at this temperature (77 K). On the other hand, when the loading increases, the additional adsorbed molecules constrain the hydrogen molecules to two different fixed positions allowing a better packing. In this way, Figure 2-20 (b) shows the density distributions together with the localisation of the hydrogen molecules at both low and high uptakes. Snapshots before and after the step show that the porosity is filled by one molecule per cavity at around 6 molecules per unit cell (purple spheres), *i.e.* 2.1 mg g^{-1} , whereas it is filled by a maximum of two molecules per cavity at higher loadings (green spheres), *i.e.* 12 molecules per unit cell or 4.2 mg g^{-1} . Figures 2-20 (c) and (d) give the same information separately, before and after the step.

When comparing the maximum uptake obtained with methane and hydrogen, we can see how the framework can accommodate inside the pore cavities a maximum of two smaller molecules such as hydrogen (diameter = 2.96 \AA), whereas it can only fit one molecule such as methane (diameter = 3.73 \AA).²⁹ In this way the maximum uptake for methane adsorption is around 6 molecules per unit cell, and the maximum theoretical uptake for hydrogen should be close to 12 molecules per unit cell. Looking at these differences during the adsorption between both molecules, it could be worth to study this material as a molecular sieve for larger molecules.

2.3.7 Gas sorption studies: the adsorption behaviour of $[\text{Mg}(\text{HCOO})_2 \cdot 2\text{H}_2\text{O}]$

The adsorption behaviour of (pre-activated) **2** was tested using CO_2 , in order to investigate its possible application as storage material for this greenhouse gas. To test the adsorptive properties of the different phases, **2** was activated at $300 \text{ }^\circ\text{C}$ to form the phase **2_{act}**. The results obtained from the CO_2 adsorption at $25 \text{ }^\circ\text{C}$ are reported in Figure 2-21.

The isotherms associated to the CO₂ adsorption were recorded at 25 °C, following the procedure recently described by Millward and Yaghi.³² At variance with other gaseous molecules, CO₂ adsorption could not be investigated at pressure higher than atmospheric, because of the limitations of the used instrument with maximum dosing pressure of 800 torr. Remarkably, during the experiments of CO₂ adsorption on metal-organic framework materials,³² a plateau is generally reached only at a higher pressure.

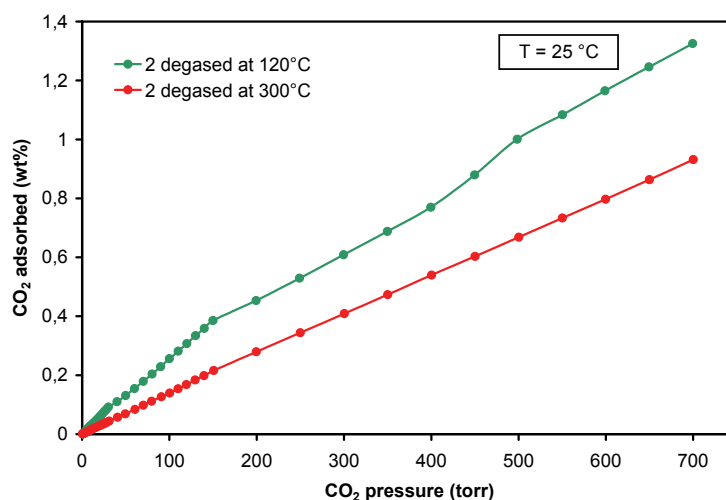


Figure 2-21. CO₂ adsorption isotherms recorded for **2** after suitable degassing treatments.

Generally pressures above 10 bar are necessary with specific values depending on the properties of the material pores, particularly their sizes. Unfortunately, such pressure was not achievable by the instrument used in this study. In spite the pressure reached during our experiments is slightly below the atmospheric pressure, the differences observed in the adsorption behaviour may be still useful to get a qualitative assessment of the different ability of the materials to store CO₂. The highest value was obtained by using **2** activated at 120 °C. Under such conditions, 1.32 wt% CO₂ was stored at ambient temperature and $p_{\text{CO}_2} = 700$ torr. After prolonged degassing of **2** at 300 °C to form the **2_{act}** phase, we observed a slight decrease of the adsorbed amount of CO₂, which could be likely interpreted as due to partial pore collapse following the prolonged heating under vacuum. This event cannot be excluded although XRPD measurements confirmed that the **2_{act}** phase is preserved after CO₂ adsorption experiments. The thermal treatment at

hand is indeed more “severe” than that used during both TG and temperature-dependent XRPD analyses which may well account for the decrease of the CO₂ adsorption. Notably, the adsorption process is fully reversible. Thus, a sequence of CO₂ adsorption experiments showing an almost perfect reproducibility of the adsorption isotherms, were performed on the **2_{act}** phase with intermediate degassing treatment at 25 °C from 12 h to 30 min. The strong carbon dioxide uptake shown by **2_{act}** is likely a consequence of the highly ionic nature of the Mg-O bond, which may induce strong dipolar interactions with polarised C=O bonds of CO₂.

2.4 Conclusions and outlook

Two polymeric magnesium formates **1** and **2** have been prepared by solvothermal syntheses and thoroughly characterised. They are polymorphs, and in the case of **1** the cubic network topology has been found for the first time. The hydrate form **2** undergoes an unexpected crystal-to-crystal phase transition when heated and soaked back into water. The final hydrate phase **2a** is monoclinic, while the starting material is orthorhombic. Beyond their interest as coordination polymers, possible applications in the fields of gas sensing and selective guest inclusion have been briefly investigated.

The polymeric formate **1**, upon activation, was shown to be a good candidate as a material for absorbing hydrogen. In fact it is a ultramicroporous material which can perfectly host hydrogen molecules. The Raman analysis shows the existence of two different cavities where the hydrogen can be physisorbed. The experimental data were confirmed by molecular simulation studies. GCMC simulations of the H₂ absorption isotherms estimate a theoretical loading corresponding to 12 molecules per unit cell, *i.e.* 4.2 mg g⁻¹. On the other hand, the value inferred from the Raman analysis is higher than the theoretical data. Hence, the full understanding of the adsorption properties of the Mg-derivative will require more detailed investigations, particularly to rationalize and define its behaviour as gas storage material.

Preliminary host-guest experiments carried out on **2_{act}** using different solvents (MeOH, *i*-PrOH, THF, DMF and MeCN) showed that it always reacts in the same

fashion producing **2a**, as checked through XRPD. This implies that **2_{act}** is selective for H₂O adsorption when put into a solvent/water mixture (*i.e.* a “wet” solvent). The ability of trapping selectively H₂O could envisage a possible application of these materials as dehydrating agents. Gas adsorption experiments evidenced that **2** possesses good sorption ability. These preliminary results suggest that, after activation, **2** could show interesting properties in the light and polar molecules storage field. The adsorption behaviour of **2_{act}** towards other light gases (such as H₂, O₂, CH₄ and CO) is currently under investigation, with the aim of applying these molecules to the important field of gas separation methodologies.³³

The formate molecule is very small and behaves as a strong coordinating molecule, thus tending to form high-density materials. As a logic extension, we are pursuing the target to prepare related materials with enlarged pore size. This may be achieved by introducing additional ligands (like tertiary amines) in the molecular structure. As a result, a hybrid material featuring a different supramolecular assembly, where the formate anion “co-crystallizes” together with the amine, could be formed. Other light metals, like calcium, titanium or aluminium, will be also investigated to verify whether their formate salts may provide further improvement in these areas.

2.5 Experimental section

2.5.1 Synthetic procedures

All starting materials and solvents were of analytical grade. They were purchased from Aldrich and used as received, without further purification.

Coupled thermogravimetric (TG) and differential thermal (DTA) analysis was performed with a Netzsch STA490C thermoanalyser under a 20 mL min⁻¹ air flux with a heating rate of 5 °C min⁻¹.

FT-IR spectra (KBr pellets) were recorded on a Perkin-Elmer Spectrum BX Series FT-IR spectrometer, in the range 4000 - 400 cm⁻¹.

Adsorption isotherms were recorded using a Micromeritics ASAP 2020 instrument. Prior to the measurements, the samples were degassed at the desired temperature (120 or 300 °C) using a heating rate of 1 °C min⁻¹, maintaining the final temperature for at least 24 h. CO₂ adsorption isotherms were recorded at 25 °C.

Elemental combustion microanalyses (C, H, N) were obtained using a elemental analyzer.

2.5.1.1 Synthesis of Magnesium(II) Formate $\text{Mg}(\text{HCOO})_2(\text{HCOOH}) \supset (\text{CH}_3)_2\text{NH}$ (**1**)

Magnesium perchlorate hexahydrate $\text{Mg}(\text{ClO}_4)_2 \cdot 6\text{H}_2\text{O}$ (1.84 g, 5.5 mmol) was dissolved together with cyclobutan-1,1'-dicarboxylic acid (0.40 g, 2.8 mmol) in 10.0 mL of *N,N*-dimethylformamide (DMF). The clear solution was transferred to a Teflon-lined stainless steel autoclave, sealed and heated under autogeneous pressure at 140 °C for 24 h. After slow overnight cooling, crystal precipitate was collected, washed with cold ethanol (4 x 10.0 mL) and dried under a nitrogen stream at rt to afford 0.51 g (45%, calculated with respect to magnesium perchlorate) of **1** as colourless plate-like crystals.

1: IR (KBr): $\tilde{\nu} = 3452\text{m}, 3027\text{w}, 2894\text{w}, 2880\text{w}, 2869\text{w}, 1681\text{s}, 1611\text{s}, 1472\text{w}, 1374\text{s}, 1349\text{s}, 1026\text{m}, 807\text{s} \text{ cm}^{-1}$. **Anal.** Calcd. for $\text{C}_5\text{H}_{11}\text{MgNO}_6$ (205.45): C, 29.23; H, 5.40; N, 6.82. Found: C, 29.82; H, 5.50; N, 6.78.¹³

2.5.1.2 Synthesis of Magnesium(II) Formate Dihydrate $\text{Mg}(\text{HCOO})_2 \cdot 2\text{H}_2\text{O}$ (**2**)

Compound **2** was already reported in the literature;¹⁷ herein, an alternative synthesis is described. Magnesium perchlorate hexahydrate $\text{Mg}(\text{ClO}_4)_2 \cdot 6\text{H}_2\text{O}$ (1.84 g, 5.5 mmol) was dissolved together with cyclobutan-1,1'-dicarboxylic acid (0.40 g, 2.8 mmol) in 5.0 mL of *N,N*-dimethylformamide (DMF). The clear solution was transferred to a Teflon-lined stainless steel autoclave, sealed and heated under autogeneous pressure at 140 °C for 24 h. After slow overnight cooling, crystal precipitate was collected, washed with cold ethanol (4 x 10.0 mL) and dried under a nitrogen stream at rt to afford 0.46 g (57%; calculated with respect to magnesium perchlorate) of **2** as colourless prismatic crystals.

2: The IR data obtained on our samples match to those reported previously in the literature.¹⁷ **Anal.** Calcd. for $\text{C}_2\text{H}_6 \text{Mg O}_6$ (150.37): C, 15.97; H, 4.02. Found: C, 16.13; H, 4.04.

2.5.2 X-ray crystallographic studies

The XRD data for **1** and **2** were collected on Enraf-Nonius CAD4 diffractometer equipped with a graphite monochromator and Mo-K α radiation. The intensity collected were corrected for Lorenz and polarization effect. During the data collection three standard reflections were monitored every 2 h. The atomic scattering factors are those reported by Cromer and Waber.³⁴ The structure was solved by direct methods using the SIR97 program.³⁵ The refinements were made by full matrix least squared on all F² data using SHELXL97.³⁶ Anisotropic thermal parameters were allotted only for the non-disordered atoms. The hydrogen atoms were found in the Fourier maps. The coordinates of the hydrogen atom of the formate were refined while the positions of the hydrogen atoms of the dimethylammonium cation were frozen. For all the hydrogen atoms an isotropic structure factor 20% bigger than the corresponding bonded atoms were chosen. The molecular drawing was made using the ORTEP-III program for Windows.³⁷ The computational work was performed using the WINGX interface.³⁸

XRPD measurements were carried out with a PHILIPS X'PERT PW3020 powder diffractometer equipped with a diffracted beam graphite monochromator and operating with CuK α radiation. 0.5° divergence and scatter slits and a 0.1 mm receiving slit were used. The step size was 0.02° of 2 θ with a counting time of 1 s/step. To minimize the effect of possible preferred orientation the sample was laterally loaded into a low background aluminium sample holder with a cut quartz monocrystal underneath. High quality X-ray diffraction pattern for the hydrated phase **2a** was collected using a Panalytical X'PERT PRO equipped with the X'Celerator[®] solid state detector in the 10 ÷ 130 ° 2 θ region. The counting time was 30 s/step.

Temperature dependent X-Ray powder diffraction spectra were collected using a Anton Paar HTK 1200N Oven camera, equipped on the right-side of the PHILIPS PW3020 diffractometer and working with a Ni filter on the diffracted beam. The heating rate was 3 °C min⁻¹ for all the compounds. The measurements were carried out at ambient pressure under a mild N₂ flow.

A complete list of the crystallographic data are collected in the Appendix (Chapter 5).

2.6 References and notes

- 1 Rossin, A.; Ienco, A.; Costantino, F.; Montini, F.; **Di Credico, B.**; Caporali, M.; Gonsalvi, L.; Fornasiero, P.; Peruzzini, M. *Cryst. Growth Des.* **2008**, *8*, 3302.
- 2 a) Cambridge Structural Database System, Cambridge Crystallographic data Centre, 12 Union Road, Cambridge, CB2 1EZ, U.K. (Version 5.30 with update Sep, 2009); b) Allen, F. H. *Acta Crystallogr., Sect. B* **2002**, *58*, 380.
- 3 a) Lipton, A. S.; Smith, M. D.; Adams, R. D.; Ellis, P. D. *J. Am. Chem. Soc.* **2002**, *124*, 410; b) Lu, J. Y.; Babb, A. M. *Chem. Commun.* **2002**, 1340; c) Baggio, R.; Stoilova, D.; Garland, M. T. *J. Mol. Struct.* **2003**, *659*, 35; d) Dybsteve, D. N.; Chun, H.; Yoon, S. H.; Kim, D.; Kim, K. *J. Am. Chem. Soc.* **2004**, *126*, 32; e) Wang, Z.; Zhang, B.; Fujiwara, H.; Kobayashi, H.; Kurmoo, M. *Chem. Commun.* **2004**, 416; f) Viertelhaus, M.; Anson, C. E.; Powell, A. K. *Z. Anorg. Allg. Chem.* **2005**, *631*, 2365; g) Viertelhaus, M.; Adler, P.; Clérac, R.; Anson, C. E.; Powell, A. K. *Eur. J. Inorg. Chem.* **2005**, 692; h) Wang, Z.; Zhang, B.; Kurmoo, M.; Green, M. A.; Fujiwara, H.; Oztuka, T.; Kobayashi, H. *Inorg. Chem.* **2005**, *44*, 1230; i) Rood, J. A.; Noll, B. C.; Henderson, K. W. *Inorg. Chem.* **2006**, *45*, 5521; j) Guo, J.-Y.; Zhang, T.-L.; Zhang, J.-G. *Chin. J. Chem.* **2006**, *24*, 745; k) Wang, Y.; Cao, R.; Bi, W.; Li, X.; Yuan, D.; Sun, D. *Microporous Mesoporous Mater.* **2006**, *91*, 215; l) Samsonenko, D. G.; Kim, H.; Sun, Y.; Kim, G.-H.; Lee, H.-S.; Kim, K. *Chem. Asian J.* **2007**, *2*, 484; m) Tian, Y.-Q.; Zhao, Y.-M.; Xu, H.-Y.; Chi, C.-Y. *Inorg. Chem.* **2007**, *46*, 1612; n) Su, J.; Wang, Y.; Yang, S.; Li, G.; Liao, F.; Lin, J. *Inorg. Chem.* **2007**, *46*, 8403; o) Wang, Z.; Zhang, X.; Batten, S. R.; Kurmoo, M.; Gao, S. *Inorg. Chem.* **2007**, *46*, 8439.
- 4 Selected examples of molecular formates include: a) $\text{Cu}(\text{HCOO})_2 \cdot 4\text{H}_2\text{O}$: Kiriya, R.; Ibamoto, H.; Matsuo, K. *Acta Cryst.* **1954**, *7*, 482; b) $\text{In}(\text{HCOO})_3$: Habeeb, J. J.; Tuck, D. G. *J. Chem. Soc. Dalton Trans.* **1973**, *3*, 243; c) Actinide formates: Casellato, U.; Vigato, P.; Vidali, M. *Coord. Chem. Rev.* **1978**, *26*, 85; d) $\text{Cd}(\text{HCOO})_2 \cdot 2\text{H}_2\text{O}$: Honkonen, R. S.; Ellis, P. D. *J. Am. Chem. Soc.* **1984**, *106*, 5488; e) $\text{Co}(\text{HCOO})_2 \cdot 2\text{H}_2\text{O}$: Arii, T.; Kishi, A. *Thermochimica Acta* **1999**, *325*, 157; f) $\text{Rb}(\text{HCOO})$ and $\text{Cs}(\text{HCOO})$: Wilson, M. P.; Alcock, N. W.; Rodger, P. M. *Inorg. Chem.* **2006**, *45*, 4539.
- 5 For MOF applications see Chapter 1 Paragraph 1.4.3.
- 6 a) Braga, D.; Grepioni, F.; Desiraju, G. R. *Chem. Rev.* **1998**, *98*, 1375; b) Moulton, B.; Zawrotko, M. J. *Chem. Rev.* **2001**, *101*, 1629; c) Seddon, K. R. *Cryst. Growth Des.* **2004**, *4*, 1087; d) Nangia, A. *Cryst. Growth Des.* **2006**, *6*, 4.
- 7 a) Doyle, R. P.; Nieuwenhuyzen, M.; Kruger, P. E. *Cryst. Eng. Comm.* **2006**, *8*, 904; b) Fu, S.-J.; Cheng, C.-Y.; Lin, K.-J. *Cryst. Growth Des.* **2007**, *7*, 1381.
- 8 Eddaoudi, M.; Moler, D. B.; Li, H. L.; Chen, B. L.; Reineke, T. M.; O'Keeffe, M.; Yaghi, O. M. *Acc. Chem. Res.* **2001**, *34*, 319; b) Janiak, C. *Dalton Trans.* **2003**, 2781; c) Rather, B.; Zawrotko, M. J. *Chem. Commun.* **2003**, 830.
- 9 a) Poizat, O.; Strommen, D. P.; Maldivi, P.; Giroud-Godquin, A.; Marchon, J. *Inorg. Chem.* **1990**, *29*, 4851; b) Gillet, P.; Badro, J.; Varrel, B.; McMillan, P. F. *Phys. Rev. B: Condens. Matter* **1995**, *51*, 11262; c) Brezesinsky, T.; Groenewolt, M.; Antonietti, M.; Smarsly, B. *Angew. Chem., Int. Ed.* **2006**, *45*, 781; d) Curtis, M. D.; Nanos, J. I.; Moon, H.; Jahng, W. S. *J. Am. Chem. Soc.* **2007**, *129*, 15072.
- 10 Clausen, H. F.; Poulsen, R. D.; Bond, A. D.; Chevallier, M.-A. S.; Iversen, B. B. *J. Solid State Chem.* **2005**, *178*, 3342.

- 11 An interesting review on the last advances in the XRPD technique is available, see: Harris, K. D. M.; Cheung, E. Y. *Chem. Soc. Rev.* **2004**, *33*, 526.
- 12 Frenkel, D.; Smit, B., *Understanding Molecular Simulations: from Algorithms to Applications*. 2nd ed.; Academic Press: San Diego, **2002**.
- 13 a) Thomas, J. M.; Thomas, W. J. *Princ. Pract. Heterogen. Catal.* **2003**, *216*, 298 and references therein; b) Cundy, C. S.; Cox, P. A. *Chem. Rev.* **2003**, *103*, 663; c) Corma, A. *J. Catal.* **2003**, *216*, 298.
- 14 Some early examples of solvothermal (or hydrothermal) syntheses applied to MOFs are the following: a) Yaghi, O. M.; Li, H. *J. Am. Chem. Soc.* **1995**, *117*, 10401; b) Yaghi, O. M.; Li, G.; Groy, T. L. *J. Solid State Chem.* **1995**, *117*, 256; c) Yaghi, O. M.; Li, G.; Li, H. *Nature* **1995**, *378*, 703; d) Yaghi, O. M.; Li, H.; Groy, T. L. *J. Am. Chem. Soc.* **1996**, *118*, 9096; e) Yaghi, O. M.; Li, H.; Groy, T. L. *Inorg. Chem.* **1997**, *36*, 4292.
- 15 A comparison of the calculated XRPD spectrum (simulated from the single-crystal data) with the experimental spectrum, recorded on the solid product, showed that, in the case of the zinc nitrate synthesis, some impurities are present, whose relative amount is presumably very small (less than 10%) with respect to the main phase. This can be inferred from the satisfactory match of the measured elemental analyses with the theoretical ones. Products from zinc perchlorate are generally less pure than those coming from nitrate, probably up to 40 - 50%, from the X-ray intensities (Figure 2-2, spectrum b).
- 16 Wang, X.-Y.; Gan, L.; Zhang, S.-W.; Gao, S. *Inorg Chem.* **2004**, *43*, 4615.
- 17 Malard, C.; Pezerat, H.; Herpin, P.; Toledano, P. *J. Solid State Chem.* **1982**, *41*, 67.
- 18 a) Stoilova, D.; Koleva, V. *J. Mol. Struct.* **2000**, *553*, 131; b) Stoilova, D. *J. Mol. Struct.* **2006**, *798*, 141; c) Stoilova, D.; Baggio, R.; Garland, M. T.; Marinova, D. *J. Mol. Struct.* **2007**, *842*, 67.
- 19 Donaldson, J. D.; Knifton, J. F.; Ross, S. D. *Spectrochim. Acta* **1964**, *20*, 547.
- 20 Powell, A. K.; Anson, C. E.; Viertelhaus, M. *Zeitschrift fuer Anorganische und Allgemeine Chemie* **2005**, *631*, 2365.
- 21 Lu, J. Y.; Babb, A. M. *Chem. Commun.* **2002**, 1340.
- 22 Rossin, A. and Di Credico, B., ICCOM-CNR, personal communication.
- 23 About GSAS: C. Larson and R. B. von Dreele, Generalized Crystal Structure Analysis System, Los Alamos National Laboratory, NM, USA, **2001**. Rietveld refinement of **2a** was performed using the GSAS program. Firstly, zero shift, cell parameters, background, and profile shape were refined; a corrected pseudo-Voigt profile function (six terms) with two terms for the correction of asymmetry at the low-angle region was used. Secondly, atomic coordinates and isotropic thermal factors were refined restraining the distances and the angles to the following values: Mg-O = 2.05(5) Å, C-O = 1.23(2) Å, O-C-O = 120(1)°. The statistical weight of these restraints was decreased as the refinement proceeded, but it was not possible to set it to zero, due to some unrealistic light atom bond distances. At the end of the refinement, the shifts in all parameters were less than their standard deviations. Crystal data and refinement details for **2a**: Monoclinic $P2_1/c$; $a = 8.6511(3)$ $b = 7.1522(3)$ $c = 9.4041(4)$ Å; $\beta = 98.166(3)^\circ$ $V = 575.97(4)$ Å³; 2θ range for data collection: 5 - 130°; N° of data = 6976, N° of reflections = 2072; $R_F2 = 0.080$, $Rwp = 0.097$, $Rp = 0.071$ ($R_F2 = \sum |F_o^2 - F_c^2| / \sum |F_o|^2$; $Rp = \sum |I_o - I_c| / \sum I_o$; $Rwp = [\sum w(I_o - I_c)^2 / \sum wI_o^2]^{1/2}$).
- 24 Gregg, S. J.; Sing, K. S. W. *Adsorption, Surface Area, and Porosity*, Academic Press: New York, **1982**.

- 25 In collaboration with Dr. Alessandra Giannasi, Istituto dei Sistemi Complessi – CNR, Florence, Italy.
- 26 Kong, L.; Cooper, V. R.; Nijem, N.; Li, K.; Li, J.; Chabal, Y.; Langreth, D. *Phys. Rev. B* **2009**, *79*, 081407(R).
- 27 In collaboration with Prof. Tina Düren and Dr. David Fairen (Edinburgh University, Scotland, UK).
- 28 Gupta, A.; Chempath, S.; Sanborn, M. J.; Clark, L. A.; Snurr, R. Q. *Molecular Simulation* **2003**, *29*, 29.
- 29 Rappé, A. K.; Casewit, C. J.; Colwell, K. S.; Goddard, W. A.; Skiff, W. M. *J. Am. Chem. Soc.* **1992**, *114*, 10024.
- 30 Feynman, R. P.; Hibbs, A. R. *Quantum Mechanics and Path Integrals* **1965**, New York, McGraw-Hill.
- 31 Gelb, L. D.; Gubbins, K. E. *Langmuir* **1999**, *15*, 305.
- 32 a) Millward, A. R.; Yaghi, O. M. *J. Am. Chem. Soc.* **2005**, *127*, 17998; b) Walton, K. S.; Millward, A. R.; Dubbeldam, D.; Frost, H.; Low, J. J.; Yaghi, O. M.; Snurr, R. Q. *J. Am. Chem. Soc.* **2008**, *130*, 406.
- 33 Unpublished H₂ adsorption experiments on **2** showed that in this case performance is much worse than with CO₂. A maximum value of 0.070 wt% (corresponding to 0.347 mmol g⁻¹) of hydrogen adsorbed at -196 °C and at p_{H₂} = 700 torr was recorded. Thus, selective gas sorption (*i.e.* gas separation) in a H₂/CO₂ mixture is achievable with **2**.
- 34 Cromer, D. T.; Waber, J. T. *Acta Crystallogr.* **1965**, *18*, 104.
- 35 Altomare, A.; Burla, M. C.; Cavalli, M.; Cascarano, G. L.; Giavovazzo, C.; Gagliardi, A.; Moliterni, A. G. G.; Polidori, G.; Spagna, R. *J. Appl. Cryst.* **1999**, *32*, 115.
- 36 Sheldrick, G. M. Program SHELXL97 (crystal structure refinement), University of Göttingen, Göttingen, Germany, **1997**.
- 37 a) *ORTEP-III*, Burnett, M. N.; Johnson, C. K. Report ORNL-6895, Oak Ridge National Laboratory, Oak Ridge, TN, USA, **1996**; b) Farrugia, L. J. *J. Appl. Chem.* **1997**, *30*, 565.
- 38 Farrugia, L. J. *J. Appl. Chem.* **1999**, *32*, 837.

Supramolecular architectures with thiazole and thiazolidine ligands

3.1 Overview

This chapter describes the coordination chemistry of different five-membered heterocyclic species such as thiazoles, oxazoles and thiazolidines. Firstly, the chapter begins with the description of a mild and selective procedure for the synthesis of 4-carboxy oxazoles, thiazoles and thiazolidines from naturally occurring amino acids (serine or cysteine) through condensation with aldehydes or acids.¹ Secondly, the coordination ability of these ligands towards a variety of transition metal ions is explored and the resulting metallorganic supramolecular architectures are presented.² The chapter concludes with the description of the synthesis of a chiral metal-organic framework with *syn*-thiazolidine-2,4-dicarboxylic acid.

3.2 Introduction

The coordination chemistry of polytopic ligands has yielded many interesting supramolecular structures.³ Ligands containing both pyridyl and/or carboxylic groups (the simplest model can be considered the pyridinecarboxylic acid, Figure 3-1), are versatile organic connectors in crystal engineering due to their ability to form multiple coordination bonds at the same time.⁴

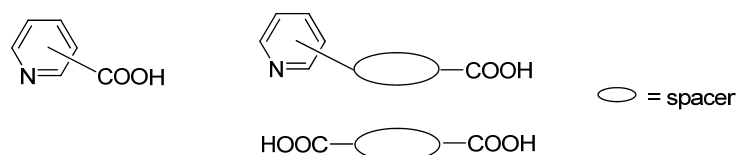


Figure 3-1. Pyridinecarboxylic acid and possible pyridyl and carboxylic scaffolds for the MOF synthesis.

Because of their intriguing chemical properties, nitrogen-containing heterocycles have also been used as building blocks for polydimensional architectures by engaging into multiple coordination to different metal centres. In particular, mixed N,S- or N,O- heterocycles such as thiazolidines, thiazoles and oxazoles have received large attention.³ The presence of these spacers within the structural skeleton of multidentate ligands may offer additional binding sites and further structural flexibility in the formation of molecular frameworks (Figure 3-2).

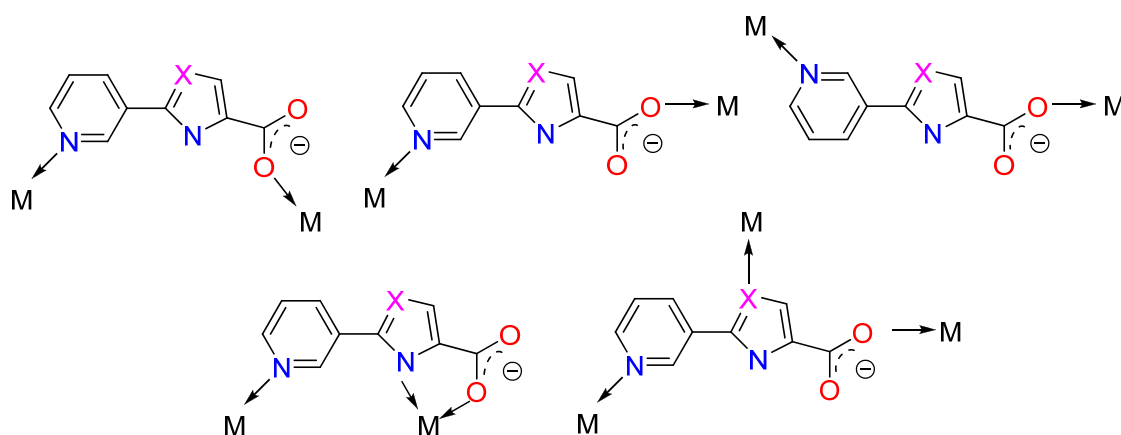


Figure 3-2. Possible coordination modes of pyridyl and carboxylate-based 2,4-di(substituted) five-membered heterocycles (X = S, O).

When the 2,4-di(substituted) five-membered heterocycles are put in between the carboxyl group and the/or pyridyl unit, the relative orientation of the coordination sites is

no longer linear like in *para*-substituted six-membered rings, but it becomes bent to a some extent, for geometric reasons related to the pentagonal ring shape. Moreover, the aromatic thiazole or oxazole ring rigidity may confer additional structural constraints able to steer the assembly of MOFs.⁵

The possibility to carry out an in-depth screening of a large class of 5-membered heterocyclic ligands is therefore necessary to gain a better insight on the substituent effects on the 3D self-assembly in the presence of transition metal centres. For this reason, a general mild and selective procedure for preparing 4-carboxy oxazole, thiazole and thiazolidine derivatives would be very desirable. Herein, we report our results in this field describing a widely-applicable and simple synthetic approach which, starting from easily available building blocks, allows multi-gram scale preparation of a variety of 2-substituted,4-carboxy heterocycles.

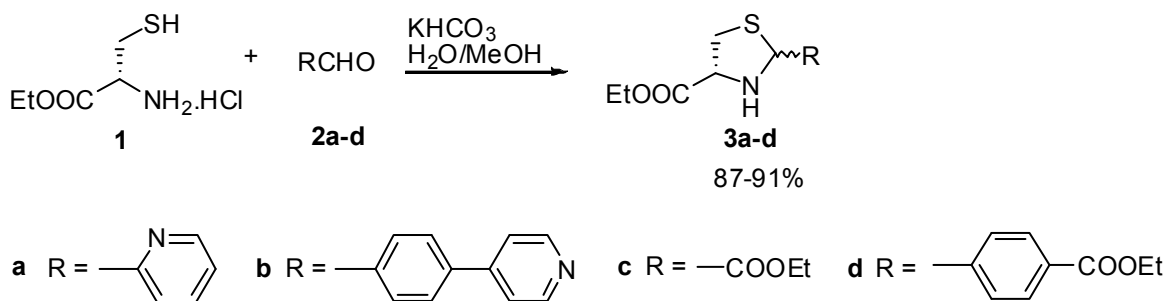
Once obtained, the thiazole and thiazolidine ligands were tested as ligands towards a variety of 3d-transition metals and led to the synthesis of novel 0D to 3D solid state assemblies. The resulting zinc(II), cobalt (II) and copper(II) thiazole complexes form supramolecular complexes in the solid state, generating hydrogen-bonded networks of polymeric nature. Indeed, many divalent transition metal ions in aqueous environment strongly tend to bind to water to complete their coordination sphere.⁶ This feature may give rise to the potential for stabilizing and extending coordination arrays *via* secondary hydrogen-bonding contacts involving the aquo ligands themselves.^{6c,5}

Finally, preliminary studies have been conducted on the aliphatic counterparts of these systems, giving hints of some interest for future developments and paving the way to their possible application as gas storage materials and catalysis. Thiazolidine-2,4-dicarboxylic acid with -COO^- groups in a *syn* conformation led to a new three-dimensional MOF with cobalt(II), whose structure shows the presence of two different types of channels (hydrophobic and hydrophilic). The presence of chirality in this system is intriguing and worth to be exploited in possible applications in the field of enantioselective catalysis and separation.

3.3 Synthesis of oxazole, thiazoles and thiazolidines

3.3.1 Results and discussion

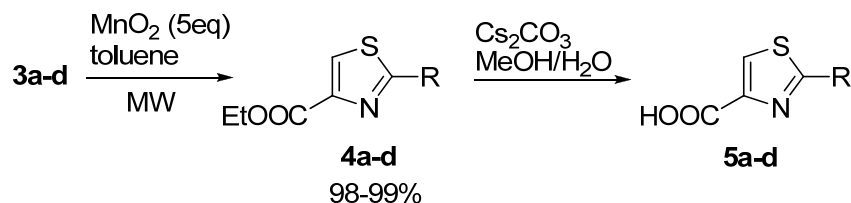
Cyclisation of cysteine side-chains onto carbonyl groups to create five-membered thiazole-based heterocycles is a well established procedure.⁷ Thus, *L*-cysteine ethyl ester **1** was reacted with different pyridyl and carboxy aldehydes **2a-d** to afford the corresponding thiazolidine derivatives **3a-d** as depicted in Scheme 3-1. Condensation reactions were carried out in aqueous methanol containing potassium bicarbonate and, as expected, mixtures of two diastereoisomers were obtained, due to the presence of a new stereogenic centre generated at the C-2 atom of the thiazolidine ring.



Scheme 3-1. First step in the synthesis of thiazole and thiazolidine ligands.

The thiazolidines synthesized by this procedure were converted into the corresponding thiazoles *via* oxidation. This was the most challenging step in the reaction sequence as we aimed at improving the existing procedures to obtain the desired thiazoles in large scale and better yield. First attempts, performed using a mixture of $\text{CBrCl}_3/\text{DBU}$ (1,8-diazabicyclo[5.4.0]undec-7-ene),⁸ yielded as expected the thiazole derivatives **4a-d**, albeit in poor yield. DDQ (2,3-dichloro-5,6-dicyanobenzoquinone) and NiO_2 ⁷ were also found to be effective, but again the yields were poor and partially reduced thiazolines were found as contaminating by-products in some cases. Oxidation was most conveniently performed with commercially available and cheap manganese dioxide, which provided the desired thiazoles in very good yields, although rather harsh conditions were necessary. The reaction was indeed carried out in benzene in the presence of pyridine for 24 h at 55 °C, using a 25-fold excess of MnO_2 . In order to find milder and more general reaction conditions, we decided to investigate the effect of

microwave irradiation on this oxidation process. Over the past few years the efficiency of microwave flash heating in accelerating oxidation processes has been successfully demonstrated.⁹ In our case, although a large excess (five equivalents) of MnO₂ was still necessary, under optimized conditions, namely 30 seconds irradiation with a 300 W microwave source at 100 °C, using toluene as solvent and in the absence of pyridine, the reactions led to quantitative formation of thiazoles **4a-d** (Scheme 3-2). Apart from providing a more “energetically-efficient” transformation, it is remarkable that when following this unconventional technique the amount of MnO₂ employed was consistently reduced, benzene could be avoided and the use of base was unnecessary. The unnecessary use of a basic additive is an important advantage of the use of MW irradiation in assisting the synthesis of the thiazoles **4**. This can in turn result in a wider applicability of this protocol, for example in the synthesis of optically active thiazoles, as the presence of external bases in the reaction mixture could lead to product racemization.¹⁰



Scheme 3-2. The oxidation and hydrolysis reactions in the synthetic pathway.

Finally, saponification with Cs₂CO₃ afforded the corresponding carboxythiazoles **5a-d** which were isolated by crystallization from acidic water and fully characterized in solution by conventional NMR and MS techniques.

Crystals of 2-(2-pyridyl)thiazole-4-carboxylic acid (Htzc-py, **5a**) suitable for a crystallographic analysis were grown from a water solution and the corresponding X-ray crystal structure is depicted in Figure 3-3. The asymmetric unit consists of two thiazoles and a crystallization water molecule hydrogen-bonded to one carboxylic group {d[O(1)•••O(5)] = 2.582(4) Å} that reduces the overall symmetry. Additional hydrogen bonding with the N atom of the thiazole ring of the neighbouring molecule {d[O(5)•••N(3)] = 3.032(5) Å, Figure 3-3(b)} is present, thus creating a 3D network. The distance between two adjacent thiazole rings is 3.73 Å, and there is evident π -stacking in

the lattice. The nitrogen atom N(2) [N(4)] in the *ortho*-pyridyl substituent is in a transoid conformation with respect to that of the thiazole ring N(1) [N(3)] [dihedral angle $\theta[\text{N}(1)\text{-C-C-N}(2)] = \theta[\text{N}(3)\text{-C-C-N}(4)] = 179.9^\circ$]. Surprisingly, in the Cambridge Database¹¹ there is only one fully organic structure containing the thiazole ring: the (oxythiamineH)(picrolonate)₂•2H₂O.¹² In this derivative, the N atom of the five-membered heterocycle is alkylated, and the overall charge is positive (thiazolium ion). This slightly modifies the bond lengths with respect to the neutral ring, without strong deviations from the ordinary C=C, C=N or C-S bonds. In particular, the d(S-C) distances seem to be the most affected: 1.668(6) / 1.715(6) vs. 1.731(4) / 1.695(4) Å for the oxythiaminium cation and the neutral **5a**, respectively. A complete list of the crystallographic data are collected in the Appendix (Chapter 5).

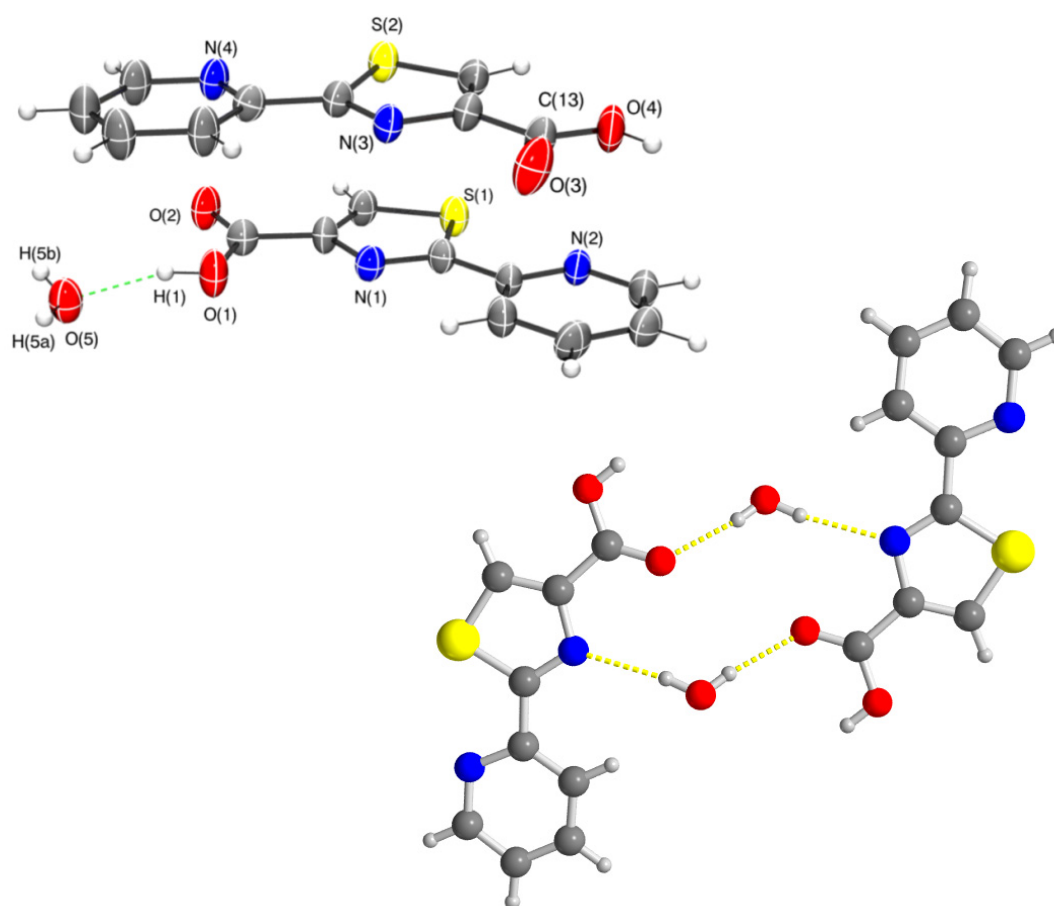
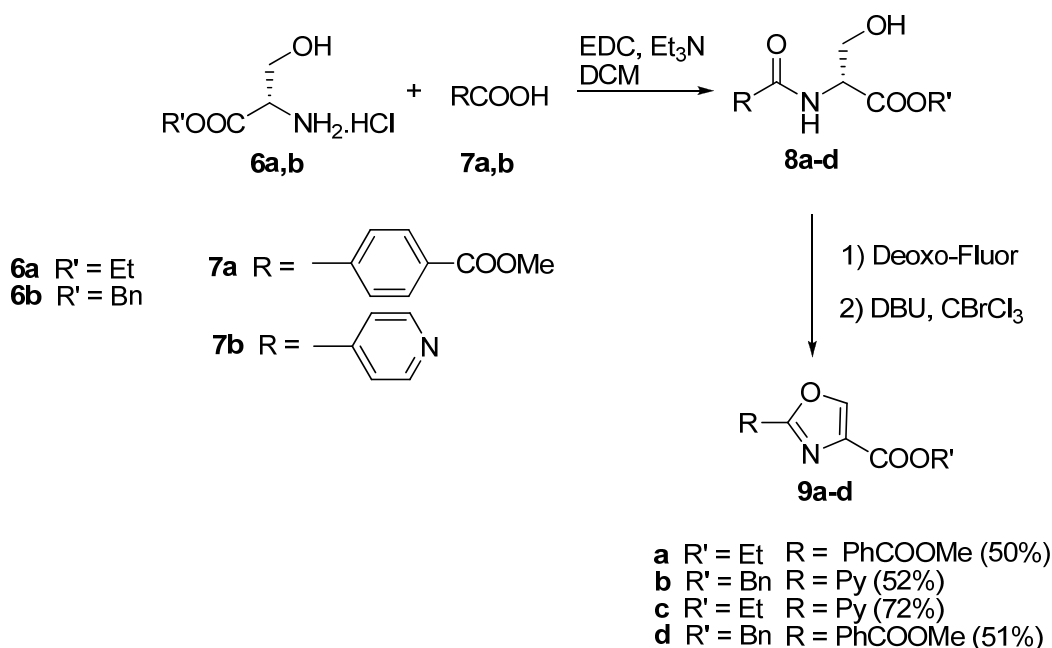


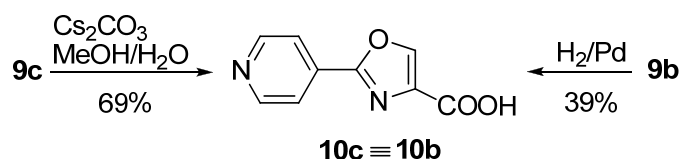
Figure 3-3. X-ray crystal structure of the asymmetric unit of **5a** (above) and double hydrogen bonding of water to neighbouring molecules in the lattice (below). Thermal ellipsoids (above in the figure) drawn at 40% probability.

The corresponding 4-carboxy-oxazolidines were also prepared. Serine ethyl or benzyl esters **6a,b** were coupled with terephthalic acid monomethyl ester **7a** or isonicotinic acid **7b** (Scheme 3-3).



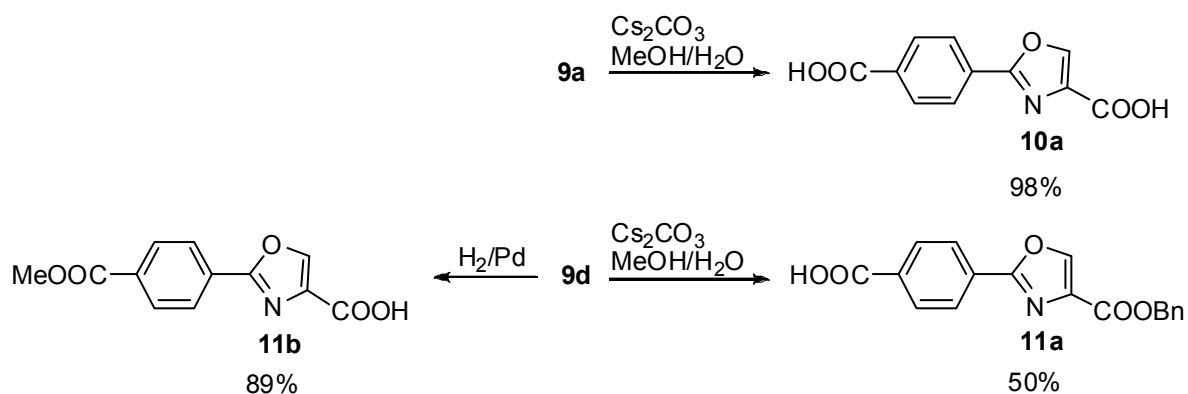
Scheme 3-3. Synthesis of oxazole ligands.

Then, cyclization was performed using bis(2-methoxyethyl)aminosulfur trifluoride solution (Deoxo-Fluor) followed by addition of BrCCl₃ and DBU (1,8-diazabicyclo[5.4.0]undec-7-ene) to afford oxazoles **9a-d** in good overall yields.¹³ Serine benzyl ester was used to evaluate a different protective group which might be particularly useful in view of demanding orthogonally protected carboxy moieties (as in compound **9d**). Saponification of **9c** with Cs₂CO₃ afforded the corresponding carboxazoles **10c** which was isolated after crystallization from acidic water and fully characterized. Alternatively, acid **10c** was obtained by hydrogenation of **9b**, albeit in quite low yield (Scheme 3-4).



Scheme 3-4. Deprotection of the functional groups of the oxazole ring.

The dicarboxylic acid **10a** was prepared by saponification of **9a** and finally the monoprotected compounds **11a** and **11b** were in turn obtained by saponification or hydrogenolysis of **9d**, confirming that benzyl ester can be advantageously used as orthogonal protective group for obtaining mono carboxy derivatives (Scheme 3-5).



Scheme 3-5. Deprotection of the functional groups of the oxazole ring.

3.4 Coordination chemistry of thiazole-based ligands

3.4.1 Introduction

The synthesis of coordination complexes containing some of the ligands described above was carried out through a solvothermal (hydrothermal) technique, applicable to the production of either molecular species or polymers, with a high degree of crystallinity in both cases. There are many factors that control the final reaction outcome, and the effect of each of them on the resulting material is not clear yet.¹⁴ Temperature, concentration, time, metal precursor and pH are all crucial elements in driving the reaction course. The commercially available thiazole-4-carboxylic acid (4-Htzc, **12**), and the synthesized thiazole-2-carboxylic acid (2-Htzc, **13**), thiazole-2,4-dicarboxylic acid (2,4-H2tzdc, **5c**) and 2-(pyridin-4-yl)thiazole-4-carboxylic acid (Htzc-py, **5a**, Figure 3-4) were reacted with zinc(II), cobalt (II) and copper(II) ions, generating hydrogen-bonded networks of polymeric nature. Among them, an unusual trigonal bipyramidal coordination geometry was found in the zinc(II) complex $\text{Zn}(\text{tzc-py})_2(\text{H}_2\text{O})$, where the dangling *ortho*-pyridyl substituent forms an intramolecular hydrogen bonding with the coordinated water molecule. This kind of arrangement is very uncommon for aromatic ligands.

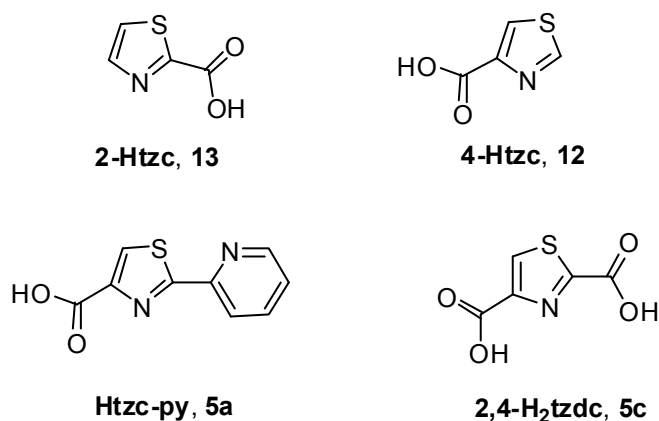


Figure 3-4. Thiazole-based ligands.

3.4.2 Ligand thermal stability

Before undertaking the preparation of metal-organic compounds, the bare ligands stability was examined through TGA-MS, in order to get an estimation of the maximum temperature at which the solvothermal synthesis could be carried out without causing an undesired ligand decomposition. The TGA-DTG plots related to the four organic spacers in use in this work are collected in Figure 3-5.

A perusal of these TGA-MS analysis shows that the most thermally robust ligand was Htzc-py, for which decomposition occurs at 243 °C. Decomposition was also observed at 115, 215 and 205 °C for 2-Htzc, 4-Htzc and 2,4-H₂tzdc, respectively. In the latter case, it was possible to detect clearly the peak at 138 °C associated with an m/z value of 44 a.m.u. on the MS spectra (recorded during the heating process) that points out CO₂ emission from a decarboxylation reaction (calculated weight loss 25%, experimental 27%), while with 2-Htzc and 4-Htzc a similar decarboxylation takes place more or less simultaneously with respect to decomposition, and the peaks strongly overlap. All the attempted preparations of metal complexes containing 2,4-H₂tzdc by hydrothermal methods led to the analogous 4-Htzc species, even when the reaction was carried out at temperatures lower than that indicated by the TG spectra. Indeed, solvothermal reactions of zinc(II) salts with 2,4-H₂tzdc in water, methanol or *N,N*-dimethylformamide in the 60–100 °C temperature range always led to crystals of Zn(4-tzc)₂•2H₂O (**14**) complex. The same result was obtained from a "classical" solution synthesis carried out under similar reaction conditions. These trials showed that the –COOH group in the 2 position is the most labile, as confirmed by the known reactivity of 2-substituted thiazoles, and zinc(II)

probably promotes the ligand decarboxylation. Another proof of evidence is the DTG signal shape related to the last weight loss in Figure 3-5 (b and c), which clearly suggests that 2,4-H₂tzdc "behaves" exactly like 4-Htzc in the last thermal decomposition step.

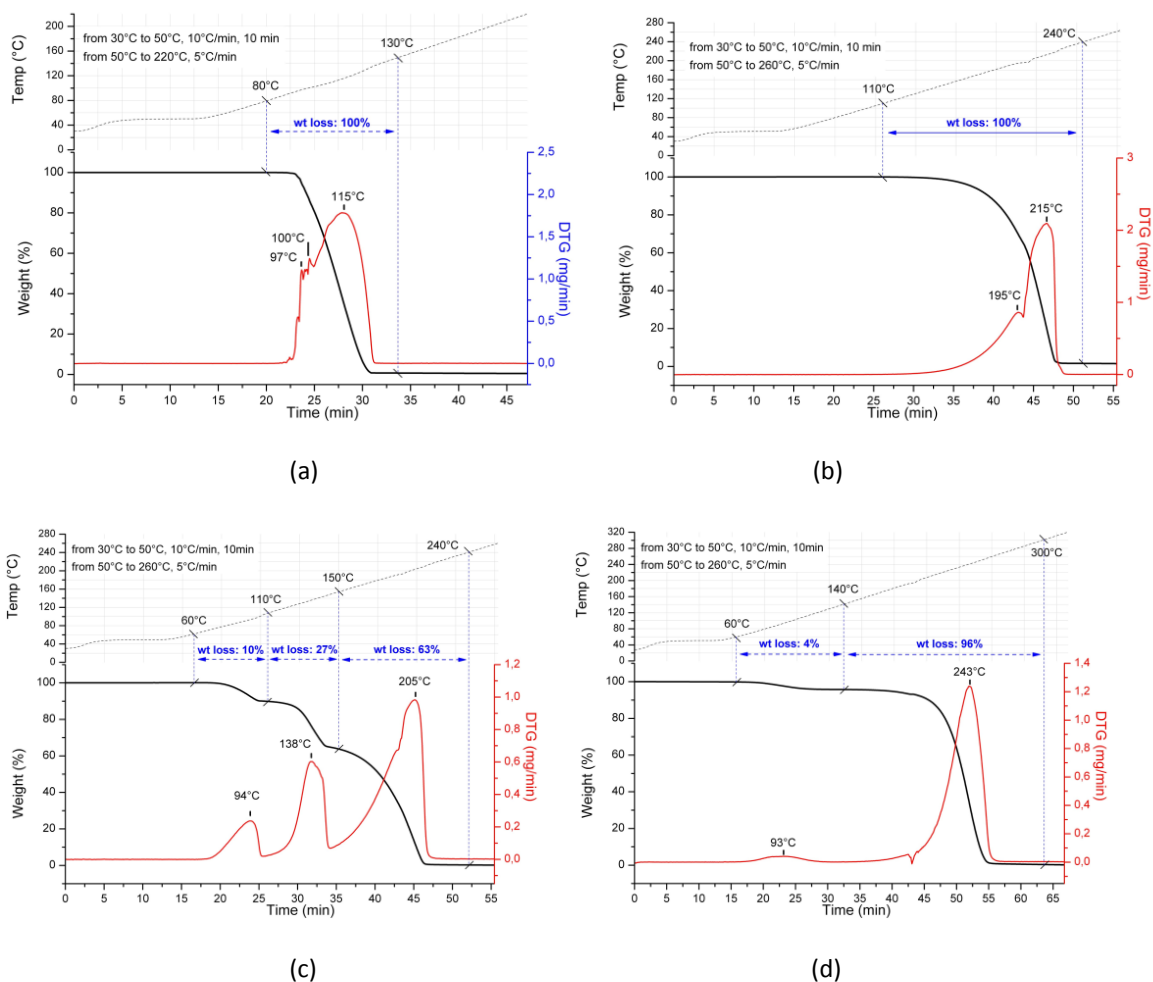


Figure 3-5. TGA-DTG plots of (a) **13**, (b) **12**, (c) **5c** and (d) **5a**.

Colorless prismatic crystals of 2-Htzc were obtained from concentrated acidic aqueous solutions, upon cooling at 4 °C. The crystal structure of the ligand is shown in Figure 3-6. The main metrical features of the heterocyclic ring are similar to those reported for the only other existing XRD structure of a thiazole-based molecule (Htzc-py).¹⁵ Hydrogen bonding between the –OH moiety of the carboxylic group and the nitrogen atom of the adjacent thiazole ring in the lattice is present $\{d[\text{O}(1)\cdots\text{N}(1)\#] = 2.665(7)\}$,¹⁵ generating a “zig-zag” disposition of the molecules in the crystal packing along the c axis that maximizes the number of these stabilizing interactions (b in Figure 3-6). Additional π -stacking among the aromatic rings is present $[d(\text{thiazole ring centroids}) = 3.884 \text{ \AA}]$, with a

slightly staggered relative disposition], generating an ordered assembly along the b axis as well (c in Figure 3-6). The overall “helicoidal” packing generates a non-centrosymmetric space group ($Pn2_1a$), with intrinsic chirality. A complete list of the crystallographic data are collected in the Appendix (Chapter 5).

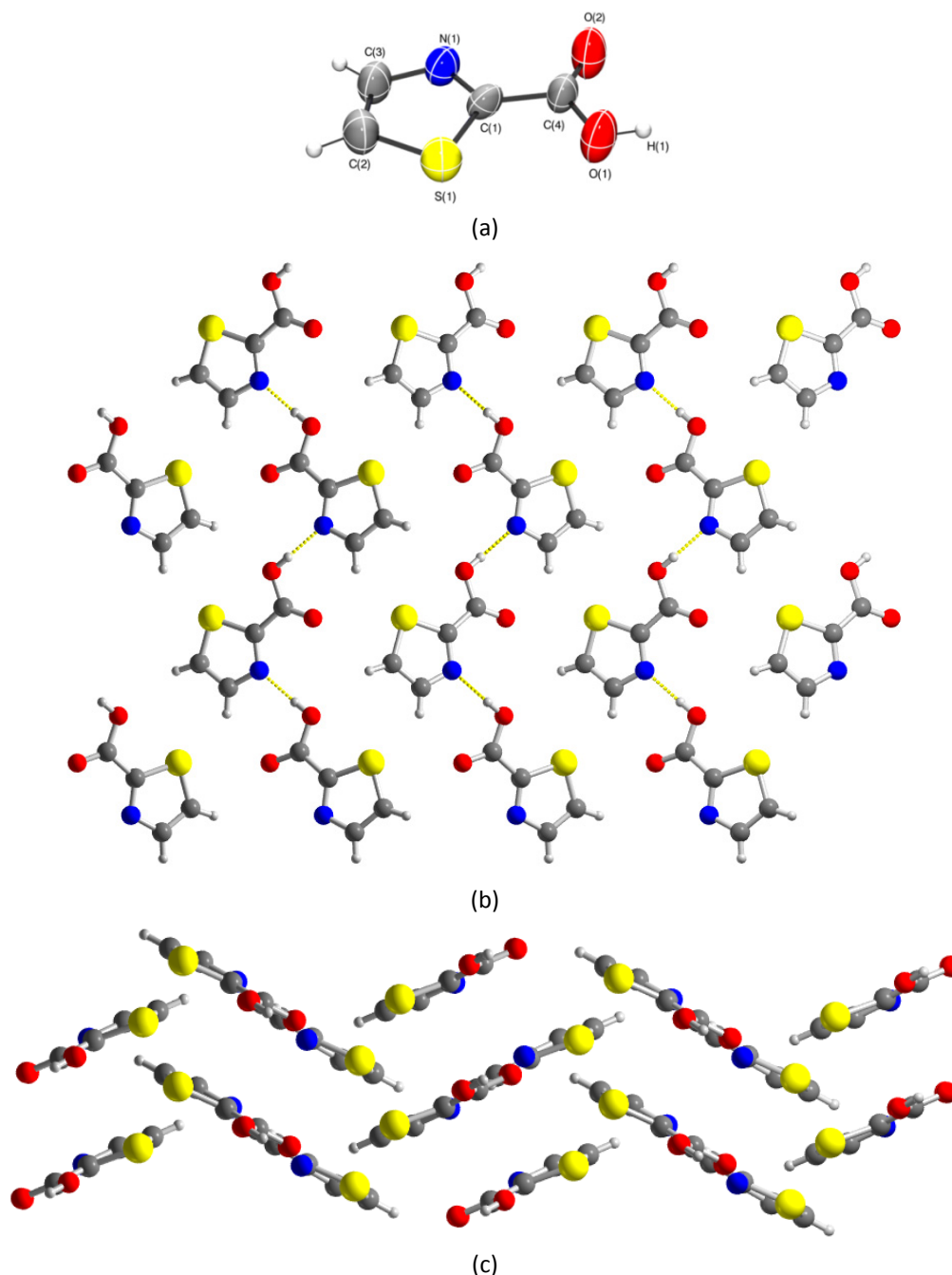
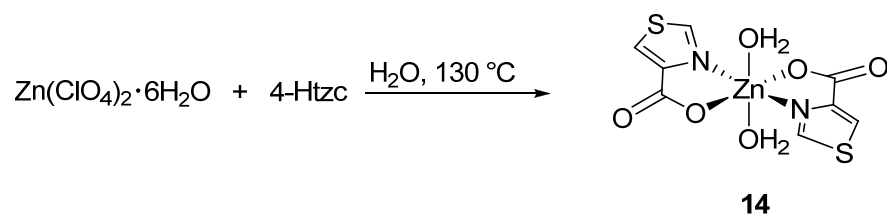


Figure 3-6. Asymmetric unit of the crystal structure of 2-Htzc (a). Views of its solid state assembly along the [001] (b) and the [010] (c) Miller planes. Atom color code: gray, C; white, H; red, O; blue, N; yellow, S. Thermal ellipsoids in (a) drawn at 60% probability. H-bonds in depicted in yellow dotted lines.

3.4.3 Synthesis of supramolecular networks *via* multiple intermolecular hydrogen bonds

The reaction between 4-Htzc and zinc(II) at 130 °C led to formation of the $\text{Zn}(4\text{-tzc})_2 \cdot 2\text{H}_2\text{O}$ (**14**) complex (Scheme 3-6). The same result was obtained at different pHs or reagent concentrations.



Scheme 3-6. Hydrothermal synthesis of **14**.

The crystal structure of **14** is shown in Figure 3-7 (a). The zinc(II) cation lying on an inversion centre, is hexacoordinated, in an octahedral coordination geometry. The two aquo ligands are *trans* to each other in axial positions, while the two (deprotonated) 4-tzc ligands are (N,O)-chelating in a bidentate fashion in the equatorial plane (see Tables 3-1 and 3-2). The Zn-N(3) and Zn-O(1) bond lengths in **14** are similar to those reported for other zinc(II) complexes of general formula $\text{Zn}(\text{L})_2(\text{H}_2\text{O})_2$, where L = 3-carboxyl-1,2,4-triazole,¹⁶ imidazole-4-carboxylate¹⁷ or 5-carboxy-4-(carboxylato)imidazole.¹⁸ In these compounds the imidazole- or triazole-based ligands exhibit an identical $\kappa^2\text{-N,O}$ chelating coordination mode, the resulting complexes being isostructural with the thiazole-based analogue **14**. On the other hand, the Zn-N(3) distance is shorter than that observed in the bis(thiazole) system (2,2'-diamino-4,4'-bi-1,3-thiazole)bis(glycinato)zinc(II) [2.1823(13) Å],¹⁹ and both Zn-N and Zn-O bonds are longer than that found in the polymeric poly{aqua[5-carboxy-4-(carboxylato)imidazole]zinc(II)} [1.985(2) and 2.020(3) Å, respectively].^{18a} The supramolecular arrangement resulting from the extensive intermolecular hydrogen bonding between the coordinated water molecules and the carboxylic groups of adjacent molecules (see Table 3-2) is similar to that seen in the aforementioned species,²⁰ and it is likely responsible for the poor solubility of **14** in aqueous solutions.

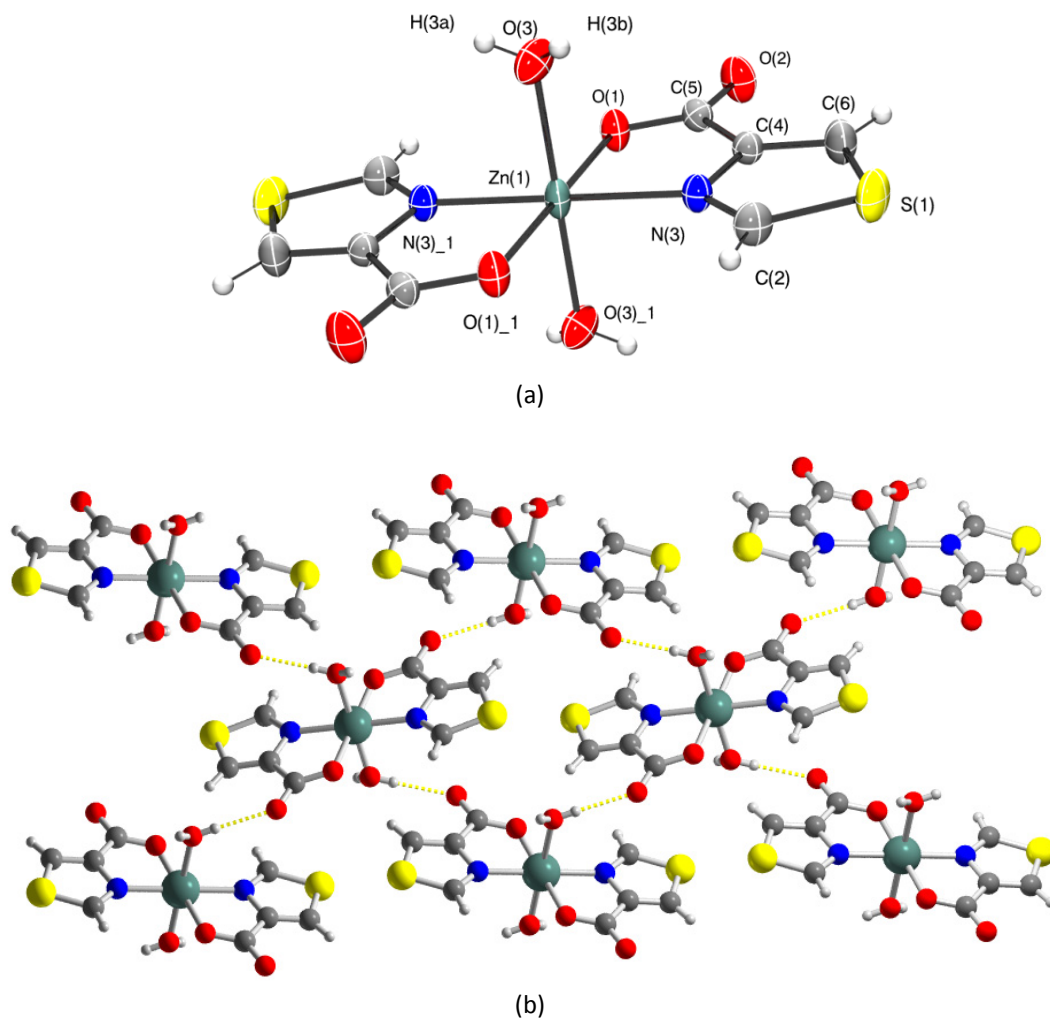


Figure 3-7. Asymmetric unit of the crystal structure of **14** (a). Views of its solid state assembly along the [100] Miller planes (b). Thermal ellipsoids in (a) drawn at 60% probability. H-bonds in depicted in yellow dotted lines.

Table 3-1. Selected bond lengths [Å] and angles [°] for **14**.

Zn(1)-N(3)	2.066(2)	O(2)-C(5)	1.238(3)	N(3)-Zn(1)-O(1)	79.74(8)
Zn(1)-O(1)	2.1273(18)	O(3)-H(3A)	0.75(4)	N(3)-Zn(1)-O(3)	89.11(9)
Zn(1)-O(3)	2.160(2)	O(3)-H(3B)	0.83(5)	O(1)-Zn(1)-O(3)	88.58(8)
O(1)-C(5)	1.268(3)	N(3)#1-Zn(1)-O(1)	100.26(8)	H(3A)-O(3)-H(3B)	113(4)

Symmetry transformations used to generate equivalent atoms: #1 -x,-y,-z

Table 3-2. Hydrogen bonds for **14** [Å and °].

D-H...A	d(D-H)	d(H...A)	d(D...A)	<(DHA)
O(3)-H(3A)...O(2)#2	0.76(4)	2.02(5)	2.779(3)	177(4)
O(3)-H(3B)...O(1)#3	0.82(5)	1.95(6)	2.769(3)	172(4)

Symmetry transformations used to generate equivalent atoms: #1 -x,-y,-z #2 -x,y-1/2,-z-1/2 #3 x-1,y,z

The reaction of 4-Htzc with the copper(I) precursor $[\text{Cu}(\text{MeCN})_4][\text{PF}_6]$ in acetonitrile led to metal oxidation under aerobic conditions, with formation of the Cu(II) complex $\text{Cu}(\text{4-tzc})_2$ (**15**, a in Figure 3-8). The coordination geometry around the four-coordinate copper centre is approximately square planar $\{\angle[\text{N}(3)\text{-Cu-O}(1)] = 83.67(15)^\circ; \angle[\text{N}(3)\text{-Cu-O}(1)\#] = 96.33(15)^\circ\}$, and the metal atom lies on an inversion centre (see Table 3-3). As already observed for 2-Htzc, an extensive π -stacking among the aromatic rings creates a columnar arrangement of the molecules along the a direction in the lattice (b in Figure 3-8). Similarly to **14**, also crystals of **15** are poorly soluble in water, suggesting the occurrence of a "polymer-like" behaviour because of the existence of an infinite number of such (weak) interactions that largely overcome solvation effects.

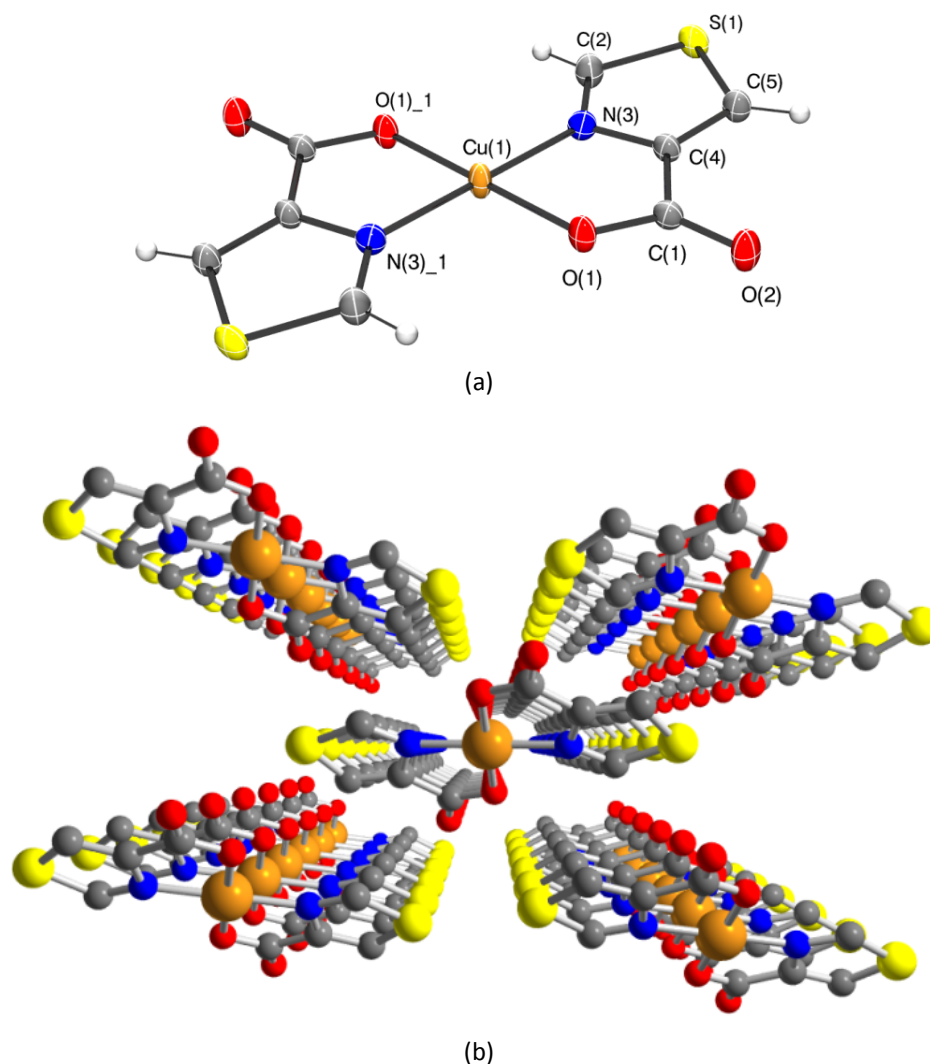


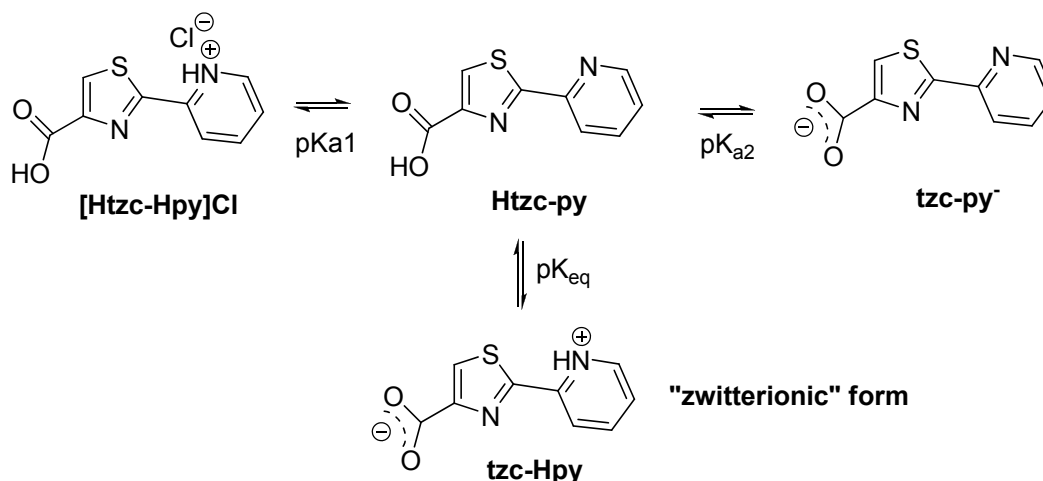
Figure 3-8. Asymmetric unit of the crystal structure of **15** (a). Views of its solid state assembly along the [100] Miller planes (b). Thermal ellipsoids in (a) drawn at 40% probability.

Table 3-3. Selected bond lengths [Å] and angles [°] for **15**.

Cu(1)-N(3)	1.951(4)	N(3)-Cu(1)-O(1)	83.67(15)	O(2)-C(1)-O(1)	124.9(4)
Cu(1)-N(3)#1	1.951(4)	N(3)#1-Cu(1)-O(1)	96.33(15)	O(2)-C(1)-C(4)	121.6(4)
Cu(1)-O(1)	1.953(4)	O(1)-Cu(1)-O(1)#1	180.0(2)	O(1)-C(1)-C(4)	113.5(4)
Cu(1)-O(1)#1	1.953(4)	C(2)-S(1)-C(5)	90.2(2)	N(3)-C(2)-S(1)	113.9(4)
S(1)-C(2)	1.693(5)	C(2)-N(3)-C(4)	111.9(4)	C(5)-C(4)-N(3)	114.1(4)
S(1)-C(5)	1.705(5)	C(2)-N(3)-Cu(1)	136.7(4)	C(5)-C(4)-C(1)	130.1(4)
N(3)-C(2)	1.300(7)	C(4)-N(3)-Cu(1)	111.1(3)	N(3)-C(4)-C(1)	115.8(4)
N(3)-C(4)	1.370(6)	C(1)-O(1)-Cu(1)	115.5(3)	(4)-C(5)-S(1)	109.9(4)

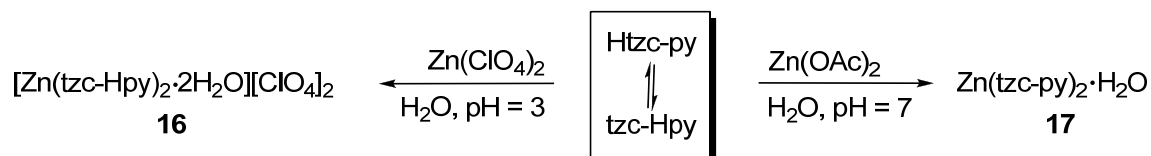
Symmetry transformations used to generate equivalent atoms: #1 -x,-y,-z

The chemical versatility of the Htzc-py ligand may be explained through its pH-dependent protonation- deprotonation equilibria in water; under this perspective, complex **15** may be compared with an amino-acid (Scheme 3-7).

**Scheme 3-7.** Protonation-deprotonation equilibria of Htzc-py in water.

The simultaneous presence of an acidic and a basic site within the same molecule makes Htzc-py a very interesting building block for achieving supramolecular aggregates, engaging in multiple coordination modes. The isomer of Htzc-py containing a *para*-pyridyl substituent in the 2-position, *i.e.* 2-(4-pyridyl)thiazole-4-carboxylic acid (pytac), generates 3D coordination polymers with both silver(I) and zinc(II),²¹ the analogous ligand with a *meta*-pyridyl dangling ring also forms polymeric species with zinc(II), cobalt(II) and copper(II).⁵ In the case of Htzc-py, the N atom of the *ortho*-pyridyl ring is not capable of forming bridges between two metal centers, due to unfavorable geometric constraints. Therefore, only discrete complexes (Scheme 3-8) are formed, where the dangling *o*-

pyridyl substituent (either protonated or deprotonated) is involved in intramolecular hydrogen bonds stabilizing its cisoid conformation with respect to the five-membered metallacycle.



Scheme 3-8. Reactivity of Htzc-py with zinc(II) salts.

The "zwitterionic" form tzc-Hpy is evident in the crystal structure of **16** (a in Figure 3-9) where the zinc atom is hexacoordinated, with two tzc-Hpy ligands occupying the equatorial plane and displaying the same $\kappa^2\text{-N,O}$ coordination mode as 4-Htzc in complex **14**. The metal sits on a crystallographic inversion centre, and two *trans* disposed water molecules complete the octahedral coordination geometry. The acidic pH environment (the perchlorate anion does not alter the initial pH conditions) protonates the nitrogen atom on the pyridyl substituent generating a "pyridinium-like" ring which is further involved in a $\text{N}(2)\text{-H}(2)\cdots\text{O}(2)\#$ hydrogen bonding interaction. Additional interactions between the aquo ligands and the C=O groups of neighbouring molecules [$\text{O}(1)\text{-H}(1a)\cdots\text{O}(3)\#$] or between the same ligands and the (disordered) perchlorate ions [$\text{O}(1)\text{-H}(1b)\cdots\text{OClO}_3$] are present (see also Table 3-4). The final result is a complex network of embedded H-bonds that gather together all the components in a compact assembly (b in Figure 3-9). The dihedral angle $\theta[\text{N}(1)\text{-C}(1)\text{-C}(5)\text{-N}(2)]$ is very small [$4.3(8)^\circ$], with the pyridyl ring almost coplanar with the thiazole ring. The two nitrogen atoms, N(pyridyl) and N(thiazole), are in a cisoid conformation, while the opposite situation is observed in the free Htzc-py ligand, where $\theta = 179.8(8)^\circ$. The Zn-O(2) distance is shorter [$2.001(4)$ vs. $2.1273(18)$ Å] and the Zn-N(1) is longer [$2.242(4)$ vs. $2.066(2)$ Å] than the corresponding values found for **16**.

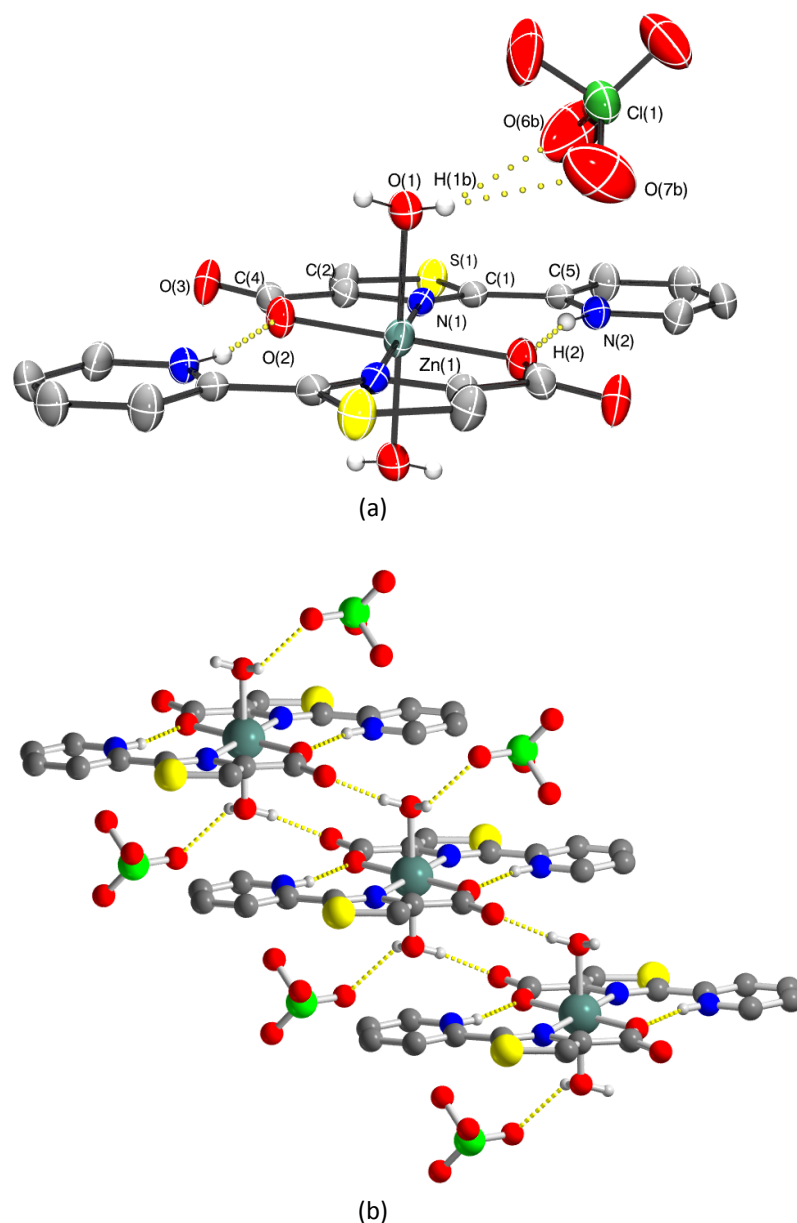


Figure 3-9. Part of the asymmetric unit of **16** (a). View of the complex H-bonded network present in the lattice (b). Hydrogen atoms not relevant for the discussion were omitted for clarity. Thermal ellipsoids in (a) are drawn at 40% probability.

Table 3-4. Selected bond lengths [Å] and angles [°] for **16**.

Zn(1)-O(2)	2.001(4)	N(1)-C(2)	1.388(7)	C(3)-S(1)-C(1)	89.5(3)
Zn(1)-O(1)	2.094(4)	O(1)-H(1A)	0.8200	C(4)-O(2)-Zn(1)	117.6(3)
Zn(1)-N(1)	2.242(4)	O(1)-H(1B)	0.7532	N(1)-C(1)-C(5)	125.8(6)
S(1)-C(3)	1.691(5)	N(2)-H(2)	0.8600	N(1)-C(1)-S(1)	114.5(4)
S(1)-C(1)	1.717(7)	O(2)-Zn(1)-O(1)	88.14(16)	C(5)-C(1)-S(1)	119.7(4)
C(1)-N(1)	1.313(6)	O(2)-Zn(1)-N(1)	81.70(15)	C(1)-N(1)-Zn(1)	146.2(4)
C(1)-C(5)	1.481(7)	O(1)-Zn(1)-N(1)	91.47(16)	C(2)-N(1)-Zn(1)	103.4(3)

Symmetry transformations used to generate equivalent atoms: #1 -x+1,-y+1,-z+1

Table 3-5. Hydrogen bonds for **16** [Å and °].

D-H...A	d(D-H)	d(H...A)	d(D...A)	<(DHA)
O(1)-H(1A)...O(3)#2	0.82	1.84	2.647(5)	169.4
O(1)-H(1B)...O(5A)	0.75	2.21	2.777(14)	133.1
O(1)-H(1B)...O(7B)	0.75	2.47	3.051(15)	135.5
N(2)-H(2)...O(2)#1	0.86	1.89	2.737(6)	166.0

Symmetry transformations used to generate equivalent atoms: #1 -x+1,-y+1,-z+1 #2 -x,-y+1,-z+1

At neutral pH conditions, obtained through slow acetate hydrolysis in the presence of Htzc-py, the five-coordinated species **17** is obtained which exhibits a distorted trigonal bipyramidal geometry around the zinc centre (Figure 3-10) with the deprotonated ligand (tzc-py⁻) adopting the usual κ^2 -N,O coordination mode. The N(thiazole) atom and the O atom occupy the axial and equatorial positions, respectively. The pyridyl substituent of one tzc-py ligand is engaged in an intermolecular H-bonding with the coordinated water molecule [O(5)-H(5a)•••N(2)]. The other hydrogen atom of the water ligand interacts with the carboxylic group of the neighboring molecule [O(5)-H(5b)•••O(3)#]. See Table 3-7 for details.

The two aromatic rings of the tzc-py ligand participating in the hydrogen bonding interaction with the coordinated water molecule are slightly twisted around the C-C linking bond: the θ [N(2)-C(3)-C(5)-N(1)] dihedral angle is 15.3(2)°, with the pyridyl ring in a (distorted) cisoid conformation to favor the interaction with water, while the other ligand maintains the same conformation found in free Htzc-py, with a transoid N(pyridyl)-N(thiazole) disposition $\{\theta$ [N(3)-C(12)-C(14)-N(4) = 178.76(15)°].

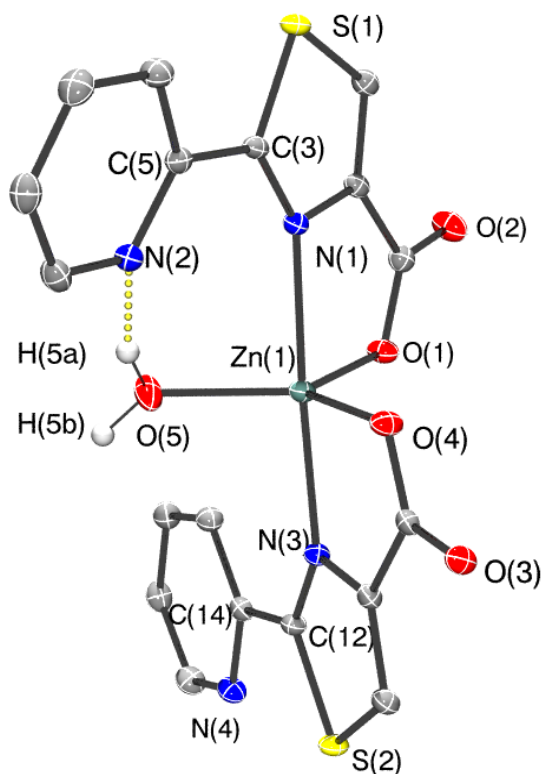


Figure 3-10. Complex 17. Hydrogen atoms on the organic ligands omitted for clarity. Thermal ellipsoids in drawn at 40% probability.

Table 3-6. Selected bond lengths [Å] and angles [°] for 17.

N(1)-Zn(1)	2.1862(16)	C(12)-N(3)-C(10)	111.06(13)	O(1)-Zn(1)-O(4)	115.55(5)
N(3)-Zn(1)	2.1603(16)	C(12)-N(3)-Zn(1)	142.31(11)	O(5)-Zn(1)-O(4)	116.33(6)
O(1)-Zn(1)	1.9685(13)	C(10)-N(3)-Zn(1)	106.62(10)	O(1)-Zn(1)-N(3)	97.15(5)
O(4)-Zn(1)	1.9899(13)	C(18)-N(4)-C(14)	117.18(16)	O(5)-Zn(1)-N(3)	95.02(5)
O(5)-Zn(1)	1.9690(13)	C(4)-O(1)-Zn(1)	118.37(10)	O(4)-Zn(1)-N(3)	81.72(5)
O(5)-H(5A)	0.8400	C(13)-O(4)-Zn(1)	116.84(10)	O(1)-Zn(1)-N(1)	81.47(5)
O(5)-H(5B)	0.8603	Zn(1)-O(5)-H(5A)	109.5	O(5)-Zn(1)-N(1)	87.86(5)
C(3)-N(1)-Zn(1)	141.86(11)	Zn(1)-O(5)-H(5B)	132.1	O(4)-Zn(1)-N(1)	96.53(5)
C(1)-N(1)-Zn(1)	106.26(9)	H(5A)-O(5)-H(5B)	116.7	N(3)-Zn(1)-N(1)	177.08(5)
C(9)-N(2)-C(5)	117.45(14)	O(1)-Zn(1)-O(5)	127.85(6)		

Table 3-7. Hydrogen bonds for 17 [Å and °].

D-H...A	d(D-H)	d(H...A)	d(D...A)	<(DHA)
O(5)-H(5A)...N(2)	0.84	1.86	2.664(2)	161.0
O(5)-H(5B)...O(3)#1	0.86	1.76	2.6153(18)	179.5

Symmetry transformations used to generate equivalent atoms: #1 x-1,y,z

Although the Zn(II) ion, in its d^{10} valence-electron configuration, has no LFSE and can adopt many different coordination numbers (between four and eight), the trigonal bipyramidal geometry is not a common structural leitmotiv; examples can be found with tripodal ligands that "force" this coordination geometry because of their sterically oriented stereochemical requirements. Some of the few known tripodal ligands giving zinc(II) trigonal bipyramidal complexes are: 2,2',2''-nitrilotriacetate (nta),²² (2-picolyl)(N-pyrrolidinyethyl)(2-hydroxy-3,5-di-tert-butylbenzyl)amine,²³ tris(pyridylmethyl)amine (tpa)²⁴ or pentadentate bis(oxazoline)-based ligands (Figure 3-11).²⁵ Much less cases are known when the ancillary ligand is aromatic.²⁶ Compound **17** belongs indeed to this scarcely represented category.

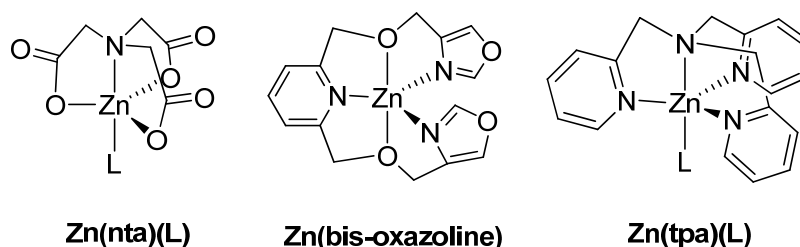


Figure 3-11. Some tripodal ligands and their coordination modes.

Reaction of cobalt(II) acetate tetrahydrate with Htzc-py under neutral pH conditions produces purple crystals of complex **18**. The coordination geometry around Co(II) is octahedral (a in Figure 3-12), with the same ligand disposition seen in **14**. The only difference is in the tzc-py⁻ conformation: the θ [N(1)-C(3)-C(5)-N(2)] dihedral angle is $161.3(3)^\circ$, with a transoid N(1)-N(2) relative orientation identical to that of the free Htzc-py. The O(3)-H(3B)•••O(1)# hydrogen bond between the aquo ligands and the carboxylic groups of neighboring molecules in the lattice is still present (Table 3-8). Finally, the N(pyridyl) engages in an additional O(3)-H(3A)•••N(2)# hydrogen bond with the other proton of the aquo ligand (b in Figure 3-12). Probably, the *trans*-(N,N) disposition is the most energetically stable; nonetheless, when the N(pyridyl) atom is protonated, the (strongly stabilizing) intramolecular H-bond balances the extra-energy coming from a *trans*- to *cis*-(N-N) conformational change.

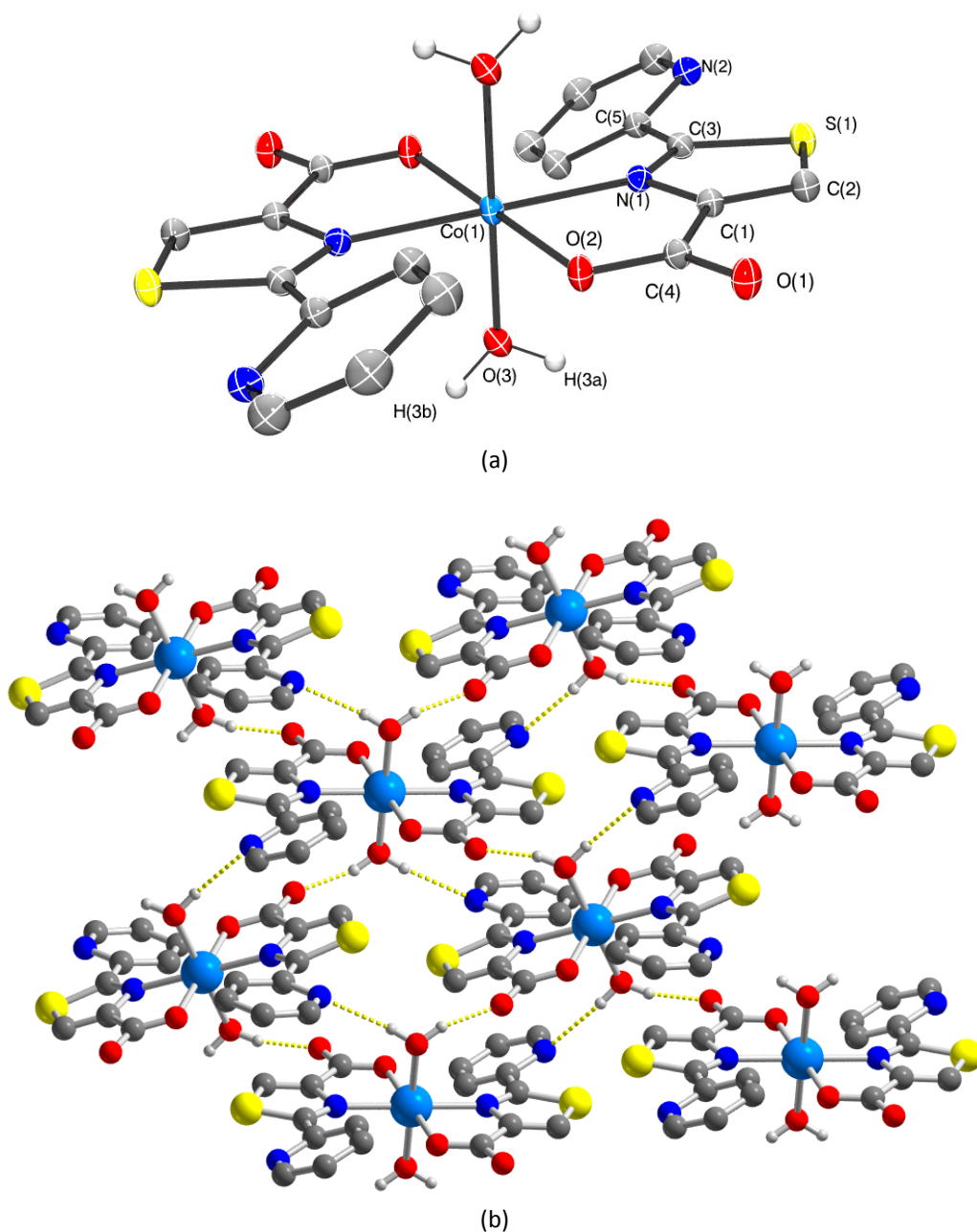


Figure 3-12. Complex **18** (a), and its solid state packing evidencing the hydrogen bonding net (b). Hydrogen atoms on the organic ligands omitted for clarity. Thermal ellipsoids in (a) is drawn at 40% probability. Weak interactions are depicted in yellow dotted lines.

Table 3-8. Selected bond lengths [Å] and angles [°] for **18**.

N(1)-Co(1)	2.201(2)	C(3)-N(1)-Co(1)	142.9(2)	Co(1)-O(3)-H(3B)	119.4
O(2)-Co(1)	2.033(2)	C(1)-N(1)-Co(1)	106.62(17)	H(3A)-O(3)-H(3B)	113.3
O(3)-Co(1)	2.134(2)	C(9)-N(2)-C(5)	117.1(3)	O(2)-Co(1)-O(3)	91.28(9)
O(3)-H(3A)	0.8400	C(4)-O(2)-Co(1)	118.12(19)	O(2)-Co(1)-N(1)	79.61(9)
O(3)-H(3B)	0.8569	Co(1)-O(3)-H(3A)	109.5	O(3)-Co(1)-N(1)	86.78(9)

Table 3-9. Hydrogen bonds for **18** [Å and °].

D-H...A	d(D-H)	d(H...A)	d(D...A)	<(DHA)
O(3)-H(3B)...O(1)#2	0.86	1.82	2.660(3)	165.2
O(3)-H(3A)...N(2)#3	0.84	2.33	3.126(4)	159.5

Symmetry transformations used to generate equivalent atoms: #1 -x+1,-y,-z+1 #2 -x+1,y+1/2,-z+1/2 #3 x,-y-1/2,z-1/2

3.5 A new chiral metal organic framework

The designed construction of chiral porous MOFs is of great current interest because of their unique applications in asymmetric catalysis and enantioselective separations.²⁷ Chiral MOFs arise from chiral ligands or by using achiral ligands under spontaneous resolution without any chiral sources.²⁸ Chiral MOFs can be built from achiral components since any MOF can crystallize in a chiral space group as a result of a particular spatial disposition of all the building units. The use of enantiopure co-ligand can direct homochiral crystallization of an intrinsically chiral MOF.²⁹ However, the bulk samples of the MOFs derived from achiral components generally tend to contain both enantiomers and are thus racemic even though the single crystals are chiral. The chirality can be introduced in the network simply by choosing chiral organic building blocks. In an ideal scenario, chiral pores with desired chemical and shape selectivities can be generated and used for highly enantioselective sorption or separation processes.³⁰

In this context, we started to explore the reactivity of thiazolidine systems having two stereogenic carbon atoms in 2 and 4 positions. The starting material of the aforementioned heterocycles is the enantiomerically pure natural amino acid *L*-cysteine; in addition, during the cycle formation a new chiral center is generated as a result of the condensation step. Therefore, the final aliphatic ring consists of a racemic mixture of two diastereomeric pairs with (*R,R*) and (*S,R*) configuration. In all cases it was not possible to separate the isomers by column chromatography because of the almost identical *R_f* values. In the case of diethyl thiazolidine-dicarboxylate (**3c**), the saponification reaction with Cs₂CO₃ afforded the corresponding thiazolidine diastereoisomers (*2S,4R*) (*cis*-H₂tdca, **19**) and (*2R,4R*) (*trans*-H₂tdca, **20**) (Figure 3-13), corresponding to *syn* and *anti* thiazolidine, which were separated by successive re-crystallisations from H₂O/MeOH (Figure 3-14).

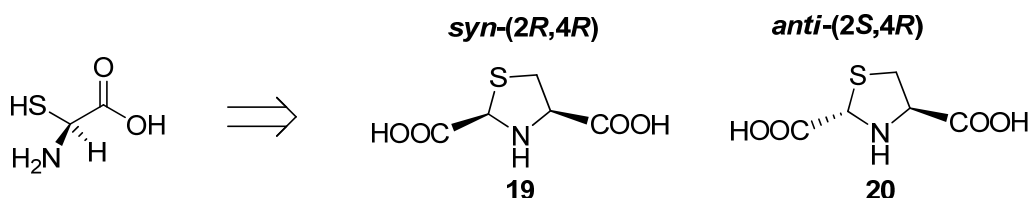


Figure 3-13. Diastereoisomeric mixture of (2*S*,4*R*)-thiazolidine-2,4-dicarboxylic acid (**19**) and (2*R*,4*R*)-thiazolidine-2,4-dicarboxylic acid (**20**) derived from the naturally occurring *L*-cysteine.

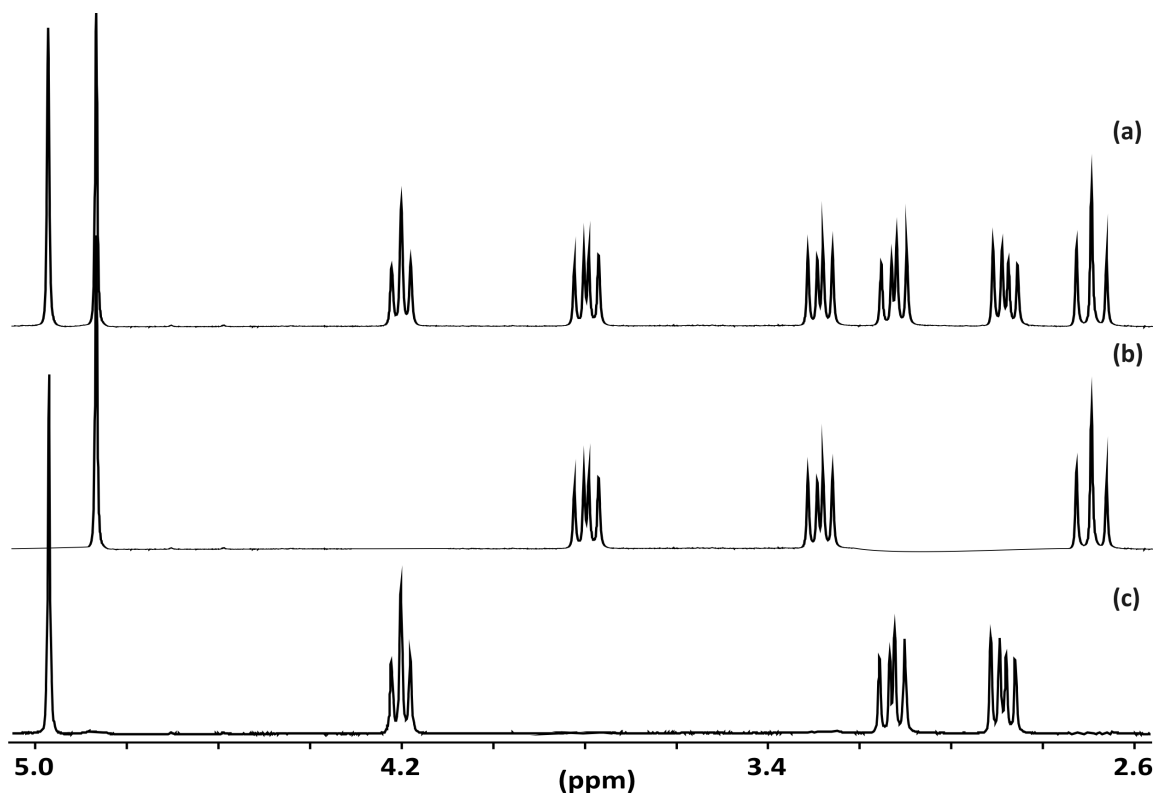


Figure 3-14. ^1H NMR ($\text{DMSO-}d_6$) spectrum of (a) the diastereomeric mixture of the *syn* diastereoisomer **19** (b) and the *anti* diastereoisomer **20**(c).

By employing the enantiopure ligand **19** as cross-linking agent, we have prepared a chiral MOF with cobalt(II) chloride, under hydrothermal conditions at 90 °C for 24h. The crystal structure of the tridimensional coordination polymer $[\text{Co}(\text{tdca})(\text{H}_2\text{O})\cdot(\text{H}_2\text{O})_{0.5}]_\infty$ (**21**) is depicted in Figure 3-15. In the asymmetric unit, the cobalt(II) cation is hexacoordinated, in an octahedral coordination geometry. The *syn* conformer of tdca is bound to the cobalt centres through the N atom of the ring and two O atoms belonging to two different carboxylate groups, in an (O,N,O)-tridentate fashion. The $-\text{COO}^-$ moieties are bridging adjacent cobalt ions in the lattice. The last coordination site on cobalt is occupied by an aquo ligand. The 3D motif is generated by the presence of a four-fold

screw axis, in the (chiral) tetragonal $P 4_1$ space group. The final network presents two different channels, one hydrophobic (with the thiazolidine sulfur atoms on the inner walls) and one hydrophilic (facing the aquo ligands), both with a cross-section of about 16 \AA^2 . In the as-synthesized material (metal-to-ligand ratio of 2:1 in water at $90 \text{ }^\circ\text{C}$ for 24 h), some residual water solvent is present into the hydrophilic channels, in non-stoichiometric amount (the exact chemical formula is $[\text{Co}(\text{tdca})(\text{H}_2\text{O})\cdot(\text{H}_2\text{O})_{0.5}]_\infty$ from the single-crystal data)

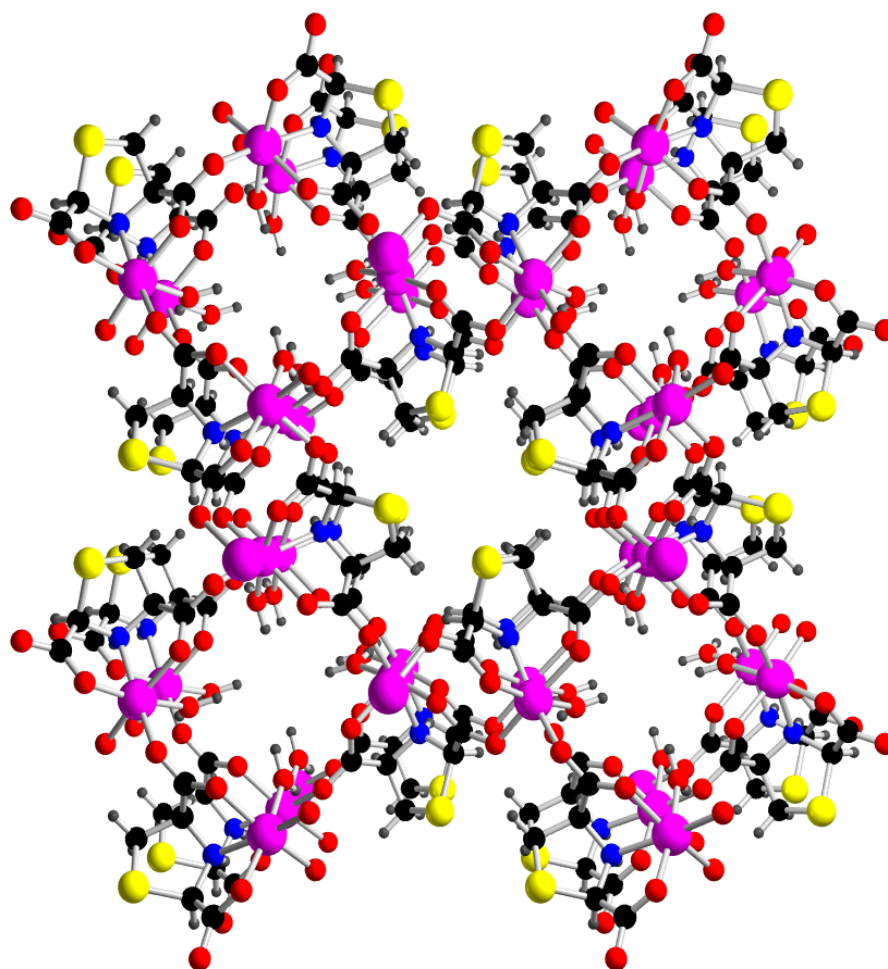


Figure 3-15. Molecular structures and atom-labelling scheme of **21**. Atom colour code: C black, O red, H grey, S yellow, N blue, Co magenta.

The thermogravimetric analysis TG-DTG for **21** is shown in Figure 3-16. No weight loss is observed for **21** up to $250 \text{ }^\circ\text{C}$. The first weight change (47%) is found between 250 and $280 \text{ }^\circ\text{C}$ and corresponds to the framework decomposition.

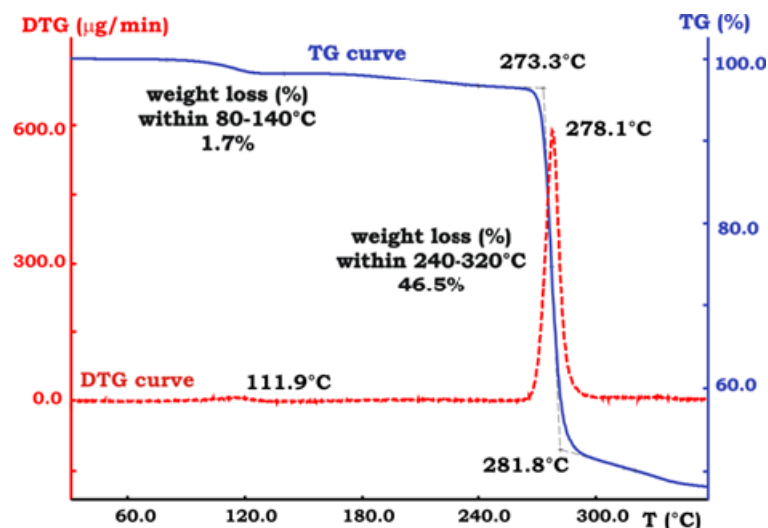


Figure 3-16. TG-DTG characterisation of **21**.

Currently, further characterisation experiments are underway to determine the surface area and pore size distribution of **21** for applications in gas storage. Our future goal will be also to exploit the intrinsic MOF chirality for enantioselective heterogeneous catalysis. Other aliphatic thiazolidine-based molecules containing pyridyl- or *p*-carboxyphenyl- substituents in the 2-position will be tested soon for the synthesis of new coordination polymers with similar properties. The synthesis of potentially chiral MOFs related to **21** with different transition metals is also planned.

3.6 Conclusions and outlook

In conclusion, we have reported a selective and general procedure for preparing 4-carboxy thiazoles and thiazolidines, for which both reaction times and use of environmentally unsafe reagents can be dramatically reduced by MW activation during the oxidation step carried out with MnO_2 . 4-carboxyoxazoles have also been prepared and the use of the benzyl protective group has been exploited to prepare orthogonally protected carboxy moieties.

Novel coordination compounds containing thiazole-based ligands have been synthesized and characterized through single-crystal X-ray diffraction. The influence of both pH and temperature on the solvothermal (hydrothermal) reactions has been carefully analyzed. Zn(II), Co(II) and Cu(II) coordination geometry in these species has been critically discussed; either octahedral or (unexpectedly) trigonal bipyramidal for zinc

and cobalt, square planar for copper. The presence of an extended hydrogen bonding network due to the presence of several polar groups in the asymmetric unit confers a "pseudo-polymeric" nature to these solids, being practically insoluble in all solvents. Nonetheless, they still are discrete entities that do not possess any kind of permanent porosity or inner surface area.

The use of more flexible aliphatic ligands such as thiazolidines opened the way to the synthesis of a new class of MOFs with interesting prospects, related to their intrinsic chirality. Under this perspective, this study has to be considered the first step towards the synthesis of MOFs for potential applications in the field of gas storage and heterogeneous enantioselective catalysis. New polytopic ligands containing thiazole, thiazolidine and oxazole rings are currently under investigation, along with their reactivity with first-row transition metal ions.

3.7 Experimental section

3.7.1 Synthetic procedures

All manipulations were performed under a dry nitrogen atmosphere using vacuum-lines and standard Schlenk techniques. Dichloromethane, benzene and methanol were dried by standard methods and distilled under nitrogen before use. All the other solvents were dried and degassed by MB SPS solvent purification system (<http://solventpurifier.com/>). All reagents were obtained from commercial suppliers and used without further purification. $[\text{Cu}(\text{MeCN})_4][\text{PF}_6]^{31}$ was prepared according to the published procedures. The syntheses of ligands were monitored by TLC on SiO_2 plates; detection was made using a KMnO_4 basic solution. Flash column chromatography was performed using glass columns (10-50 mm wide) and SiO_2 (230-400 mesh).

Microwave irradiation experiments were performed using a single-mode Discover System BenchMate 220VAC750Hz from CEM Corporation,³² using standard Pyrex vessels or flasks in open vessel mode.

TG and DTA analysis was performed with a Netzsch STA490C thermoanalyser under a 20 mL min^{-1} air flux with a heating rate of 5 $^\circ\text{C min}^{-1}$.

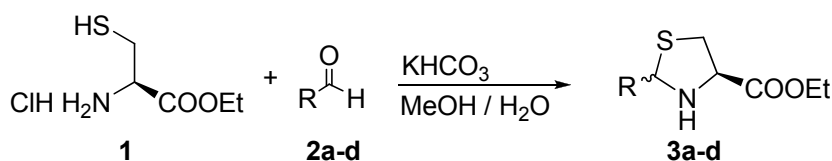
Deuterated solvents for routine NMR measurements were dried over molecular sieves. ^1H NMR spectra were recorded operating at 300.1 and 400.1 MHz; $^{13}\text{C}\{^1\text{H}\}$ NMR spectra were recorded operating at 75.5 and 100.6 MHz. Peak positions are relative to

tetramethylsilane (^1H) and were calibrated against the residual solvent resonance. Coupling constants (J) were reported in Hz. When a mixture of diastereoisomers is present, signals of the minor diastereoisomer are reported in parentheses.

FT-IR spectra were measured using KBr pellets or solution cells. Elemental combustion microanalyses (C, H, N) were obtained using an elemental analyzer.

Mass spectra were obtained at a 70 eV ionization potential and are reported in the form m/z (intensity relative to base = 100). ESI-MS spectra were done on a LCQ Orbitrap mass spectrometer equipped with a conventional ESI source by direct injection of the sample solution. 80 scans were accumulated and averaged for each spectrum. The instrument parameters were the following: flow rate 3 $\mu\text{l}/\text{min}$, capillary voltage 60 V, tube lens 185 V, nominal resolution (@ 400 m/z) 60000. 80 scans were accumulated and averaged for each spectrum.

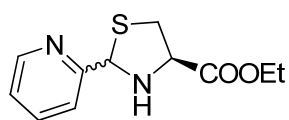
3.7.1.1 General procedure to ethyl 2(*R,S*)-substituted-thiazolidine-4(*R*)-carboxylate (**3a-d**)



Aldehydes **2a-d** (1.1 eq) were suspended in MeOH. Then a solution of the commercially available *L*-cysteine ethyl ester hydrochloride **1** (1.1 eq) in H₂O together with KHCO₃ (1.0 eq) was added and the resulting mixture was stirred at rt overnight. After evaporation of MeOH the aqueous layer was extracted with ethyl acetate. The combined organic layers were washed with brine and dried over Na₂SO₄. Evaporation of the solvent afforded compounds **3a-d** which were used without further purification.

Ethyl-2(*R,S*)-(pyridin-2-yl)thiazolidine-4(*R*)-carboxylate (**3a**)³³

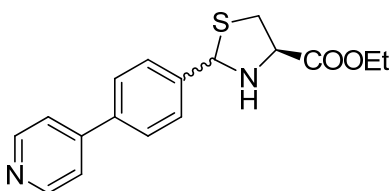
Reaction of **1** (7.71 g, 41.5 mmol,) with 2-pyridinecarboxaldehyde (4.7 mL, 49.8 mmol) and KHCO₃ (41.50 g, 41.5 mmol) in MeOH (210.0 mL) and H₂O (210.0 mL) gave 9.75 g (99%) of **3a** as a yellow oil containing a 1:1 mixture of diastereoisomers.



3a: R_f 0.5 (petroleum ether/AcOEt = 2/1). **IR** (CHCl_3 , KBr): $\tilde{\nu}$ = 3290 (NH), 1747 (CO) cm^{-1} . **$^1\text{H NMR}$** (300.1 MHz, CDCl_3 , 25 °C): δ 8.64-8.61 (8.58-8.55) (m, 1H); 7.70-7.62 (m, 1H); 7.35-7.16 (m, 2H); 5.85 (5.65) (bs+d, J = 11.25 Hz, 1H); 4.51 (bs, 1H); 4.27 (4.26) (q, J = 7.1 Hz, 2H); 3.48-3.29 (m, 3H); 1.32 (1.31) (t, J = 7.1 Hz, 3H). **$^{13}\text{C}\{^1\text{H}\}$ NMR** (75.5 MHz, CDCl_3 , 25 °C): δ 171.62 (170.61); 158.69 (156.64); 149.84 (149.56); 136.73; 123.32 (122.88); 122.05 (121.43); 71.56 (71.04); 66.32 (65.59); 61.58 (61.50); 39.38 (38.74); 14.13. **MS**, m/z (%): 238(3) [M^+]; 166(100) [(M-COOEt) $^+$].

Ethyl 2(*R,S*)-(4-(pyridin-4-yl)phenyl)thiazolidine-4(*R*)-carboxylate (**3b**)

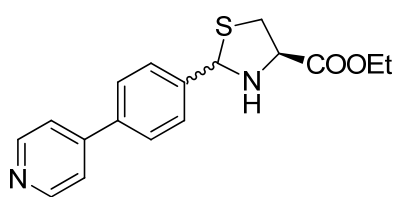
Reaction of **1** (2.00 g, 10.8 mmol,) with 4-(4-formylphenyl)-pyridine (2.18 g, 11.9 mmol) and KHCO_3 (10.80 g, 10.8 mmol) in MeOH (54.0 mL) and H_2O (54.0 mL) gave 9.75 g (99%) of **3b** as a yellow solid containing a 1:1.5 mixture of diastereoisomers.



3b: **IR** (KBr): $\tilde{\nu}$ = 3255 (NH), 1730 (CO) cm^{-1} . **$^1\text{H NMR}$** (400.1 MHz, CDCl_3 , 25 °C): δ 8.63-8.60 (m, 2H); 7.70-7.62 (m, 1H); 7.61 (7.56) (bs, 4H); 7.47-7.44 (m, 2H); 5.86 (5.58) (s, 1H); 4.24 (4.23) (q, J = 7.1 Hz, 2H); 4.16-4.12 (3.99-3.94) (m, H); 3.48-3.44 (3.40-3.35) (m, 1H); 3.17-3.08 (m, 1H); 2.74 (bs, 1H); 1.29 (1.28) (t, J = 7.1 Hz, 3H). **$^{13}\text{C}\{^1\text{H}\}$ NMR** (100.6 MHz, CDCl_3 , 25 °C): δ 171.37 (170.86); 150.02 (150.01); 147.52 (147.35); 142.61, 138.15 (139.07, 137.20); 128.02 (127.41); 127.04 (126.77); 121.31 (121.27); 71.83 (70.01); 65.46 (64.19); 61.54 (61.43); 39.08 (38.07); 13.95. **MS**, m/z (%): 314(3) [M^+]; 241(52) [(M-COOEt) $^+$]; 214(100).

Diethyl thiazolidine-2(*R,S*),4(*R*)-dicarboxylate (**3c**)

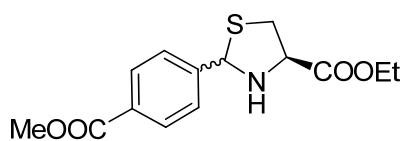
Reaction of **1** (8.00 g, 43.1 mmol) with ethyl glyoxalate (50% in toluene) (9.0 mL, 90.5 mmol) and KHCO_3 (4.31 g, 43.1 mmol) in MeOH (215.0 mL) and H_2O (215.0 mL) gave 9.23 g (92%) of **3c** as a yellow oil containing a 1:3 mixture of diastereoisomers.



3c: R_f 0.7 (hexane/AcOEt = 3/2). **IR** (CHCl_3 , KBr): $\tilde{\nu}$ = 3293 (NH), 1740 (CO) cm^{-1} . **$^1\text{H NMR}$** (300.1 MHz, CDCl_3 , 25 °C): δ 4.88 (5.07) (s, 1H); 4.26-4.17 (4.25-4.16) (m, 2H+2H); 4.15-4.13 (4.40-4.36) (bt, J_{app} = 6.2 Hz, 1H); 3.84-3.78 (3.7-3.71) (dd, J_{AB} = 6.0, J_{BX} = 10.2 Hz, 1H); 3.29-3.23 (3.23-3.17) (dd, J_{AX} = 10.2, J_{AB} = 6.0 Hz, 1H); 2.75 (t, J_{app} = 10.2 Hz, 1H); 1.26 (1.25) (t, J = 7.1 Hz, 3H). **$^{13}\text{C}\{^1\text{H}\}$ NMR** (75.5 MHz, CDCl_3 , 25 °C): δ 170.27 (171.04); 169.76 (170.85); 66.43 (65.41); 64.60 (65.16); 62.00; 61.61 (61.57); 37.72 (37.35); 13.98; 13.90. **MS**, m/z (%): 233(2) [M^+]; 160(100) [(M-COOEt) $^+$].

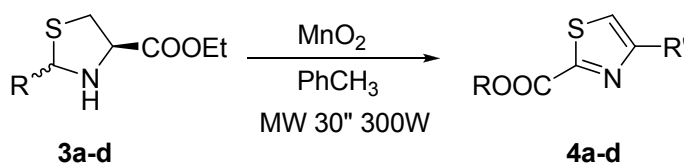
Ethyl 2(*R,S*)-(4-(methoxycarbonyl)phenyl)thiazolidine-4(*R*)-carboxylate (**3d**)

Reaction of **1** (8.00 g, 43.1 mmol) with methyl 4-formylbenzoate (7.78 g, 47.4 mmol) and KHCO_3 (4.31 g, 43.1 mmol) in MeOH (215 mL) and H_2O (215.0 mL) gave 12.43 g (98%) of **3d** as a yellow oil containing a 1:1 mixture of diastereoisomers.



3d: R_f 0.4 (hexane/AcOEt = 2/1). **IR** (CHCl_3 , KBr): $\tilde{\nu}$ = 3290 (NH); 1725 (CO) cm^{-1} . **$^1\text{H NMR}$** (300.1 MHz, CDCl_3 , 25 °C): δ 7.96 -7.90 (m, 2H); 7.54 (7.45) (m, 2H); 5.80 (5.51) (s, 1H); 4.23-4.14 (m, 2H+2H); 4.19 (4.18) (q, J = 7.1, 2H); 3.84 (3.83) (s, 3H); 3.43-3.37 (3.31-3.24) (dd, J_{AB} = 10.3, J_{AX} = 7.1 Hz, 1H); 3.11-3.04 (m, 2H); 2.91 (bs, 1H); 1.24 (1.23) (t, J_{app} = 7.1 Hz, 3H). **$^{13}\text{C}\{^1\text{H}\}$ NMR** (75.5 MHz, CDCl_3 , 25 °C): δ 171.27 (170.24); 166.44 (166.25); 146.76 (143.06); 129.66 (129.43); 129.23 (129.17); 127.25 (126.54); 71.73 4 (69.84); 65.41 (64.16); 61.52 (61.42); 51.92 (51.83); 38.96 (38.03); 13.91. **MS**, m/z (%): 295 (8) [M^+]; 223(100) [(M-COOEt) $^+$].

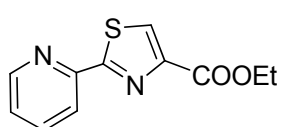
3.7.1.2 General procedure to ethyl 2-substituted-thiazole-4-carboxylate (**4a-d**)



To a solution of the 2(*S,R*)-substituted-4(*R*)-carbethoxy-1,3-thiazolidine **3a-d** (1.0 eq) in toluene, activated MnO₂ (5.0 eq) was added. The sealed flask was inserted into the cavity of a Discovery Microwave System apparatus and heated for 30 seconds at 100 °C and 300W irradiation (value preset on the Microwave oven). The reaction mixture was then filtered through celite and washed with toluene. The filtrate and washings were put together and concentrated under vacuum to afford thiazoles **4a-d** which were purified by flash chromatography.

Ethyl 2-(pyridin-2-yl)-thiazole-4-carboxylate (**4a**)³⁴

Reaction of **3a** (10.00 g, 42.1 mmol) with MnO₂ (18.30 g, 210.5 mmol) in toluene (421.0 mL) gave 6.87 g (70%) of **4a** as white solid after purification by silica gel column chromatography (hexane: AcOEt = 2: 1).



4a: R_f 0.5 (petroleum ether /AcOEt = 2/1). IR (KBr): $\tilde{\nu}$ = 1724 (CO) cm⁻¹. ¹H NMR (300.1 MHz, CDCl₃, 25 °C): δ 8.56 (ddd, *J* = 4.8, 1.7, 1.1 Hz, 1H); 8.28 (dt_{app}, *J* = 7.7, 1.1 Hz, 1H); 8.21 (s, 1H); 7.77 (t_{appd}, *J* = 7.7, 1.7 Hz, 1H); 7.31 (ddd, *J* = 7.7, 4.8, 1.1 Hz, 1H); 4.40 (q, *J* = 7.1 Hz, 2H); 1.38 (t, *J* = 7.1 Hz, 3H). ¹³C{¹H} NMR (75.5 MHz, CDCl₃, 25 °C): δ 161.30; 169.79; 150.32; 149.28; 148.09; 137.00; 129.38; 125.01; 120.13; 61.37; 14.23. MS, *m/z* (%): 234(5) [M⁺]; 161(100) [(M-COOEt)⁺]. Anal. Calcd for C₁₁H₁₀N₂O₂S (234.27): C, 56.39; H, 4.30; N, 11.96. Found: C, 56.22; H, 4.61; N, 12.01.

Ethyl-2-(4-(pyridin-4-yl)phenyl)-thiazole-4-carboxylate (**4b**)

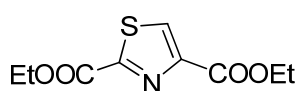
Reaction of **3b** (2.90 g, 9.2 mmol) with MnO₂ (4.00 g, 46.0 mmol) in toluene (92.0 mL) gave 1.86 g (65%) of **4b** as yellow solid after purification by silica gel column chromatography (hexane: AcOEt = 2: 1).



4b: R_f 0.3 (petroleum ether /AcOEt = 2/1). IR (KBr): $\tilde{\nu}$ = 1720 (CO) cm^{-1} . $^1\text{H NMR}$ (400.1 MHz, CDCl_3 , 25 °C): δ 8.67 (dd, J = 4.6, 1.6 Hz, 2H); 8.17 (s, 1H); 8.11 (d, J = 8.4, 1.1 Hz, 2H); 7.70 (dd, J = 6.6, 1.8 Hz, 2H); 7.52 (dd, J = 4.6, 1.6 Hz, 2H); 4.44 (q, J = 7.1 Hz, 2H); 1.42 (t, J = 7.1 Hz, 3H). $^{13}\text{C}\{^1\text{H}\}$ NMR (100.6 MHz, CDCl_3 , 25 °C): δ 167.77; 161.26; 150.33; 148.21; 146.98; 140.07; 133.21; 127.56; 127.46; 127.31; 121.37; 61.52; 14.29. **MS**, m/z (%): 238(100) [(M-COOEt) $^+$]. **Anal.** Calcd for $\text{C}_{17}\text{H}_{14}\text{N}_2\text{O}_2\text{S}$ (310.37): C, 65.79; H, 4.55; N, 9.03. Found: C, 66.01; H, 4.56; N, 9.22.

Diethyl thiazole-2,4-dicarboxylate (**4c**)

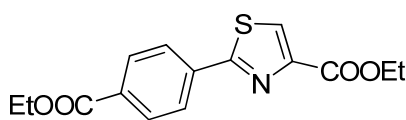
Reaction of **3c** (6.10 g, 26.1 mmol) with MnO_2 (11.35 g, 130.5 mmol) in toluene (261.0 mL) gave 4630 mg (77%) of **4c** as white solid after purification by silica gel column chromatography (hexane: AcOEt = 5: 2).



4c: R_f 0.7 (hexane/AcOEt = 3/2). IR (KBr): $\tilde{\nu}$ = 1731 (CO) cm^{-1} . $^1\text{H NMR}$ (400.1 MHz, CDCl_3 , 25 °C): δ 8.30 (s, 1H); 4.25 (q, J = 7.0 Hz, 2H); 4.19 (q, J = 7.0 Hz, 2H); 1.20 (t, J = 7.0 Hz, 3H); 1.16 (t, J = 7.0 Hz, 3H). $^{13}\text{C}\{^1\text{H}\}$ NMR (100.6 MHz, CDCl_3 , 25 °C): δ 180.02; 158.81; 158.41; 148.14; 132.00; 62.26; 61.04; 13.62; 13.53. **MS**, m/z (%): 229(5) [M^+]; 157(100) [(M-CO $_2$ Et) $^+$]. **Anal.** Calcd for $\text{C}_9\text{H}_{11}\text{NO}_4\text{S}$ (229.25): C, 47.15; H, 4.84; N, 6.11. Found: C, 48.25; H, 5.02; N, 6.02.

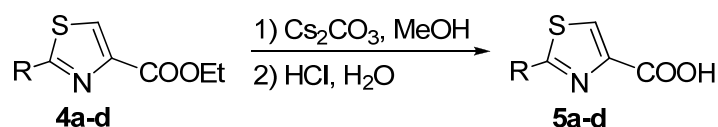
Ethyl 2-(4-(methoxycarbonyl)phenyl)thiazole-4-carboxylate (**4d**)

Reaction of **3d** (12.00 g, 40.8 mmol) with MnO_2 (17.74 g, 204.0 mmol) in toluene (410.0 mL) gave 8.25 g (69%) of **4d** as yellow solid after purification by silica gel column chromatography (hexane: AcOEt = 2: 1).



4d: R_f 0.4 (hexane/AcOEt = 2/1). IR (KBr): $\tilde{\nu}$ = 1720 (CO) cm^{-1} . $^1\text{H NMR}$ (300.1 MHz, CDCl_3 , 25 °C): δ 8.20 (s, 1H); 8.11-8.05 (m, 4H); 4.44 (q, J = 7.1 Hz, 2H); 3.93 (s, 3H); 1.42 (t, J = 7.1 Hz, 3H). $^{13}\text{C}\{^1\text{H}\}$ NMR (75.5 MHz, CDCl_3 , 25 °C): δ 167.37; 166.27; 161.20; 148.41; 136.44; 131.75; 130.18; 127.83; 126.79; 61.59; 52.30; 14.29. **MS**, m/z (%): 291(100) [M^+]; 218(100) [(M-CO $_2$ Et) $^+$]. **Anal.** Calcd for $\text{C}_{14}\text{H}_{13}\text{NO}_4\text{S}$ (291.32): C, 57.72; H, 4.50; N, 4.81. Found: C, 58.01; H, 4.68; N, 5.00.

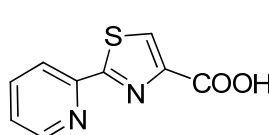
3.7.1.3 General procedure to 2-substituted thiazole-4-carboxylic acid (5a-d)



2-Substituted-4-carboethoxy-1,3-thiazole **4a-d** (1 eq) was dissolved in MeOH. A solution of cesium carbonate (2 eq) in H₂O was added and the mixture was stirred at rt overnight. The reaction mixture was then concentrated in *vacuo* to remove MeOH. The aqueous phase was washed with ethyl acetate then acidified with concentrated HCl ($1 \leq \text{pH} \leq 4$) to let carboxylic acid gradually precipitate from the reaction medium. The solid was collected by filtration on paper and washed several times with EtOH, H₂O and Et₂O to afford the pure acids **5a-d**.

2-(Pyridin-4-yl)thiazole-4-carboxylic acid (Htzc-py, 5a)

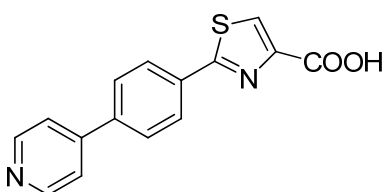
Reaction of **4a** (6.88 g, 29.5 mmol) with Cs₂CO₃ (19.23 g, 59.0 mmol), in MeOH (295.0 mL) and H₂O (295.0 mL) gave 4.41 g (72%) of **5a** as a white solid.



5a: IR (KBr): $\tilde{\nu} = 3114$ (OH), 1709 (CO) cm⁻¹. ¹H NMR (300.1 MHz, DMSO-*d*₆, 25 °C): δ 8.66 (dm, $J = 4.8$, Hz, 1H); 8.57 (s, 1H); 8.15 (dm, $J = 7.9$ Hz, 1H); 8.00 (dt_{app}, $J = 7.8, 1.7$ Hz, 1H); 7.54 (ddd, $J = 7.8, 4.8, 1.1$ Hz, 1H). ¹³C{¹H} NMR (100.6 MHz, DMSO-*d*₆, 25 °C): δ 168.80; 162.07; 149.85; 149.81; 148.44; 138.04; 130.85; 125.70; 119.42. ESI-MS, m/z (%): 206(100) [M⁺]. Anal. Calcd for C₉H₆N₂O₂S·1/2H₂O (215.23): C, 50.02; H, 3.28; N, 13.02. Found: C, 50.47; H, 3.31; N, 12.98.

2-(4-(Pyridin-4-yl)phenyl)thiazole-4-carboxylic acid (5b)

Reaction of **4b** (1.76 g, 5.7 mmol) with Cs₂CO₃ (3.70 g, 11.3 mmol), in MeOH (50.0 mL) and H₂O (50.0 mL) gave 1.25 g (78%) of **5b** as a white solid.

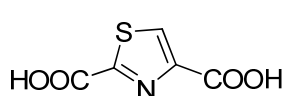


5b: IR (KBr): $\tilde{\nu} = 3122$ (OH), 1690 (CO) cm⁻¹. ¹H NMR (400.1 MHz, DMSO-*d*₆, 25°C): δ 8.68 (d, $J = 5.9$, Hz, 2H); 8.55 (s, 1H); 8.12 (d, $J = 8.3$ Hz, 2H); 8.00 (d, $J = 8.3$ Hz, 2H); 7.80

(d, $J = 5.9$, 2H). $^{13}\text{C}\{^1\text{H}\}$ NMR (100.6 MHz, DMSO- d_6 , 25°C): δ 166.99; 162.49; 150.80; 148.94; 146.23; 139.48; 133.52; 129.54; 128.19; 127.56; 121.59. **ESI-MS**, m/z (%): 283(100) [(M+H) $^+$]. **Anal.** Calcd for $\text{C}_{15}\text{H}_{10}\text{N}_2\text{O}_2\text{S}\cdot 1/2\text{H}_2\text{O}$ (282.32): C, 61.84; H, 3.81; N, 9.62. Found: C, 61.71; H, 3.64; N, 9.56.

Thiazole-2,4-dicarboxylic acid (2,4-H₂tzdc, 5c)

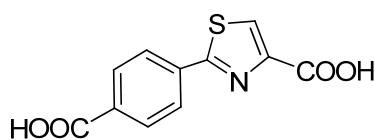
Reaction of **4c** (3.90 g, 17.0 mmol) with Cs_2CO_3 (22.17 g, 68.0 mmol) in MeOH (170.0 mL) and H_2O (170.0 mL) gave 2.46 g (83%) of **5c** as a white solid.



5c: IR (KBr): $\tilde{\nu} = 3140$ (OH), 1719 (CO) cm^{-1} . ^1H NMR (300.1 MHz, DMSO- d_6 , 25 °C): δ 8.73 (s, 1H). ^{13}C NMR (75.5 MHz, DMSO- d_6 , 25 °C): δ 162.79; 161.57; 160.68; 149.66; 134.95. **ESI-MS**, m/z (%): 173(100) [M^+]; 128(30) [(M-CO₂H) $^+$]. **Anal.** Calcd for $\text{C}_5\text{H}_3\text{NO}_4\text{S}\cdot\text{H}_2\text{O}$ (191.16): C, 31.41; H, 2.64; N, 7.33. Found: C, 31.68; H, 2.36; N, 7.35.

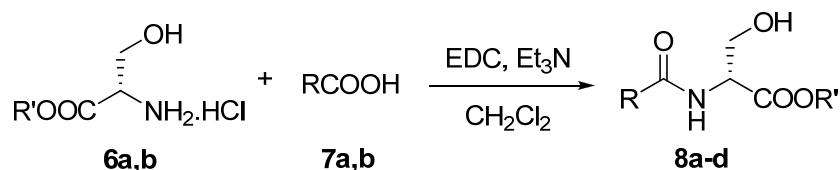
2-(4-Carboxyphenyl)thiazole-4-carboxylic acid (5d)

Reaction of **4d** (8.25 g, 28.3 mmol) with Cs_2CO_3 (36.90 g, 113.2 mmol) in MeOH (280.0 mL) and H_2O (280.0 mL) gave 5.39 g (76%) of **5d** as a white solid.



5d: IR (KBr): $\tilde{\nu} = 3134$ (OH), 1695 (CO) cm^{-1} . ^1H NMR (400.1 MHz, CDCl_3 , 25 °C): δ 8.55 (s, 1H); 8.11-8.05 (m, 4H). $^{13}\text{C}\{^1\text{H}\}$ NMR (100.6 MHz, DMSO- d_6 , 25 °C): δ 167.25; 166.50; 162.67; 136.41; 133.34; 130.71; 130.62; 129.54; 126.91. **ESI-MS**, m/z (%): 249(15) [M^+]; 248(100) [(M-H) $^+$]. **Anal.** Calcd for $\text{C}_{11}\text{H}_7\text{NO}_4\text{S}\cdot\text{H}_2\text{O}$ (267.26): C, 49.43; H, 3.39; N 5.24. Found: C, 49.76; H, 3.30; N 5.21.

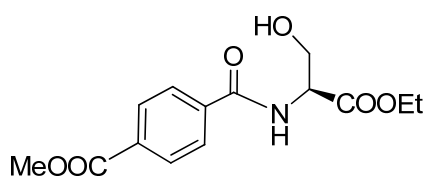
3.7.1.4 General procedure to methyl 2(*R*)-amido-3-hydroxypropanoate-3-hydroxy amide (**8a-d**)³⁵



L-serine ester hydrochloride **6a,b** (1.0 eq) was dissolved in CH₂Cl₂ together with acid **7a,b** (1.1 eq) Et₃N (1.1 eq) and EDC (*N*-(3-dimethylaminopropyl)-*N'*-ethylcarbodiimide, 1.1 eq). After stirring overnight, the solution was washed with H₂O, NaHCO₃ sat. sol., and brine, then dried over Na₂SO₄. Evaporation of the solvent gave amide **8a-d**, which were used without further purification.

(*R*)-Methyl 4-(1-ethoxy-3-hydroxy-1-oxopropan-2-ylcarbamoyl)benzoate (**8a**)

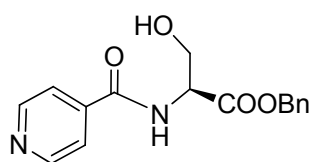
Reaction of **6a** (2.14 g, 12.6 mmol) with **7a** (2.50 g, 13.9 mmol), 0.7 mL of Et₃N (13.9 mmol) and EDC (2.66 g, 13.9 mmol) in CH₂Cl₂ (90.0 mL) gave 3.56 g (95%) of **8a** as a white solid.



8a: IR (KBr): $\tilde{\nu}$ = 3547 (NH), 3277 (OH), 1723 (CO), 1640 (CO) cm⁻¹. ¹H NMR (400.1 MHz, CDCl₃, 25 °C): δ 8.05 (d, *J* = 8.3 Hz, 2H); 7.88 (d, *J* = 8.3 Hz, 2H); 7.38 (bd, *J* = 3.2 Hz, 1H); 4.85-4.79 (m, 1H); 4.28 (q, *J* = 7.1 Hz, 2H); 4.10 (dd, *J*_{AB} = 11.3, *J*_{AX} = 3.6 Hz, 1H); 4.05 (dd *J*_{AB} = 11.3, *J*_{BX} = 3.2 Hz, 1H); 3.9 (s, 3H); 1.31 (t, *J* = 7.1 Hz, 3H). ¹³C{¹H} NMR (100.6 MHz, CDCl₃, 25 °C): δ 170.39; 166.75; 166.15; 137.39; 132.93; 129.72; 127.22; 63.12; 62.04; 55.30; 52.36; 14.07. ESI-MS, *m/z* (%): 296(100) [(M+H)⁺].

(*S*)-Benzyl 3-hydroxy-2-(isonicotinamido)propanoate (**8b**)

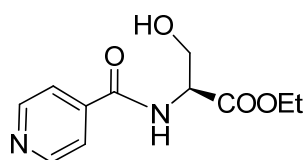
Reaction of **6b** (2.47 g, 10.6 mmol) with **7b** (1.44 g, 11.7 mmol), Et₃N (1.6 mL, 11.7 mmol), EDC (2.24 g, 11.7 mmol) in CH₂Cl₂ (90.0 mL) gave 2.28 g (72%) of **8b** as a white solid.



8b: IR (KBr): $\tilde{\nu}$ = 3289 (NH), 3250 (OH), 1748 (CO), 1644 (CO) cm^{-1} . $^1\text{H NMR}$ (300.1 MHz, CDCl_3 , 25 °C): δ 8.73 (dd, J = 4.5, 1.6 Hz, 1H); 7.64 (dd, J = 4.5, 1.6 Hz, 1H); 7.19 (bd, J = 3.2 Hz, 1H); 7.37 (bs, 5H); 5.26 (s, 1H); 4.92-4.87 (m, 2H); 4.15 (dd, J_{AB} = 11.3, J_{AX} = 3.4 Hz, 1H); 4.06 (dd, J_{AB} = 11.3, J_{BX} = 3.2 Hz, 1H). $^{13}\text{C}\{^1\text{H}\}$ NMR (75.5 MHz, CDCl_3 , 25 °C): δ 170.06; 165.50; 150.66; 141.00; 135.11; 128.74; 128.27; 127.55; 120.96; 67.87; 63.12; 55.19. **ESI-MS**, m/z (%): 301(100) [(M+H) $^+$].

(R)-Ethyl 3-hydroxy-2-(isonicotinamido)propanoate (8c)

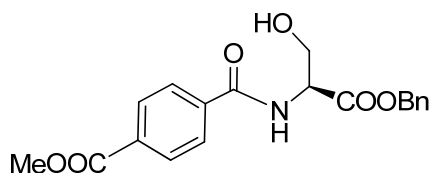
Reaction of **6a** (5.00 g, 29.5 mmol) with **7b** (3.99 g, 32.4 mmol), Et_3N (4.5 mL, 32.4 mmol) and EDC (6.21 g, 32.4 mmol) in CH_2Cl_2 (250.0 mL) gave 6.55 g (93%) of **8c** as a white solid.



8c: IR (KBr): $\tilde{\nu}$ = 3328 (NH), 3260 (OH), 1749 (CO), 1644 (CO) cm^{-1} . $^1\text{H NMR}$ (300.1 MHz, CDCl_3 , 25 °C): δ 8.75 (dd, J = 4.4, 1.7 Hz, 1H); 7.66 (dd, J = 4.4, 1.7 Hz, 1H); 7.12 (bd, J = 3.0 Hz, 1H); 4.85-4.81 (m, 1H); 4.29 (q, J = 7.1, 2H); 4.13 (dd, J_{AB} = 11.3, J_{AX} = 3.5 Hz, 1H); 4.07 (dd, J_{AB} = 11.3, J_{BX} = 3.2 Hz, 1H); 1.33 (t, J = 7.1, 3H). $^{13}\text{C}\{^1\text{H}\}$ NMR (75.5 MHz, CDCl_3 , 25 °C): δ 170.17; 165.46; 150.62; 140.71; 120.98; 63.16; 62.30; 55.23; 14.14. **ESI-MS**, m/z (%): 239(100) [(M+H) $^+$].

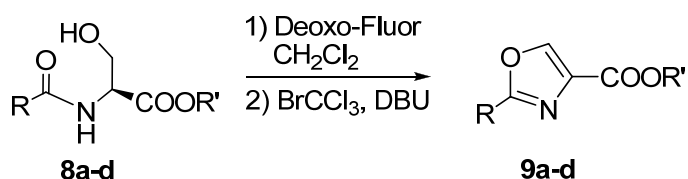
(R)-Methyl 4-(1-(benzyloxy)-3-hydroxy-1-oxopropan-2-ylcarbamoyl)benzoate (8d)

Reaction of **6b** (2.42 g, 10.4 mmol) with 2.06 g of mono-methyl terephthalate **7a** (11.4 mmol), 1.6 mL of Et_3N (11.4 mmol) and EDC (2.185 g, 11.4 mmol) in CH_2Cl_2 (110.0 mL) gave 2.75 g (74%) of **8d** as a white solid.



8d: IR (KBr): $\tilde{\nu}$ = 3495 (NH), 3285 (OH), 1724 (CO), 1628 (CO) cm^{-1} . $^1\text{H NMR}$ (400.1 MHz, CDCl_3 , 25 °C): δ 8.08 (d, J = 8.7 Hz, 2H); 7.86 (d, J = 8.7 Hz, 2H); 7.35 (bs, 5H); 7.22 (bd, J = 7.2 Hz, 1H); 5.24 (s, 2H); 4.93-4.88 (m, 1H); 4.12 (dd, J_{AB} = 11.3, J_{AX} = 3.6 Hz, 1H); 4.05 (dd, J_{AB} = 11.3, J_{BX} = 3.3 Hz, 1H); 3.9 (s, 3H). $^{13}\text{C}\{^1\text{H}\}$ NMR (100.6 MHz, CDCl_3 , 25 °C): δ 170.27; 166.74; 166.20; 137.34; 134.97; 133.06; 129.84; 128.69; 128.61; 128.19; 127.23; 67.73; 63.29; 55.27; 52.43. **ESI-MS**, m/z (%): 358(100) [(M+H) $^+$].

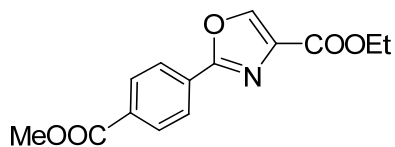
3.7.1.5 General procedure to 2-substituted oxazole-4-carboxylate (**9a-d**)



A solution of **8a-d** (1.0 eq) in CH_2Cl_2 was cooled to $-20\text{ }^\circ\text{C}$. Deoxo-Fluor (50% in THF) (2.2 eq) was added dropwise, and the mixture was stirred at $-20\text{ }^\circ\text{C}$ for 50 min. After addition of BrCCl_3 (3.6 eq) and DBU (3.6 eq) the reaction was left at $0\text{ }^\circ\text{C}$ for 5h and then quenched with NaHCO_3 sat. sol. and extracted with ethyl acetate. The combined organic layers were washed with brine, dried over Na_2SO_4 . Evaporation of the solvent and purification by flash chromatography gave compounds **9a-d**.

Ethyl 2-(4-(methoxycarbonyl)phenyl)oxazole-4-carboxylate (**9a**)

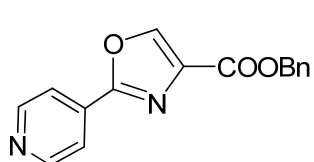
Reaction of **8a** (3.72 g, 12.6 mmol) with Deoxo-Fluor (5.7 mL, 26.5 mmol), BrCCl_3 (4.5 mL, 45.4 mmol) and DBU (6.8 mL, 45.4 mmol) in CH_2Cl_2 (125 mL) gave 1.72 g (50%) of **9a** as a white solid after purification by silica gel column chromatography (hexane: AcOEt = 1: 2).



9a: R_f 0.35 (hexane/AcOEt = 1/2). IR (KBr): $\tilde{\nu}$ = 1721 (CO) cm^{-1} . $^1\text{H NMR}$ (400.1 MHz, CDCl_3 , $25\text{ }^\circ\text{C}$): δ 8.35 (s, 1H); 8.17 (d, J = 8.4 Hz, 2H); 8.12 (d, J = 8.4 Hz, 2H); 4.42 (q, J = 7.0 Hz, 2H); 3.93 (s, 3H); 1.40 (t, J = 7.0 Hz, 3H). $^{13}\text{C}\{^1\text{H}\}$ NMR (100.6 MHz, CDCl_3 , $25\text{ }^\circ\text{C}$): δ 160.21; 161.42; 161.07; 144.14; 132.23; 130.46; 130.09; 130.02; 126.76; 61.41; 52.34; 14.27. **MS**, m/z (%): 275(30) [M^+]; 163(100). **Anal.** Calcd for $\text{C}_{14}\text{H}_{13}\text{NO}_5$ (275.26): C, 61.09; H, 4.76; N, 5.09. Found: C, 61.55; H, 4.73; N, 4.97.

Benzyl 2-(pyridin-4-yl)oxazole-4-carboxylate (**9b**)

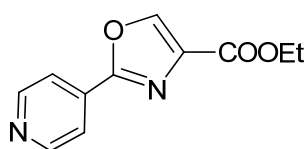
Reaction of **8b** (2.27 g, 7.6 mmol) with Deoxo-Fluor (3.5 mL, 16.1 mmol), BrCCl_3 (2.7 mL, 27.4 mmol) and DBU (4.1 mL, 27.4 mmol) in CH_2Cl_2 (76.0 mL) gave 1.10 g (52%) of **9b** as a white solid after purification by silica gel column chromatography (hexane: AcOEt = grad).



9b: R_f 0.25 (hexane/AcOEt = 1/1). IR (KBr): $\tilde{\nu}$ = 1734 (CO) cm^{-1} . $^1\text{H NMR}$ (400.1 MHz, CDCl_3 , 25 °C): δ 8.77 (d, J = 6.0 Hz, 2H); 8.35 (s, 1H); 7.96 (dd, J = 6.0 Hz, 2H); 7.35-7.44 (m, 5H); 5.41 (s, 2H). $^{13}\text{C}\{^1\text{H}\}$ NMR (100.6 MHz, CDCl_3 , 25 °C): δ 160.34; 159.86; 150.40; 144.64; 134.98; 134.59; 132.92; 128.36; 128.28; 120.00; 67.01. **MS**, m/z (%): 280(5) [M^+]; 146(100) [($\text{M}-\text{CO}_2\text{Bn}$) $^+$]. **Anal.** Calcd for $\text{C}_{16}\text{H}_{12}\text{N}_2\text{O}_3$ (280.28): C, 68.56; H, 4.32; N, 9.99. Found: C, 68.28; H, 4.81; N, 10.17.

Ethyl 2-(pyridin-4-yl)oxazole-4-carboxylate (9c)

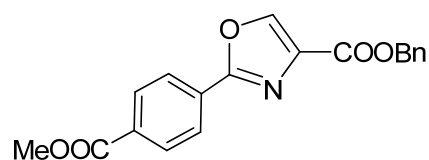
Reaction of **8c** (1.70 g, 7.1 mmol) with Deoxo-Fluor (3.4 mL, 15.7 mmol), BrCCl_3 (2.5 mL, 25.7 mmol) and DBU (3.8 mL, 25.7 mmol) in CH_2Cl_2 (75.0 mL) gave 1.02 g (72%) of **9c** as a white solid after purification by silica gel column chromatography (hexane: AcOEt = 2: 1).



9c: R_f 0.65 (hexane/AcOEt = 1/2). IR (KBr): 1734 (CO) cm^{-1} . $^1\text{H NMR}$ (400.1 MHz, CDCl_3 , 25 °C): δ 8.77 (d, J = 6.0 Hz, 2H); 8.35 (s, 1H); 7.96 (d, J = 6.0 Hz, 2H); 4.43 (q, J = 7.2 Hz, 2H); 1.40 (t, J = 7.2 Hz, 3H). $^{13}\text{C}\{^1\text{H}\}$ NMR (100.6 MHz, CDCl_3 , 25 °C): δ 160.80; 160.14; 150.68; 144.53; 135.25; 133.28; 120.30; 61.54; 14.26. **MS**, m/z (%): 218(22) [M^+]; 106(100). **Anal.** Calcd for $\text{C}_{11}\text{H}_{10}\text{N}_2\text{O}_3$ (218.21): C, 60.55; H, 4.62; N, 12.84. Found: C, 60.68; H, 4.85; N, 13.01.

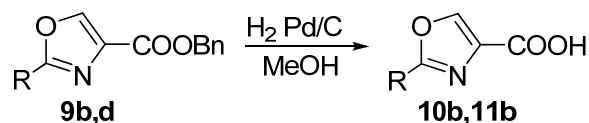
Benzyl 2-(4-(methoxycarbonyl)phenyl)oxazole-4-carboxylate (9d)

Reaction of **8d** (2.7 g, 7.6 mmol) with Deoxo-Fluor (3.5 mL, 16.1 mmol), BrCCl_3 (2.7 mL, 27.4 mmol) and DBU (4.1 mL, 27.4 mmol) in CH_2Cl_2 (75.0 mL) gave 1.30 g (51%) of **9d** as a white solid after purification by silica gel column chromatography (hexane: AcOEt = 2: 1).



9d: R_f 0.6 (hexane/AcOEt = 1/1). IR (KBr): $\tilde{\nu}$ = 1722 (CO) cm^{-1} . $^1\text{H NMR}$ (400.1 MHz, CDCl_3 , 25 °C): δ 8.32 (s, 1H); 8.21-8.12 (m, 4H); 7.48-7.34 (m, 5H); 5.41 (s, 2H); 3.95 (s, 3H). $^{13}\text{C}\{^1\text{H}\}$ NMR (100.6 MHz, CD_2Cl_2 , 25 °C): δ 166.09; 161.42; 160.83; 144.68; 135.63; 134.68; 132.38; 130.19; 130.02; 129.87; 128.64; 126.66; 66.83; 52.30. **MS**, m/z (%): 246 (2) [($\text{M}-\text{CO}_2\text{Bn}$) $^+$]; 163(100). **Anal.** Calcd for $\text{C}_{19}\text{H}_{15}\text{NO}_5$ (337.33): C, 67.65; H, 4.48; N 4.15. Found: C, 68.08; H, 4.56; N 4.23.

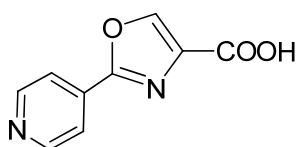
3.7.1.6 General procedure for debenzoylation



A solution of carbobenzyloxy-oxazole **9b,d** (1 eq) in MeOH was purged with N₂ and Pd (10 wt%) on carbon was added. H₂ was bubbled 10 min, then the mixture was stirred under H₂ for 3h. Filtration through celite and evaporation of the solvent gave **10b** or **11b**.

2-(2-Pyridyl)-1,3-oxazole-4-carboxylic acid (**10b**)

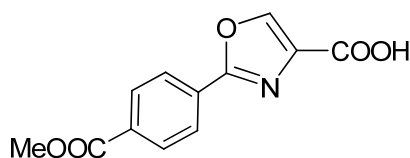
Reaction of **9b** (1.93 g, 6.9 mmol) and Pd/C (193 mg) in MeOH (140.0 mL) gave, after filtration, 513 mg (39%) of **10b** as white solid.



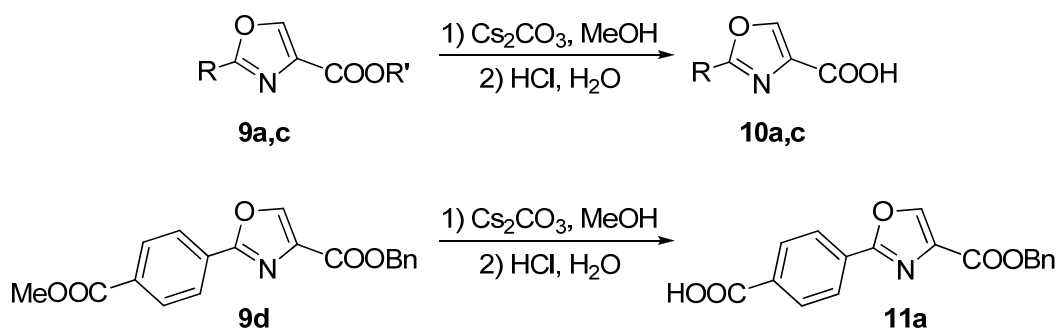
10b: IR (KBr): $\tilde{\nu}$ = 3378 (OH), 1726 (CO) cm⁻¹. ¹H NMR (400.1 MHz, DMSO-*d*₆, 25 °C): δ 8.93 (s, 1H); 8.79 (d, *J* = 3.5 Hz, 2H); 7.93 (d, *J* = 3.5 Hz, 2H). ¹³C{¹H} NMR (100.6 MHz, DMSO-*d*₆, 25 °C): δ 162.24; 159.44; 151.25; 146.66; 146.60; 133.45; 120.38. ESI-MS, *m/z* (%): 191(100) [(M+H)⁺]. Anal. Calcd for C₉H₆N₂O₃ (190.16): C, 56.85; H, 3.18; N, 14.73. Found: C, 56.32; H, 3.20; N, 14.74.

2-(4-(Methoxycarbonyl)phenyl)oxazole-4-carboxylic acid (**11b**)

Reaction of **9d** (900 mg, 2.7 mmol) and Pd/C (9 mg) in MeOH (55.0 mL) gave, after filtration, 600 mg (89%) of **11b** as white solid.



11b: IR (KBr): $\tilde{\nu}$ = 2958 (OH), 1718 (CO), 1687(CO) cm⁻¹. ¹H NMR (400.1 MHz, DMSO-*d*₆, 25 °C): δ 8.92 (s, 1H); 8.16-8.10 (m, 4H); 3.89 (s, 3H). ¹³C{¹H} NMR (100.6 MHz, DMSO-*d*₆, 25 °C): δ 165.94; 162.28; 160.60; 132.29; 131.96; 130.45; 129.52; 128.24; 126.99; 52.84. ESI-MS, *m/z* (%): 246(100) [(M-H)⁺]. Anal. Calcd for C₁₂H₉NO₅ (247.20): C, 58.30; H, 3.67; N 5.67. Found: C, 58.81; H, 3.50; N 5.76.

3.7.1.7 General procedure to 2-substituted oxazole-4-carboxylic acids (**10a,c** and **11a**)

Compound **9a,c,d** (1 eq) was dissolved in MeOH and reacted with a solution of cesium carbonate (2.0 eq) in H₂O. The mixture stirred at rt overnight, then MeOH was removed. The aqueous phase was washed with ethyl acetate, then acidified with concentrated HCl (1 ≤ pH ≤ 4) to let carboxylic acid gradually precipitate from the reaction medium. The solid was collected by filtration and washed several times with EtOH, H₂O and Et₂O to afford products **10a,c** or **11b**.

2-(4-Carboxyphenyl)oxazole-4-carboxylic acid (**10a**)

Reaction of **9a** (1.72 g, 6.2 mmol) and Cs₂CO₃ (8.15 g, 25.0 mmol) in MeOH (50.0 mL) and H₂O (50.0 mL) gave 1.45 g (98%) of **10a** as a yellow solid.

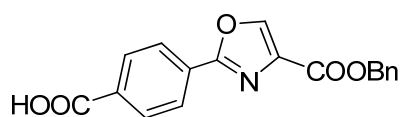
10a: IR (KBr): $\tilde{\nu}$ = 3000 (OH), 1696 (CO) cm⁻¹. ¹H NMR (400.1 MHz, CDCl₃, 25 °C): δ 8.88 (s, 1H); 8.09 (m, 2H); 8.02 (bs, 2H). ¹³C{¹H} NMR (100.6 MHz, DMSO-*d*₆, 25 °C): δ 167.17; 167.09; 162.36; 146.43; 134.93; 133.28; 130.63; 129.94; 126.93. **ESI-MS**, *m/z* (%): 248(100) [(M-H)⁺]; 249(15) [M⁺]. **Anal.** Calcd for C₁₁H₇NO₅ (233.18): C, 56.66; H, 3.03; N, 6.01. Found: C, 57.01; H, 3.24; N, 5.98.

2-(Pyridin-4-yl)oxazole-4-carboxylic acid **10c** (≡**10b**)

Reaction of **9c** (1.00 g, 4.6 mmol) and Cs₂CO₃ (3.00 g, 9.2 mmol) in MeOH (40.0 mL) and H₂O (40.0 mL) gave 605 mg (69%) of **10c** as a white solid.

4-(4-(Benzyloxycarbonyl)oxazol-2-yl)benzoic acid (11a)

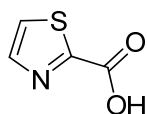
Reaction of **9d** (1.30 g, 3.9 mmol) and Cs₂CO₃ (2.54 g, 7.9 mmol) in MeOH (40.0 mL) and H₂O (40.0 mL) gave 695 mg (50%) of **11a** as a white solid.



11a: IR (KBr): $\tilde{\nu}$ = 3378 (OH), 1725 (CO) cm⁻¹. ¹H NMR (400.1 MHz, CDCl₃, 25 °C): δ 8.97 (s, 1H); 8.40-7.98 (m, 9H); 5.52 (s, 2H). ¹³C{¹H} NMR (100.6 MHz, CDCl₃, 25 °C): δ 167.03; 162.31; 160.77; 146.47; 135.22; 133.26; 130.59; 130.11; 129.89; 128.11; 126.88; 63.30. ESI-MS, *m/z* (%): 248(100) [(M-H)⁺]; 322(100) [M⁺]. Anal. Calcd for C₁₈H₁₃NO₅ (323.30): C, 66.87; H, 4.05; N, 4.33. Found: C, 67.11; H, 3.98; N, 4.07.

3.7.1.8 Synthesis of thiazole-2-carboxylic acid (13)

To a solution of *n*-BuLi (7.0 mL, 13.0 mmol) in 195.0 mL of diethyl ether cooled at -78 °C was added quickly a solution of re-distillate 2-bromothiazole (1.92 g, 11.7 mmol) in 5.0 mL of diethyl ether. After stirring the mixture at -78 °C for 10 min, CO₂ gas was bubbled for 10 min with immediate precipitation of a white solid. After stirring for another hour at -78 °C, the reaction was warmed up slowly to rt and quenched by adding H₂O. The aqueous phase was washed with ethyl acetate then acidified with concentrated HCl (pH = 1) to let carboxylic acid gradually precipitate from the reaction medium. The solid was collected by filtration on paper and washed several times with H₂O and Et₂O to afford 0.10 g (66.7%) of **13** as a white crystalline solid.

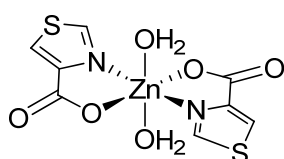


13: IR (KBr): $\tilde{\nu}$ = 3140 (OH), 1719 (CO) cm⁻¹. ¹H NMR (300.1 MHz, DMSO-*d*₆, 25 °C): δ 8.10 (d, *J* = 3.0 Hz, 1H); 8.08 (d, *J* = 3.0 Hz, 1H). ¹³C{¹H} NMR (75.5 MHz, DMSO-*d*₆, 25 °C): δ 161.20; 159.50; 145.25; 127.14. ESI-MS, *m/z* (%): 129 (100) [M⁺]. Anal. Calcd for C₄H₃NO₂S (129.14): C, 37.20; H, 2.34; N, 10.85. Found: C, 37.17; H, 2.45; N, 10.59.

3.7.1.9 Synthesis of Zn(4-tztc)₂•2H₂O (14)

Zinc perchlorate hexahydrate Zn(ClO₄)₂•6H₂O (1.73 g, 4.6 mmol) was dissolved together with 4-Htzc (0.30 g, 2.3 mmol) in 10.0 mL of deionized water. The clear solution was transferred to a teflon-lined stainless steel autoclave, sealed and heated under autogeneous pressure at 130 °C for 24 h. After slow overnight cooling, **14** was collected,

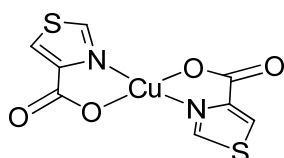
washed with cold ethanol (4 x 10.0 mL) and dried under a nitrogen stream at rt to afford 0.20 g (48.1%; calculated with respect to the ligand) of **14** as colorless cube-like crystals.



14: IR (KBr): $\tilde{\nu}$ = 3219 m (br), 3130 m, 3114 m, 1615 vs, 1514 w, 1443 s, 1345 vs, 1313 s, 1198 m, 1129 m, 967 s, 891 s, 858 s, 803 s, 782 s, 620 m cm^{-1} . **Anal.** Calcd for $\text{C}_8\text{H}_8\text{N}_2\text{O}_6\text{S}_2\text{Zn}$ (357.70): C, 26.84; H, 2.23; N, 7.83. Found: C, 26.92; H, 2.05; N, 7.82.

3.7.1.10 Synthesis of $\text{Cu}(4\text{-tzc})_2$ (**15**)

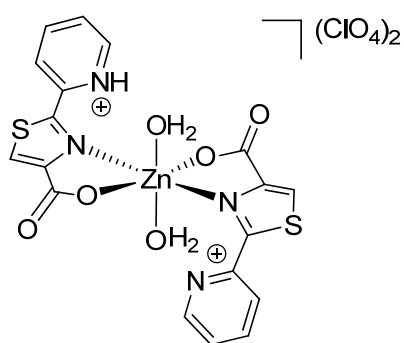
Tetrakis(acetonitrile)copper(I) hexafluorophosphate, $[\text{Cu}(\text{MeCN})_4][\text{PF}_6]$, (0.54 g, 1.1 mmol) was dissolved together with 4-Htzc (0.30 g, 2.3 mmol) in 8.0 mL of degassed acetonitrile. The clear solution was transferred to a teflon-lined stainless steel autoclave, sealed and heated under autogeneous pressure at 110 °C for 24 h. After slow overnight cooling, **15** was collected, washed with cold ethanol (4 x 10.0 mL) and dried under a nitrogen stream at rt to afford 0.10 g (26.9%; calculated with respect to the ligand) of **15** as blue crystals.



15: IR (KBr): $\tilde{\nu}$ = 3094 s, 1634 vs, 1436 s, 1332 s, 1300 vs, 1189 m, 1108 m, 977 s, 879 s, 865 s, 802 s, 787 s, 623 s, 547 m, 459 s cm^{-1} . **Anal.** Calcd for $\text{C}_8\text{H}_4\text{CuN}_2\text{O}_4\text{S}_2$ (319.80): C, 30.05; H, 1.26; N, 8.76. Found: C, 29.97; H, 1.15; N, 9.44.

3.7.1.11 Synthesis of $[\text{Zn}(\text{tzc-Hpy})_2 \cdot 2\text{H}_2\text{O}][\text{ClO}_4]_2$ (**16**)

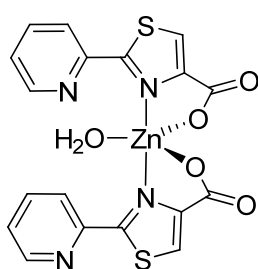
Zinc perchlorate hexahydrate $\text{Zn}(\text{ClO}_4)_2 \cdot 6\text{H}_2\text{O}$ (1.08 g, 2.9 mmol) was dissolved together with **5a** (0.30 g, 1.45 mmol) in 5.0 mL of deionized water. The clear solution was transferred to a teflon-lined stainless steel autoclave, sealed and heated under autogeneous pressure at 130 °C for 24 h. After slow overnight cooling, **16** was collected, washed with cold ethanol (4 x 10.0 mL) and dried under a nitrogen stream at rt to afford 0.40 g (74.6%; calculated with respect to the ligand) of **16** as colorless crystals.



16: IR (KBr): $\tilde{\nu}$ = 3524 m, 3112 m, 3091 m, 3058 w, 2536 w(br), 1697 m, 1596 m, 1462 m, 1349 m, 1294 s, 1239 s, 1144 s, 1114 s, 1048 s, 788 m, 745 m, 625 m, 564 w cm^{-1} .
Anal. Calcd for $\text{C}_{18}\text{H}_{16}\text{N}_4\text{Cl}_2\text{O}_{14}\text{S}_2\text{Zn}$ (709.88): C, 30.33; H, 2.26; N, 7.86. Found: C, 30.32; H, 2.21; N, 7.92.

3.7.1.12 Synthesis of $\text{Zn}(\text{tzc-py})_2 \cdot \text{H}_2\text{O}$ (**17**)

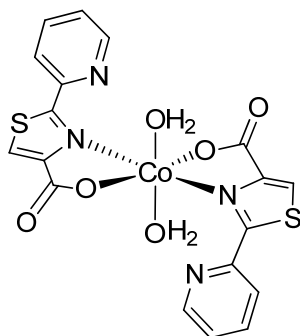
Zinc acetate dihydrate $\text{Zn}(\text{OAc})_2 \cdot 2\text{H}_2\text{O}$ (0.64 g, 2.9 mmol) was dissolved together with **5a** (0.30 g, 1.45 mmol) in 5.0 mL of deionized water. The clear solution was transferred to a teflon-lined stainless steel autoclave, sealed and heated under autogeneous pressure at 130 °C for 24 h. After slow overnight cooling, **17** was collected, washed with cold ethanol (4 x 10.0 mL) and dried under a nitrogen stream at rt to afford 0.08 g (22.3%; calculated with respect to the ligand) of **17** as colorless crystals.



17: IR (KBr): $\tilde{\nu}$ = 3425 w(br), 3130 w, 3089 m, 2870 w(br), 1654 vs, 1609 vs, 1483 m, 1435 m, 1365 s, 1320 s, 1280 s, 1059 w, 1023 m, 786 m, 640 w, 565 w cm^{-1} . **Anal.** Calcd for $\text{C}_{18}\text{H}_{12}\text{N}_4\text{O}_5\text{S}_2\text{Zn}$ (493.85): C, 43.78; H, 2.45; N, 11.34. Found: C, 43.67; H, 2.51; N, 11.22.

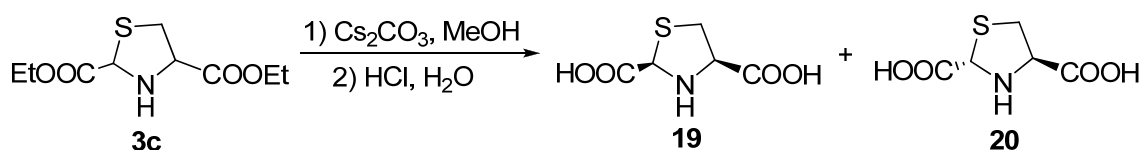
3.7.1.13 Synthesis of $\text{Co}(\text{tzc-py})_2 \cdot 2\text{H}_2\text{O}$ (**18**)

Cobalt acetate tetrahydrate $\text{Co}(\text{OAc})_2 \cdot 4\text{H}_2\text{O}$ (0.72 g, 2.9 mmol) was dissolved together with **5a** (0.30 g, 1.45 mmol) in 5.0 mL of deionized water. The clear solution was transferred to a teflon-lined stainless steel autoclave, sealed and heated under autogeneous pressure at 130 °C for 24 h. After slow overnight cooling, **18** was collected, washed with cold ethanol (4 x 10.0 mL) and dried under a nitrogen stream at rt to afford 0.19 g (51.7%; calculated with respect to the ligand) of **18** as hexagonal light-yellow crystals

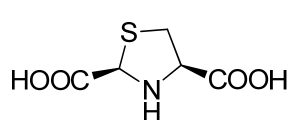


18: IR (KBr): $\tilde{\nu}$ = 3428 m, 3140 s, 3060 w, 2987 w, 1609 vs, 1439 s, 1361 vs, 1279 w, 1235 w, 1023 m, 893 m, 807 s, 792 s, 746 w, 686 w, 557 vw cm^{-1} . **Anal.** Calcd for $\text{C}_{18}\text{H}_{14}\text{CoN}_4\text{O}_6\text{S}_2$ (505.39): C, 42.78; H, 2.79; N, 11.09. Found: C, 42.81; H, 2.73; N, 11.32.

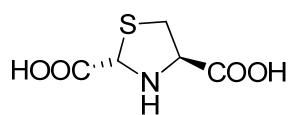
3.7.1.14 Synthesis of (2*R*,4*R*)-thiazolidine-2,4-dicarboxylic acid (**19**) and (2*S*,4*R*)-thiazolidine-2,4-dicarboxylic acid (**20**)



Diethyl thiazolidine-2(*R,S*),4(*R*)-dicarboxylate **3c** (4.0 g, 17.0 mmol) was dissolved in MeOH (170.0 mL). A solution of cesium carbonate (22.20 g, 68.0 mmol) in H_2O (170.0 mL) was added and the mixture was stirred at rt overnight. The reaction mixture was then concentrated in *vacuo* to remove MeOH. The aqueous phase was washed with ethyl acetate then acidified with concentrated HCl ($1 \leq \text{pH} \leq 4$) to let carboxylic acid gradually precipitate from the reaction medium. The solid was collected by filtration on paper and washed several times with EtOH, H_2O and Et_2O to afford) gave 3.0 g (100%), as a white solid containing a 1:1 mixture of diastereoisomers **19** and **20**. The diastereoisomeric isomers was separated by successive crystallizations from $\text{H}_2\text{O}/\text{MeOH}$.



19: IR (KBr): $\tilde{\nu}$ = 3295 (NH), 1682 (CO) cm^{-1} . $^1\text{H NMR}$ (300.1 MHz, $\text{DMSO}-d_6$, 25 $^\circ\text{C}$): δ 4.88 (s, 1H); 3.82 (dd, $J_{\text{AB}} = 6.0$, $J_{\text{BX}} = 10.0$ Hz, 1H); 3.31 (dd, $J_{\text{AX}} = 10.0$, $J_{\text{AB}} = 6.0$ Hz, 1H); 2.74-2.67 (bt, $J_{\text{app}} = 6.0$ Hz, 1H). $^{13}\text{C}\{^1\text{H}\}$ NMR (75.5 MHz, $\text{DMSO}-d_6$, 25 $^\circ\text{C}$): δ 172.53; 65.89; 55.38; 37.43. **ESI-MS**, m/z (%): 177(2) [M^+]. **Anal.** Calcd for $\text{C}_5\text{H}_7\text{NO}_4\text{S}$ (177.18): C, 33.89; H, 3.98; N, 7.91. Found: C, 33.84; H, 4.00; N, 7.89.



20: IR (KBr): $\tilde{\nu}$ = 3295 (NH), 1684 (CO) cm^{-1} . $^1\text{H NMR}$ (300.1 MHz, DMSO- d_6 , 25 °C): δ 4.88 (s, 1H); 4.24-4.19 (bt, J_{app} = 6.0 Hz, 1H); 3.14 (dd, J_{AB} = 6.0, J_{BX} = 10.0 Hz, 1H); 2.90 (dd, J_{AX} = 10.0, J_{AB} = 6.0 Hz, 1H). $^{13}\text{C}\{^1\text{H}\}$ NMR (75.5 MHz, DMSO- d_6 , 25 °C): δ 172.53; 65.89; 55.38; 37.43. **ESI-MS**, m/z (%): 177(2) [M^+]. **Anal.** Calcd for $\text{C}_5\text{H}_7\text{NO}_4\text{S}$ (177.18): C, 33.89; H, 3.98; N, 7.91. Found: C, 33.86; H, 3.95; N, 7.93.

3.7.1.15 Synthesis of $[\text{Co}(\text{tdca})(\text{H}_2\text{O})\cdot(\text{H}_2\text{O})_{0.5}]_{\infty}$ (**21**)

Cobalt chloride hexahydrate $\text{CoCl}_2\cdot 6\text{H}_2\text{O}$ (1.10 g, 4.6 mmol) was dissolved together with **19** (0.4 g, 2.3 mmol) in 7.0 mL of deionized water. The clear solution was transferred to a teflon-lined stainless steel autoclave, sealed and heated under autogeneous pressure at 90 °C for 24 h. After slow overnight cooling, **21** was collected, washed with fresh ethanol (4 x 10.0 mL) and dried under a nitrogen stream at rt to afford 0.25 g (40%; calculated with respect to the ligand) of **21** as magenta prismatic crystals.

21: IR (KBr): $\tilde{\nu}$ = 3428 m, 3120 m (br), 3084 s, 1636 vs, 1432 s, 1339 s, 1320 vs, 1199 m, 1110 m, 957 s, 875 s, 855 s, 810 s, 777 s, 625 s, 556 m, 461 s cm^{-1} . **Anal.** Calcd for $\text{C}_5\text{H}_9\text{CoNO}_6\text{S}$ (270.13): C, 22.23; H, 3.36; N, 5.19. Found: C, 22.32; H, 3.31; N, 5.21.

3.7.2 X-ray crystallographic studies

X-Ray data were collected at low temperature (150 K) either on an Enraf-Nonius CAD4 diffractometer equipped with a graphite monochromator (for **14** and **15**) or on an Oxford Diffraction XCALIBUR 3 diffractometer equipped with a CCD area detector (for all the other compounds presented), in both cases using Mo K_{α} radiation ($\lambda = 0.7107 \text{ \AA}$).

The intensity collected in the first case were corrected for Lorentz and polarization effects, and their consistency checked every 2 hours by collecting three standard reflections repeatedly.

In the second case, the program used for the data collection was CrysAlis CCD 1.171.³⁶ Data reduction was carried out with the program CrysAlis RED 1.171³⁷ and the absorption correction was applied with the program ABSPACK 1.17.³⁶ Direct methods implemented in Sir97³⁸ were used to solve the structures and the refinements were performed by full-matrix least-squares against F^2 implemented in SHELX97.³⁹ All the non-hydrogen atoms

were refined anisotropically while the hydrogen atoms of the aromatic rings were fixed in calculated positions and refined isotropically with the thermal factor depending on the one of the atom to which they are bound. The hydrogen atoms of the carboxylic groups and the hydrogen on the coordinated water molecules, in **5a**, **14**, **16**, **17**, **18** and **21**, and on the protonated pyridyl ring of tzc-Hpy in **16**, were found on the Fourier density maps, and their positions were free to refine, while their thermal factors were related to the oxygen (or nitrogen) atom they are bound to. Geometrical calculations were performed by PARST97⁴⁰ and molecular plots were produced by the program ORTEP3.⁴¹

A complete list of the crystallographic data are collected in the Appendix (Chapter 5).

3.7 References and notes

- 1 "Synthesis of 2-Substituted 4-Carboxy Oxazoles, Thiazoles and Thiazolidines from Serine or Cysteine Amino Acids" **Di Credico, B.**; Gonsalvi, L.; Peruzzini, M., Reginato, G.; Rossin, A., *submitted*.
- 2 "Coordination chemistry of thiazole-based ligands: novel hydrogen-bonded architectures" Rossin, A., **Di Credico, B.**; Giambastiani, G.; Gonsalvi, L.; Peruzzini, M.; Reginato, G. *manuscript in preparation*.
- 3 a) Zhao, B.; Cheng, P.; Chen, X.Y.; Cheng, C.; Shi, W.; Liao, D.Z.; Yan, S.P.; Jiang, Z.H. *J. Am. Chem. Soc.* **2006**, *126*, 3012; b) Liu, Y.-H.; Lu, Y.-L.; Wu, H.-C.; Wang, J.-C.; Lu, K.-L. *Inorg. Chem.* **2002**, *41*, 2592; c) Ghosh, S. K.; Savitha, G.; Bharadwaj, P. K. *Inorg. Chem.* **2004**, *43*, 5495; d) Kurmoo, M.; Estournés, C.; Oka, Y.; Kumagai, H.; Inoue, K. *Inorg.Chem.* **2005**, *44*, 217; e) Li, X. J.; Cao, R.; Sun, Y. Q.; Bi, W. H. ; Li, X.; Wang, Y. Q. *Eur. J. Inorg. Chem.* **2005**, *44*, 321; f) Noro, S.-I.; Miyasaka, H.; Kitagawa, S.; Wada, T.; Okubo, T.; Yamashita, M.; Mitani, T. *Inorg. Chem.* **2005**, *44*, 133.
- 4 a) Dong, Y.-B.; Smith, M. D.; zur Loye, H.-C. *Angew. Chem., Int. Ed.* **2000**, *39*, 4271; b) Zheng, L. M.; Hitefield, T.; Wang, X. Q.; Jacobson, A. J. *Angew. Chem., Int. Ed.* **2000**, *39*, 4528; c) Maggard, P. A.; Yan, B. B.; Luo, J. H. *Angew. Chem., Int. Ed.* **2005**, *55*, 2553.
- 5 Chen, X. D.; Wu, H. F.; Zhao, X.-H.; Zhao, X. J.; Du, M. *Cryst. Growth Des.* **2007**, *7*, 124 and reference therein.
- 6 a) Du, M.; Li, C.-P.; Zhao, X.-J. *Cryst. Growth Des.* **2006**, *6*, 335; b) Du, M.; Li, C.-P. *Inorg. Chim. Acta.* **2006**, *359*, 1690; c) Du, M.; Zhao, X.-J.; Wang, Y. *Dalton Trans.* **2004**, 2065; d) Li, X.; Cao, R.; Sun, Y.-Q.; Shi, Q.; Yuan, D.-Q.; Sun, D.-F.; Bi, W.-H.; Hong, M.-C. *Cryst. Growth Des.* **2004**, *4*, 255.
- 7 Groarke, M.; McKervey, M. A.; Moncrieff, H.; Nieuwenhuyzen, M. *Tetrahedron Lett.* **2000**, *41*, 1279 and references therein.
- 8 Williams, D. R.; Lowder, P. D.; Yu, Y.-G.; D. A. Brooks *Tetrahedron Lett.* **1997**, *38*, 331.
- 9 a) Varma, R. S.; Saini, R. K.; Dahiya, R. *Tetrahedron Lett.* **1997**, *38*, 7823; b) Polshettiwar, V.; Varma, R. *Acc. Chem. Res.* **2008**, *41*, 629.
- 10 See for instance: You, S.-L.; Kelly, J. W. *J. Org. Chem.* **2003**, *68*, 9506.
- 11 a) Cambridge Structural Database System, Cambridge Crystallographic data Centre, 12 Union Road, Cambridge, CB2 1EZ, U.K. (Version 5.30 with update Sep, 2009); b) Allen, F. H. *Acta Crystallogr., Sect. B* **2002**, *58*, 380.
- 12 Hu, N.-H.; Tokuno, T.; Aoki, K. *Inorg. Chim. Acta* **1999**, *295*, 71.

- 13 Phillips, A. J.; Uto, Y.; Wipf, P.; Reno, M. J.; Williams, D. R. *Org. Lett.* **2000**, *2*, 1165.
- 14 a) Robin, A. Y.; Fromm, K. M. *Coord. Chem. Rev.* **2006**, *250*, 2127; b) Yaghi, O. M.; O'Keeffe, M.; Ockwig, N. W.; Chae, H. K.; Eddaoudi, M.; Kim, J. *Nature* **2003**, *423*, 705; c) Moulton, B.; Zaworotko, M. J. *Chem. Rev.* **2001**, *101*, 1629; d) Braga, D.; Grepioni, F.; Desiraju, G. R. *Chem. Rev.* **1998**, *98*, 1375; e) Yaghi, O. M.; Li, H.; Davis, C.; Richardson, D.; Groy, T. L. *Acc. Chem. Res.* **1998**, *31*, 474.
- 15 Symmetry transformation used (#) = -x, y+1/2, -z+2
- 16 Liu, Y.-Y. *J. Coord. Chem.* **2007**, *60*, 2597.
- 17 Gryz, M.; Starosta, W.; Leciejewicz, J. *J. Coord. Chem.* **2007**, *60*, 539.
- 18 a) Lin, X.-F. *Acta Cryst.* **2006**, *E62*, m2039-m2040; b) Liu, J.-W.; Gao, S.; Huo, L.-H.; Gu, C.-S.; Zhao, H.; Zhao, J.-G. *Acta Cryst.* **2004**, *E60*, m1697-m1699.
- 19 Liu, B.-X.; Yu, J.-Y.; Xu, D.-J. *Acta Cryst.* **2006**, *E62*, m67-m68.
- 20 See also: Zhong, Y.-R.; Cao, M.-L.; Mo, H.-Y.; Ye, B.-H. *Cryst. Growth Des.* **2008**, *8*, 2282.
- 21 Ellsworth, J. M.; Su, C.-Y.; Khaliq, Z.; Hipp, R. E.; Goforth, A. M.; Smith, M. D.; zur Loye, H.-C. *J. Mol. Struct.* **2006**, *796*, 86.
- 22 Puchta, R.; van Eikema Hommes, N.; Meier, R.; van Eldik, R. *Dalton Trans.* **2006**, 3392.
- 23 Abufrag, A.; Varenkamp, H. *Inorg. Chem.* **1995**, *34*, 3279.
- 24 Canary, J. W.; Allen, C. S.; Castagnetto, J. M.; Wang, Y. *J. Am. Chem. Soc.* **1995**, *117*, 8484.
- 25 Seitz, M.; Stempfhuber, S.; Zabel, M.; Schütz, M.; Reiser, O. *Angew. Chem., Int. Ed.* **2005**, *44*, 242.
- 26 a) Yamada, T.; Kitagawa, H. *J. Am. Chem. Soc.* **2009**, *131*, 6312; b) Kirchner, C.; Krebs, B. *Inorg. Chem.* **1987**, *26*, 3569.
- 27 a) Lee, S. J.; Hu, A.; Lin, W. *J. Am. Chem. Soc.* **2002**, *124*, 12948; b) Xiong, R.-G.; You, X.-Z.; Abrahams, B. F.; Xue, Z.-L.; Che, C.-M. *Angew. Chem., Int. Ed.* **2001**, *40*, 4422; c) Kitagawa, S.; Kitaura, R.; Noro, S. *Angew. Chem., Int. Ed.* **2002**, *41*, 1159.
- 28 Lin, W. *Journal of Solid State* **2005**, *178*, 2486 and references therein.
- 29 Kepert, C. J.; Prior, T. J.; Rosseinsky, M. J. *J. Am. Chem. Soc.* **2000**, *122*, 5158.
- 30 a) Seo, J.S.; Whang, D.; Lee, H.; Jun, S. I.; Oh, J.; Jeon, Y. J.; Kimoon, K. *Nature* **2000**, *404*, 982; b) Evans, O. R.; Ngo, H. L.; Lin, W. *J. Am. Chem. Soc.* **2001**, *123*, 10395; c) Cui, Y.; Lee, S. J.; Lin, W. *J. Am. Chem. Soc.* **2003**, *125*, 6014; d) Hu, A.; Ngo, H. L.; Lin, W. *J. Am. Chem. Soc.* **2003**, *125*, 11490; e) Wu, C.-D.; Hu, A.; Zhang, L.; Lin, W. *J. Am. Chem. Soc.* **2005**, *127*, 8940.
- 31 Stephens, R. D. *Inorg. Synth.* **1979**, *19*, 90.
- 32 For more information, see: CEM Corporation Website: www.cem.com.
- 33 Brunner, H.; Becker, R.; Riepl, G. *Organomet.* **1984**, *3*, 1354.
- 34 Kwon, I.-C.; Kho, Y. K.; Choi, J.-H.; Kim, H.-S. *J. Heterocyclic Chem.* **1996**, *33*, 1883.
- 35 Fennell, K. A.; Miller, M. J. *Org. Lett.* **2007**, *9*, 1683.
- 36 CrysAlisCCD 1.171.31.2 (release 07-07-2006), CrysAlis171 .NET, Oxford Diffraction Ltd.
- 37 CrysAlis RED 1.171.31.2 (release 07-07-2006), CrysAlis171 .NET, Oxford Diffraction Ltd.
- 38 Altomare, A.; Burla, M. C.; Cavalli, M.; Cascarano, G. L.; Giacovazzo, C.; Guagliardi, A.; Moliterni, A. G.; Polidori, G.; Spagna, R. *J. Appl. Cryst.* **1999**, *32*, 115.
- 39 Sheldrick, G. M. *Acta Cryst.* **2008**, *A64*, 112.
- 40 Nardelli, M. *Comput. Chem.* **1983**, *7*, 95.
- 41 Farrugia, L. J. *J. Appl. Chem.* **1999**, *32*, 837.

Phosphine ligands and ruthenium(II) complexes

4.1 Overview

This chapter describes the coordination chemistry of alkynyl phosphine ligands with cyclopentadienyl ruthenium(II) moieties.¹ The chapter begins with the description of the new synthetic approach which we have developed to prepare the wished alkynyl phosphine ligands. Then, the reactivity study of these ligands have been tested with simple {CpRu} synthons to afford a variety of new supramolecular structures with interesting stereochemical features. The synthesis of metal organic macrocycles resulting in two new complexes, a dinuclear compound and a square tetranuclear complex, is finally presented. The chapter concludes with the characterisation of all the new compounds by electrochemical methods and, for the electrogenerated paramagnetic species, by ESR spectroscopy.

4.2 Introduction

Macrocyclic molecular squares, rectangles or boxes have received much attention for possible applications in “host-guest” chemistry, molecular recognition, sensing and modeling for biological systems.^{2,3} The large cavities presented into the MOMs can indeed be occupied by small guest molecules that in turn modify the chemical properties and the reactivity of the host molecule. Organometallic half-sandwich complexes of the late transition metals are versatile building blocks for supramolecular chemistry, in particular to built metallamacrocyclic receptors and coordination cages.⁴ The cyclopentadienyl or arene ruthenium(II) complexes, exemplified by $[\text{CpRuCl}(\text{PPh}_3)_2]$ and $[\{(p\text{-cymene})\text{RuCl}_2\}_2]$, are among the most stable ruthenium precursors. Complexes of this class are characterized by robust organic π -ligands, that are inert towards the substitution reactions, and by the presence of three facial coordination sites, opposite to the π -ligand, that can coordinate various donor groups. The possibility to have labile ancillary co-ligands for the three additional coordination sites of these complexes is of central importance to construct metallamacrocycles as well as coordination cages.

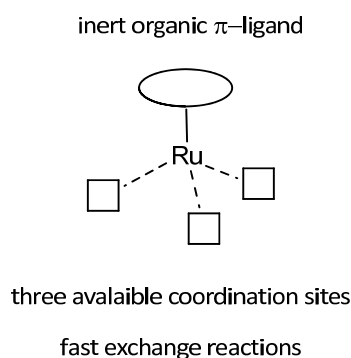


Figure 4-1. Organometallic half-sandwich complex of Ru(II). Adapted from ref 4.

Ligands with one or more phosphorus donor atoms have been widely used to obtain linear or cross-linked complexes by self-assembly of ditopic or multitopic metal units.⁵ Although the use of alkenyl and alkynylphosphines has several precedents in the coordination chemistry of a wide range of transition metals,⁶ ruthenium(II) complexes bearing these ligands are rare.⁷ Remarkably, the only complex containing a diphosphinoalkyne ligand, described in the literature by Dyson

et al.,⁸ is the linear complex $[\{(p\text{-cymene})\text{RuCl}_2\}_x(\text{dppa})]$ ($x = 1, 2$; $\text{dppa} =$ diphenylphosphinoacetylene). Aiming at expanding this chemistry, we have investigated the synthesis and structural characterisation of a family of cyclopentadienyl ruthenium(II) complexes with the bi- and tridentate phosphines 1,4-bis[(diphenylphosphino)ethynyl]benzene (dppab, **1**) and 1,3,5-tris[(diphenylphosphino)ethynyl]benzene (tppab, **2**, Figure 4-2).

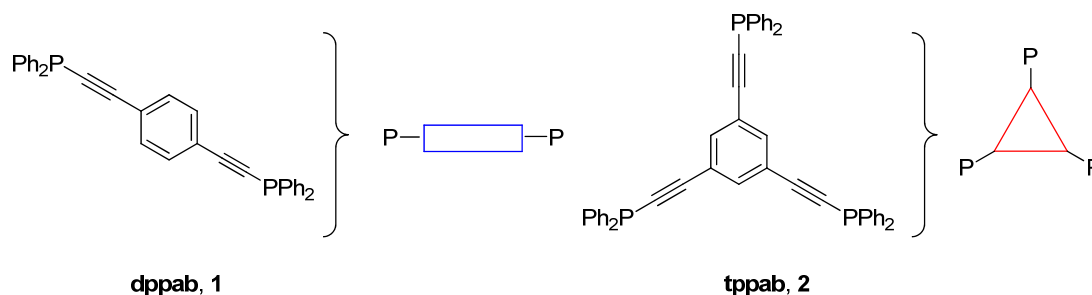


Figure 4-2. Structural formulas and sketches of the bidentate and tridentate alkynylphosphines.

Our choice to concentrate our efforts to the alkynylphosphines dppab and tppab was dictated by the ligands rigidity that could help to spontaneously assemble large macrocyclic systems instead of discrete complexes due to the larger spatial requirements of such phosphine in comparison to Dyson's dppa which contains a mere acetylene as a spacer.⁹ In addition, the presence of two linearly arranged C-C triple bonds and conjugated with an aromatic ring could favour an effective electronic communication between the two metal centres held together by the alkynylphosphino bridge, while assuring a larger separation of the metal ions.

Applying metal-directed self-assembly methodologies, we obtained two linear bimetallic complexes $[\{\text{CpRuCl}(\text{PPh}_3)\}_2(\mu\text{-dppab})]$ (**3**) and $[\{\text{CpRu}(\text{dppe})\}_2(\mu\text{-dppab})](\text{PF}_6)_2$ (**4**) as well as the trimetallic $[\{\text{CpRuCl}(\text{PPh}_3)\}_3(\mu_3\text{-tppab})]$ (**5**) species [$\text{dppe} = 1,2\text{-bis}(\text{diphenylphosphino})\text{ethane}$]. Moreover, the mononuclear complex $[\text{CpRuCl}(\text{PPh}_3)(\eta^1\text{-dppab})]$ (**6**), containing a "dangling" phosphine arm, was synthesised, showing that ligand **1** may exhibit either $\mu\text{-}\eta^2\text{-}$ (end-on) or $\eta^1\text{-}$ coordination modes. Besides these open-chain complexes, the neutral cyclic species $[\text{CpRuCl}(\mu\text{-dppab})]_2$ (**7**) was also prepared, under different experimental conditions. Finally, starting from pre-assembled metal-based mono- and dinuclear moieties, mentioned above, metallamacrocycles of diverse shapes and sizes were

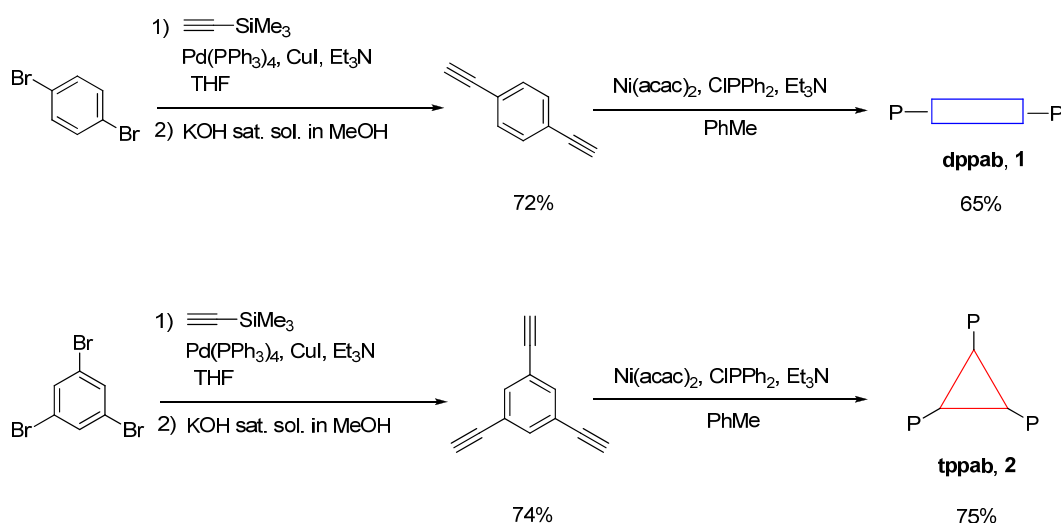
synthesized. Thus, self-assembly of the dimetal linear complex **3** with additional equivalents of dppab led to an approximately 1:1 mixture of the cyclic dimer $[\text{CpRu}(\text{PPh}_3)(\mu\text{-dppab})]_2(\text{PF}_6)_2$ (**8**) and the tetramer $[\text{CpRu}(\text{PPh}_3)(\mu\text{-dppab})]_4(\text{PF}_6)_4$ (**9**), based on *cis* ligation of the $\{\text{CpRu}(\text{PPh}_3)\}$ moiety.

All the ruthenium complexes were characterized by elemental analysis, and conventional spectroscopic methods including IR and multinuclear NMR spectroscopy and ESI-MS methods. Single-crystal X-ray diffraction analysis was carried out on selected complexes disclosing the intriguing coordination abilities of these alkynyldiphosphines. Electrochemical methods were used to characterize the redox profiles of most species and, for the electrogenerated paramagnetic species, X-band ESR spectroscopy (electron spin resonance) was used to further investigate these complexes.

4.3 Results and discussion

4.3.1 Alkynyldiphosphine ligands: synthesis and characterisation

The synthesis of the alkynyldiphosphines **1**¹⁰ and **2**^{6e} have been already reported in the literature with reaction protocols involving the use of dangerous and flammable alkynyl magnesium or alkali metal reagents. In order to eliminate the use of sodium, lithium or magnesium ethynyl reagents, we developed a new synthetic pathway which also provides better yields of both ligands (Scheme 4-1).



Scheme 4-1. Synthesis of the bidentate and tridentate ligands dppab (**1**) and tppab (**2**).

Thus, dppab (**1**) and tppab (**2**) were prepared from the corresponding terminal alkynes by Ni-catalyzed cross-coupling reaction with chlorodiphenylphosphine in the presence of NEt₃ (Scheme 4-1). Using the Sonogashira reaction of aryl bromides with trimethylsilyl acetylene, the terminal alkyne was obtained, after hydrolysis of the SiMe₃ protecting groups.

The adopted synthetic approach consists of a nucleophilic substitution at the phosphorous atom of halophosphines R₂PX,¹¹ thus representing an “*umpolung*” process alternative to the conventional reaction of secondary phosphines, R₂PH, with R-X substrates (Figure 4-3).¹²

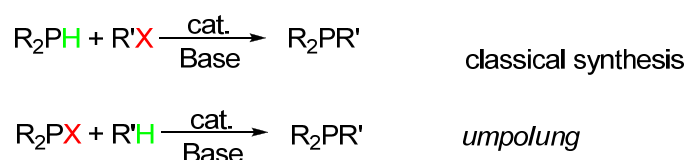


Figure 4-3. Different approaches to the synthesis of alkynyl phosphine ligands

We have also used the alternative classical synthesis of alkynyl phosphines that goes through the direct lithiation of the terminal C≡C-H bond, followed by reaction of the *in situ* generated acetylide carbanion with R₂PX.^{6e,13} The final yields of both phosphines following this methodology were always significantly lower than those achieved by the method developed by us.

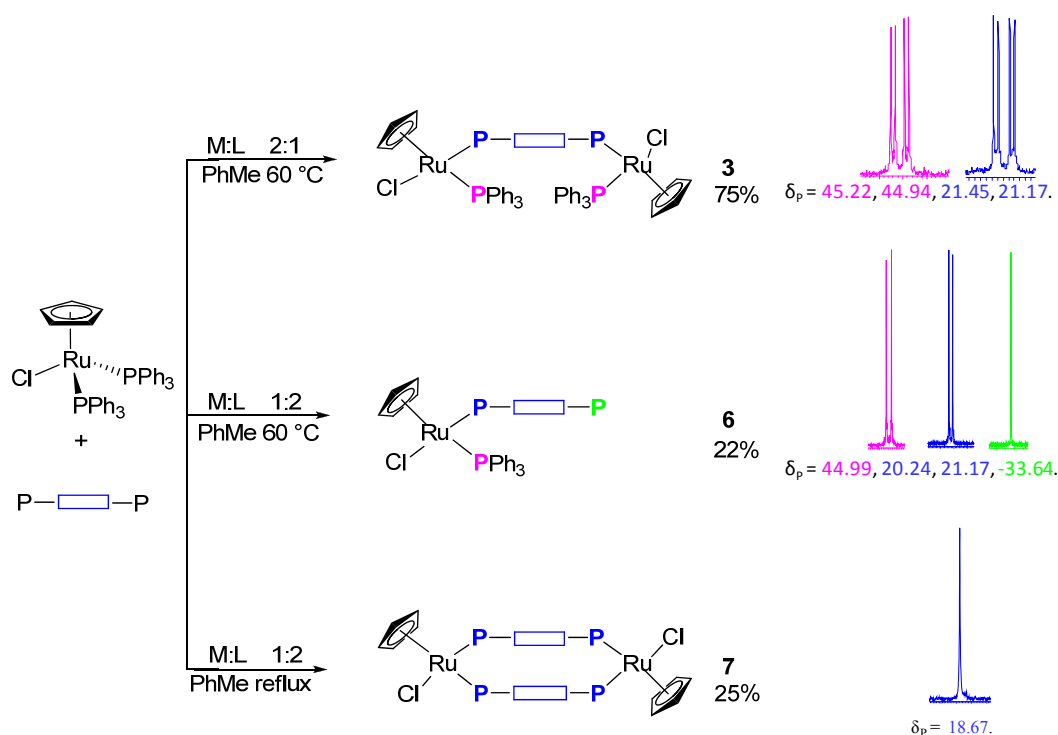
4.3.2 Neutral ruthenium complexes with dppab

In order to explore the coordination properties of the alkynylphosphines towards transition metals, the reactivity of both **1** and **2** was investigated towards a variety of Ru(II) precursors, such as [CpRu(η⁶-C₁₀H₈)]PF₆, [(η⁶-*p*-cymene)RuCl₂]₂ and [Ru(PPh₃)₃Cl₂]. In almost all the cases, mixtures of several products were formed and neither simple ³¹P-NMR identification nor isolation of pure products after workup was possible. The easy-to-make, readily available and stable Ru(II) precursor [CpRuCl(PPh₃)₂] (**10**)¹⁴ gave the best results affording single compounds or mixtures of well defined species which could be often separated after work-up. All of the new alkynylphosphino-ruthenium complexes were found to be moderately air-stable, and could be handled in the air without special precautions,

although they are better stored under nitrogen in Schlenk tubes. In keeping with their stability towards air oxidation, most of the CpRu derivatives could be purified by column chromatographic techniques which afford analytically pure microcrystalline materials.

Replacement of either the chloride or the PPh₃ ligand from the coordination sphere of the {CpRu} moiety is mandatory to create the coordination vacancy where the alkynylphosphine may bind the metal. As far as the exchange of phosphine in precursor **10** is concerned, the substitution may be easily achieved by the straightforward reaction of **10** with dppab at high temperature in high boiling apolar solvents such as benzene or toluene. Halide abstraction may in turn easily be obtained using TlPF₆ in the presence of the alkynyl diphosphine. The control of the reaction temperature and the metal-to-ligand molar ratio were also particularly important to drive the reaction towards the formation of a certain product.

In a first experiment aimed at synthesizing coordination complexes with double coordination of the dialkynylphosphine the biphosphine **1**, was reacted in a 2:1 M:L ratio at 60 °C in purified toluene. Monitoring the reaction by ³¹P{¹H} NMR spectroscopy was extremely helpful in understanding which products are formed and therefore to strictly define the optimised reaction time to target the formation of a certain derivative. Thus inspection of the reaction by ³¹P{¹H} NMR allowed us to observe the immediate formation of the bimetallic complex **3**, which could be isolated and purified in excellent yield as an orange microcrystalline powder after chromatographic work up (Scheme 4-2). Remarkably, complex **3** presents two Ru stereogenic centres due to the presence of four different substituents on a distorted piano stool coordination polyhedron. In keeping with such stereochemical arrangement, two pairs of 1:1 doublets can be observed in the ³¹P{¹H} NMR spectrum of **3**.¹⁵ Correspondingly, the ¹H NMR spectrum shows two distinct and partially overlapped resonances in the Cp region, thus confirming the formation of a pair of enantiomers (*R*_{Ru}*R*_{Ru} and *S*_{Ru}*S*_{Ru}) together with the *meso* form (*R*_{Ru}*S*_{Ru} and *S*_{Ru}*R*_{Ru}). The absence of any dynamic process which could have been expected from a pair of equilibrating rotamers was easily ruled out. Indeed, when an acetonitrile-*d*₃ solution of **3** was warmed to 80 °C (NMR tube test), no significant change in the intensity ratio of the two pairs of doublets was observed.

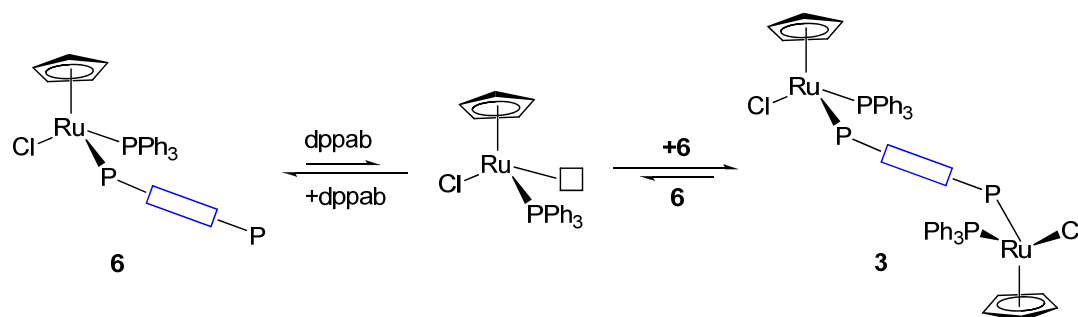


Scheme 4-2. Synthesis of ruthenium dppab complexes **3**, **6** and **7**. The P atom colour-code refers to the related $^{31}\text{P}\{^1\text{H}\}$ NMR signals shown on the right side of the Scheme.

The simultaneous presence of two stereogenic metal atoms in a dinuclear complex has not many precedents,^{16,17} while chiral (*carbon*) centres are normally located on the ligand backbone. Attempts to separate the diastereomeric mixture *via* chromatographic methods (dichloromethane: acetone 20:1) were carried out without success, due to the practically identical R_f values of the two diastereoisomers.

When the reaction was repeated using an 1:2 M:L ratio, an equilibrium mixture between the species **6**, **3**, **1** was observed. Among these products, the main one in the reaction crude was complex **6** containing a dangling uncoordinated diphosphine arm. Work-up of the reaction solution allowed to obtain a pure sample of **6**, but the isolated yield, never exceeding 22%, was quite low, likely in agreement with the participation of **6** in a room temperature equilibrium affording the dinuclear complex **3**. The latter, may indeed be generated via dppab dissociation from **6** followed by reaction of the coordinatively unsaturated $\{\text{CpRuCl}(\text{PPh}_3)\}$ fragment with a second equivalent of **6** (Scheme 4-3). Notably, the ligand redistribution $(\mathbf{6}) + (\mathbf{6}) \rightleftharpoons (\mathbf{1}) + (\mathbf{3})$ in solution did not allow to run exhaustive and

reliable ESI-MS data for **6**. The $^{31}\text{P}\{^1\text{H}\}$ NMR spectroscopy also confirms the existence of the dynamic process showing that as the signals belonging to **6** decrease, those ascribable to free **1** and complex **3** grow in parallel. Recently, Dyson *et al.* observed a similar behaviour for the Ru(II) complex $[(\eta^6\text{-}p\text{-cymene})\text{RuCl}_2(\eta^1\text{-dppa})]$ which also contains a bridging bidentate phosphine.⁸



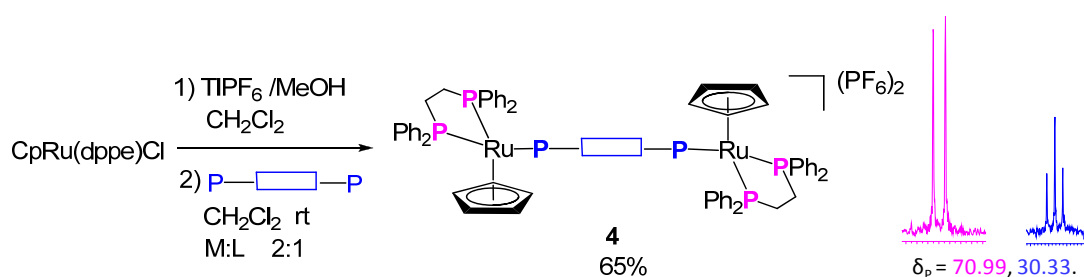
Scheme 4-3. Proposed mechanism for the $(\mathbf{6}) + (\mathbf{6}) \rightleftharpoons (\mathbf{1}) + (\mathbf{3})$ reaction.

The stable thermodynamic product was the diruthenamacrocycle **7** which forms when the reaction is carried out using an 1:2 ratio between $[\text{CpRu}(\text{PPh}_3)_2\text{Cl}]$ and **1**, in toluene at reflux. Probably, the driving force transforming **6** into **7** is the total replacement of the triphenylphosphine ligand in **6** *via* intermolecular thermal exchange with the pending PPh_2 end of a second equivalent of the same ruthenium complex to afford the complex **7**. The absence of chirality at Ru depends on the presence of two identical phosphine ligands, as shown by the presence of a singlet resonance in the $^{31}\text{P}\{^1\text{H}\}$ NMR spectrum ($\delta = 18.67$). Complex **7** belongs to the class of diruthenium complexes in which two $\{\text{CpRuL}\}$ moieties ($\text{L} = \sigma\text{-donor ligand}$) are held together by a pair of bidentate ligands.^{17,18}

4.3.3 Cationic ruthenium complexes with dppab

In order to favour the formation of either cationic linear complexes or macrocyclic species, we explored the reactivity of alkynylphosphine towards the ruthenium precursor after removal of the chloride ligand in $\{\text{CpRuCl}\}$ species during the reaction. This interesting possibility was firstly explored using the known precursor $[\text{CpRuCl}(\text{dppe})]$ (**11**) which contains the chelating ancillary diphosphine 1,2-bis(diphenylphosphino)ethane, dppe, instead of two monodentate phosphines

such as PPh_3 . In the presence of TIPF_6 as effective halide scavenger, in $\text{CH}_2\text{Cl}_2/\text{MeOH}$ at rt, a 2:1 M:L solution afforded, as expected, the bridged product **4** in quantitative NMR yield (Scheme 4-4). Complex **4** contains a bridging dppab ligand which held together two $\{\text{CpRu}(\text{dppe})\}$ cations providing a structural motif similar to complex **3**. The real difference between the two complexes is, apart from the cationic vs neutral nature, the lack of stereogenicity at the metal centres due to the presence of a pair of dppe chelating ligands.

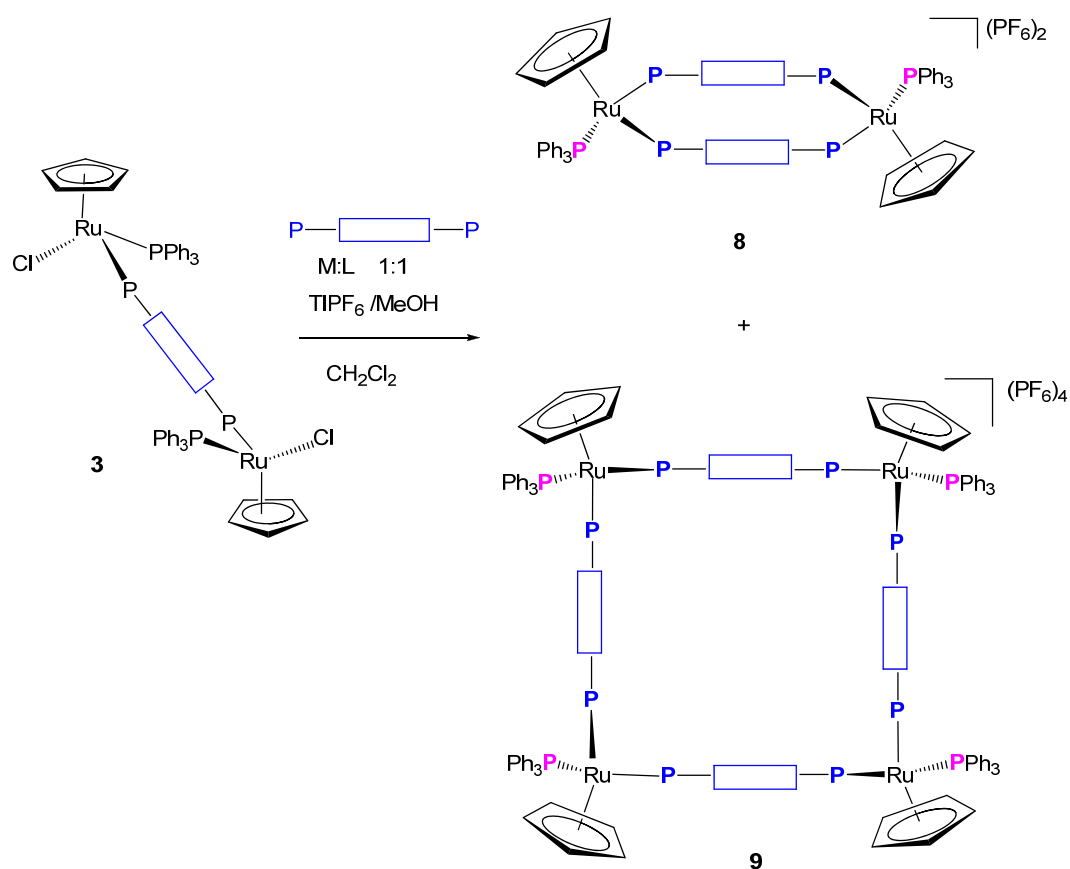


Scheme 4-4. Synthesis of the dinuclear complex **4**. The P atom colour-code refers to the related $^{31}\text{P}\{^1\text{H}\}$ NMR signals shown on the right side of the Scheme.

The addition of TIPF_6 to a solution of **3** in the presence of an additional equivalent of dppab is an efficient way to grow polynuclear macrocyclic complexes using an 1:1 M:L ratio. Thus, the removal of the chloride ligand from a dichloromethane solution **3** with TIPF_6 must be done in the presence of dppab; otherwise the reaction afforded a mixture of unidentifiable products. After filtering out solid TiCl_4 , a dark orange powder was obtained, consisting of an approximate 1:1 mixture of complexes **8** and **9** which were assigned as dinuclear $(\text{M}_2\text{L}_2)^{2+}$ and tetranuclear $(\text{M}_4\text{L}_4)^{4+}$ species, respectively (Scheme 4-5).

The formation of discrete macrocycles of formula $[\text{cyclo-}\{\text{CpRu}(\text{PPh}_3)(\mu, \eta^{1:1}\text{-dppab})\}_n]$ ($n = 2, 4$) was favoured with respect to open-chain metallorganic polymers $[\{\text{CpRu}(\text{PPh}_3)(\mu, \eta^{1:1}\text{-dppab})\}]_\infty$, due to enthalpic effects.¹⁹ The enthalpic preference for the cyclic structure with respect to the linear one may be explained from the higher bond energy due to the increased number of M-L bonds per complex subunit. For example, the cyclic tetramer $[\text{CpRu}(\text{PPh}_3)(\mu\text{-dppab})]_4(\text{PF}_6)_4$ contains two metal-phosphorus bonds per each $\text{Ru}(\mu\text{-dppab})$ subunit while the corresponding linear tetraruthenium chain has only 1.75 ruthenium-phosphorus

bonds per Ru(μ -dppab) subunit. In turn, entropic factors would favour the formation of small cycles over larger ones.



Scheme 4-5. Synthesis of complexes **8** and **9**.

However, the observed 1:1 ratio between **8** and **9** may find explanation from the rigidity of dppab and the L-Ru-L bond angle at nearly 90° (95.53° for **8**, see below), which would lead to the thermodynamically most stable square arrangement featured by **9**. A similar behaviour has been observed for a family of Re-Pd polymetallamacrocycles by Rheingold *et al.*³ Complexes **8** and **9** were separated by fractional crystallization from a diluted dichloromethane/*n*-hexane solution from which analytically pure samples of **8** and **9** were then obtained as dark orange and yellow microcrystals, respectively. The proposed formulas were unambiguously confirmed by a combination of chemico-physical data (elemental analysis, molar conductivity in solution, high-resolution mass spectral analysis and multinuclear NMR spectroscopy). Particularly, the ³¹P{¹H} NMR spectra provide confirmatory evidence for the coordination of two different dppab ligands to each

{CpRu(PPh₃)} moiety showing two practically superimposed AM₂ spin systems which (top trace in Figure 4-4). Thus, **8** exhibited a high-frequency triplet ($\delta_p = 38.95$) and a lower frequency doublet ($\delta_p = 20.26$) with ${}^2J_{p,p} = 37.5$ Hz). In contrast, the tetramer **9** showed a doublet at 23.88 ppm and a slightly highfield shifted triplet ($\delta_p = 39.23$) (${}^2J_{p,p} = 38.5$ Hz), in accordance with the proposed structures (Scheme 4-5).

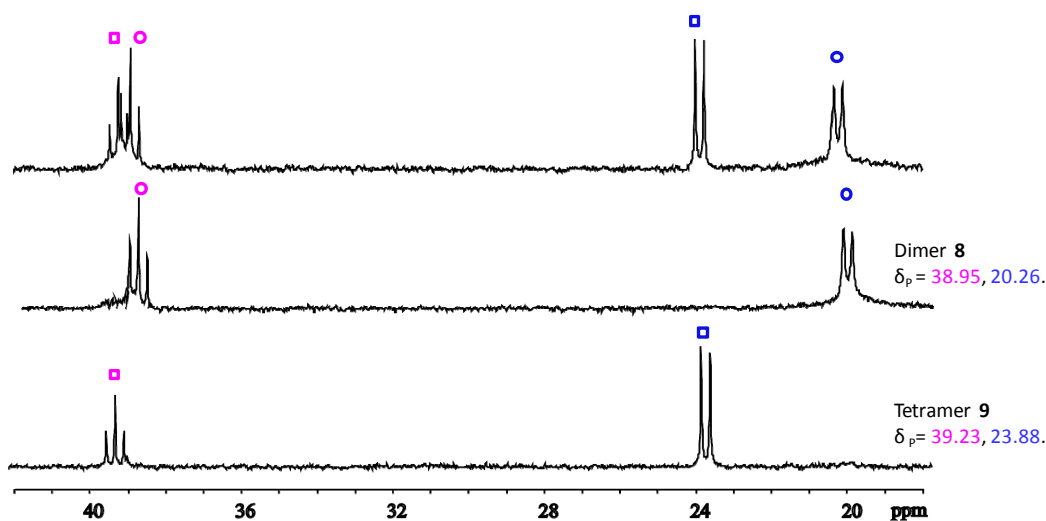


Figure 4-4. ${}^{31}\text{P}\{^1\text{H}\}$ NMR (CD_2Cl_2) spectrum of the crude reaction mixture **6**/TIPF₆/dppab consisting of **8** and **9** (top) and the AM₂ patterns due to the isolated complexes (**8**, middle; **9**, bottom).

To assess the dimeric vs. tetrameric nature of **8** and **9**, respectively, high resolution ESI-MS spectra of the two complexes were collected. Figure 4-5 (a) shows a mass spectrum portion of the mixture of **8** and **9**. The signal at $m/z = 1991.3$ corresponds at the $(\text{M}-2\text{PF}_6)^{2+}$ peak of the tetraruthenamacrocycle **9** with $Z = 2$, and also at the $(\text{M}-\text{PF}_6)^+$ peak of the dimetallic complex **8** with $Z = 1$, in agreement with the expected isotopic pattern of ruthenium fragment. Experimental isotopic pattern well matches the calculated values (b and c in Figure 4-5), thus validating the di- and tetranuclear nature of these interesting ruthenamacrocycles.

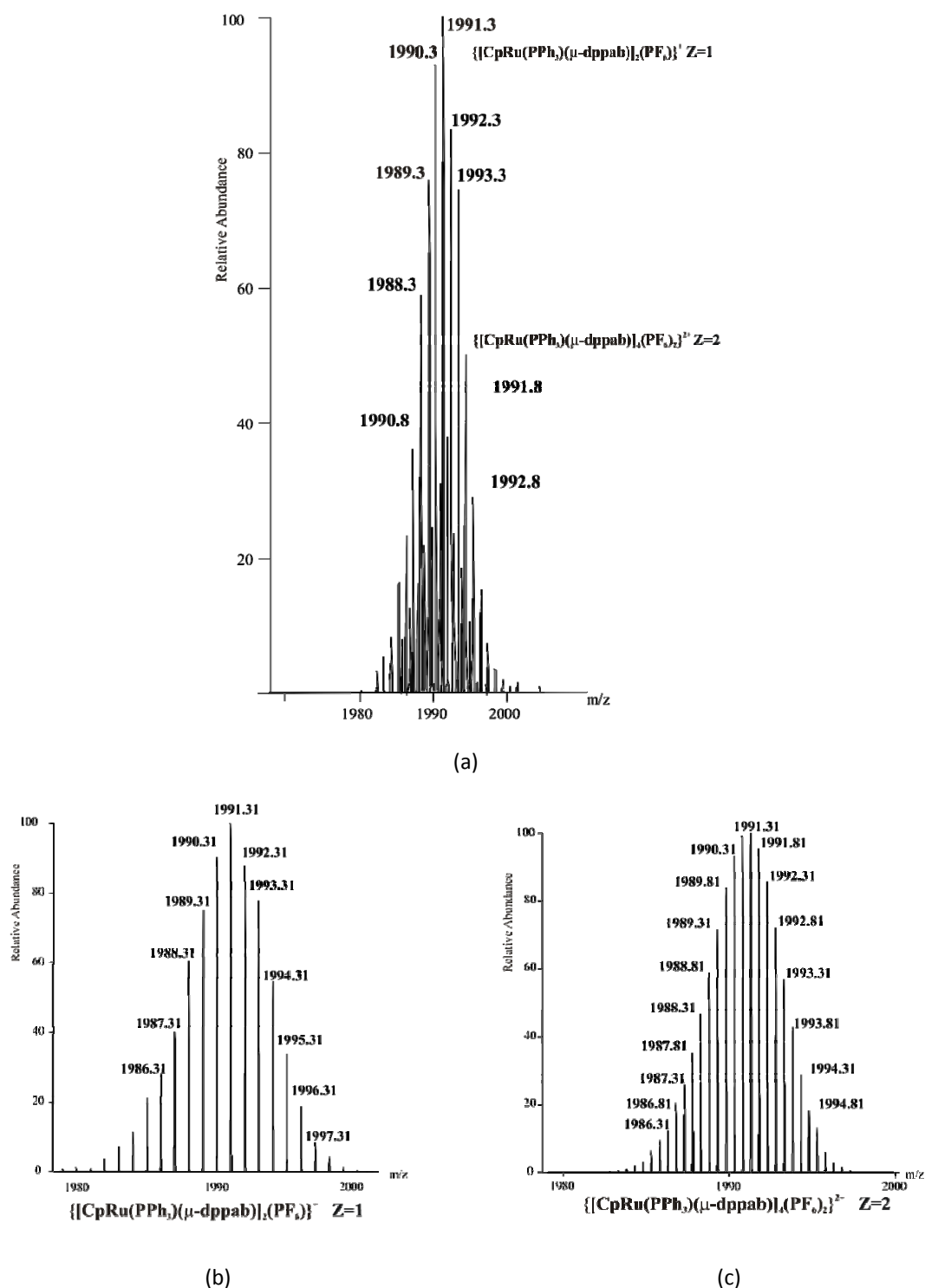


Figure 4-5. Selected region of experimental (a) and the calculated ESI-MS spectra (b and c) belonging to a solution of **8** and **9** (ca. 1:1 ratio by $^{31}\text{P}\{^1\text{H}\}$ NMR).

To verify whether dynamic processes could account for the interconversion of **9** into **8**, $^{31}\text{P}\{^1\text{H}\}$ NMR spectra of these species in CD_3CN were registered at different temperatures. In an NMR-tube test experiment an acetonitrile- d_3 solution of **8** was heated to 80 °C without showing no transformation to **8**. This experiment clearly

points out that **9** does not form via intermolecular aggregation of two dinuclear dications **8**. Similarly, the $^{31}\text{P}\{^1\text{H}\}$ NMR spectrum of a CD_3CN solution of the tetramer **9** did not change on increasing the temperature in the working window of CD_3CN , from 20 to 80 °C.

Although no definitive mechanistic picture can be traced out at the present time, the NMR high-temperature behaviour of both **8** and **9** is mechanistically intriguing as it confirms that does not exist any interconversion to each other. Consequently, the two macrocycles should be assembled through different reaction pathways. Remarkably, the observed behaviour markedly diverge from that reported by Navarro and *co-workers* who proposed a temperature dependent ring contraction for the related tetraruthenium macrocycle $[(\eta^6\text{-}p\text{-cymene})_4\text{Ru}_4(\mu\text{-}4,7\text{-phen-N}^4, \text{N}^7)_2(\mu\text{-OH})_4](\text{NO}_3)_4$ bearing a bridging phenanthroline ligand.²⁰

4.3.4 Crystallographic studies²¹

Single crystals of **7** and **8** were grown by slow evaporation of diluted $\text{C}_2\text{H}_4\text{Cl}_2/\text{EtOH}$ solutions. Selected bond lengths (°) and angles (Å) for **7** and **8** are provided in Table 4-1. A complete list of the crystallographic data are collected in the Appendix (Chapter 5).

Table 4-1. Selected bond lengths (Å) and angles (°) for ruthenium dinuclear species **7** and **8**.

7		8	
Ru1-P1	2.284(4)	Ru1-P1	2.325(2)
Ru1-P2	2.309(4)	Ru1-P3	2.333(2)
Ru1-Cl1	2.420(5)	Ru1-P2	2.3595(19)
Ru2-P3	2.293(5)		
Ru2-P4	2.270(5)		
Ru2-Cl2	2.444(4)		
P1-Ru1-P2	93.98(14)	P1-Ru1-P3	95.44(7)
P1-Ru1-Cl1	92.2(2)	P1-Ru1-P2	96.98(7)
P2-Ru1-Cl1	96.48(16)	P3-Ru1-P2	94.59(7)
P3-Ru2-P4	93.65(18)		
P3-Ru2-Cl2	95.57(15)		
P4-Ru2-Cl2	91.63(17)		

Figure 4-6 provided a view (balls and sticks) of the crystallographically authenticated dimers and gives the opportunity to compare the structure of the two dinuclear species. The two presented views are drawn perpendicularly to the

central benzene rings (left side) and along the metal-metal vector (right side). While the asymmetric unit of **7** consists of a single neutral molecule, that of **8** consists of half of the dinuclear dicationic dimer of $[\{\text{CpRu}(\text{PPh}_3)(\mu,\eta^{1:1}\text{-dppab})\}_2]^{2+}$. In the latter complex one PF_6^- anion and four 1,2 dichloroethane solvent molecules complete the asymmetric unit. No clathrated solvent molecule has been found for the neutral dimer **7**.

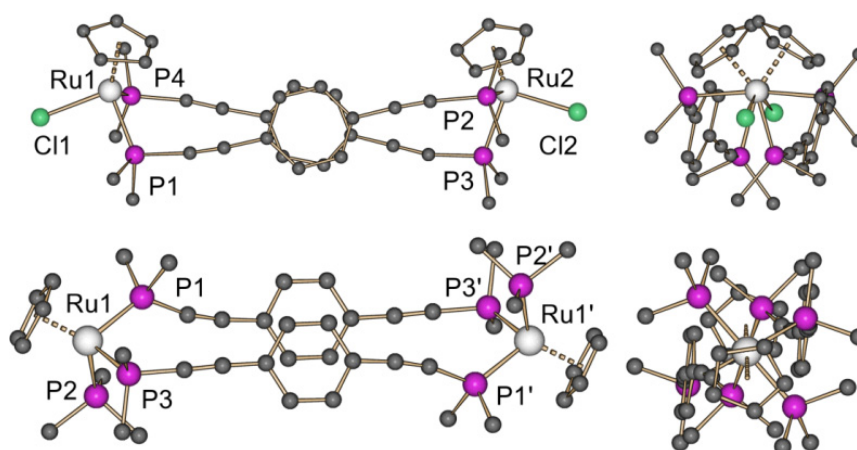


Figure 4-6. Ball and stick diagrams of dimer **7** (top) and **8** (bottom). Two views are shown. On the left, the molecules are perpendicular to the benzene rings of the dppab ligands in order to show π - π stacking. On the right, the complexes are viewed along the metal-metal line. The hydrogen atoms, the carbon atoms of the PPh_3 ligand (except for the C_{ipso} carbons), the PF_6^- anions and the 1,2 dichloroethane solvent molecules are omitted for clarity.

The two compounds share a similar coordination polyhedron around ruthenium with the metal atom octahedrally coordinated by two *cis* disposed phosphorus atoms belonging to two different dppab ligands. A Cp ring η^5 -coordinated to the metal and sitting over three contiguous coordination sites and a chlorine atom (**7**) or a triphenylphosphine ligand (**8**), respectively, complete the coordination octahedron. The separation of the two ruthenium atoms Ru1 and Ru2 in the neutral complex **7** is 12.74 Å with the dinuclear structure supported by two bridging dppab ligands. A larger intermetallic separation figures out complex **8** with the two ruthenium atoms lying apart 14.83 Å to each other. Related diruthenium species are practically missing which makes impossible any crystallographic comparison of the metrical parameters. However, it is worth mentioning that the metal separation in **7** is in the order of that found by Manners *et al.* for the dppab

square planar dipalladium derivatives $[\text{Pd}_2(\text{dppab})]_2$ and $[\text{Pt}_2(\text{dppab})]_2$ ($d_{\text{Pd-Pd}} = 11.66$ and 11.67 \AA , respectively).²²

The Ru-P bond distances in the doubly charged cation **8** are also comparable with the Ru-P(PPh_3) separation [$d_{\text{Ru1-P2}} = 2.3595(19) \text{ \AA}$] slightly longer than the other Ru-P bond length involving the dppab ligand [$d_{\text{Ru1-P1}} = 2.325(2)$, $d_{\text{Ru1-P3}} = 2.333(2) \text{ \AA}$]. Due to the presence of two positive charges in the dinuclear structure of **7**, the Ru-P(dppab) bond lengths in **8** are slightly longer than those found in the neutral dimer **7** [$d_{\text{Ru1-P1}} = 2.284(4)$, $d_{\text{Ru1-P2}} = 2.309(4)$, $d_{\text{Ru2-P3}} = 2.293(5)$ and $d_{\text{Ru2-P4}} = 2.270(5) \text{ \AA}$]. Likewise, the Ru-Cp_{centroid} distance is shorter in **7** [$1.863(2)$, $1.865(2) \text{ \AA}$] than in **8** [$1.881(3) \text{ \AA}$].

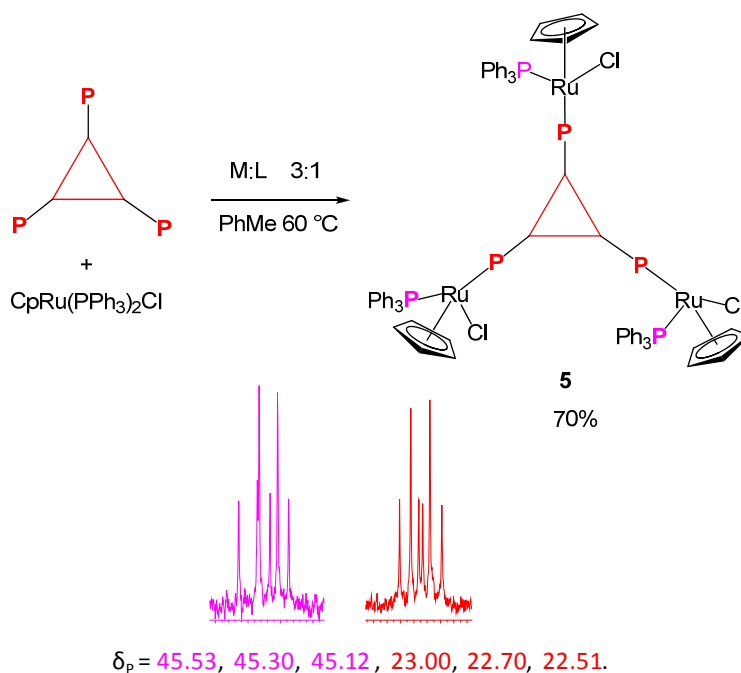
A meaningful change in the two structures concerns the central benzene rings of the two dppab molecules. The aromatic units are indeed perfectly stacked in an eclipsed conformation in **7**, but not in **8** where a staggered disposition is observed. The arene centroids are set apart by $3.629(3) \text{ \AA}$ in **7** and $3.398(2) \text{ \AA}$ in **8**, which points out a more close contact of the aryl rings in our complexes than in the Pd and Pt Manners' dimers, $[\text{Pd}_2(\text{dppab})]_2$ and $[\text{Pt}_2(\text{dppab})]_2$, where the separation between the phenyl rings of the dppab ligands are 5.814 \AA and 5.772 \AA , respectively.

An helical arrangement is evident for the two dppab ligands in **7** with the two helices rolled-up and slightly stretched and the two dppab aromatic rings almost laying one over the other. In contrast, the two dppab ligands are almost parallel to each other in **8** with the aryl groups slightly slipped. The same structural motif was found in the platinum and palladium dimers. Furthermore, the two chlorine atoms coordinated to Ru in **7** are mutually rotated [$\text{Cl1-Ru1-Ru2-Cl2} = -60.7(6)^\circ$] while in **8** the presence of a crystallographically active inversion centre relates the two terminal PPh_3 ligands. The overall conformation of **7** is similar to that determined in $[\{\text{Cp}^*_2\text{Mo}_2(\text{dppdfb})\}_2]$ ²³ ($\text{Cp}^* = (\text{pentamethyl-cyclopentadienyl})$; $\text{dppdfb} = \mu^2\text{-1,4-bis(diphenylphosphino)-2,5-difluorobenzene}$) which exhibits a similar separation of the aryl centroids (3.604 \AA) and a similar rolled-up disposition of the bridging ligands. As a final consideration, it is likely that any difference in the structure adopted by **7** and **8** is mostly associated to external supramolecular forces rather than the ligand conformation.²⁴

4.3.5 Coordination chemistry of tppab towards [CpRuCl(PPh₃)₂]

The coordination chemistry of the tridentate ligand tppab towards {CpRu} fragments was also briefly investigated. In toluene at 60 °C, tppab gave the trimetallic species **5** upon reaction of **10** with **2** in an 3:1 M:L ratio.

Scheme 4-6 shows the ³¹P{¹H} NMR spectrum of **5** displaying three sets of AM patterns, which do not correspond to the (two) expected sets of signals deriving from a symmetric system containing a C₃ axis. This is a consequence of the presence of two non-equivalent ligand dispositions around the Ru centres, that causes the concomitant loss of the C₃ symmetry. If the two stereochemically different Ru atoms are present in a 2:1 ratio, the resulting complex still possesses a symmetry plane, giving three sets of signals on the ³¹P-NMR (two diastereoisomers and a *meso* form). To the best of our knowledge, complex **5** is the first example of a ruthenium complex containing three different stereogenic centers with chirality on the metal atom. Generally, the chirality in chiral trinuclear metal complexes known is associated with the presence of chiral or atropisomeric ligands.²⁵ Further studies on the characterization and the reactivity of this trinuclear complex are planned in our laboratory.



Scheme 4-6. Synthesis of complex **5**. The P atom colour-code refers to the related ³¹P{¹H} NMR signals shown in the Scheme (bottom).

4.3.6 Electrochemistry and spectroelectrochemistry²⁶

The electrochemical behaviour of some of the most representative ruthenium complexes described above was investigated. These studies have dealt with the mononuclear chloro complex **10**, the dinuclear species **3** and **7** and the trinuclear tppab derivative **5**. All the investigated ruthenium compounds display a substantially identical redox profile in cyclic voltammetry which is exemplified for complex **3** in Figure 4-7 showing its cyclic voltammetric behaviour in dichloromethane.

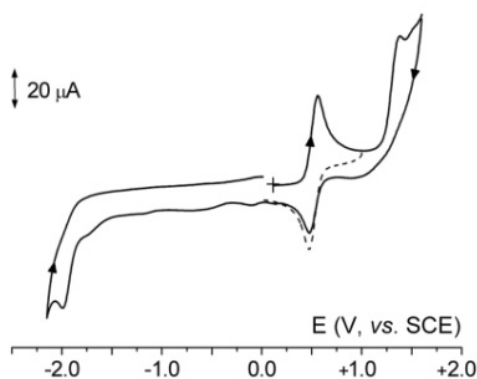


Figure 4-7. Cyclic voltammogram recorded at a platinum electrode in CH_2Cl_2 of **3** ($0.8 \times 10^{-3} \text{ mol dm}^{-3}$). $[\text{NBu}_4][\text{PF}_6]$ (0.2 mol dm^{-3}) supporting electrolyte. Scan rate 0.2 V s^{-1} .

The diruthenium complex undergoes an oxidation process at $E^{\circ'} = +0.52 \text{ V}$, which features chemical and electrochemical reversibility in the time scale proper of cyclic voltammetry. This first oxidation step is followed by a further irreversible oxidation which is almost overlapping with the wave due to the solvent discharge. At very negative potential values, an irreversible reduction is also evident. Controlled potential coulometry set at the potential of the first anodic process ($E_w = +0.9 \text{ V}$) indicated that two electrons per molecule are consumed with turning of the starting yellow colour to reddish orange. The cyclic voltammetry of this electrolysed solution is quite complementary to the original one, thus confirming the stability of the dication $\mathbf{3}^{2+}$ also during the long times requested to carry out the macroelectrolysis.

A qualitative similar redox behaviour may be easily recognised for the mononuclear complex **10**, the dinuclear derivative **7** and the trinuclear complex **5**,

resulting in all cases in the electrochemical formation of the high stable cations **10**⁺, **7**²⁺ and **5**³⁺.

The electrode potentials of the pertinent redox changes are summarized in Table 4-2. Both first oxidation and reduction steps can be assumed as metal-based processes. Such an assumption is also corroborated by a careful comparison with the redox behaviour of the well studied benzene ruthenium half-sandwich complexes [(C₆H₆)RuCl₂(PR₃)].²⁷

Table 4-2. Formal electrode potentials (V vs. SCE) and peak-to-peak separations (mV) for the redox changes exhibited by selected dppab and tppab ruthenium complexes in CH₂Cl₂ solution.

Compound	oxidation			reduction
	E _p ^{a,b}	E ^{o'}	ΔE _p ^b	E _p ^{a,b}
1	+1.4			
10	+1.5	+0.48	110	
3	+1.4	+0.52 ^c	80	-2.0
7	+1.5	+0.50 ^c	80	-2.0
5	+1.4	+0.57 ^d	85	-2.0
8	+1.5	+0.50 ^c	100	-1.7 ^b

(a) Peak potential value for irreversible processes; (b) measured at 0.2 V s⁻¹; (c) two-electron process; (d) three-electron process.

A charge-localised Robin-Day class I electrochemical behaviour may be safely attributed to the mixed-valent ruthenium cations, because the metal oxidation in derivatives **3**, **7** and **5** is occurring as.²⁸ The spectroelectrochemical experiments are in agreement with such an assignment (see below).

On the opposite electrochemical process, dealing with the irreversible reduction of **3**, **7** and **5**, we may recall a recent study on the similar complex [(η⁵-ind)RuCl(PPh₃)₂] (ind = indenyl, C₉H₇⁻) which gives confirmatory evidence of the instability of the electrogenerated 19-electron species and that the chloride atom is rapidly decoordinated.²⁹ Thus, it was obvious to hypothesise that a similar decoordination could take place also in the case at hand. As a final comment, a comparison of these electrochemical tests with the redox behaviour of the free dppab ligand (**1**) suggests that the irreversible oxidation mentioned above can be plausibly ascribed to this latter species.

Replacement of the chloride ligand by a PPh_3 unit which is a prerequisite for the formation of complexes **8** and **9** causes severe poisoning of the working-electrode during the electrochemical investigation. Nonetheless, sufficiently reliable cyclic voltammograms have been obtained for **8** at a gold electrode with a good estimation of its redox potential values. As reported in Table 4-1, also in this case both the Ru(II)/Ru(III) electrochemical process and the dppab oxidation do not differ with respect to the chloro derivative **7**, while the cathodic process moves to a less negative value. The need for repeated, lengthy and tedious electrode cleaning procedures after each cycle forced us to do not carry out further measurements on this compound.

Due to the electrode poisoning, no reliable cyclic voltammogram of the tetramer **9** could be obtained either working with at gold or a platinum electrode, except for the constant appearance of severe adsorption processes around -0.5 V. In consequence of this fact, we decided to use an ITO working electrode, which presents a much larger electrode area (in the order of cm^2 vs. mm^2). As a result of this experimental modification, the growth of a film was recorded (Figure 4-8).

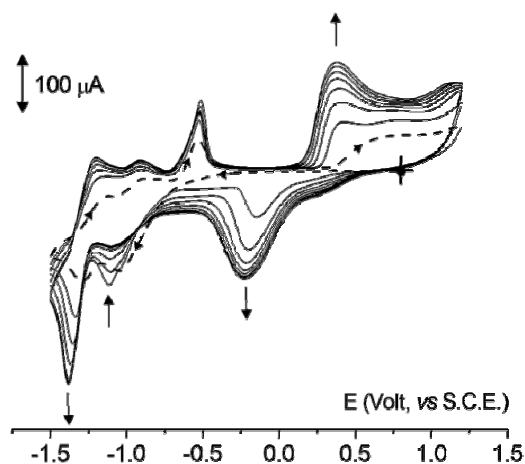


Figure 4-8. Electrodeposition of a film at an ITO electrode in CH_2Cl_2 solution of **9** ($0.1 \times 10^{-3} \text{ mol dm}^{-3}$). $[\text{NBu}_4][\text{PF}_6]$ (0.2 mol dm^{-3}) supporting electrolyte. Scan rate 0.05 Vs^{-1} . (---) Return profile of the first cycle. • Starting potential.

The observed electrochemical processes show only a negligible correspondence with the parent dinuclear derivative **8**: in fact, there is an oxidation process, with features of electrochemical *quasi*-reversibility ($E_{\text{pa}} = +0.38 \text{ V}$, $E_{\text{pc}} = -0.23 \text{ V}$), which could correspond to the Ru(II)/Ru(III) redox change, while the

reduction at -1.4 V, which triggers the film deposition, corresponds to an unidentified redox process. It is generally assumed that 19-electron organometallic centres undergo structural reorganization following the loss of one ligand.²⁹ The nature of the film grown onto the ITO electrode is still unknown and will be the subject of future work.

The spectroelectrochemical analysis in an OTTLE cell allowed us to further confirm the valence-localised nature of the mixed-valent species featuring the electron transfer processes of **3**, **7** and **5**. Our efforts were directed mainly to check for the appearance of an intervalence transition (IT) band that would eventually contrast the Robin-Day classification suggested by cyclic voltammetry. All the UV/vis spectral data pertaining to the studied complexes are shown in Table 4-3.

Table 4-3. Electronic spectral data for complexes **10**, **3**, **7**, **5** and their electrogenerated cations [OTTLE cell, THF / $[\text{NBu}_4][\text{PF}_6]$ (0.2 mol dm^{-3}) solution].

Compound	λ (nm)
10	354, 440 ^a
10 ⁺	345, 383, 532, 1250
3	371
3 ²⁺	388, 550, 1183
7	355
7 ²⁺	378, 535, 1116
5	361
5 ³⁺	388, 540, 1170

(a) shoulder

Irrespective of the investigated species, a general pattern is observed: the spectrum of the neutral complexes is dominated by an intense band in the high energy region, which can be reasonably ascribed to a metal-to-ligand charge transfer. This band is slightly affected by the oxidation in that, in the spectrum of the cations, two new bands appear at $532\div 550$ nm (weak) and at $1116\div 1250$ nm (very weak), which can be both ascribed to a Ru(III) d-d electron transfer. In agreement with the electrochemical results, also the UV/vis spectra of the Cl-containing compounds are very similar to the mononuclear parent complex **10**, in line with the spectral changes observed throughout the oxidation. Remarkably, the

spectra of the bi- and trinuclear compounds change monotonically along with the subsequent electron removals. This would support the localised nature of the mixed-valent species. Moreover, no IT band has been detected in the experimental window (low energy limit = 3300 nm).

In view of the chemical stability of the various electrogenerated cations, we decided to investigate their magnetic properties by ESR analysis. Since, as discussed above, the different complexes undergo oxidation processes involving a different number of electrons *per* molecule, in all cases we drew the electrogenerated species after the removal of about 0.7 electrons/molecule.

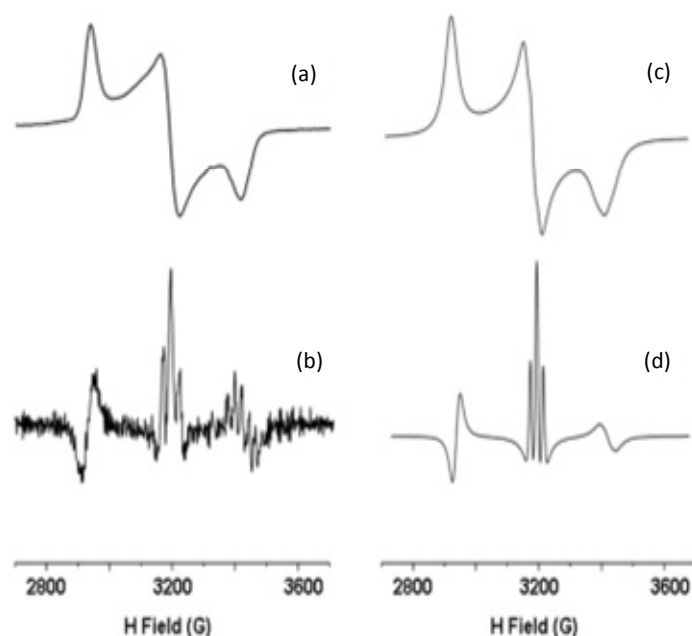


Figure 4-9. The liquid nitrogen X-band spectrum of **7** after the removal of one electron, in frozen CH_2Cl_2 solution [(a) experimental first derivative spectrum; (b) experimental second derivative spectrum; (c) and (d) simulated first and second derivative spectra, respectively].

In agreement with the formation of low-spin Ru(III) complex cations, the EPR absorption pattern is typical of one-electron paramagnetic species, with magnetic features (g_i , a_i , ΔH_i) characterized by large anisotropies.^{30 31} The computed lineshape analysis³² can be suitably carried out assuming the following $S = 1/2$ Electron Spin Hamiltonian $H = \beta \cdot H \cdot g \cdot S + \sum_i I_i \cdot a_i \cdot S$, which accounts for the actual well resolved rhombic spectral symmetry ($\beta \cdot H \cdot g \cdot S$ = electron spin Zeeman interaction between the unpaired electron and the applied magnetic field, H ; $\sum_i I_i \cdot a_i \cdot S$ = superhyperfine

coupling Hamiltonian (shpf) relevant to the sum of the magnetic interactions of the unpaired electron with the different magnetically active nuclei present in the ligand framework).³⁰ Figure 4-9 shows the frozen solution spectra (CH_2Cl_2 ; $T = 104 \text{ K}$) of complex **7** after controlled-potential one-electron removal.

On the basis of the multiple derivative approach carried out on the experimental spectra and performing the related computer simulation, there is no evidence for hyperfine (hpf) features arising from the naturally occurring isotopes Ru-99 ($I = 5/2$, natural abundance = 12.8%) and Ru-101 ($I = 5/2$, natural abundance = 19.0%).^{30,31} Such a spectral behaviour is not unusual for glassy solutions of low-spin Ru(III) compounds, in that they exhibit broad and poorly resolved (first derivative) rhombic lineshapes due to the very low ligand field symmetries experienced by the paramagnetic metal centres.³⁰ As a matter of fact, the spread of the hpf signals of the two magnetically active Ru-99 and Ru-101 nuclei (if any), joined to the effective unpaired electron delocalization on the ligand framework, does not favour a significant spectral resolution (three largely overlapping anisotropic sextuplets would be expected for the two isotopes of each ruthenium centre). Thus, no evidence for magnetic coupling of the unpaired electron with the two naturally occurring Cl-35 ($I = 3/2$, natural abundance = 75.4%) and Cl-37 ($I = 3/2$, natural abundance = 24.6%) was detected.

The appearance of the three well separated absorptions characterized by g_i values significantly diverse from that of the free electron ($g_{electron} = 2.0023$) is in agreement with the existence of low spin Ru(III) spin-orbit coupling.³⁰ Multiple derivative procedures testify to the presence of two magnetically different phosphine ligands. In fact, the g_m lineshape, particularly resolved in the underlying shpf interactions (first to third derivative mode), puts in evidence three well separated signals (theoretical relative intensity 1:2:1) characterized by slightly different linewidths and heights. Such a spectral pattern supports the presence of active ^{31}P magnetic interactions (second and third derivative modes) arising from the interaction of the unpaired electron with two nearly equivalent P nuclei. By analogy, similar spectral features are expected for the unresolved g_l and g_h regions, even if the g_h absorption is affected by the presence of a number of intense spike signals which largely superimpose the underlying phosphorus absorptions (second

derivative mode). Figure 4-9 (c) and (d) show the simulated lineshapes, performed on the basis of “mean” shpf $a(\text{P-31})$ values; accordingly, the a_l and a_h parameters are evaluated as upper limits for shpf interactions relevant to the corresponding ΔH_i as: $a_l \leq \Delta H_l$, and $a_h \leq \Delta H_h$.

The computed values for whole set of $S = 1/2$ complexes here studied are collected in Table 4-4.

Upon rising the temperature the anisotropic signal rapidly reduces, before disappearing at the glassy-fluid transition phase ($T = 120$ K). Rapidly refreezing the room temperature solution makes the rhombic spectrum to recover even if with some loss of intensity likely due to the slight instability of the complex upon contact with air.

Such a spectral behaviour holds for all the tested paramagnetic species. On the basis of the anisotropic g_i features and related $a_i(\text{P-31})$ couplings, the actual SOMO is expected to be mainly constituted by the 4d Ru(III) orbitals with important contributions arising from the 3s-3p orbitals of the two coordinating P atoms.²⁴

Table 4-4. X-band EPR spectra of the studied ruthenium complexes after one-electron removal. CH_2Cl_2 solution. Liquid nitrogen temperature ($T = 104$ K).

Complex	g_{ll}	g_m	g_h	$\langle g \rangle$	δg_{l-h}	a_l	a_m	a_h	$\langle a \rangle$	μ_{eff}
10	2.388	2.120	1.949	2.152	0.439	≤ 29	32	≤ 35	≤ 32	1.86
3	2.342	2.124	1.968	2.145	0.374	≤ 27	27	≤ 29	≤ 29	1.86
7	2.302	2.117	1.975	2.131	0.327	≤ 27	34	≤ 36	≤ 32	1.85
5	2.349	2.113	1.963	2.142	0.386	≤ 28	25	≤ 31	≤ 28	1.86

$g_i: \pm 0.008$; $a_i: \pm 1\text{G}$; $\mu_{\text{eff}}: \pm 0.01$; $\langle g \rangle = 1/3(g_l + g_m + g_h)$; $\langle a \rangle = 1/3(a_l + a_m + a_h)$; l = low field, m = medium field, h = high field; $\delta g_{l-h} = g_l - g_h$. For the cations $[\mathbf{3}]^+$, $[\mathbf{7}]^+$, $[\mathbf{6}]^+$ the a_i values refer to mean shpf values (2 nearly magnetically equivalent P-31).

In conclusion, in spite of the different molecular structures of the electrogenerated cations, the X-band multiple derivative approach performed under glassy conditions points to: (i) the presence of identical rhombic spectral symmetries as supported by similar δg_{l-h} parameters; (ii) the existence of significant Ru/³¹P magnetic interactions in the g_m and g_h regions; (iii) the absence of detectable Ru/³⁵Cl and Ru/³⁷Cl magnetic interactions. In keeping with these experimental

evidence, the related μ_{eff} parameters are quite identical and significantly higher than the spin-only value ($\mu_{\text{eff}} = 1.73 \text{ BM}$), as expected in the presence of effective nd metal orbital contributions.

4.4 Conclusions and outlook

An alternative method to that reported in the literature has been developed to synthesize the rigid alkynyl diphosphines dppab and tppab. This approach provides better yields and avoids the use of dangerous organolithium or magnesium derivatives. The coordination behaviour of the two alkynylphosphines has been then investigated towards the {CpRu} synthon using different stoichiometries and reaction conditions. As a result, mononuclear, dinuclear and tetranuclear complexes have been prepared where the alkynyl diphosphine may act as terminal or bridging ligand between two {CpRu} units. The presence of stereogenic metal centres in some of these complexes is responsible for the formation of diastereomeric pairs well discernable by NMR methods. In keeping with this behaviour, the triruthenium complex obtained by extending this chemistry to the tppab ligand, represents a rare example of trinuclear chiral-at-metal complex.

The two polycations **8** and **9** are intriguing examples of polyruthenamacycles which do not interconvert to each other at high temperature, then suggesting that different and independent reaction pathways are responsible for their formation. The dppab ligand in the dimetallic dimer may assume either a parallel or a helical conformation as shown by the single crystal X-ray diffraction studies for **7** and **8**, respectively. The central benzene rings of the two dppab diphosphines are almost perfectly aligned in **8** while in **7** they are slipped one respect the other. The preference for one or the other shape seems to be imposed by external packing forces in the solid state.

Electrochemistry, supported by spectroelectrochemistry and ESR spectroscopy studies, have shown that the investigated ruthenium complexes with dppab and tppab ligands do not show any efficient communication path between the redox active Ru centres.

4.5 Experimental section

4.5.1 Synthetic procedures

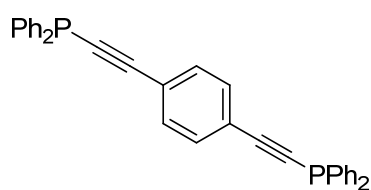
All manipulations were performed under a dry nitrogen atmosphere using vacuum-lines and standard Schlenk techniques. Dichloromethane and methanol were dried by standard methods and distilled under nitrogen before use. All the other solvents were dried and degassed by MB SPS solvent purification system (<http://solventpurifier.com/>). 1,4-diethynylbenzene,³³ 1,3,5-triethynylbenzene,³⁴ $[\text{CpRu}(\text{PPh}_3)_2\text{Cl}]^{35}$ and $[\text{CpRu}(\text{dppe})\text{Cl}]^{36}$ were prepared from literature methods. Other reagents were obtained from commercial suppliers and used without further purification. Reactions were monitored by TLC on SiO_2 ; detection was made using a KMnO_4 basic solution. Flash column chromatography was performed using glass columns (10-50 mm wide) and SiO_2 (230-400 mesh).

Deuterated solvents for routine NMR measurements were dried over molecular sieves. ^1H and $^{13}\text{C}\{^1\text{H}\}$ NMR spectra were recorded on Bruker Avance DRX-300 spectrometer (operating at 300.1 (^1H) and 75.5 (^{13}C) MHz) and a Bruker DRX-400 instrument (operating at 400.1 (^1H), 100.6 (^{13}C)). Peak positions are relative to tetramethylsilane (^1H) and were calibrated against the residual solvent resonance. $^{31}\text{P}\{^1\text{H}\}$ NMR spectra were recorded on the same instruments operating at 162.0 MHz and 121.5 MHz. Chemical shifts were measured relative to external 85% H_3PO_4 , with downfield shifts reported as positive. FT-IR spectra were measured using KBr pellets or solution cells. Elemental combustion microanalyses (C, H, N) were obtained using a elemental analyzer.

Mass spectra were obtained at a 70 eV ionization potential and are reported in the form m/z (intensity relative to base = 100). ESI-MS spectra were done on a LCQ Orbitrap mass spectrometer equipped with a conventional ESI source by direct injection of the sample solution. 80 scans were accumulated and averaged for each spectrum. The instrument parameters were the following: flow rate 3 $\mu\text{l}/\text{min}$, capillary voltage 60 V, tube lens 185 V, nominal resolution (@ 400 m/z) 60000. 80 scans were accumulated and averaged for each spectrum.

4.5.1.1 Synthesis of 1,4-bis((diphenylphosphino)ethynyl)benzene (dppab) (1)

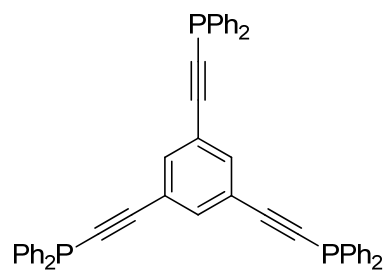
Chlorodiphenylphosphine (1.8 mL, 9.6 mmol), Ni(acac)₂ (0.31 g, 0.12 mmol), Et₃N (4 mL, 28.8 mmol) were added to a solution of 1,4-diethynylbenzene (0.50 g, 4.0 mmol) in toluene (50.0 mL). The mixture was stirred at 80 °C for 5 h. The solution was extracted with CH₂Cl₂ (3 × 40.0 mL) and the combined organic phases were washed with brine (50.0 mL), dried over Na₂SO₄ and concentrated. The crude product was purified by silica gel column chromatography to afford **1** (1.29 g, 65%) as a white low melting solid.



1: R_f = 0.6 (*n*-hexane/CH₂Cl₂ 2/1). IR (KBr): $\tilde{\nu}$ = 2163 (C≡C) cm⁻¹. ¹H NMR (400.1 MHz, CDCl₃, 25 °C): δ 7.38-7.35 (m, 12H, P-C₆H₅); 7.50 (s, 4H, C₆H₄); 7.68-7.63 ppm (m, 8H, P-C₆H₅). ¹³C{¹H} NMR (100.6 MHz, CDCl₃, 25 °C): δ 135.90 (d, ¹J(C,P) = 6.3 Hz, P-*ipso*C₆H₅), 132.62 (d, ²J(C,P) = 20.7 Hz, P-*o*C₆H₅); 131.67 (s, C₆H₄); 131.65 (s, C₆H₄); 129.13 (s, P-*p*C₆H₅); 128.67 (d, ³J(C,P) = 7.4 Hz, P-*m*C₆H₅); 123.09 (s, *ipso*C₆H₄); 107.06 (d, ²J(C,P) = 3.7 Hz, P-C≡); 88.42 (d, ¹J(C,P) = 8.1 Hz, ≡C-C₆H₅). ³¹P{¹H} NMR (162.0 MHz, CDCl₃, 25 °C): δ = -33.3 (s, 2P, PC₆H₅). MS, *m/z* (%): 494 (15) [M⁺]; 77 (100) [C₆H₅⁺]. Anal. Calcd. (%) for C₃₄H₂₄P₂ (494.14): C, 82.58; H, 4.86. Found: C, 83.01; H, 4.55.

4.5.1.2 Synthesis of 1,3,5-tris((diphenylphosphino)ethynyl)benzene (tppab) (2)

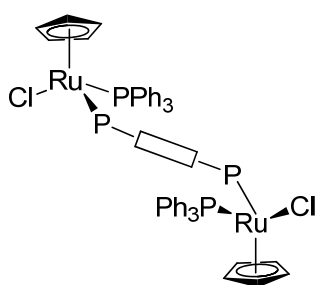
Chlorodiphenylphosphine (2.0 mL, 10.9 mmol), Ni(acac)₂ (0.25 g, 0.1 mmol), Et₃N (3.3 mL, 23.76 mmol) were added to a solution of 1,3,5-triethynylbenzene (0.50 g, 3.3 mmol) in toluene (50.0 mL). The mixture was stirred at 80 °C for 5 h. The solution was extracted with CH₂Cl₂ (3 × 40.0 mL) and the combined organic phases were washed with brine (50.0 mL), dried over Na₂SO₄ and concentrated. The crude product was purified by silica gel column chromatography to afford **2** (1.51 g, 75%) as a white solid.



2: $R_f = 0.5$ (*n*-hexane/ CH_2Cl_2 2/1). **m.p.** 110 °C. **IR** (KBr): $\tilde{\nu} = 1577$ ($\text{C}\equiv\text{C}$) cm^{-1} . **^1H NMR** (400.1 MHz, CDCl_3 , 25 °C): δ 7.73-7.60 (m, 22H, P- C_6H_5); 7.43-7.40 (m, 26H, C_6H_4 , P- C_6H_5). **$^{13}\text{C}\{^1\text{H}\}$ NMR** (100.6 MHz, CDCl_3 , 25 °C): δ 135.56 (d, $^1J(\text{C},\text{P})=5.9$ Hz, P-*ipso* C_6H_5); 134.69 (s, C_6H_4); 132.69 (d, $^2J(\text{C},\text{P}) = 21.1$ Hz, P-*o* C_6H_5); 129.16 (s, C_6H_4); 128.68 (d, $^3J(\text{C},\text{P}) = 7.8$ Hz, P-*m* C_6H_5); 123.56 (s, P-*p* C_6H_5); 105.35 (d, $^2J(\text{C},\text{P}) = 3.0$ Hz, P- $\text{C}\equiv$); 88.22 (d, $^1J(\text{C},\text{P})=10.0$ Hz, $\equiv\text{C}-\text{C}_6\text{H}_5$). **$^{31}\text{P}\{^1\text{H}\}$ NMR** (162.0 MHz, CDCl_3 , 25 °C): δ -33.5 (s, 3P, PC_6H_5). **MS**, m/z (%): 702 (11) [M^+]; 77 (100) [C_6H_5^+]. **Anal.** Calcd. (%) for $\text{C}_{48}\text{H}_{33}\text{P}_3$ (702.14): C, 82.04; H, 4.73. Found: C, 81.86; H, 4.90.

4.5.1.3 Synthesis of $[\{\text{CpRuCl}(\text{PPh}_3)_2\}_2(\mu\text{-dppab})]$ (**3**)

A solution of dppab (0.68 g, 0.14 mmol) in toluene (10.0 mL) was added to a solution of $[\text{CpRu}(\text{PPh}_3)_2\text{Cl}]$ (0.20 g, 0.28 mmol) in toluene (10.0 mL). The mixture was stirred at 60 °C for 4 h. The solvent was removed *in vacuo*, and the residue washed with *n*-hexane at 60 °C, filtered and concentrated under vacuum. The crude product was purified by silica gel column chromatography to afford **3** (0.17 g, 89%) as an orange solid consisting of a 1:1 mixture of two diastereoisomers (NMR signals due to the second diastereoisomer are given in parenthesis).

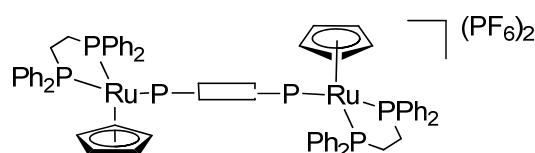


3: $R_f = 0.8$ (CH_2Cl_2 /acetone 20/1). **IR** (KBr): $\tilde{\nu} = 2166$ ($\text{C}\equiv\text{C}$), 1720, 802 cm^{-1} . **^1H NMR** (400.1 MHz, CD_2Cl_2 , 25 °C): δ 7.95-7.88 (m, 5H); 7.68-7.62 (m, 5H); 7.40-7.33 (m, 9H); 7.26-7.10 (m, 30H); 4.22 (4.23) (s, 10 H). **$^{13}\text{C}\{^1\text{H}\}$ NMR** (100.6 MHz, CD_2Cl_2 , 25 °C): δ 140.30 (136.16) (d, $^1J(\text{C},\text{P}) = 50.4$ Hz, RuP-*ipso*(C_6H_5)₂); 137.07 (d, $^1J(\text{C},\text{P}) = 40.4$ Hz, RuP-*ipso*(C_6H_5)₃); 134.08 (d, $^2J(\text{C},\text{P}) = 10.7$ Hz, RuP-*o*(C_6H_5)₃); 132.38 (131.84) (d, $^3J(\text{C},\text{P}) = 11.1$, 3.0 Hz, RuP-*m*(C_6H_5)₂); 131.90 (s, C_6H_4), 129.38 (d, $^4J(\text{C},\text{P}) = 1.5$ Hz, RuP-*p*(C_6H_5)₂); 129.07 (d, $^4J(\text{C},\text{P}) = 1.9$ Hz, RuP-*p*(C_6H_5)₃); 128.13 (127.99) (d, $^3J(\text{C},\text{P}) = 10.2$ Hz, RuP-*m*(C_6H_5)₃); 127.49 (d, $^2J(\text{C},\text{P}) = 9.6$ Hz, RuP-*o*(C_6H_5)₂); 122.97 (122.96) (s, RuP-*ipso* C_6H_4), 107.34 (d, $^2J(\text{C},\text{P}) = 9.3$ Hz, $\text{PC}\equiv\text{C}$); 89.08 (dd, $^1J(\text{C},\text{P}) = 72.4$, 2.0 Hz, $\text{PC}\equiv\text{C}$); 82.01 (m, Ru-

C_5H_5). $^{31}P\{^1H\}$ NMR (162.0 MHz, CD_2Cl_2 , 25 °C): δ 45.22 (44.94) (d, $^2J(P,P)=14.1$ Hz, 2P, $RuP-(C_6H_5)_3$); 21.45 (21.17) (d, $^2J(P,P) = 12.8$ Hz, 2P; $RuP-(C_6H_5)_2$). **ESI-MS** (MeOH) positive ion: m/z (%): 1422 (21) $[M]^+$; 1387 (20) $[M^+-Cl]$; 673 (100) $[CpRuCl(PPh_3)(Ph_2P-C\equiv C)^+]$. **Anal.** Calcd. (%) for $C_{80}H_{64}Cl_2P_4Ru_2$ (1422.14): C, 67.56; H, 4.54. Found: C, 66.36; H, 4.11.

4.5.1.4 Synthesis of $\{[CpRu(dppe)]_2(\mu-dppab)\}(PF_6)_2$ (**4**)

A solution of $TiPF_6$ (0.13 g, 0.37 mmol) in MeOH (0.5 mL) was added to a solution of $[CpRu(dppe)Cl]$ (0.10 g, 0.17 mmol) in dichloromethane (30.0 mL). The mixture was stirred for 4 h and the supernatant was separated from $TiCl$. A solution of $dppab$ (0.04 g, 0.08 mmol) in dichloromethane (10.0 mL) was then mixed together with the previous solution and stirred at room temperature overnight. After this time, the solvent was removed *in vacuo*, and the solid residue washed with warm *n*-hexane (2 x 20.0 mL at 60 °C) and dried under vacuum. The crude product was purified by silica gel column chromatography to afford **4** (0.10 g, 65%) as an orange solid.

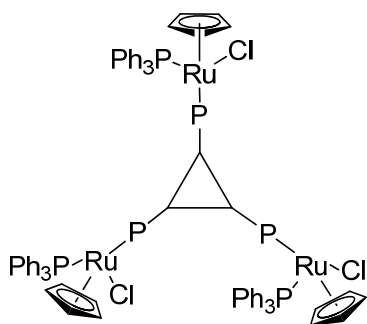


4: $R_f = 0.3$ (CH_2Cl_2 /acetone 20/1). **IR** (KBr): $\tilde{\nu} = 2171$ ($C\equiv C$), 840 (P-F) cm^{-1} . 1H NMR (400.1 MHz, CD_2Cl_2 , 25 °C): δ 7.68 (m, 4H); 7.47-7.17 (m, 60H); 6.96-6.89 (m, 8H); 4.99 (s, 10H); 3.21-3.15 (m, 4H); 2.71-2.73 (m, 4H). $^{13}C\{^1H\}$ NMR (100.6 MHz, CD_2Cl_2 , 25 °C): δ 135.34 (m, $RuP-ipso(C_6H_5)_2$); 134.77 (m, $RuP-ipso(C_6H_5)dppe$); 133.22 (s, C_6H_4); 131.78-131.68 (m, $RuP-m(C_6H_5)dppe$); 131.53-131.43 (m, $RuP-m(C_6H_5)dppe$); 131.27 (m, $^2J(C,P) = 12.6$ Hz, $RuP-o(C_6H_5)dppe$); 130.52 (m, $^2J(C,P) = 12.6$ Hz, $RuP-o(C_6H_5)dppe$); 130.07 (bs, $RuP-p(C_6H_5)_2$); 128.84-128.66 (m, $RuP-m(C_6H_5)_2+RuP-p(C_6H_5)dppe$); 128.41 (d, $^2J(C,P) = 11.1$ Hz, $RuP-o(C_6H_5)_2$); 122.33 (d, $^3J(C,P) = 2.2$ Hz, $RuP-ipsoC_6H_4$); 106.58-106.44 (m, $RuPC\equiv C$); 88.34-87.60 (m; $RuPC\equiv C$); 86.22 ppm (m, $Ru-C_5H_5$); 26.70 (dm, $^1J(P,P)=23.7$ Hz, $RuP-CH_2$); 26.48 (dm, $^1J(P,P) = 22.2$ Hz, $RuP-CH_2$). $^{31}P\{^1H\}$ NMR (162.0 MHz, CD_2Cl_2 , 25 °C): δ 70.99 (d, $^2J(P,P) = 36.5$ Hz, 1P, $RuP-(C_6H_5)_2$); 30.33 (t, $^2J(P,P) = 36.5$ Hz, 2P, $RuP-(C_6H_5)_2$); -144.4 ppm (sept, $^1J(P,F) = 711.2$ Hz, 2P, PF_6). **ESI-**

MS (MeOH) positive ion: m/z (%): 1796 (19) $[M-PF_6]^+$. **Anal.** Calcd. (%) for $C_{96}H_{82}F_{12}P_8Ru_2$ (1913.59): C, 60.25; H, 4.32. Found: C, 60.46; H, 4.70.

4.5.1.5 Synthesis of $[\{CpRuCl(PPh_3)\}_3(\mu_3\text{-tppab})]$ (**5**)

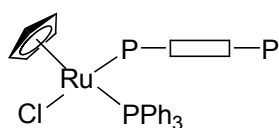
A solution of tppab (0.15 g, 0.20 mmol) in toluene (35.0 mL) was added to a solution of $[CpRu(PPh_3)_2Cl]$ (0.47 g, 0.60 mmol) in the same solvent (30.0 mL). The mixture was stirred at 60 °C for 3 h. The solvent was removed *in vacuo*, and the solid residue washed with warm hexane (2 x 20.0 mL at 60 °C) and dried under vacuum. The crude product was purified by silica gel column chromatography to afford **5** (0.30 g, 70%) as an orange solid containing a 1:2:1 mixture of three diastereoisomers (^{31}P -NMR signals of diastereoisomers are given in parenthesis).



5: $R_f = 0.6$ (CH_2Cl_2 /acetone 30:1). **IR** (KBr): $\tilde{\nu} = 2175$ ($C\equiv C$), 840 (P-F) cm^{-1} . **1H NMR** (400.1 MHz, CD_2Cl_2 , 25 °C): δ 7.86-7.76 (m, 8H); 7.71-7.61 (m, 8H); 7.38-7.03 (m, 62H); 4.22 ppm (s, 15H). **$^{13}C\{^1H\}$ NMR** (100.6 MHz, CD_2Cl_2 , 25 °C): δ 139.95 (135.91) (d, $^1J(C,P) = 46.5$ Hz, RuP-*ipso*(C_6H_5)₂); 136.91 (d, $^1J(C,P) = 40.7$ Hz, RuP-*ipso*(C_6H_5)₃); 134.04 (d, $^2J(C,P) = 10.7$ Hz, RuP-*o*(C_6H_5)₃); 132.60-132.36 (132.82-131.59) (m, RuP-*m*(C_6H_5)₂); 129.45 (bs, 3C, C_6H_3); 129.26 (bs, RuP-*p*(C_6H_5)₂), 129.12 (bs, RuP-*p*(C_6H_5)₃); 128.17 (127.99) (d, $^3J(C,P) = 10.0$ Hz, RuP-*m*(C_6H_5)₃); 127.48 (d, $^2J(C,P) = 9.3$ Hz, RuP-*o*(C_6H_5)₂); 122.82 (bs, RuP-*ipso*(C_6H_4)₃); 105.11 (d, $^2J(C,P) = 8.9$ Hz, RuPC \equiv C); 88.83 (bd, $^1J(C,P) = 68.1$ Hz, RuPC \equiv); 82.00 ppm (m, Ru- C_5H_5). **$^{31}P\{^1H\}$ NMR** (162.0 MHz, CD_2Cl_2 , 25 °C): δ 45.53 (45.30, 45.129) (d, $^2J(P,P) = 46.7$ Hz, 3P, RuP-(C_6H_5)₃); 23.00 (22.70, 22.51) (d, $^2J(P,P) = 46.7$ Hz, 3P, RuP-(C_6H_5)₂). **ESI-MS** (MeOH) positive ion: m/z (%): 673 (17) $[M-C_6H_3-(CpRuCl(PPh_3)(C\equiv CPh_2))_2]^+$; 2059 (100) $[M-Cl]^+$; 2094 (15) $[M]^+$. **Anal.** Calcd. (%) for $C_{117}H_{93}Cl_3P_6Ru_3$ (2094.40): C, 67.10, H, 4.48. Found: C, 66.86; H, 4.91.

4.5.1.6 Synthesis of [CpRuCl(η^1 -dppab)] (6)

A solution of **1** (0.15 g, 0.30 mmol) in toluene (10.0 mL) was added to a solution of [CpRu(PPh₃)₂Cl] (**10**) (0.11 g, 0.15 mmol) in toluene (10.0 mL). The mixture was stirred at 60 °C for 1 h. The solvent was removed *in vacuo*, and the solid residue washed with warm *n*-hexane (2 x 20.0 mL) and dried under *vacuum*. The crude product was purified by silica gel column chromatography to afford **6** (0.31 g, 22%) as a yellow solid.

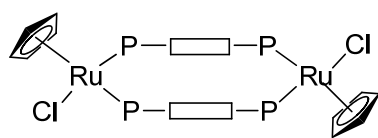


6: $R_f = 0.7$ (CH₂Cl₂/acetone 20:1). IR (KBr): $\tilde{\nu}=2172$ (C \equiv C) cm⁻¹. ¹H NMR (400.1 MHz, CD₂Cl₂, 25 °C): δ 7.97-7.91 (m, 2H); 7.69-7.50 (m, 8H); 7.39-7.29 (m, 17H); 7.23-7.17 (m, 4H); 7.13-7.06 (m, 8H); 4.23 (s, 5H, C₅H₅). ¹³C{¹H} NMR (100.6 MHz, CD₂Cl₂, 25 °C): δ 140.58 (dd, J (C,P) = 50.0, 3.3 Hz, RuP-*ipso*(C₆H₅)₂); 137.02 (dd, J (C,P) = 40.6, 1.7 Hz, RuP-*ipso*(C₆H₅)₃); 135.99 (d, 1J (C,P) = 42.2 Hz, \equiv C-*ipso*P(C₆H₅)₂); 135.98 (d, 3J (C,P) = 6.7 Hz, RuP-*m*(C₆H₅)₂); 134.03 (d, 2J (C,P) = 10.7 Hz, RuP-*o*(C₆H₅)₃); 132.73 (s, C₆H₄); 132.52 (s, C₆H₄); 131.94 (d, 4J (C,P) = 1.1 Hz, RuP-*p*(C₆H₅)₂); 131.71 (d, 4J (C,P) = 1.5 Hz, \equiv C-P(C₆H₅)₂); 129.05 (d, 4J (C,P) = 1.85 Hz, RuP-*p*(C₆H₅)₃); 128.81 (d, 2J (C,P) = 7.4 Hz, RuP-*p*(C₆H₅)₂); 128.79 (s, C₆H₄); 128.08 (d, 3J (C,P)=10.0 Hz, RuP-*m*(C₆H₅)₃); 127.91 (d, 3J (C,P) = 10.0 Hz, RuP-*m*(C₆H₅)₃); 127.47 (d, 2J (C,P) = 9.6 Hz, \equiv C-*po*(C₆H₅)₂); 123.60 (d, 3J (C,P) = 1.5 Hz, C₆H₄); 122.50 (d, 1J (C,P) = 2.2 Hz, RuPC \equiv); 107.40 (d, 2J (C,P) = 10.0 Hz, RuPC \equiv C); 107.06 (d, 1J (C,P) = 10.0 Hz, \equiv C-P(C₆H₅)₂); 88.83 (d, 1J (C,P) = 9.6 Hz, C \equiv C-P(C₆H₅)₂); 82.00 ppm (m, Ru-C₅H₅). ³¹P{¹H} NMR (162.0 MHz, CD₂Cl₂, 25 °C): δ 44.99 (d, 2J (P,P) = 45.9 Hz, 1P, RuP-(C₆H₅)₃); 20.24 (d, 2J (P,P) = 45.9 Hz, 1P, RuP-(C₆H₅)₂); -33.64 ppm (s, 1P, \equiv C-P(C₆H₅)₂). ESI-MS (MeOH) positive ion: m/z (%): 958 (12) [M]⁺. Anal. Calcd. (%) for C₅₇H₄₄ClP₃Ru (058.40): C, 71.43; H, 4.63. Found: C, 72.31; H, 4.75.

4.5.1.7 Synthesis of [{CpRuCl}(μ -dppab)]₂ (7)

A solution of dppab (0.68 g, 0.40 mmol) in toluene (10.0 mL) was added to a solution of [CpRu(PPh₃)₂Cl] (0.15 g, 0.20 mmol) in toluene (20.0 mL). The mixture was gently brought to reflux and stirred for 4 h. After this time, the supernatant was

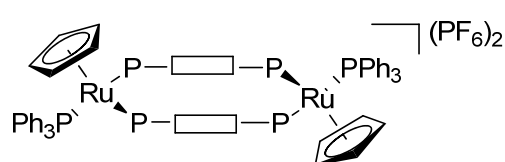
filtered off and the solid residue washed with warm *n*-hexane (2 x 20.0 mL at 60 °C) and dried under vacuum. The crude product was purified by silica gel column chromatography to afford **7** (0.67 g, 25%) as an orange solid.



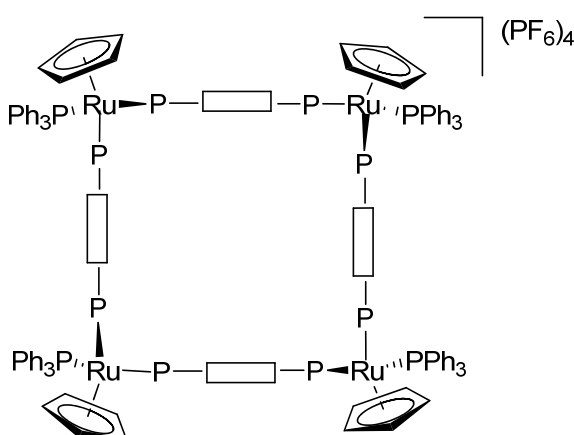
7: $R_f = 0.8$ ($\text{CH}_2\text{Cl}_2/\text{acetone}$ 20:1). IR (KBr): $\tilde{\nu} = 2172$ ($\text{C}\equiv\text{C}$) cm^{-1} . $^1\text{H NMR}$ (400.1 MHz, CD_2Cl_2 , 25 °C): δ 8.18-8.13 (m, 8H); 7.58-7.53 (m, 8H); 7.39-7.32 (m, 12H); 7.21 (s, 8H); 7.00-6.96 (m, 4H); 6.89-6.86 (m, 8H); 4.49 (s, 10H). $^{13}\text{C}\{^1\text{H}\}$ NMR (100.6 MHz, CD_2Cl_2 , 25 °C): δ 140.41 (m, RuP-*ipso*(C_6H_5)₂); 135.24 (m, RuP-*ipso*(C_6H_5)₂); 131.87 (m, RuP-*o*(C_6H_5)₂); 131.46 (m, RuP-*o*(C_6H_5)₂+ C_6H_4); 129.49 (s, RuP-*p*(C_6H_5)₂); 128.70 (s, RuP-*p*(C_6H_5)₂); 128.07 (m, RuP-*m*(C_6H_5)₂); 127.54 (m, RuP-*m*(C_6H_5)₂); 122.60 (s, C_6H_4); 107.82 (m, RuPC \equiv C); 86.74 (m, RuPC \equiv); 83.29 (s, Ru- C_5H_5). $^{31}\text{P}\{^1\text{H}\}$ NMR (162.0 MHz, CD_2Cl_2 , 25 °C): δ 18.67 (s, 4P, P(C_6H_5)₂). ESI-MS (MeOH) positive ion: m/z (%): 1359 (20) [M-Cl] $^+$; 1392 (35) [M] $^+$. Anal. Calcd. (%) for $\text{C}_{78}\text{H}_{58}\text{Cl}_2\text{P}_4\text{Ru}_2$ (1932.24): C, 67.29; H, 4.20. Found: C, 66.95; H, 4.70.

4.5.1.8 Synthesis of $[\text{CpRu}(\text{PPh}_3)(\mu\text{-dppab})_2](\text{PF}_6)_2$ (**8**) and $[\text{CpRu}(\text{PPh}_3)(\mu\text{-dppab})_4](\text{PF}_6)_4$ (**9**)

A solution of TlPF_6 (0.40 g, 0.15 mmol) in MeOH (0.5 mL) was added to a solution of **3** (0.74 g, 0.52 mmol) and dppab (0.26 g, 0.52 mmol) in dichloromethane (30.0 mL). The mixture was stirred for 2 h and the supernatant was separated from TlCl by filtration. After this time, the solvent was removed *in vacuo* and the solid residue dried. The crude product was purified by silica gel column chromatography (dichloromethane/acetone 20:1) to afford an orange solid (0.87 g, 57% based on **3**) consisting of a mixture of **8** and **9** in an approximate 1:1 ratio. Dissolution of the solid mixture in *ca.* 150.0 mL CH_2Cl_2 , followed by slow addition of *n*-hexane, led to selective precipitation of **9** (0.47 g, 21% based on **3**) as a yellow solid. The remaining red solution was concentrated to dryness to afford pure **8** (0.40 g, 36% based on **3**).



8: $R_f = 0.6$ ($\text{CH}_2\text{Cl}_2/\text{acetone}$ 20:1). IR (KBr): $\tilde{\nu} = 2168$ ($\text{C}\equiv\text{C}$), 837 (P-F) cm^{-1} . $^1\text{H NMR}$ (400.1 MHz, CD_2Cl_2 , 25 °C): δ 7.70-7.47 (m, 40H); 7.37-7.11 (m, 30H); 7.03 (s, 8H); 4.83 (s, 10H). $^{13}\text{C}\{^1\text{H}\}$ NMR (100.6 MHz, CD_2Cl_2 , 25 °C): δ 135.95-135.23 (m, RuP-*ipso*(C_6H_5)₃+RuP-*ipso*(C_6H_5)₂); 133.54 (d, $^2J(\text{C,P}) = 10.4$ Hz, RuP-*o*(C_6H_5)₃); 132.01-131.91 (m, RuP-*o*(C_6H_5)₂); 131.70 (bs, C_6H_4); 131.11-130.56 (m, RuP-*m*(C_6H_5)₂); 130.20 (bs, RuP-*p*(C_6H_5)₃); 128.83-128.35 (m, RuP-*p*(C_6H_5)₂+RuP-*m*(C_6H_5)₃); 122.16 (s, RuP-*ipso*(C_6H_4)); 108.27-108.17 (m, RuPC \equiv C); 87.92 (d, $^1J(\text{C,P}) = 79.1$ Hz, RuPC \equiv C); 86.18 ppm (m, Ru- C_5H_5). $^{31}\text{P}\{^1\text{H}\}$ NMR (162.0 MHz, CD_2Cl_2 , 25 °C): δ 38.95 (t, $^2J(\text{P,P}) = 37.5$ Hz, 4P, RuP-(C_6H_5)₂); 20.26 (d, $^2J(\text{P,P}) = 37.5$ Hz, 2P, RuP-(C_6H_5)₂); -144.6 (sept, $^1J(\text{P,F}) = 706.3$ Hz, 2P, PF_6). ESI-MS (MeOH) positive ion: m/z (%): 1991 (100) $[\text{M-PF}_6]^+$. Anal. Calcd. (%) for $\text{C}_{114}\text{H}_{88}\text{F}_{12}\text{P}_8\text{Ru}_2$ (2135.83): C, 64.11; H, 4.15. Found: C, 64.36; H, 4.98.



9: $R_f = 0.4$ ($\text{CH}_2\text{Cl}_2/\text{acetone}$ 20:1). IR (KBr): $\tilde{\nu} = 2168$ ($\text{C}\equiv\text{C}$), 837 (P-F) cm^{-1} . $^1\text{H NMR}$ (400.1 MHz, CD_2Cl_2 , 25 °C): δ 7.72-7.67 (m, 20H); 7.53-7.43 (m, 60H); 7.28-7.20 (m, 60H); 7.08 (bs, 16H); 4.84 (s, 20H). $^{13}\text{C}\{^1\text{H}\}$ NMR (100.6 MHz, CD_2Cl_2 , 25 °C): δ 137.45-136.64 (m, RuP-*ipso*(C_6H_5)₃+RuP-*ipso*(C_6H_5)₂); 133.59 (d, $^2J(\text{C,P}) = 10.4$ Hz, RuP-*o*(C_6H_5)₃); 133.05-132.92 (m, RuP-*o*(C_6H_5)₂); 132.09-131.97 (m, RuP-*o*(C_6H_5)₂); 131.84 (bs, C_6H_4); 131.81-130.83 (m, RuP-*m*(C_6H_5)₂); 129.71 (bs, RuP-*p*(C_6H_5)₃); 128.91-128.40 (m, RuP-*p*(C_6H_5)₂+RuP-*m*(C_6H_5)₃); 122.17 (s, RuP-*ipso*(C_6H_4)); 107.34-107.25 (m, RuPC \equiv C); 87.92 (d, $^1J(\text{C,P}) = 80.4$ Hz, RuPC \equiv C); 86.22 (m, Ru- C_5H_5). $^{31}\text{P}\{^1\text{H}\}$ NMR (162.0 MHz, CD_2Cl_2 , 25 °C): δ 39.23 (t, $^2J(\text{P,P}) = 38.5$ Hz, 8P, RuP-(C_6H_5)₂); 23.88 (d, $^2J(\text{P,P}) = 38.5$ Hz, 4P, RuP-(C_6H_5)₂); -144.6 (sept, $^1J(\text{P,F}) = 706.3$ Hz, 4P, PF_6). ESI-MS (MeOH) positive ion: m/z (%): 923 (100) $[\text{Cp}_2\text{Ru}_2(\text{PPh}_3)_2(\text{dppab})_2]^{2+}$; 1991 (5) $[\text{M}-2\text{PF}_6]^{2+}$. Anal. Calcd. (%) for $\text{C}_{228}\text{H}_{176}\text{F}_{24}\text{P}_{16}\text{Ru}_4$ (4271.66): C, 64.11; H, 4.15. Found: C, 64.23; H, 4.21.

4.5.2 X-ray crystallographic studies

X-ray data for complexes **7** and **8** were collected at low temperature (150 K) on an Oxford Diffraction XCALIBUR 3 diffractometer equipped with a CCD area detector using Mo K_{α} radiation ($\lambda = 0.7107 \text{ \AA}$). The program used for the data collection was CrysAlis CCD 1.171.³⁷ Data reduction was carried out with the program CrysAlis RED 1.171³⁸ and the absorption correction was applied with the program ABSPACK 1.17.³⁷ Direct methods implemented in Sir97³⁹ were used to solve the structures and the refinements were performed by full-matrix least-squares against F^2 implemented in SHELX97.⁴⁰ In compound **7** a merohedral twinning is present and the twin component was found to be 0.50(7). The cyclopentadienyl ring bonded to Ru2 was fitted as a rigid group and the carbon atoms were restrained to have the same Uij components. All the non-hydrogen atoms were refined anisotropically and the H atoms were fixed in calculated positions and refined isotropically with thermal factors related to those of the atom they are bound to. A complete list of the crystallographic data are collected in the Appendix (Chapter 5).

4.5.3 Electrochemical and spectroelectrochemical studies

Anhydrous 99.9% dichloromethane was purchased from Aldrich product. Fluka $[\text{NBu}_4][\text{PF}_6]$ (electrochemical grade) was used as supporting electrolyte (0.2 mol dm^{-3}). Cyclic voltammetry was performed in a three electrode cell containing a platinum working electrode surrounded by a platinum-spiral counter electrode, and an aqueous saturated calomel reference electrode (SCE) mounted with a Luggin capillary. A BAS 100W electrochemical analyzer was used as polarizing unit. All the potential values are referred to the saturated calomel electrode (SCE). Under the present experimental conditions, the one-electron oxidation of ferrocene in CH_2Cl_2 solution occurs at $E^{\circ'} = +0.39 \text{ V}$. Controlled potential coulometry was performed in an H-shaped cell with anodic and cathodic compartments separated by a sintered-glass disk. The working macroelectrode was a platinum gauze; a mercury pool was used as the counter electrode. The UV/vis spectroelectrochemical measurements were carried out using a Perkin-Elmer Lambda 900 UV/vis spectrophotometer and an OTTE (optically transparent thin-layer electrode) cell equipped with a Pt-

minigrad working electrode (32 wires/cm), Pt minigrad auxiliary electrode, Ag wire pseudoreference and CaF_2 windows.⁴¹ The electrode potential was controlled during electrolysis by an Amel potentiostat 2059 equipped with an Amel function generator 568. Nitrogen-saturated solutions of the compound under study were used with $[\text{NBu}_4][\text{PF}_6]$ (0.2 mol dm^{-3}) as supporting electrolyte. Working potential was kept fixed at the peak potential of the process under study and spectra were progressively collected every 2 min of electrolysis.

X-band EPR spectra were recorded at an ER 200-SRCB Bruker spectrometer. The external magnetic field H was calibrated with a Microwave Bridge ER041 MR Bruker wavemeter and the temperature was controlled with an ER 4111VT Bruker device (accuracy = $\pm 1 \text{ K}$). The diphenylpicrylhydrazyl (DPPH) free radical was used as suitable "field-marker" ($g_{\text{iso}}(\text{DPPH}) = 2.0036$) for the determination of accurate g_i values. In order to ensure quantitative spectral reproducibility, the paramagnetic samples were placed into a calibrated quartz capillary tube permanently positioned in the resonance cavity.

4.6 References and notes

- 1 **Di Credico, B.**; Fabrizi de Biani, F.; Gonsalvi, L.; Guerri, A.; Ienco, A.; Laschi, F.; Peruzzini, M.; Reginato, G.; Rossin, A.; Zanello, P. *Chem. Eur. J.* **2009**, *15*, 11985.
- 2 a) Stang, P. J.; Olenyuk, B. *Acc. Chem. Res.* **1997**, *30*, 502; b) Kumar, A.; Sun, S.-S.; Lees, A. J. *Coord. Chem. Rev.* **2008**, *252*, 922; c) Tashiro, S.; Tominaga, M.; Kawano, M.; Therrien, B.; Ozeki, T.; Fujita, M. *J. Am. Chem. Soc.* **2005**, *127*, 4546; d) Boyer, J. L.; Kuhlman, L. M.; Rauchfuss, T. B. *Acc. Chem. Res.* **2007**, *40*, 233.
- 3 Slove, R. V.; Benkstein, K. D.; Bélanger, S.; Hupp, J. T.; Guzei, I. A.; Rheingold, A. L. *Coord. Chem. Rev.* **1998**, *171*, 221.
- 4 Severin, K. *Chem. Commun.* **2006**, 3859.
- 5 a) McAuliffe, C. A.; Levason, W. *Studies in Inorganic Chemistry* **1978**, Vol.1: *Phosphine, Arsine and Stibine Complexes of the Transition Elements*, Elsevier, Amsterdam, Neth; b) Alyea, C. E.; Meek, D. W. *Advances in Chemistry Series* **1982**, Vol. 196: *Catalytic Aspects of Metal Phosphine Complexes*, American Chemical Society, Washington; c) Cotton, F. A.; Wilkinson, G.; Murillo, C. A.; Bochman, M. *Advanced Inorganic Chemistry* **1999**, John Wiley & Sons, New York; d) Mayer H. A.; Kaska, W. C. *Chem. Rev.* **1994**, *94*, 1239.
- 6 a) De Simone, T.; Dickson, R. S.; Skelton, B. W.; White, A. W. *Inorg. Chim. Acta* **1992**, *240*, 323; b) Beer, P. D. *Chem. Commun.* **1996**, 689; c) Baumgartner, T.; Huynh, K.; Schleidt, S.; Lough, A. J.; Manners, I. *Chem. Eur. J.* **2002**, 4622; d) Hong, F.-E.; Ho, Y.-J.; Chang, Y.-C.; Lai, Y.-C. *Tetrahedron* **2004**, *60*, 2639; e) Constable, E. C.; Housecroft, C. E.; Krattinger, B.; Neuburger, M.; Zehnder, M. *Organometallics* **1999**, *18*, 2565.

- 7 a) Adams, J.; Bruce, M. I.; Skelton, B. W.; White, A. H. *Inorg. Chem.* **1992**, *31*, 3336; b) Berenguer, J. R.; Bernechea, M.; Forniés, J.; García, A.; Lalinde, E. *Organometallics* **2004**, *23*, 4288; Álvarez, P., Lastra, E.; Gimeno, J.; Braña, P.; Sordo, J. A.; Gomez, J.; Falvello, L. R.; Bassetti, M. *Organometallics* **2004**, *23*, 2956.
- 8 Chaplin, A. B.; Scoppelitti, R.; Dyson, P. *Eur. J. Inorg. Chem.* **2005**, *23*, 4762.
- 9 a) Clark, H. C.; Ferguson, G.; Kapoor, P. N.; Parvez, M. *Inorg. Chem.* **1985**, *24*, 3924; b) Oberhauser, W.; Bachmann, C.; Stampfl, T.; P. Brüggeler *Inorg. Chim. Acta* **1997**, *256*, 223; c) Xu, D.; Murfee H. J.; v. d. Veer, W. E.; Hong, B. *J. Organomet. Chem.* **2000**, *596*, 53; d) Falvello, L. R.; Forniés, J.; Gómez, J.; Lalinde, E., Martín, A.; Martínez, F.; Moreno, M. T. *J. Chem. Soc., Dalton Trans.* **2001**, 2132.
- 10 Nast, R.; Grouhi, H. *J. Organomet. Chem.* **1979**, *182*, 197.
- 11 Beletskaya, I. P.; Afanasiev, V. V.; Kazankova, M. A.; Efimova, I. V. *Org. Lett.* **2003**, *5*, 4309.
- 12 a) Gelman, D.; Jiang, L.; Buchwald, S. L. *Org. Lett.* **2002**, *5*, 2315; b) Prim, D.; Campagne, J.-M.; Joseph, D.; Andrioletti, B. *Tetrahedron* **2002**, *58*, 2041; c) Allen, D. V.; Venkataraman, D. *J. Org. Chem.* **2003**, *68*, 4590.
- 13 Liu, B.; Wang, K. K.; Petersen, J. L. *J. Org. Chem.* **1996**, *61*, 8503.
- 14 Bruce, M. I.; Hameister, C.; Swincer, A. G.; Wallis, R. C. *Inorg. Synth.* **1982**, *21*, 78.
- 15 Nelson, J. H. *Coord. Chem. Rev.* **1995**, 245.
- 16 a) Arena, C. G.; Drago, D.; Panzalorto, M.; Bruno, G.; Faraone, F. *Inorg. Chim. Act.* **1999**, *292*, 84; b) Suss-Fink, G., Therrien, B. *Organometallics* **2007**, *26*, 766; c) Pachhunga, K.; Therrien, B.; Kreisel, K. A.; Yap, G. P. A.; Kollipara, M. R. *Polyhedron* **2007**, *26*, 3638.
- 17 Tschan, M. J.-L.; Chérioux, F.; Therrien, B.; Suss-Fink, G. *Eur. J. Inorg. Chem.* **2007**, 509.
- 18 a) Fackler, J. P. *Metal-Metal Bonds and Clusters in Chemistry and Catalysis* **1990**, Plenum: New York; R. D. Adams and F. A. Cotton, *Catalysis by Di- and Polynuclear Metal Cluster Complexes* **1998**, Wiley-VCH: New York; b) Di Vaira, M.; Costantini, S. S.; Mani, F.; Peruzzini, M.; Stoppioni, P. *J. Organomet. Chem.* **2004**, *689*, 1757; c) Miyake, Y.; Endo, S.; Yuki, M.; Tanabe, Y.; Nishibayashi, Y. *Organometallics* **2008**, *27*, 6039.
- 19 a) Lawrence, D. S.; Jiang, T.; Levett, M. *Chem. Rev.* **1995**, *95*, 2229; b) Chi, X.; Guerin, A. J.; Haycock, R. A.; Hunter, C. A.; Sarson, L. D. *J. Chem. Soc., Chem. Commun.* **1995**, 2563; c) Chi, X.; Guerin, A. J.; Haycock, R. A.; Hunter, C. A.; Sarson, L. D. *J. Chem. Soc., Chem. Commun.* **1995**, 2567.
- 20 Galindo, M. A.; Quirós, M.; Romero, M. A.; Navarro, J. A. R. *J. Inorg. Biochem.* **2008**, *102*, 1025.
- 21 In collaboration with Dr. Andrea Ienco, ICCOM – CNR, Florence, Italy and Dr. Annalisa Guerri, Università degli Studi di Firenze, Florence, Italy.
- 22 a) Chan, W. Y.; Baumgartner, T.; Lough, A. J.; Manners, I. *Acta Cryst.* **2007**, *E63*, m2886; b) Baumgartner, T.; Huynh, K.; Schleidt, S.; Lough, A. J., Manners, I. *Private communication to the Cambridge Structural Database* deposition number CCDC 661295.
- 23 Hogarth, G.; Norman, T. *J. Chem. Soc., Dalton Trans.* **1996**, 1077.
- 24 Grirrane, A.; Pastor, A.; Galindo, A.; Orlandini, A.; DelRio, D.; Mealli, C.; Ienco, A.; Caneschi, A.; Sanz, J. F. *Angew. Chem. Int. Ed.* **2005**, *44*, 3429.
- 25 a) Wärnmark, K.; Heyke, O.; Thomas, J. A.; Lehn, J.-M. *Chem. Commun.* **1996**, 2603; b) Rueford, T. J.; Gijte, O. V.; Mesmaeker, A. K.-D.; Keene, F. R. *Inorg. Chem.* **1997**, *36*, 4465; c) Keene, F. R. *Chem. Soc. Rev.* **1998**, *27*, 185; d) Rutherford, T. J.; Keene, F. R. *J. Chem. Soc., Dalton Trans.* **1998**,

- 1155; e) Sato, H.; Kameda, J.; Fukuda, Y.; Haga, M.; Yamagishi, A. *Chemistry Letters* **2008**, *37*, 716; f) Chandrasekhar, V.; Azhakar, R.; Zacchini, S.; Bickley, J. F.; Steiner, A. *Inorg. Chem.* **2009**, *44*, 4608.
- 26 In collaboration with Prof. Piero Zanello, Prof. Franco Laschi and Dr. Fabrizia Fabrizi de Biani, Università degli Studi di Siena, Siena, Italy.
- 27 a) Devanne, D.; Dixneuf, P. H. *J. Organomet. Chem.* **1990**, *390*, 371; b) Bennet, M. A.; Edwards, A. J.; Harper, J. R.; Khimiyak, T.; Willis, A. C. *J. Organomet. Chem.* **2001**, *629*, 7; c) Bhalla, R.; Boxwell, C. J.; Duckett, S. B.; Dyson, P. J.; Humphrey, D. G.; Steed, J. W.; Suman, P. *Organometallics* **2002**, *21*, 924; d) Therrien, B.; Vieille-Petit, L.; Jeanette-Gris, J.; Stepnicka, P.; Süß-Fink, G. *J. Organomet. Chem.* **2004**, *689*, 2456.
- 28 Zanello, P. *Inorganic Electrochemistry. Theory, Practice and Application.* **2003**, RSC, Cambridge, UK.
- 29 Santi, S.; Broccardo, L.; Bassetti, M.; Alvarez, P. *Organometallics* **2003**, *22*, 3478.
- 30 a) Mabbs, F. E.; Collison, D. *Electron Paramagnetic Resonance of d Transition Metal Compounds* **1992**, Vol.16 of the series: *Studies in Inorganic Chemistry*, Elsevier, New York; b) J. R. Pilbrow, *Transition Ion Electron Paramagnetic Resonance* **1990**, Oxford Science Publication; c) Drago, R. S. *Physical Methods for Chemists* **1992**, Saunders College Publ., New York.
- 31 a) Osella, D.; Arman, G.; Gobetto, R.; Laschi, F.; Zanello, P.; Goodfellow, V.; Housecroft, C. E.; Owen, S. M. *Organometallics* **1989**, *8*, 2689; b) Bianchini, C.; Peruzzini, M.; Ceccanti, A.; Laschi, L.; Zanello, P. *Inorg. Chim. Acta* **1997**, *259*, 61; c) Diversi, P.; Fontani, M.; Fuligni, M.; Laschi, F.; Matteoni, S.; Pinzino, C.; Zanello, P. *J. Organomet. Chem.* **2001**, *626*, 145-156.
- 32 Romanelli, M. *CU23GPN1 Simulation Program.*
- 33 Takahashi, S.; Kuroyama, Y.; Sonogashira, K.; Hagihara, N. *Synthesis* **1980**, 627.
- 34 Leininger, S.; Stang, J. *Organometallics* **1998**, *17*, 3981.
- 35 Bruce, M. I.; Hameister, C.; Swincer, A. G.; Wallis, R. C. *Inorg. Synth.* **1982**, *21*, 78.
- 36 Alonzo, A. G.; Reventós, L. B. *J. Organomet. Chem.* **1988**, *338*, 249.
- 37 CrysAlisCCD 1.171.31.2 (release 07-07-2006), CrysAlis171 .NET, Oxford Diffraction Ltd.
- 38 CrysAlis RED 1.171.31.2 (release 07-07-2006), CrysAlis171 .NET, Oxford Diffraction Ltd.
- 39 Altomare, A.; Burla, M. C.; Cavalli, M.; Cascarano, G. L.; Giacovazzo, C.; Guagliardi, A.; Moliterni, A. G. G.; Polidori, G.; Spagna, R. *J. Appl. Cryst.* **1999**, *32*, 115.
- 40 Sheldrick, G. M. *Acta Cryst.* **2008**, *A64*, 112.
- 41 Krejčík, M.; Daněk, M.; Hartl, F. J. *Electroanal. Chem.* **1991**, *317*, 179.

Chapter 5

Appendix

5.1 Appendix to Chapter 2

Table 5-1. Crystal data and structure refinement for **Mg(HCOO)₂(HCOOH) · (CH₃)₂NH** (**Compound 1** in the **Chapter 2**).

Empirical formula	C ₅ H ₁₁ NO ₆ Mg	
Formula weight	205.46	
Temperature	293(2) K	
Wavelength	0.71069 Å	
Crystal system	Trigonal	
Space group	R -3c	
Unit cell dimensions	$a = 8.149(3)$ Å	$\alpha = 90^\circ$
	$b = 8.149(3)$ Å	$\beta = 90^\circ$
	$c = 22.598(8)$ Å	$\gamma = 120^\circ$
Volume	1299.6(8) Å ³	
Z	6	
Density (calculated)	1.575 mg/m ³	
Absorption coefficient	0.205 mm ⁻¹	
F(000)	648	
Crystal size	20 x 0.15 x 0.10 mm ³	
Theta range for data collection	3.40 to 24.96°	
Index ranges	-9 ≤ h ≤ 9, -4 ≤ k ≤ 9, -26 ≤ l ≤ 14	
Reflections collected	710	
Independent reflections	259 [R(int) = 0.0236]	
Completeness to theta = 24.96°	100.0 %	
Refinement method	Full-matrix least-squares on F ²	
Data / restraints / parameters	259 / 2 / 25	
Goodness-of-fit on F ²	1.160	
Final R indices [I > 2σ(I)]	R1 = 0.0333, wR2 = 0.0902	
R indices (all data)	R1 = 0.0374, wR2 = 0.0961	
Largest diff. peak and hole	0.219 and -0.281 e.Å ⁻³	

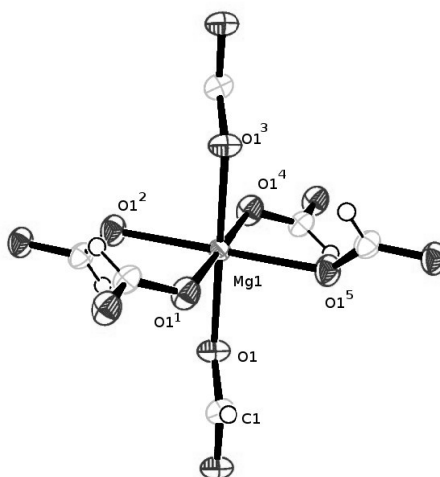


Figure 5-1. ORTEP plot for $\text{Mg}(\text{HCOO})_2(\text{HCOOH}) \cdot (\text{CH}_3)_2\text{NH}$.

Table 5-2. Bond lengths [Å] and angles [°] for $\text{Mg}(\text{HCOO})_2(\text{HCOOH}) \cdot (\text{CH}_3)_2\text{NH}$ (Compound 1 in the Chapter 2).

Mg(1)-O(1)#2	2.0914(15)	O(1)#2-Mg(1)-O(1)	89.40(7)
Mg(1)-O(1)#3	2.0914(15)	O(1)#3-Mg(1)-O(1)	90.60(7)
Mg(1)-O(1)	2.0914(15)	O(1)#1-Mg(1)-O(1)#4	89.40(7)
Mg(1)-O(1)#4	2.0914(15)	O(1)#2-Mg(1)-O(1)#4	90.60(7)
Mg(1)-O(1)#5	2.0914(15)	O(1)#3-Mg(1)-O(1)#4	89.40(7)
O(1)-C(1)	1.235(2)	O(1)-Mg(1)-O(1)#4	180.00(7)
C(1)-O(1)#6	1.235(2)	O(1)#1-Mg(1)-O(1)#5	89.40(7)
C(1)-H(1)	0.87(4)	O(1)#2-Mg(1)-O(1)#5	90.60(7)
C(2)-N(1)	1.432(7)	O(1)#3-Mg(1)-O(1)#5	180.00(11)
C(2)-N(1)#3	1.432(7)	O(1)-Mg(1)-O(1)#5	89.40(7)
C(2)-N(1)#1	1.432(7)	O(1)#6-C(1)-O(1)	127.2(3)
N(1)-N(1)#3	1.280(16)	O(1)-C(1)-H(1)	116.39(16)
N(1)-N(1)#1	1.280(16)	N(1)-C(2)-N(1)#3	53.1(6)
N(1)-C(2)#7	1.432(7)	N(1)-C(2)-N(1)#1	53.1(6)
O(1)#1-Mg(1)-O(1)#2	180.00(7)	N(1)#3-C(2)-N(1)#1	53.1(6)
O(1)#1-Mg(1)-O(1)#3	90.60(7)	N(1)#3-N(1)-N(1)#1	60.000(2)
O(1)#2-Mg(1)-O(1)#3	89.40(7)	N(1)#3-N(1)-C(2)	63.4(3)
O(1)#1-Mg(1)-O(1)	90.60(7)	N(1)#1-N(1)-C(2)	63.4(3)
N(1)#3-N(1)-C(2)#7	63.4(3)	N(1)#1-N(1)-C(2)#7	63.4(3)
C(2)-N(1)-C(2)#7	117.8(7)	O(1)#6-C(1)-H(1)	116.39(16)

5.2 Appendix to Chapter 3

Table 5-3. Crystal data and structure refinement for **2-(Pyridin-4-yl)thiazole-4-carboxylic acid (Compound 5a in the Chapter 3)**.

CCDC number	748497
Empirical formula	$C_{18}H_{14}N_4O_5S_2 = [2(C_9H_6N_2O_2S) \cdot H_2O]$
Formula weight	430.45
Temperature	150(2) K
Wavelength	0.71069 Å
Crystal system	Triclinic
Space group	<i>P</i> -1
Unit cell dimensions	a = 7.441(6) Å $\alpha = 99.954(6)^\circ$ b = 10.681(8) Å $\beta = 98.837(6)^\circ$ c = 12.041(8) Å $\gamma = 97.748(6)^\circ$
Volume	918.5(12) Å ³
Z	2
Density (calculated)	1.556 mg/m ³
Absorption coefficient	0.331 mm ⁻¹
F(000)	444
Crystal size	0.03 x 0.05 x 0.1 mm ³
Theta range for data collection	3.93 to 24.38°.
Index ranges	-8 ≤ h ≤ 8, -12 ≤ k ≤ 11, -11 ≤ l ≤ 13
Reflections collected	4831
Independent reflections	2266 [R(int) = 0.0329]
Absorption correction	Semi-empirical from equivalents
Completeness to theta = 20.77°	98.5 %
Refinement method	Full-matrix least-squares on F ²
Data / restraints / parameters	2266 / 0 / 268
Goodness-of-fit on F ²	1.043
Final R indices [I > 2σ(I)]	R1 = 0.0535, wR2 = 0.1383
R indices (all data)	R1 = 0.0748, wR2 = 0.1497
Largest diff. peak and hole	0.347 and -0.299 e.Å ⁻³

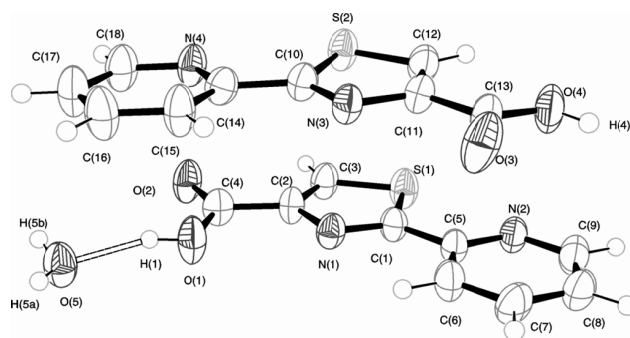


Figure 5-2. ORTEP plot for 2-(Pyridin-4-yl)thiazole-4-carboxylic acid.

Table 5-4. Bond lengths [Å] and angles [°] for 2-(Pyridin-4-yl)thiazole-4-carboxylic acid (Compound 5a in the Chapter 3).

C(1)-N(1)	1.304(5)	C(15)-C(16)	1.362(5)
C(1)-C(5)	1.462(5)	C(15)-H(15)	0.9500
C(1)-S(1)	1.731(4)	C(16)-C(17)	1.368(6)
C(2)-C(3)	1.364(5)	C(16)-H(16)	0.9500
C(2)-N(1)	1.377(5)	C(17)-C(18)	1.382(6)
C(2)-C(4)	1.482(5)	C(17)-H(17)	0.9500
C(3)-S(1)	1.695(4)	C(18)-N(4)	1.338(5)
C(3)-H(3)	0.9500	C(18)-H(18)	0.9500
C(4)-O(2)	1.229(5)	O(1)-H(1)	0.8400
C(4)-O(1)	1.296(4)	O(4)-H(4)	0.8400
C(5)-N(2)	1.338(5)	O(5)-H(5A)	0.84(4)
C(5)-C(6)	1.393(5)	O(5)-H(5B)	0.77(4)
C(6)-C(7)	1.377(5)	N(1)-C(1)-C(5)	125.0(3)
C(6)-H(6)	0.9500	N(1)-C(1)-S(1)	114.9(3)
C(7)-C(8)	1.367(6)	C(5)-C(1)-S(1)	120.1(3)
C(7)-H(7)	0.9500	C(3)-C(2)-N(1)	115.1(3)
C(8)-C(9)	1.386(6)	C(3)-C(2)-C(4)	124.1(4)
C(8)-H(8)	0.9500	N(1)-C(2)-C(4)	120.8(3)
C(9)-N(2)	1.337(5)	C(2)-C(3)-S(1)	110.6(3)
C(9)-H(9)	0.9500	C(2)-C(3)-H(3)	124.7
C(10)-N(3)	1.309(5)	S(1)-C(3)-H(3)	124.7
C(10)-C(14)	1.468(5)	O(2)-C(4)-O(1)	124.6(4)
C(10)-S(2)	1.721(4)	O(2)-C(4)-C(2)	121.1(3)
C(11)-C(12)	1.353(5)	O(1)-C(4)-C(2)	114.3(3)
C(11)-N(3)	1.381(5)	N(2)-C(5)-C(6)	122.4(3)
C(11)-C(13)	1.479(5)	N(2)-C(5)-C(1)	116.3(3)
C(12)-S(2)	1.692(4)	C(6)-C(5)-C(1)	121.4(3)
C(12)-H(12)	0.9500	C(7)-C(6)-C(5)	118.9(4)
C(13)-O(3)	1.218(5)	C(7)-C(6)-H(6)	120.6
C(13)-O(4)	1.310(5)	C(5)-C(6)-H(6)	120.6
C(14)-N(4)	1.345(5)	C(8)-C(7)-C(6)	119.0(4)
C(14)-C(15)	1.378(5)	C(8)-C(7)-H(7)	120.5
C(6)-C(7)-H(7)	120.5	C(16)-C(15)-C(14)	119.6(4)
C(7)-C(8)-C(9)	119.1(4)	C(16)-C(15)-H(15)	120.2
C(7)-C(8)-H(8)	120.4	C(14)-C(15)-H(15)	120.2
C(9)-C(8)-H(8)	120.4	C(15)-C(16)-C(17)	119.2(4)
N(2)-C(9)-C(8)	122.7(4)	C(15)-C(16)-H(16)	120.4
N(2)-C(9)-H(9)	118.6	C(17)-C(16)-H(16)	120.4
C(8)-C(9)-H(9)	118.6	C(16)-C(17)-C(18)	118.2(4)
N(3)-C(10)-C(14)	124.9(3)	C(16)-C(17)-H(17)	120.9

N(3)-C(10)-S(2)	115.2(3)	C(18)-C(17)-H(17)	120.9
C(14)-C(10)-S(2)	119.9(3)	N(4)-C(18)-C(17)	123.8(4)
C(12)-C(11)-N(3)	115.7(3)	N(4)-C(18)-H(18)	118.1
C(12)-C(11)-C(13)	125.2(4)	C(17)-C(18)-H(18)	118.1
N(3)-C(11)-C(13)	119.1(3)	C(1)-N(1)-C(2)	110.2(3)
C(11)-C(12)-S(2)	110.5(3)	C(9)-N(2)-C(5)	117.9(3)
C(11)-C(12)-H(12)	124.8	C(10)-N(3)-C(11)	109.2(3)
S(2)-C(12)-H(12)	124.8	C(18)-N(4)-C(14)	116.7(3)
O(3)-C(13)-O(4)	125.0(4)	C(4)-O(1)-H(1)	109.5
O(3)-C(13)-C(11)	121.9(4)	C(13)-O(4)-H(4)	109.5
O(4)-C(13)-C(11)	113.1(4)	H(5A)-O(5)-H(5B)	115(5)
N(4)-C(14)-C(15)	122.5(3)	C(3)-S(1)-C(1)	89.22(18)
N(4)-C(14)-C(10)	115.3(3)	C(12)-S(2)-C(10)	89.36(19)
C(15)-C(14)-C(10)	122.2(3)		

Table 5-5. Hydrogen bonds for **2-(Pyridin-4-yl)thiazole-4-carboxylic acid (Compound 5a** in the **Chapter 3**) [\AA and $^\circ$].

D-H...A	d(D-H)	d(H...A)	d(D...A)	$\angle(\text{DHA})$
O(1)-H(1)...O(5)	0.84	1.78	2.582(4)	160.1
O(4)-H(4)...O(2)#1	0.84	1.89	2.648(4)	148.8
O(5)-H(5A)...N(3)#2	0.84(4)	2.20(4)	3.032(5)	170(4)
O(5)-H(5A)...O(3)#2	0.84(4)	2.57(4)	3.051(4)	118(4)
O(5)-H(5B)...O(3)#3	0.77(4)	1.97(4)	2.734(4)	173(5)

Symmetry transformations used to generate equivalent atoms:

#1 $x, y+1, z$ #2 $-x+1, -y, -z+1$ #3 $x, y-1, z$

Table 5-6. Crystal data and structure refinement for **thiazole-2-carboxylic acid (Compound 13)** in the **Chapter 3**.

Empirical formula	C ₄ H ₃ NO ₂ S	
Formula weight	129.13	
Temperature	293(2) K	
Wavelength	0.71069 Å	
Crystal system	Orthorhombic	
Space group	<i>P n 2₁ a</i>	
Unit cell dimensions	a = 13.436(4) Å	α = 90°
	b = 10.116(6) Å	β = 90°
	c = 3.884(19) Å	γ = 90°
Volume	527.9(6) Å ³	
Z	4	
Density (calculated)	1.625 mg/m ³	
Absorption coefficient	0.503 mm ⁻¹	
F(000)	264	
Crystal size	0.05 x 0.1 x 0.1 mm ³	
Theta range for data collection	4.03 to 27.40°.	
Index ranges	-17 ≤ h ≤ 17, -12 ≤ k ≤ 12, -5 ≤ l ≤ 5	
Reflections collected	4204	
Independent reflections	1051 [R(int) = 0.0698]	
Completeness to theta = 25.00°	99.2 %	
Refinement method	Full-matrix least-squares on F ²	
Data / restraints / parameters	1051 / 1 / 74	
Goodness-of-fit on F ²	1.108	
Final R indices [I > 2σ(I)]	R1 = 0.0658, wR2 = 0.1719	
R indices (all data)	R1 = 0.0842, wR2 = 0.1868	
Absolute structure parameter	10(10)	
Largest diff. peak and hole	0.401 and -0.506 e.Å ⁻³	

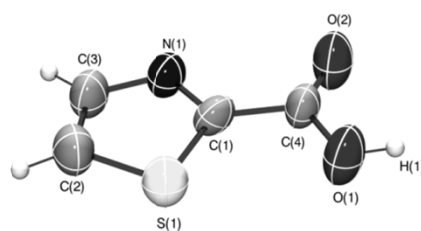


Figure 5-3. ORTEP plot for thiazole-2-carboxylic acid (Compound 13 in the Chapter 3).

Table 5-7. Selected bond lengths [\AA] and angles [$^\circ$] for **thiazole-2-carboxylic acid** (Compound 13 in the Chapter 3).

C(1)-N(1)	1.306(6)	N(1)-C(1)-C(4)	123.1(5)
C(1)-C(4)	1.469(7)	N(1)-C(1)-S(1)	114.0(4)
C(1)-S(1)	1.712(6)	C(4)-C(1)-S(1)	122.9(4)
C(2)-C(3)	1.359(10)	C(3)-C(2)-S(1)	109.8(5)
C(2)-S(1)	1.685(7)	N(1)-C(3)-C(2)	115.5(6)
C(3)-N(1)	1.358(8)	O(2)-C(4)-O(1)	125.5(5)
C(4)-O(2)	1.207(7)	O(2)-C(4)-C(1)	123.1(5)
C(4)-O(1)	1.324(6)	O(1)-C(4)-C(1)	111.4(5)
O(1)-H(1)	0.8200	C(1)-N(1)-C(3)	110.6(5)
		C(2)-S(1)-C(1)	90.1(3)

Table 5-8. Crystal data and structure refinement for **Zn(4-tzc)₂•2H₂O (Compound 14** in the **Chapter 3)**

Empirical formula	C ₈ H ₈ N ₂ O ₆ S ₂ Zn
Formula weight	357.65
Temperature	293(2) K
Wavelength	0.71069 Å
Crystal system	Monoclinic
Space group	<i>P</i> 2 ₁ / <i>c</i>
Unit cell dimensions	a = 5.261(2) Å α = 90° b = 11.3280(12) Å β = 98.25(2)° c = 9.880(2) Å γ = 90°
Volume	582.7(3) Å ³
Z	2
Density (calculated)	2.038 mg/m ³
Absorption coefficient	2.490 mm ⁻¹
F(000)	360
Crystal size	0.15 x 0.2 x 0.22 mm ³
Theta range for data collection	2.75 to 24.97°.
Index ranges	-6 ≤ h ≤ 6, 0 ≤ k ≤ 13, 0 ≤ l ≤ 11
Reflections collected	1089
Independent reflections	1027 [R(int) = 0.0410]
Completeness to theta = 24.97°	100.0 %
Refinement method	Full-matrix least-squares on F ²
Data / restraints / parameters	1027 / 0 / 96
Goodness-of-fit on F ²	1.392
Final R indices [I > 2σ(I)]	R1 = 0.0364, wR2 = 0.0952
R indices (all data)	R1 = 0.0383, wR2 = 0.0964
Largest diff. peak and hole	1.034 and -0.762 e.Å ⁻³

Table 5-9. Crystal data and structure refinement for **Cu(4-tzc)₂** (**Compound 15** in the **Chapter 3**)

Empirical formula	C ₈ H ₄ CuN ₂ O ₄ S ₂	
Formula weight	319.79	
Temperature	293(2) K	
Wavelength	0.71069 Å	
Crystal system	Monoclinic	
Space group	<i>P</i> 2 ₁ / <i>c</i>	
Unit cell dimensions	a = 5.211(5) Å	α = 90°
	b = 11.634(3) Å	β = 91.52(5)°
	c = 8.136(2) Å	γ = 90°
Volume	493.1(5) Å ³	
Z	2	
Density (calculated)	2.154 mg/m ³	
Absorption coefficient	2.640 mm ⁻¹	
F(000)	318	
Crystal size	0.13 x 0.15 x 0.4 mm ³	
Theta range for data collection	3.06 to 24.96°	
Index ranges	-6 ≤ h ≤ 6, 0 ≤ k ≤ 13, 0 ≤ l ≤ 9	
Reflections collected	930	
Independent reflections	865 [R(int) = 0.0954]	
Completeness to theta = 24.96°	100.0 %	
Refinement method	Full-matrix least-squares on F ²	
Data / restraints / parameters	865 / 0 / 79	
Goodness-of-fit on F ²	1.069	
Final R indices [I > 2σ(I)]	R1 = 0.0504, wR2 = 0.1259	
R indices (all data)	R1 = 0.0632, wR2 = 0.1342	
Largest diff. peak and hole	0.897 and -0.979 e.Å ⁻³	

Table 5-10. Crystal data and structure refinement for **[Zn(tzc-Hpy)₂•2H₂O][ClO₄]₂** (Compound 16 in the Chapter 3)

Empirical formula	C ₁₈ H ₁₆ Cl ₂ N ₄ O ₁₄ S ₂ Zn
Formula weight	712.74
Temperature	293(2) K
Wavelength	0.71069 Å
Crystal system	Triclinic
Space group	<i>P</i> -1
Unit cell dimensions	a = 6.4580(10) Å α = 88.5250(10)° b = 8.7600(10) Å β = 88.1780(14)° c = 11.912(2) Å γ = 72.4360(13)°
Volume	642.05(16) Å ³
Z	1
Density (calculated)	1.843 mg/m ³
Absorption coefficient	1.406 mm ⁻¹
F(000)	360
Crystal size	0.05 x 0.05 x 0.1 mm ³
Theta range for data collection	3.81 to 27.65°.
Index ranges	-6 ≤ h ≤ 8, -9 ≤ k ≤ 11, -14 ≤ l ≤ 13
Reflections collected	2983
Independent reflections	1988 [R(int) = 0.0350]
Completeness to theta = 25.00°	81.7 %
Refinement method	Full-matrix least-squares on F ²
Data / restraints / parameters	1988 / 0 / 201
Goodness-of-fit on F ²	1.028
Final R indices [I > 2σ(I)]	R1 = 0.0591, wR2 = 0.1520
R indices (all data)	R1 = 0.0865, wR2 = 0.1640
Largest diff. peak and hole	0.791 and -0.609 e.Å ⁻³

Table 5-11. Crystal data and structure refinement for **Zn(tzc-py)₂•H₂O (Compound 17** in the **Chapter 3)**

Empirical formula	C ₁₈ H ₁₂ N ₄ O ₅ S ₂ Zn
Formula weight	493.81
Temperature	150(2) K
Wavelength	0.71069 Å
Crystal system	Triclinic
Space group	<i>P</i> -1
Unit cell dimensions	a = 6.717(3) Å α = 103.600(4)° b = 10.782(4) Å β = 97.122(3)° c = 13.001(6) Å γ = 97.087(3)°
Volume	896.7(7) Å ³
Z	2
Density (calculated)	1.829 mg/m ³
Absorption coefficient	1.646 mm ⁻¹
F(000)	500
Crystal size	0.04 x 0.08 x 0.1 mm ³
Theta range for data collection	3.85 to 32.45°
Index ranges	-9 ≤ h ≤ 8, -15 ≤ k ≤ 15, -19 ≤ l ≤ 17
Reflections collected	11296
Independent reflections	5762 [R(int) = 0.0222]
Completeness to theta = 30.44°	99.4 %
Refinement method	Full-matrix least-squares on F ²
Data / restraints / parameters	5762 / 0 / 272
Goodness-of-fit on F ²	0.930
Final R indices [I > 2σ(I)]	R1 = 0.0302, wR2 = 0.0682
R indices (all data)	R1 = 0.0443, wR2 = 0.0710
Largest diff. peak and hole	0.506 and -0.635 e.Å ⁻³

Table 5-12. Crystal data and structure refinement for **Co(tzc-py)₂•2H₂O (Compound 18 in the Chapter 3)**

Empirical formula	C ₁₈ H ₁₄ CoN ₄ O ₆ S ₂	
Formula weight	505.39	
Temperature	150(2) K	
Wavelength	0.71069 Å	
Crystal system	Monoclinic	
Space group	<i>P</i> 2 ₁ / <i>c</i>	
Unit cell dimensions	a = 8.732(5) Å	α = 90°
	b = 11.196(5) Å	β = 97.991(5)°
	c = 9.520(6) Å	γ = 90°
Volume	921.7(8) Å ³	
Z	2	
Density (calculated)	1.821 mg/m ³	
Absorption coefficient	1.207 mm ⁻¹	
F(000)	514	
Crystal size	0.02 x 0.08 x 0.1 mm ³	
Theta range for data collection	3.87 to 32.45°.	
Index ranges	-12 ≤ h ≤ 12, -16 ≤ k ≤ 16, -13 ≤ l ≤ 13	
Reflections collected	12294	
Independent reflections	3079 [R(int) = 0.0525]	
Completeness to theta = 32.45°	92.6 %	
Refinement method	Full-matrix least-squares on F ²	
Data / restraints / parameters	3079 / 0 / 143	
Goodness-of-fit on F ²	1.214	
Final R indices [I > 2σ(I)]	R1 = 0.0685, wR2 = 0.1073	
R indices (all data)	R1 = 0.0897, wR2 = 0.1131	
Largest diff. peak and hole	0.692 and -0.971 e.Å ⁻³	

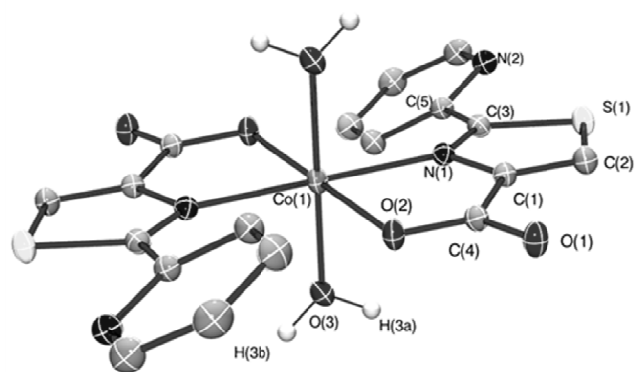


Figure 5-4. ORTEP plot for $\text{Co}(\text{tzc-py})_2 \cdot 2\text{H}_2\text{O}$ (Compound 18 in the Chapter 3).

Table 5-13. Bond lengths [\AA] and angles [$^\circ$] for $\text{Co}(\text{tzc-py})_2 \cdot 2\text{H}_2\text{O}$ (Compound 18 in the Chapter 3).

C(1)-N(1)	1.477(4)	O(1)-C(4)-O(2)#3	124.4(3)
C(1)-C(2)	1.523(4)	O(1)-C(4)-C(3)#3	116.1(3)
C(1)-C(5)#1	1.537(4)	O(2)#3-C(4)-C(3)#3	119.4(3)
C(2)-S(1)	1.809(3)	O(3)#4-C(5)-O(5)	122.4(3)
C(3)-N(1)	1.483(4)	O(3)#4-C(5)-C(1)#4	119.0(3)
C(3)-S(1)	1.839(3)	O(5)-C(5)-C(1)#4	118.6(3)
C(4)-O(1)	1.250(4)	C(1)-N(1)-C(3)	112.4(2)
C(5)-O(5)	1.264(4)	C(1)-N(1)-Co(1)	109.11(19)
N(1)-Co(1)	2.154(3)	C(3)-N(1)-Co(1)	108.53(19)
N(1)-H(1)	0.80(4)	C(1)-N(1)-H(1)	110(3)
O(1)-Co(1)	2.069(2)	C(3)-N(1)-H(1)	110(3)
O(2)-Co(1)	2.056(2)	Co(1)-N(1)-H(1)	110(3)
O(3)-Co(1)	2.080(2)	C(4)-O(1)-Co(1)	123.3(2)
O(4)-Co(1)	2.075(3)	C(4)#2-O(2)-Co(1)	115.5(2)
O(4)-H(4A)	0.840(19)	C(5)#1-O(3)-Co(1)	116.7(2)
O(4)-H(4B)	0.812(19)	Co(1)-O(4)-H(4A)	125(3)
O(5)-Co(1)	2.109(2)	Co(1)-O(4)-H(4B)	124(3)
N(1)-C(1)-C(2)	107.9(2)	H(4A)-O(4)-H(4B)	108(4)
N(1)-C(1)-C(5)#1	110.5(2)	C(5)-O(5)-Co(1)	133.6(2)
C(2)-C(1)-C(5)#1	112.3(2)	O(6)#4-O(6)-O(6)#1	165.2(6)
N(1)-C(1)-H(1A)	108.7	C(2)-S(1)-C(3)	90.56(15)
C(2)-C(1)-H(1A)	108.7	O(2)-Co(1)-O(1)	98.32(9)
C(5)#1-C(1)-H(1A)	108.7	O(2)-Co(1)-O(4)	175.48(10)
C(1)-C(2)-S(1)	104.0(2)	O(1)-Co(1)-O(4)	84.56(10)
C(1)-C(2)-H(2A)	111.0	O(2)-Co(1)-O(3)	93.42(9)
S(1)-C(2)-H(2A)	111.0	O(1)-Co(1)-O(3)	66.89(9)
C(1)-C(2)-H(2B)	111.0	O(4)-Co(1)-O(3)	83.38(10)
S(1)-C(2)-H(2B)	111.0	O(2)-Co(1)-O(5)	90.93(10)
H(2A)-C(2)-H(2B)	109.0	O(1)-Co(1)-O(5)	92.68(9)
N(1)-C(3)-C(4)#2	113.2(3)	O(4)-Co(1)-O(5)	92.42(11)
N(1)-C(3)-S(1)	107.6(2)	O(3)-Co(1)-O(5)	92.96(9)
C(4)#2-C(3)-S(1)	107.2(2)	O(2)-Co(1)-N(1)	81.32(11)
N(1)-C(3)-H(3)	109.6	O(1)-Co(1)-N(1)	97.11(10)
C(4)#2-C(3)-H(3)	109.6	O(4)-Co(1)-N(1)	94.90(11)
S(1)-C(3)-H(3)	109.6	O(3)-Co(1)-N(1)	78.84(10)
		O(5)-Co(1)-N(1)	168.29(10)

Symmetry transformations used to generate equivalent atoms:
 #1 $y, -x, z-1/4$ #2 $-x+1, -y, z+1/2$ #3 $-x+1, -y, z-1/2$; #4 $-y, x, z+1/4$

Table 5-14. Bond lengths [Å] and angles [°] for [Co(tdca)(H₂O)•(H₂O)_{0.5}]_∞ (Compound 21 in the Chapter 3).

Empirical formula	C ₅ H ₉ CoNO ₆ S	
Formula weight	270.13	
Temperature	100(2) K	
Wavelength	0.71069 Å	
Crystal system	Tetragonal	
Space group	<i>P</i> 4 ₁	
Unit cell dimensions	a = 12.335(4) Å	α = 90°
	b = 12.335(4) Å	β = 90°
	c = 5.265(3) Å	γ = 90°
Volume	801.1(9) Å ³	
Z	4	
Density (calculated)	2.165 Mg/m ³	
Absorption coefficient	2.398 mm ⁻¹	
F(000)	528	
Crystal size	0.05 x 0.05 x 0.1 mm ³	
Theta range for data collection	4.21 to 28.95°.	
Index ranges	-15 ≤ h ≤ 16, -15 ≤ k ≤ 16, -7 ≤ l ≤ 7	
Reflections collected	4373	
Independent reflections	1769 [R(int) = 0.0325]	
Completeness to theta = 28.95°	87.4 %	
Refinement method	Full-matrix least-squares on F ²	
Data / restraints / parameters	1769 / 3 / 131	
Goodness-of-fit on F ²	0.996	
Final R indices [I > 2σ(I)]	R1 = 0.0280, wR2 = 0.0610	
R indices (all data)	R1 = 0.0333, wR2 = 0.0627	
Absolute structure parameter	-0.010(17)	
Largest diff. peak and hole	0.551 and -0.421 e.Å ⁻³	

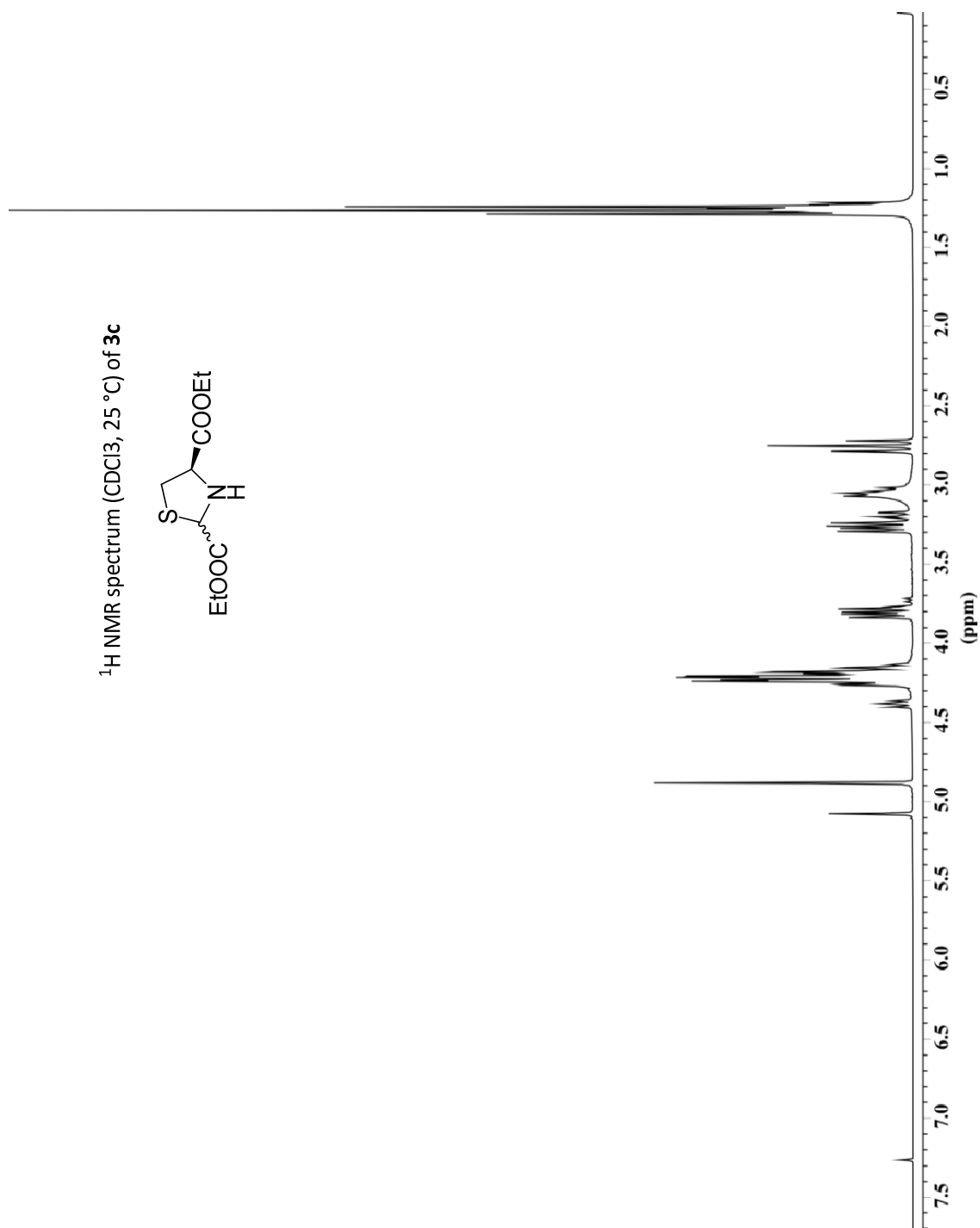
Table 5-15. Bond lengths [Å] and angles [°] for **[Co(tdca)(H₂O)•(H₂O)_{0.5}]_∞** (Compound 21 in the Chapter 3).

C(1)-N(1)	1.477(4)	O(1)-C(4)-C(3)#3	116.1(3)
C(1)-C(2)	1.523(4)	O(2)#3-C(4)-C(3)#3	119.4(3)
C(1)-C(5)#1	1.537(4)	O(3)#4-C(5)-O(5)	122.4(3)
C(2)-S(1)	1.809(3)	O(3)#4-C(5)-C(1)#4	119.0(3)
C(3)-N(1)	1.483(4)	O(5)-C(5)-C(1)#4	118.6(3)
C(3)-S(1)	1.839(3)	C(1)-N(1)-C(3)	112.4(2)
C(4)-O(1)	1.250(4)	C(1)-N(1)-Co(1)	109.11(19)
C(5)-O(5)	1.264(4)	C(3)-N(1)-Co(1)	108.53(19)
N(1)-Co(1)	2.154(3)	C(1)-N(1)-H(1)	110(3)
N(1)-H(1)	0.80(4)	C(3)-N(1)-H(1)	113(3)
O(1)-Co(1)	2.069(2)	Co(1)-N(1)-H(1)	103(3)
O(2)-Co(1)	2.056(2)	C(4)-O(1)-Co(1)	123.3(2)
O(3)-Co(1)	2.080(2)	C(4)#2-O(2)-Co(1)	115.5(2)
O(4)-Co(1)	2.075(3)	C(5)#1-O(3)-Co(1)	116.7(2)
O(4)-H(4A)	0.840(19)	Co(1)-O(4)-H(4A)	125(3)
O(4)-H(4B)	0.812(19)	Co(1)-O(4)-H(4B)	124(3)
O(5)-Co(1)	2.109(2)	H(4A)-O(4)-H(4B)	108(4)
N(1)-C(1)-C(2)	107.9(2)	C(5)-O(5)-Co(1)	133.6(2)
N(1)-C(1)-C(5)#1	110.5(2)	O(6)#4-O(6)-O(6)#1	165.2(6)
C(2)-C(1)-C(5)#1	112.3(2)	C(2)-S(1)-C(3)	90.56(15)
N(1)-C(1)-H(1A)	108.7	O(2)-Co(1)-O(1)	98.32(9)
C(2)-C(1)-H(1A)	108.7	O(2)-Co(1)-O(4)	175.48(10)
C(5)#1-C(1)-H(1A)	108.7	O(1)-Co(1)-O(4)	84.56(10)
C(1)-C(2)-S(1)	104.0(2)	O(2)-Co(1)-O(3)	93.42(9)
C(1)-C(2)-H(2A)	111.0	O(1)-Co(1)-O(3)	166.89(9)
S(1)-C(2)-H(2A)	111.0	O(4)-Co(1)-O(3)	83.38(10)
C(1)-C(2)-H(2B)	111.0	O(2)-Co(1)-O(5)	90.93(10)
S(1)-C(2)-H(2B)	111.0	O(1)-Co(1)-O(5)	92.68(9)
H(2A)-C(2)-H(2B)	109.0	O(4)-Co(1)-O(5)	92.42(11)
N(1)-C(3)-C(4)#2	113.2(3)	O(3)-Co(1)-O(5)	92.96(9)
N(1)-C(3)-S(1)	107.6(2)	O(2)-Co(1)-N(1)	81.32(11)
C(4)#2-C(3)-S(1)	107.2(2)	O(1)-Co(1)-N(1)	97.11(10)
N(1)-C(3)-H(3)	109.6	O(4)-Co(1)-N(1)	94.90(11)
C(4)#2-C(3)-H(3)	109.6	O(3)-Co(1)-N(1)	78.84(10)
S(1)-C(3)-H(3)	109.6	O(5)-Co(1)-N(1)	168.29(10)
O(1)-C(4)-O(2)#3	124.4(3)		

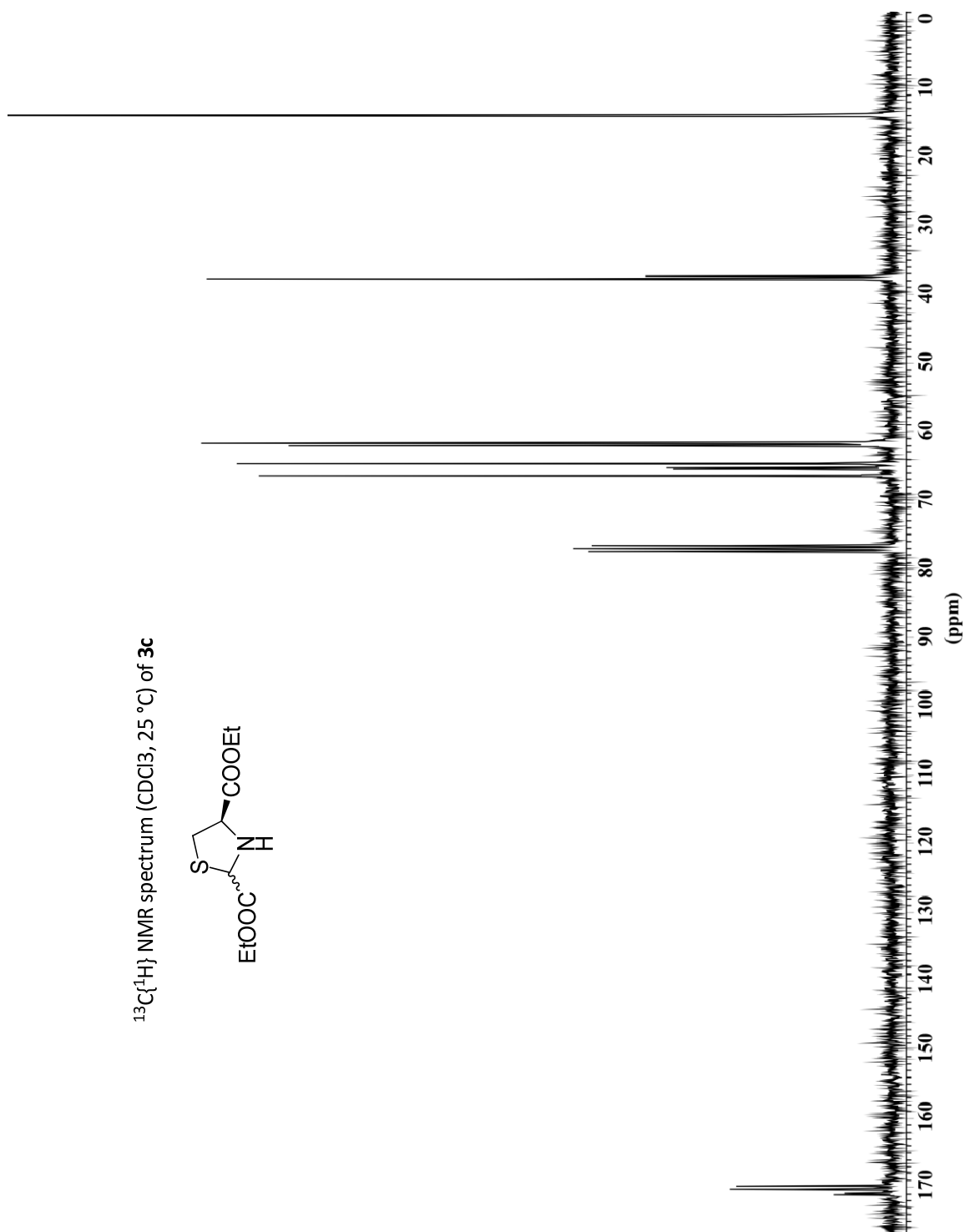
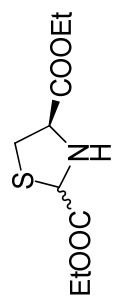
Symmetry transformations used to generate equivalent atoms:

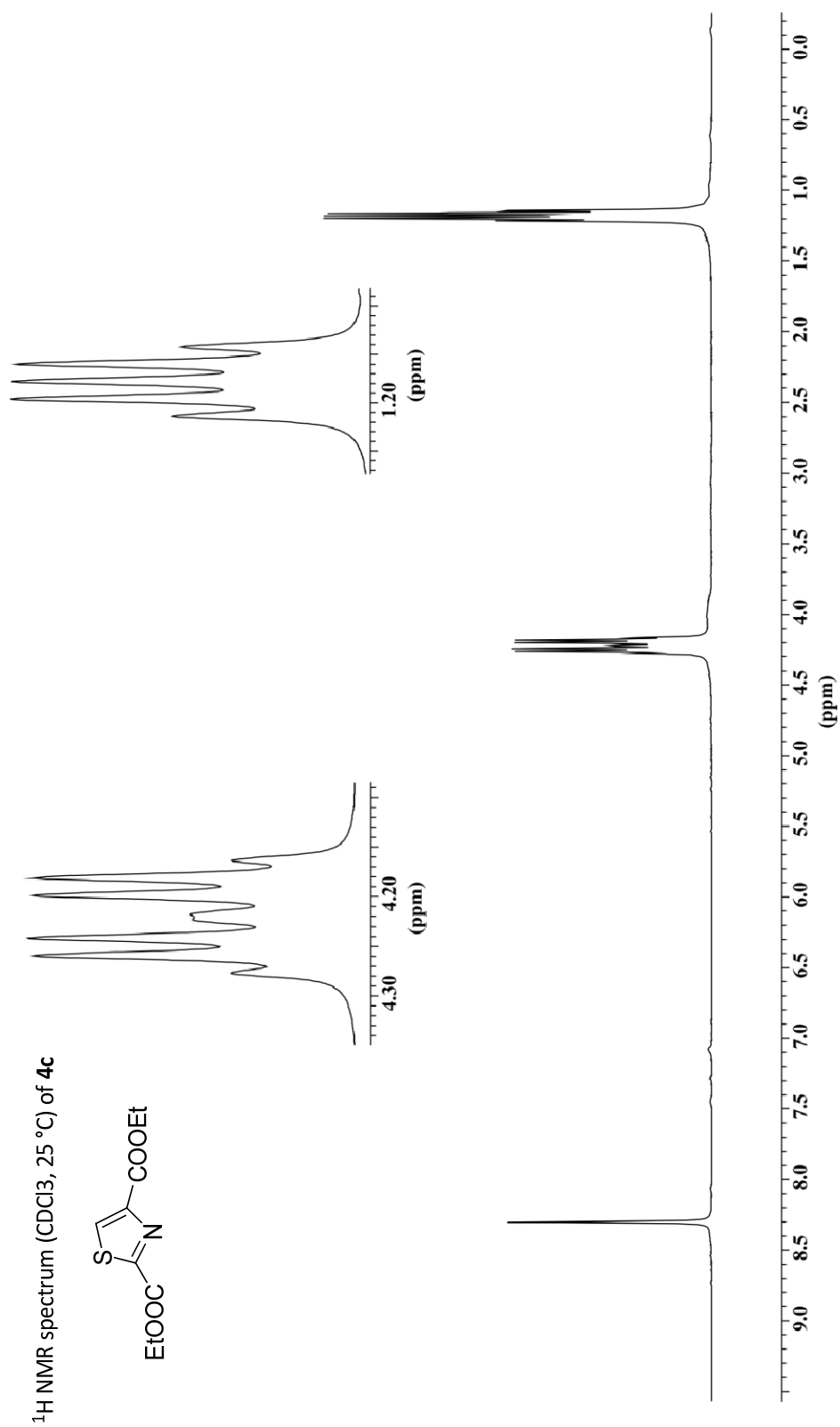
#1 $y, -x, z-1/4$ #2 $-x+1, -y, z+1/2$ #3 $-x+1, -y, z-1/2$ #4 $-y, x, z+1/4$

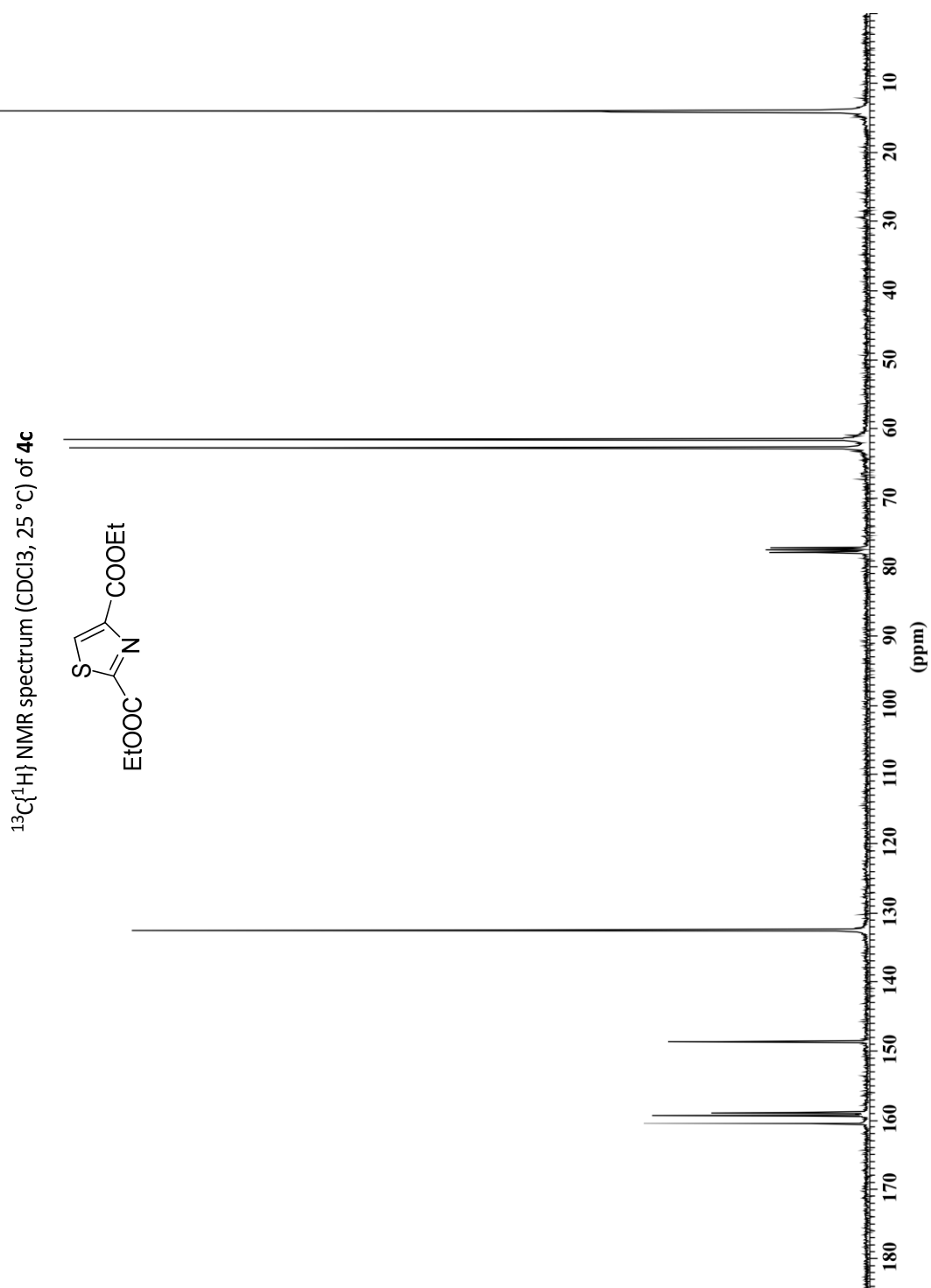
Selected ^1H and $^{13}\text{C}\{^1\text{H}\}$ NMR spectra of thiazole ligands and precursors
(Chapter 3)



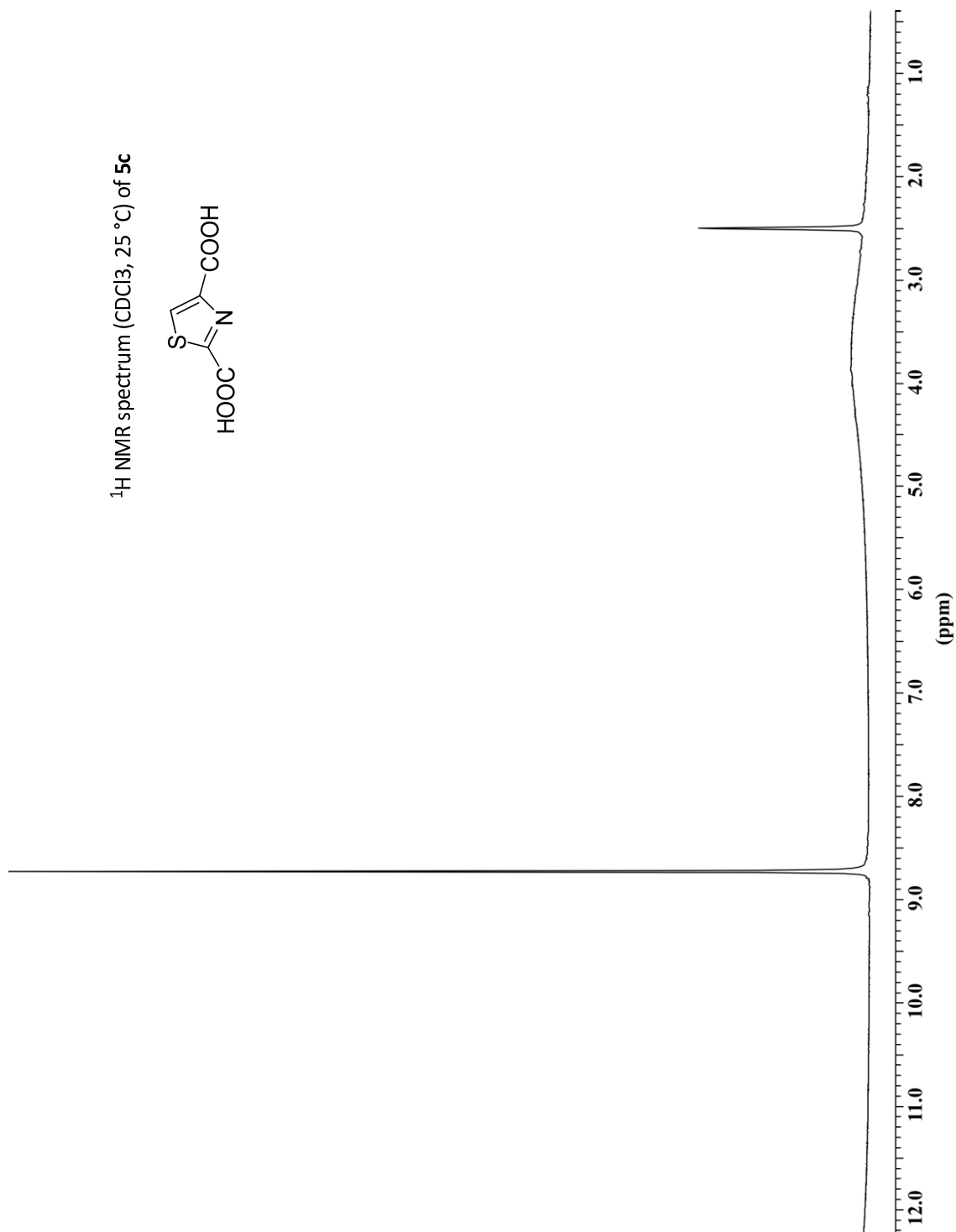
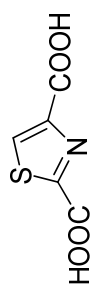
$^{13}\text{C}\{^1\text{H}\}$ NMR spectrum (CDCl_3 , 25 °C) of **3c**



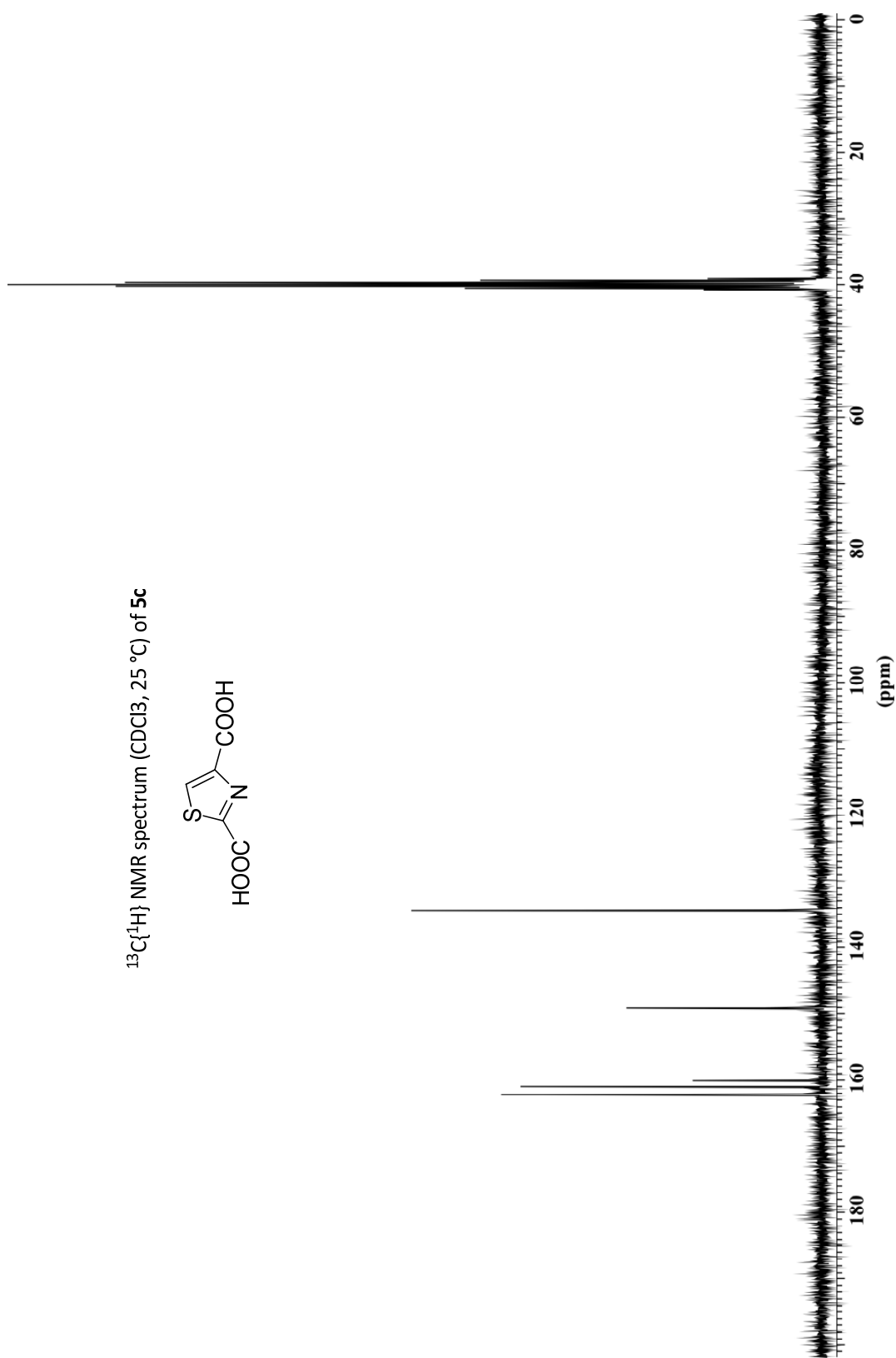
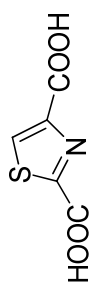




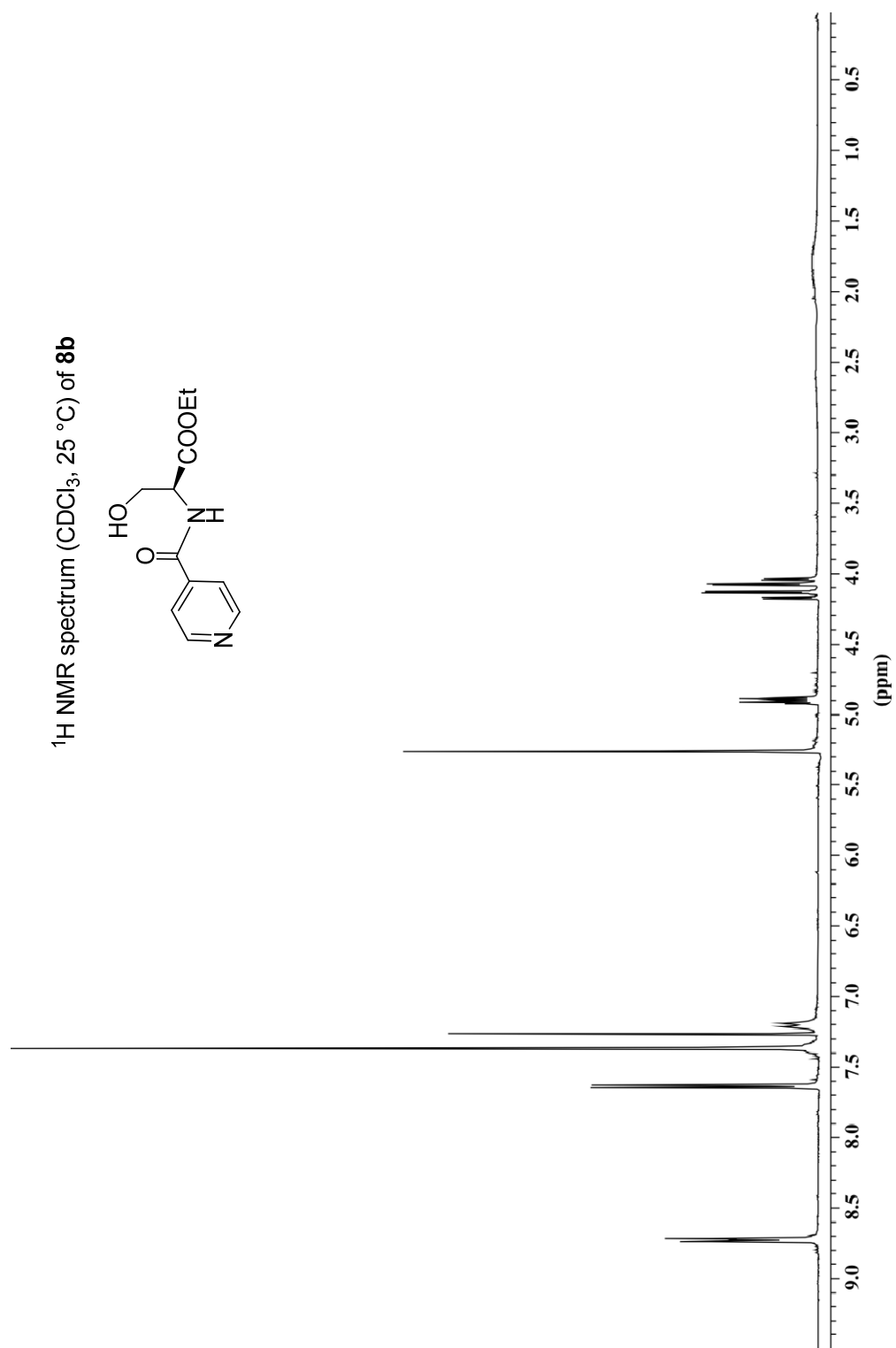
^1H NMR spectrum (CDCl_3 , 25°C) of **5c**

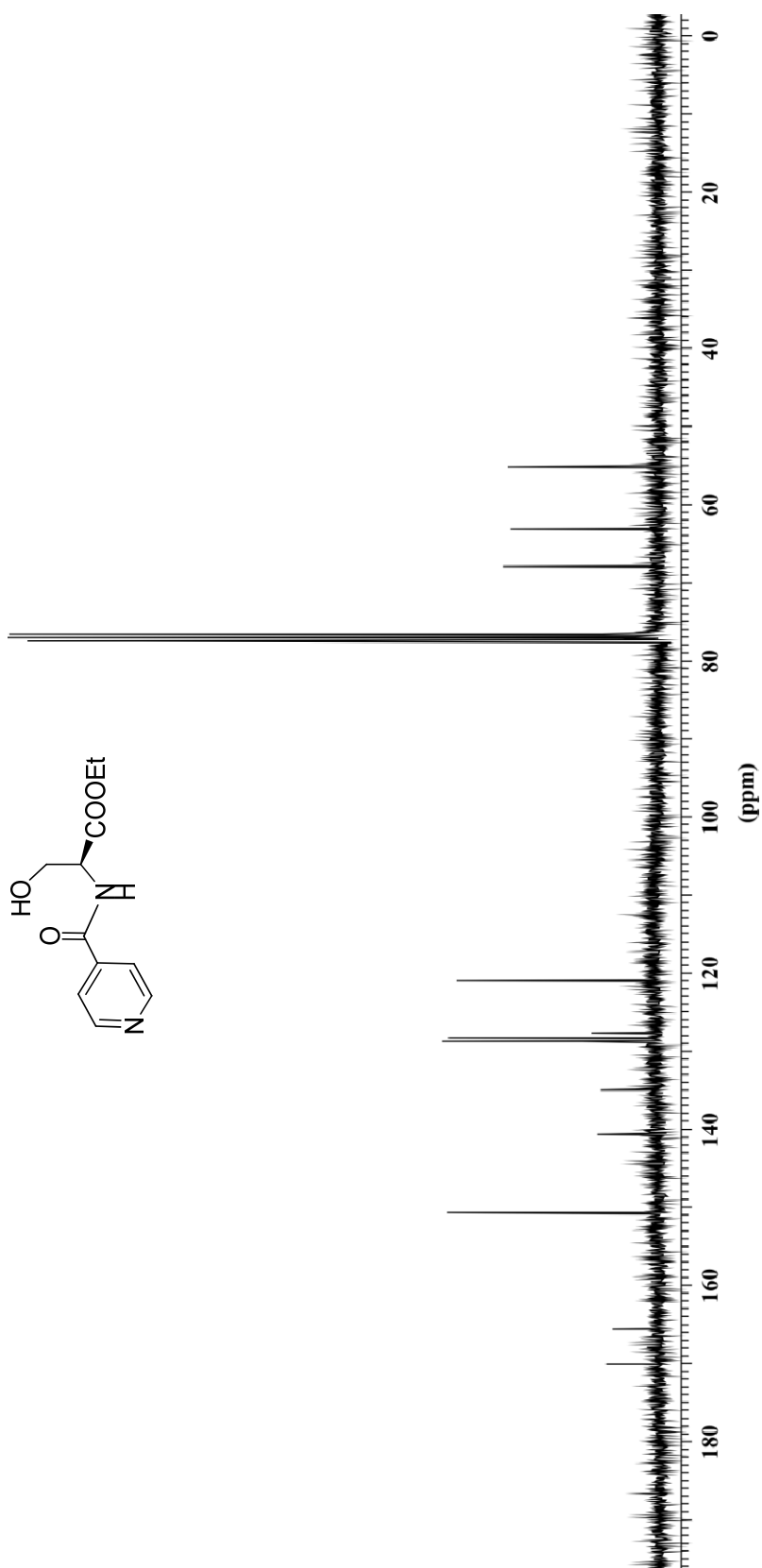


$^{13}\text{C}\{^1\text{H}\}$ NMR spectrum (CDCl_3 , 25°C) of **5c**

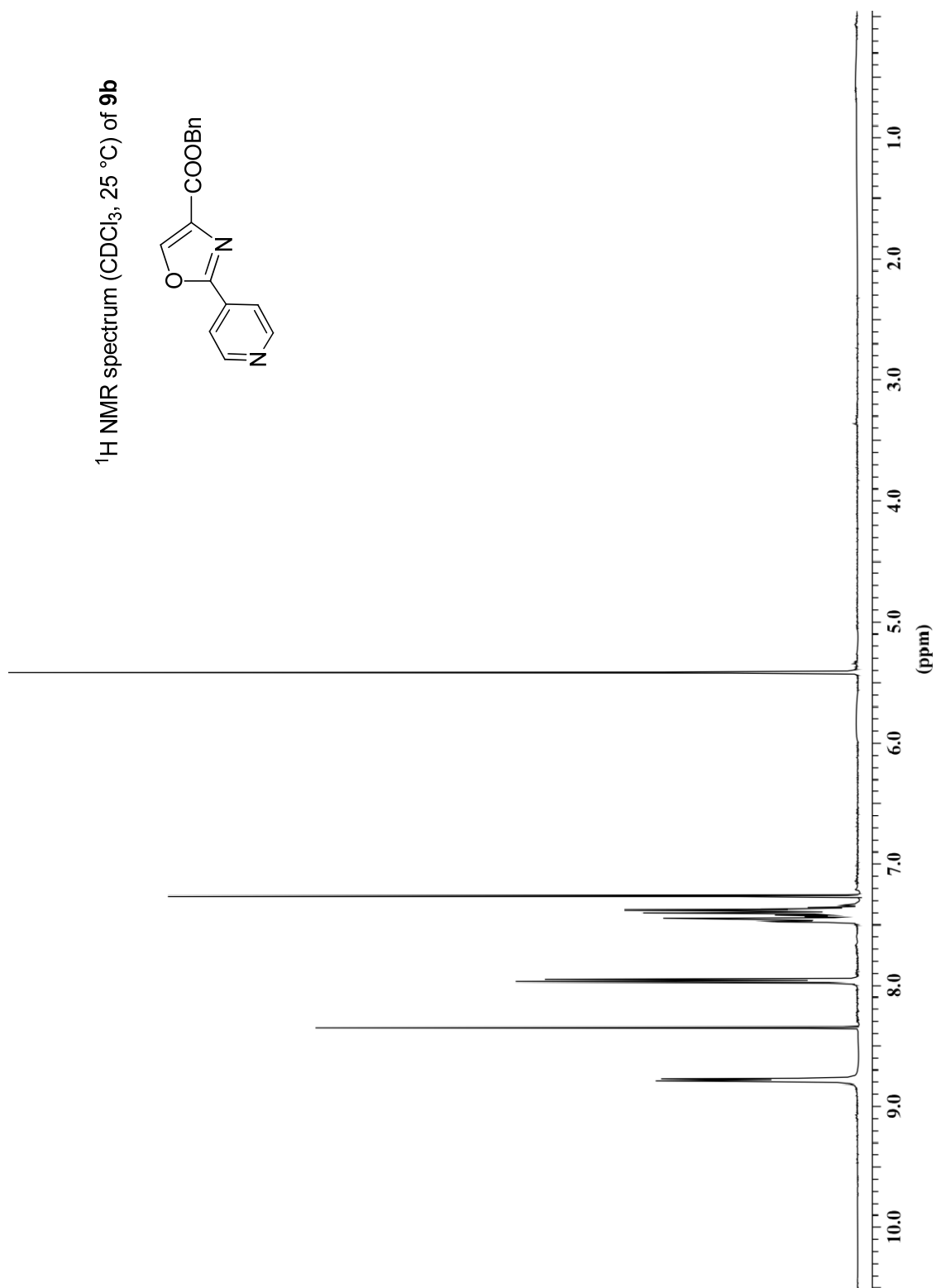
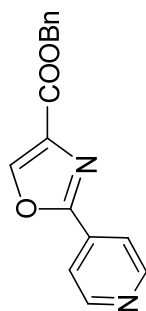


Selected ^1H and $^{13}\text{C}\{^1\text{H}\}$ NMR spectra of oxazole ligands and precursors
(Chapter 3)

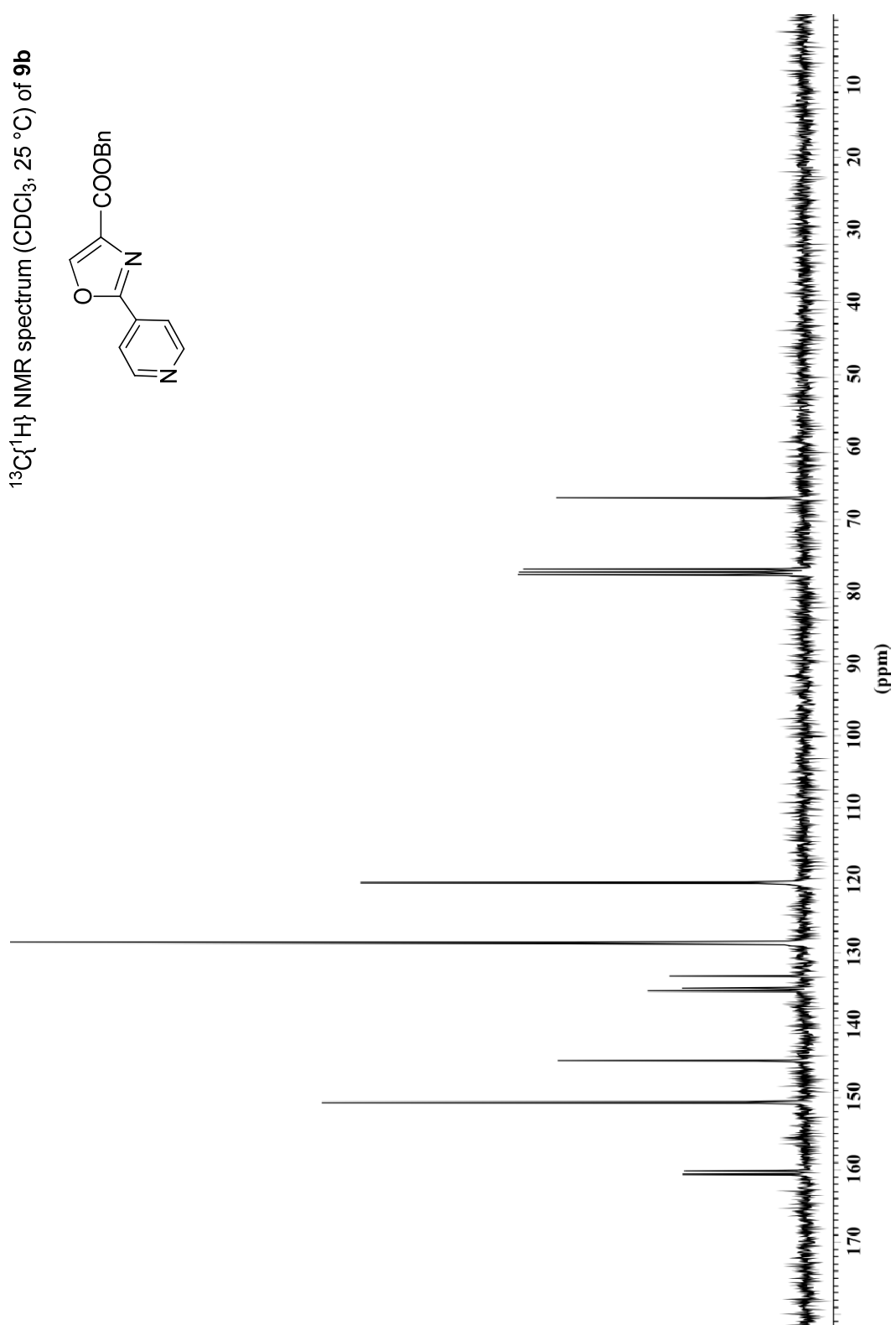
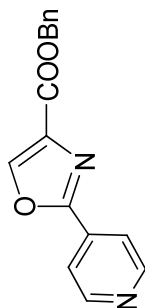


$^{13}\text{C}\{^1\text{H}\}$ NMR spectrum (CDCl_3 , $25\text{ }^\circ\text{C}$) of **8b**

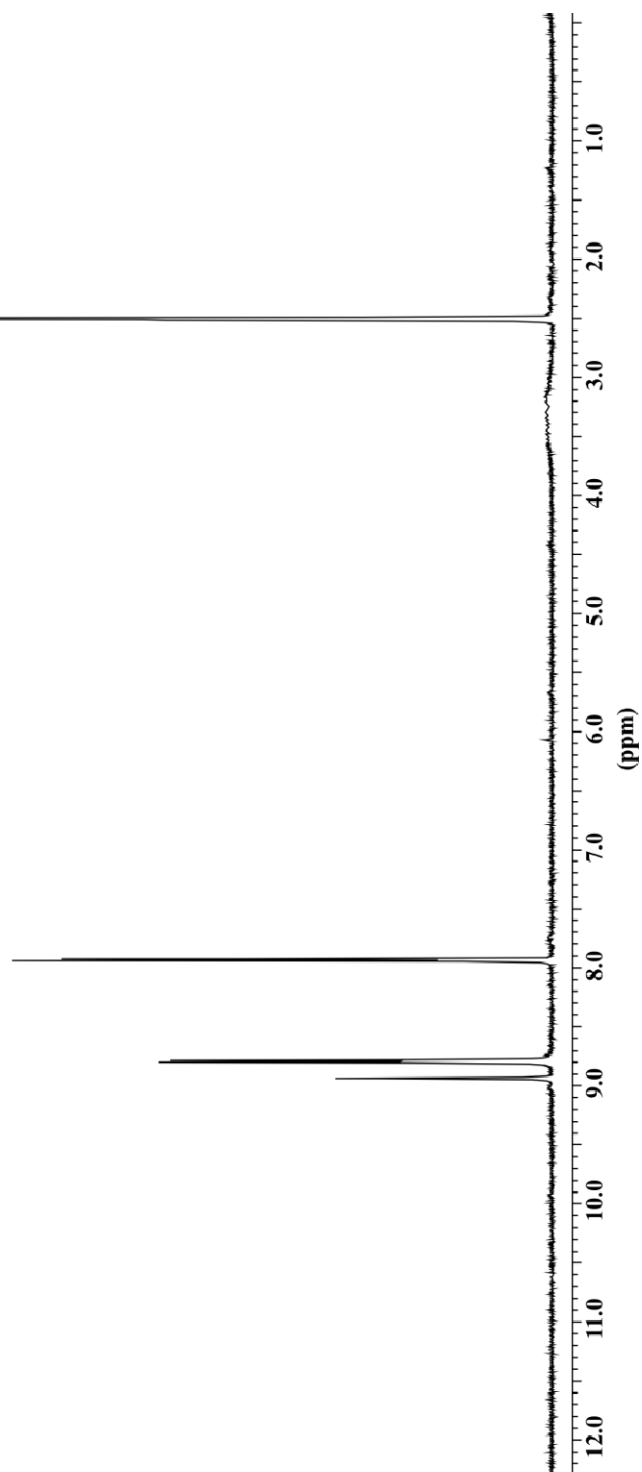
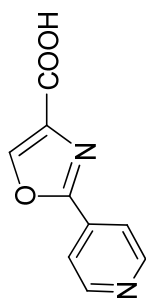
^1H NMR spectrum (CDCl_3 , 25 °C) of **9b**



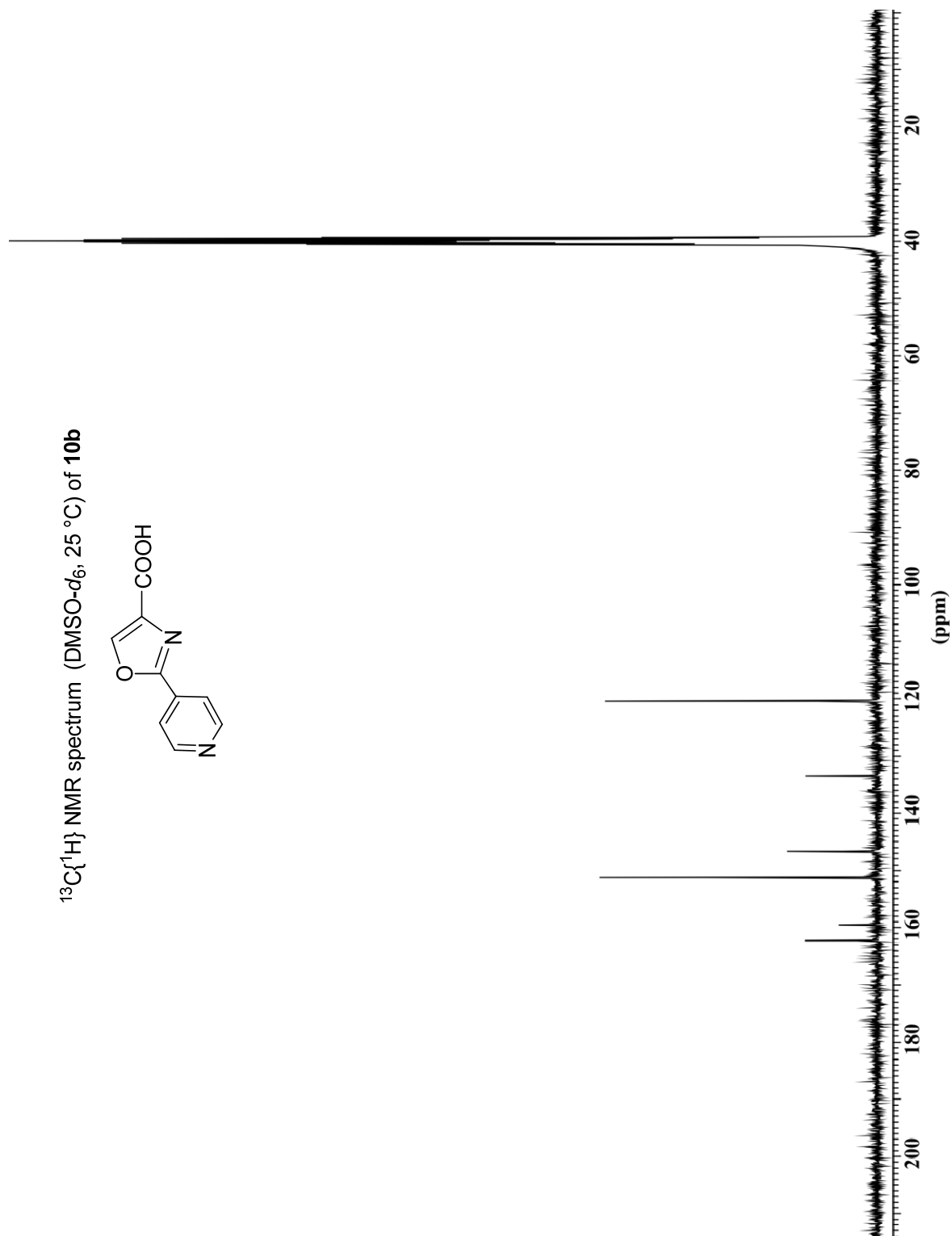
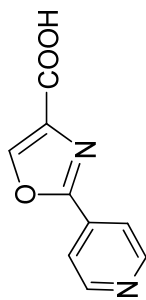
$^{13}\text{C}\{^1\text{H}\}$ NMR spectrum (CDCl_3 , 25 °C) of **9b**



¹H NMR spectrum (DMSO-*d*₆, 25 °C) of **10b**



$^{13}\text{C}\{^1\text{H}\}$ NMR spectrum (DMSO- d_6 , 25 °C) of **10b**



5.3 Appendix to Chapter 4

Table 5-16. Crystal data and structure refinement for $[\{\text{CpRuCl}\}_{\mu\text{-dppab}}]_2$ (Compound 7 in the Chapter 4).

Empirical formula	$\text{C}_{78}\text{H}_{58}\text{Cl}_2\text{P}_4\text{Ru}_2$	
Formula weight	1392.16	
Temperature	150(2) K	
Wavelength	0.71069 Å	
Crystal system	Orthorhombic	
Space group	$P\ c\ a\ 21$	
Unit cell dimensions	$a = 18.7930(10)$ Å	$\alpha = 90^\circ$
	$b = 17.3350(10)$ Å	$\beta = 90^\circ$
	$c = 20.0080(10)$ Å	$\gamma = 90^\circ$
Volume	$6518.1(6)$ Å ³	
Z	4	
Density (calculated)	1.419 mg/m ³	
Absorption coefficient	0.688 mm ⁻¹	
F(000)	2832	
Crystal size	0.15 x 0.07 x 0.05 mm ³	
Theta range for data collection	3.75 to 25°	
Index ranges	$-22 \leq h \leq 15, -20 \leq k \leq 20, -23 \leq l \leq 23$	
Reflections collected	23772	
Independent reflections	10001 [R(int) = 0.0907]	
Completeness to theta = 25°	99.2 %	
Absorption correction	Semi-empirical from equivalents	
Max. and min. transmission	1 and 0.47465	
Refinement method	Full-matrix least-squares on F ²	
Data / restraints / parameters	10001 / 31 / 767	
Goodness-of-fit on F ²	1.033	
Final R indices [$I > 2\sigma(I)$]	R1 = 0.0803, wR2 = 0.1669	
R indices (all data)	R1 = 0.1675, wR2 = 0.2168	
Absolute structure parameter	0.50(7)	
Largest diff. peak and hole	0.956 and -0.678 e.Å ⁻³	

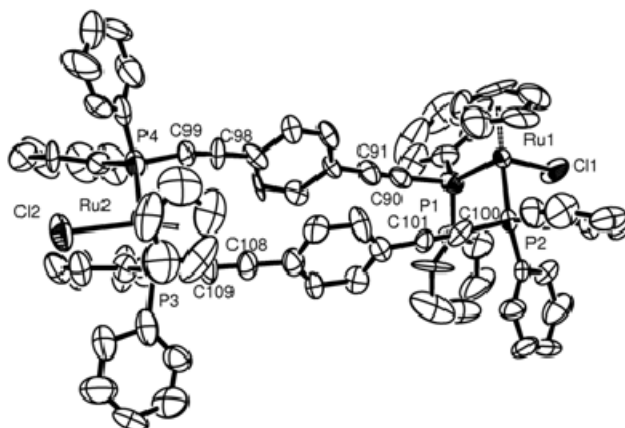


Figure 5-5. ORTEP plot for $[\{\text{CpRuCl}\}(\mu\text{-dppab})]_2$.

Table 5-17. Selected bond lengths [Å] and angles [°] for $[\{\text{CpRuCl}\}(\mu\text{-dppab})]_2$ (Compound 7 in the Chapter 4).

Ru(1)-C(3)	2.216(17)	C(102)-C(107)	1.39(2)
Ru(1)-C(4)	2.238(16)	C(102)-C(103)	1.40(2)
Ru(1)-C(1)	2.243(14)		
Ru(1)-P(1)	2.284(4)	C(2)-Ru(1)-C(3)	35.9(7)
Ru(1)-C(5)	2.286(16)	C(2)-Ru(1)-C(4)	62.4(8)
Ru(1)-P(2)	2.309(4)	C(3)-Ru(1)-C(4)	38.3(7)
Ru(1)-Cl(1)	2.420(5)	C(2)-Ru(1)-C(1)	36.7(6)
Ru(2)-C(9)	2.193(14)	C(3)-Ru(1)-C(1)	61.5(7)
Ru(2)-C(8)	2.197(15)	C(4)-Ru(1)-C(1)	63.2(8)
Ru(2)-C(10)	2.226(13)	C(2)-Ru(1)-P(1)	112.7(6)
Ru(2)-C(7)	2.233(15)	C(3)-Ru(1)-P(1)	90.3(4)
Ru(2)-C(6)	2.251(16)	C(4)-Ru(1)-P(1)	103.1(6)
Ru(2)-P(4)	2.270(5)	C(1)-Ru(1)-P(1)	149.1(6)
Ru(2)-P(3)	2.293(5)	C(2)-Ru(1)-C(5)	61.0(8)
Ru(2)-Cl(2)	2.444(4)	C(3)-Ru(1)-C(5)	62.6(7)
Ru(1)-Cp(centroid)	1.865	C(4)-Ru(1)-C(5)	38.9(7)
Ru(2)-Cp(centroid)	1.863	C(1)-Ru(1)-C(5)	36.3(7)
P(1)-C(11)	1.779(17)	P(1)-Ru(1)-C(5)	141.7(5)
P(1)-C(90)	1.833(18)	C(2)-Ru(1)-P(2)	95.7(6)
P(1)-C(21)	1.853(16)	C(3)-Ru(1)-P(2)	126.6(6)
P(2)-C(100)	1.782(18)	C(4)-Ru(1)-P(2)	156.1(6)
P(2)-C(41)	1.826(18)	C(1)-Ru(1)-P(2)	93.7(6)
P(2)-C(31)	1.830(16)	P(1)-Ru(1)-P(2)	93.98(14)
P(3)-C(109)	1.785(15)	C(5)-Ru(1)-P(2)	123.6(5)
P(3)-C(61)	1.79(2)	C(2)-Ru(1)-Cl(1)	151.3(5)
P(3)-C(51)	1.846(17)	C(3)-Ru(1)-Cl(1)	136.5(6)
P(4)-C(71)	1.80(2)	C(4)-Ru(1)-Cl(1)	99.4(7)
P(4)-C(99)	1.840(16)	C(1)-Ru(1)-Cl(1)	116.5(6)
P(4)-C(81)	1.842(17)	P(1)-Ru(1)-Cl(1)	92.2(2)
C(1)-C(2)	1.38(2)	C(5)-Ru(1)-Cl(1)	90.7(6)
C(98)-C(99)	1.149(18)	P(2)-Ru(1)-Cl(1)	96.48(16)
C(100)-C(101)	1.193(18)	C(9)-Ru(2)-C(8)	37.7(2)
C(101)-C(102)	1.45(2)	C(9)-Ru(2)-C(10)	37.5(2)
C(8)-Ru(2)-C(10)	62.6(2)	C(109)-P(3)-C(51)	102.3(8)

C(9)-Ru(2)-C(7)	62.5(3)	C(61)-P(3)-C(51)	97.6(8)
C(8)-Ru(2)-C(7)	37.4(2)	C(109)-P(3)-Ru(2)	109.4(6)
C(10)-Ru(2)-C(7)	62.0(3)	C(61)-P(3)-Ru(2)	117.8(7)
C(9)-Ru(2)-C(6)	62.2(3)	C(51)-P(3)-Ru(2)	125.2(5)
C(8)-Ru(2)-C(6)	62.2(3)	C(71)-P(4)-C(99)	103.9(8)
C(10)-Ru(2)-C(6)	37.0(2)	C(71)-P(4)-C(81)	99.2(9)
C(7)-Ru(2)-C(6)	36.9(2)	C(99)-P(4)-C(81)	98.6(8)
C(9)-Ru(2)-P(4)	101.2(5)	C(71)-P(4)-Ru(2)	117.6(8)
C(8)-Ru(2)-P(4)	95.0(5)	C(99)-P(4)-Ru(2)	111.3(5)
C(10)-Ru(2)-P(4)	135.6(7)	C(81)-P(4)-Ru(2)	123.1(5)
C(7)-Ru(2)-P(4)	122.8(7)	C(2)-C(1)-C(5)	107.0(19)
C(6)-Ru(2)-P(4)	157.1(5)	C(2)-C(1)-Ru(1)	66.9(10)
C(9)-Ru(2)-P(3)	103.1(6)	C(5)-C(1)-Ru(1)	73.5(10)
C(8)-Ru(2)-P(3)	140.9(6)	C(3)-C(2)-C(1)	114(2)
C(10)-Ru(2)-P(3)	85.1(4)	C(3)-C(2)-Ru(1)	75.8(13)
C(7)-Ru(2)-P(3)	142.0(6)	C(1)-C(2)-Ru(1)	76.4(12)
C(6)-Ru(2)-P(3)	105.2(6)	C(2)-C(3)-C(4)	107.5(16)
P(4)-Ru(2)-P(3)	93.65(18)	C(2)-C(3)-Ru(1)	68.3(12)
C(9)-Ru(2)-Cl(2)	156.4(4)	C(3)-C(4)-C(5)	104.1(17)
C(8)-Ru(2)-Cl(2)	122.2(6)	C(3)-C(4)-Ru(1)	70.0(10)
C(10)-Ru(2)-Cl(2)	132.7(7)	C(5)-C(4)-Ru(1)	72.3(9)
C(7)-Ru(2)-Cl(2)	93.9(4)	C(1)-C(5)-C(4)	107.0(18)
C(6)-Ru(2)-Cl(2)	99.2(5)	C(1)-C(5)-Ru(1)	70.2(8)
P(4)-Ru(2)-Cl(2)	91.63(17)	C(4)-C(5)-Ru(1)	68.8(8)
P(3)-Ru(2)-Cl(2)	95.57(15)	C(10)-C(6)-Ru(2)	70.6(5)
C(11)-P(1)-C(90)	100.3(7)	C(7)-C(6)-Ru(2)	70.9(5)
C(11)-P(1)-C(21)	99.8(8)	C(8)-C(7)-Ru(2)	69.9(6)
C(90)-P(1)-C(21)	102.9(7)	C(6)-C(7)-Ru(2)	72.2(6)
C(11)-P(1)-Ru(1)	117.4(6)	C(7)-C(8)-Ru(2)	72.7(6)
C(90)-P(1)-Ru(1)	111.9(5)	C(9)-C(8)-Ru(2)	71.0(5)
C(21)-P(1)-Ru(1)	121.6(5)	C(8)-C(9)-Ru(2)	71.3(6)
C(100)-P(2)-C(41)	100.1(8)	C(10)-C(9)-Ru(2)	72.5(6)
C(100)-P(2)-C(31)	101.2(7)	C(6)-C(10)-Ru(2)	72.4(6)
C(41)-P(2)-C(31)	102.0(7)	C(9)-C(10)-Ru(2)	70.0(6)
C(100)-P(2)-Ru(1)	108.8(5)	C(108)-C(109)-P(3)	166.5(17)
C(41)-P(2)-Ru(1)	115.3(5)		
C(31)-P(2)-Ru(1)	125.9(6)		
C(109)-P(3)-C(61)	101.0(9)		

Symmetry transformations used to generate equivalent atoms: #1 -x-1,-y,-z+1.

Table 5-18. Crystal data and structure refinement for **[CpRu(PPh₃)(μ-dppab)]₂(PF₆)₂** (**Compound 8** in the **Chapter 4**).

Empirical formula	C ₁₃₀ H ₁₂₀ Cl ₁₆ F ₁₂ P ₈ Ru ₂
Formula weight	2927.36
Temperature	150(2) K
Wavelength	0.71069 Å
Crystal system	Triclinic
Space group	P -1
Unit cell dimensions	a = 12.7488(5) Å α = 67.404(5)° b = 15.2991(8) Å β = 74.656(4)° c = 19.4914(9) Å γ = 83.577(4)°
Volume	3384.5(3) Å ³
Z	1
Density (calculated)	1.436 mg/m ³
Absorption coefficient	0.697 mm ⁻¹
F(000)	1488
Crystal size	0.2 x 0.15 x 0.1 mm ³
Theta range for data collection	3.73 to 27.49°.
Index ranges	-15 ≤ h ≤ 15, -18 ≤ k ≤ 19, -25 ≤ l ≤ 23
Reflections collected	22066
Independent reflections	12383 [R(int) = 0.0431]
Completeness to theta = 25°	96.4 %
Absorption correction	Semi-empirical from equivalents
Max. and min. transmission	1 and 0.76941
Refinement method	Full-matrix least-squares on F ²
Data / restraints / parameters	12383 / 9 / 727
Goodness-of-fit on F ²	1.061
Final R indices [I > 2σ(I)]	R1 = 0.0978, wR2 = 0.2762
R indices (all data)	R1 = 0.1393, wR2 = 0.3073
Largest diff. peak and hole	2.184 and -1.121 e.Å ⁻³

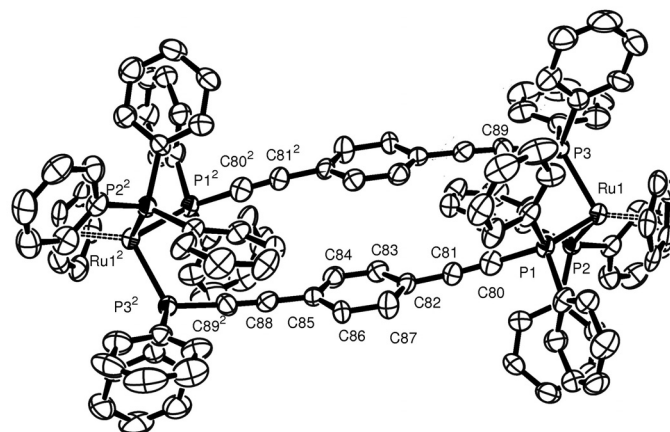


Figure 5-6. ORTEP plot for $[\text{CpRu}(\text{PPh}_3)(\mu\text{-dppab})]_2(\text{PF}_6)_2$.

Table 5-19. Selected bond lengths [Å] and angles [°] for $[\text{CpRu}(\text{PPh}_3)(\mu\text{-dppab})]_2(\text{PF}_6)_2$ (Compound 8 in the Chapter 4)

Ru(1)-C(95)	2.205(8)	Cl(5)-C(205)	1.66(4)
Ru(1)-C(94)	2.222(7)	Cl(6)-C(206)	1.62(3)
Ru(1)-C(92)	2.239(8)	C(205)-C(206)	1.518(19)
Ru(1)-C(93)	2.240(7)	Cl(7)-C(207)	1.80(2)
Ru(1)-C(91)	2.253(8)	Cl(8)-C(208)	1.79(2)
Ru(1)-P(1)	2.325(2)	C(207)-C(208)	1.56(2)
Ru(1)-P(3)	2.333(2)		
Ru(1)-P(2)	2.3595(19)	C(95)-Ru(1)-C(94)	37.2(3)
Ru(1)-Cp(centroid)	2.222	C(95)-Ru(1)-C(92)	61.2(3)
P(1)-C(80)	1.769(8)	C(94)-Ru(1)-C(92)	62.2(3)
P(1)-C(41)	1.829(8)	C(95)-Ru(1)-C(93)	62.0(3)
P(1)-C(51)	1.854(8)	C(94)-Ru(1)-C(93)	37.5(3)
P(2)-C(21)	1.836(7)	C(92)-Ru(1)-C(93)	37.4(3)
P(2)-C(31)	1.845(7)	C(95)-Ru(1)-C(91)	35.6(3)
P(2)-C(11)	1.860(7)	C(94)-Ru(1)-C(91)	61.0(3)
P(3)-C(89)	1.761(8)	C(92)-Ru(1)-C(91)	36.8(3)
P(3)-C(61)	1.830(8)	C(93)-Ru(1)-C(91)	61.5(3)
P(3)-C(71)	1.845(8)	C(95)-Ru(1)-P(1)	86.4(2)
C(55)-H(55)	0.95	C(94)-Ru(1)-P(1)	92.7(2)
C(80)-C(81)	1.206(11)	C(92)-Ru(1)-P(1)	147.6(2)
C(85)-C(88)	1.398(10)	C(93)-Ru(1)-P(1)	128.3(2)
C(85)-C(86)	1.401(10)	C(91)-Ru(1)-P(1)	114.4(2)
C(86)-C(87)	1.398(11)	C(95)-Ru(1)-P(3)	121.1(2)
C(89)-C(88)#1	1.226(11)	C(94)-Ru(1)-P(3)	156.2(2)
C(91)-C(95)	1.362(13)	C(92)-Ru(1)-P(3)	101.0(2)
P(4)-F(4)	1.487(11)	C(93)-Ru(1)-P(3)	135.3(2)
P(4)-F(2)	1.503(11)	C(91)-Ru(1)-P(3)	95.3(2)
P(4)-F(6)	1.532(12)	P(1)-Ru(1)-P(3)	95.44(7)
P(4)-F(5)	1.559(11)	C(95)-Ru(1)-P(2)	143.8(2)
P(4)-F(1)	1.607(9)	C(94)-Ru(1)-P(2)	106.6(2)
P(4)-F(3)	1.635(11)	C(92)-Ru(1)-P(2)	109.1(2)
Cl(1)-C(200)	1.745(15)	C(93)-Ru(1)-P(2)	89.0(2)
Cl(2)-C(201)	1.814(14)	C(91)-Ru(1)-P(2)	145.9(2)
C(200)-C(201)	1.352(17)	P(1)-Ru(1)-P(2)	96.98(7)
P(3)-Ru(1)-P(2)	94.59(7)	C(74)-C(73)-C(72)	119.9(11)

C(80)-P(1)-C(41)	98.2(4)	C(75)-C(74)-C(73)	119.2(10)
C(80)-P(1)-C(51)	98.3(4)	C(74)-C(75)-C(76)	119.0(11)
C(41)-P(1)-C(51)	100.2(3)	C(71)-C(76)-C(75)	123.5(10)
C(80)-P(1)-Ru(1)	125.4(3)	C(81)-C(80)-P(1)	167.8(7)
C(41)-P(1)-Ru(1)	113.8(2)	C(89)#1-C(88)-C(85)	175.7(8)
C(51)-P(1)-Ru(1)	116.7(3)	C(88)#1-C(89)-P(3)	177.2(8)
C(21)-P(2)-C(31)	102.9(3)	C(95)-C(91)-Ru(1)	70.3(5)
C(21)-P(2)-C(11)	100.5(3)	C(92)-C(91)-Ru(1)	71.1(4)
C(31)-P(2)-C(11)	98.9(3)	C(93)-C(92)-C(91)	107.3(7)
C(21)-P(2)-Ru(1)	121.7(2)	C(93)-C(92)-Ru(1)	71.4(4)
C(31)-P(2)-Ru(1)	113.3(2)	C(91)-C(92)-Ru(1)	72.1(5)
C(11)-P(2)-Ru(1)	116.2(3)	C(92)-C(93)-C(94)	106.8(7)
C(89)-P(3)-C(61)	100.6(4)	C(92)-C(93)-Ru(1)	71.3(4)
C(89)-P(3)-C(71)	101.6(4)	C(94)-C(93)-Ru(1)	70.5(4)
C(61)-P(3)-C(71)	99.1(3)	C(95)-C(94)-C(93)	107.0(8)
C(89)-P(3)-Ru(1)	115.6(3)	C(95)-C(94)-Ru(1)	70.7(4)
C(61)-P(3)-Ru(1)	117.7(2)	C(93)-C(94)-Ru(1)	72.0(4)
C(71)-P(3)-Ru(1)	119.1(3)	C(91)-C(95)-C(94)	110.0(8)
C(16)-C(11)-C(12)	117.5(7)	C(91)-C(95)-Ru(1)	74.1(5)
C(16)-C(11)-P(2)	122.1(6)	C(94)-C(95)-Ru(1)	72.1(4)
C(12)-C(11)-P(2)	120.0(6)	F(4)-P(4)-F(2)	89.4(10)
C(22)-C(21)-P(2)	122.4(6)	F(4)-P(4)-F(6)	91.8(9)
C(26)-C(21)-P(2)	120.6(6)	F(2)-P(4)-F(6)	90.9(9)
C(23)-C(22)-C(21)	122.4(7)	F(4)-P(4)-F(5)	101.9(10)
C(32)-C(31)-P(2)	125.4(6)	F(2)-P(4)-F(5)	66.7(9)
C(36)-C(31)-P(2)	117.0(6)	F(6)-P(4)-F(5)	95.9(8)
C(33)-C(32)-H(32)	119.1	F(4)-P(4)-F(1)	168.9(10)
C(31)-C(32)-H(32)	119.1	F(2)-P(4)-F(1)	79.6(7)
C(32)-C(33)-H(33)	119.2	F(6)-P(4)-F(1)	88.8(6)
C(34)-C(33)-H(33)	119.2	F(5)-P(4)-F(1)	89.1(7)
C(46)-C(41)-P(1)	120.5(6)	F(4)-P(4)-F(3)	92.3(9)
C(42)-C(41)-P(1)	120.7(6)	F(2)-P(4)-F(3)	88.5(7)
C(43)-C(42)-C(41)	119.0(8)	F(6)-P(4)-F(3)	175.9(7)
C(44)-C(43)-C(42)	122.5(9)	F(5)-P(4)-F(3)	83.9(7)
C(52)-C(51)-P(1)	121.9(6)	F(1)-P(4)-F(3)	87.0(6)
C(56)-C(51)-P(1)	117.5(7)	C(201)-C(200)-Cl(1)	116.5(12)
C(62)-C(61)-P(3)	121.2(7)	C(200)-C(201)-Cl(2)	116.3(11)
C(66)-C(61)-P(3)	120.5(6)	C(204)-C(203)-Cl(3)	112(2)
C(72)-C(71)-P(3)	122.8(7)	C(203)-C(204)-Cl(4)	128(2)
C(76)-C(71)-P(3)	120.2(7)	C(206)-C(205)-Cl(5)	119(3)
C(71)-C(72)-C(73)	121.3(10)	C(205)-C(206)-Cl(6)	109(3)

Symmetry transformations used to generate equivalent atoms: #1 -x,-1,-y,-z+1.

5.4 Autoclave



Figure 5-7. Home-made stainless steel autoclaves with inner Teflon beaker. Autoclave assembled (above) and constituent components (below). BDC would like to thank Mr Carlo Bartoli at ICCOM-CNR for making the autoclaves used for solvothermal syntheses.

Curriculum Vitae

BARBARA DI CREDICO

10/01/1974 Pescara, Italy

via A. Bafile 13, Francavilla al Mare, Italy

+39.333.7973567

barbara_di_credico@hotmail.com

barbara.dicredico@iccom.cnr.it

EDUCATION

- High school diploma: MATURITA' CLASSICA at Liceo Classico "Gabriele D'Annunzio" of Pescara.
- DEGREE IN CHEMISTRY with mark **110/110 Magna Cum Laude** at the University "La Sapienza" of Rome in July 2001. Degree thesis on "Stereochemistry and reactivity of 5-X-adamantan-2-ones in epoxidation reactions". Supervisors: Prof. Giorgio Di Maio, Dr. Elisabetta Vecchi.
- MASTER in "Synthetic Methodologies of Synthesis in Organic Chemistry" with mark **110/110 Magna Cum Laude** at the University of Florence in April 2005. Supervisors: Dr. Alessandro Mordini, Dr. Gianna Reginato.
- DOCTORAL CANDIDATE (Dottorato di Ricerca in "Scienze Chimiche", University of Florence, Ciclo XXII, a.a. 2009)

EXPERIENCES

- **2002** Collaboration to the research project "Synthesis of Securinega alkaloids" at "Universitat Autònoma de Barcelona" as winner of a scholarship of the University "La Sapienza" of Rome. Supervisor: Prof. Marta Figueredo Galimany.
- **2003** Collaboration to the research project "Synthesis of conductor polymers" at the University of Teramo. Supervisor: Dr. Claudio Lo Sterzo.
- **2004/2005** *Stage* of about six months in Medicinal Chemistry Department of "Istituto di Ricerche di Biologia Molecolare P. Angeletti" (part of Merck Basic Research Global Sites) in Pomezia (Rome). Supervisors: Dr. Steven Harper, Dr. Malte Meppen.
- **2005/2006** CNR Research Grant, sponsored by Glaxo-SmithKline-Verona for the project "Synthetic studies toward the identification of robust routes for the preparation of basic spacers and scaffolds of interest for CNS-based lead compounds"

at "Istituto di Chimica dei Composti Organo Metallici" (ICCOM)-CNR Firenze.
Supervisor: Dr. Gianna Reginato.

- **2007/2009** CNR Research Grant, for the project "Synthesis of metal organic frameworks-MOF" at "Istituto di Chimica dei Composti Organo Metallici" (ICCOM)-CNR Firenze. Supervisor: Dr Maurizio Peruzzini, Dr. Gianna Reginato.

TECHNICAL SKILLS

- Studies of kinetic and stereochemistry in organic reactions.
- Deep knowledge of the majority of the organic synthetic procedures, methods and work-up.
- Manipulation, synthesis and purification of air-sensitive organometallic and inorganic compounds using Schlenk and glove box techniques.
- Pd cross-coupling reactions and synthesis of substituted heterocycles.
- Supramolecular synthesis.
- Proficient use of GC, HPLC, IR and NMR (Varian and Bruker) instruments.

FOREIN LANGUAGES

- Good knowledge of English, French and Spanish languages.

COMPUTER SKILLS

- Good knowledge of Windows (Word, Excel), SigmaPlot (graphic scientific software), ChemWindow and Isisdraw (software of graphic chemistry), Beilstein Commander and SciFinder (programs of bibliographical search), PCMODEL (accounts of molecular mechanics) and of Internet.

PUBLICATIONS

- 1 "Sulfur Ylides in Reactions with 5-X-adamantan-2-ones. Stereochemistry and Reactivity." Catanoso, G.; Di Credico, B.; Vecchi, E. *Heterocycles* **2005**, *65* (9), 2151-2160.
- 2 "A New Versatile and Diastereoselective Synthesis of Polysubstituted 2-Oxopiperazines from Naturally Occurring Amino Acids." Reginato, G.; **Di Credico, B.**; Andreotti, D.; Mingardi, A.; Paio, A.; Donati, D. *Tetrahedron: Asymmetry* **2007**, *18*, 2680-2688.
- 3 "Biocombustibili e Biocarburanti – Soluzioni, strumenti, agevolazioni" (coauthor Di Credico, B.) Edizioni IPSOA Wolters Kluwer S.r.l. **2007**.
- 4 "Crystal-to-crystal phase transition and CO₂ adsorption properties of polymeric magnesium formate" Rossin, A.; Ienco, A.; Costantino, F.; Montini, F.; Di Credico, B.; Caporali, M.; Gonsalvi, L.; Fornasiero, P.; Peruzzini, M. *Cryst. Growth Des.* **2008**, *8*, 3302.
- 5 "Reactivity Studies of Cyclopentadienyl Ruthenium(II) Complexes towards Alkynylphosphine Ligands." Di Credico, B.; Fabrizi de Biani, F.; Gonsalvi, L.; Guerri, A.; Ienco, A.; Laschi, F.; Peruzzini, M.; Reginato, G.; Rossin, A.; Zanello, P. *Chem. Eur. J.* **2009**, *15*, 11985.
- 6 "Synthesis of New Polysubstituted Piperazines and Dihydro-2H-Pyrazines by Selective Reduction of 2-Oxopiperazines." Reginato, G.; Di Credico, B.; Andreotti, D.; Mingardi, A.; Paio, A.; Donati, D.; Pezzati, B.; Mordini, A. *Tetrahedron: Asymmetry*, *accepted for publication*.
- 7 "Synthesis of 2-Substituted 4-Carboxy Oxazoles, Thiazoles and Thiazolidines from Serine or Cysteine Amino Acids" Di Credico, B.; Gonsalvi, L.; Peruzzini, M., Reginato, G.; Rossin, A. *submitted*.
- 8 "Coordination chemistry of thiazole-based ligands: novel hydrogen-bonded architectures" Rossin, A., Di Credico, B.; Giambastiani, G.; Gonsalvi, L.; Peruzzini, M.; Reginato, G. *manuscript in preparation*.

ORAL PRESENTATION

- 1 "TUMA 2009 - XXVIII Congresso Interregionale Toscana Umbria Marche Abruzzo", Tirrenia (Italy), 20-22 September **2009**. Presentazione orale: "Nuovi complessi macrociclici di Ru(II) con leganti alchilfosfinici" (Di Credico, B.; Fabrizi de Biani, F.; Guerri, A.; Ienco, A.; Laschi, F.; Reginato, G.; Rossin, A.; Gonsalvi, L.; Zanello, P.; Peruzzini, M.).

POSTER PRESENTATIONS

- 1 "International School of Organometallic Chemistry", Camerino (Italy), 8-12 September **2007**. "New metal formates for hydrogen storage." (Rossin, A; Ienco, A.; Costantino, F.; Montini, F.; Di Credico, B.; Caporali, M.; Gonsalvi, L.; Fornasiero, P.; Peruzzini, M.).
- 2 "Co.G.I.C.O. 2008 - VIII Congresso del Gruppo Interdivisionale di Chimica Organometallica", Perugia (Italy), 25-28 June **2008**. "Reactivity Studies of Cyclopentadienyl Ruthenium(II) Complexes towards Alkynylphosphine Ligands." (Di Credico, B.; Fabrizi de Biani, F.; Guerri, A.; Ienco, A.; Laschi, F.; Reginato, G.; Rossin, A.; Gonsalvi, L.; Zanello, P.; Peruzzini, M.).
- 3 "2nd EuCheMS Chemistry Congress", Turin (Italy), 16-20 September **2008**. "Synthesis of new ruthenium(II) complexes and macrocycles bearing alkynylphosphine ligands." (Di Credico, B.; Fabrizi de Biani, F.; Guerri, A.; Ienco, A.; Laschi, F.; Reginato, G.; Rossin, A.; Gonsalvi, L.; Zanello, P.; Peruzzini, M.).
- 4 "MOF08 - 1st International Conference on Metal-Organic Frameworks and Open Framework Compounds", Augsburg (Germany), 8-10 October **2008**. "Phase transitions and CO₂ adsorption of polymeric magnesium formate." (Rossin, A; Ienco, A.; Costantino, F.; Montini, F.; Di Credico, B.; Caporali, M.; Gonsalvi, L.; Fornasiero, P.; Peruzzini, M.).
- 5 "MOFCAT Workshop 2009", Oslo (Norway), 17-19 June **2009**. "Phase transitions and H₂ uptake by H[Mg(HCOO)₃] · (CH₃)₂NH." (Rossin, A; Di Credico, B.; Giannasi, A.; Giambastiani, G.; Ienco, A.; Ziparo, C.; Ulivi, L.; Gonsalvi, L.; Zoppi, M.; Peruzzini, M.).
- 6 "XXIII Congresso Nazionale della Società Chimica Italiana", Sorrento (Italy), 5-10 July **2009**. "Metal-Organic Coordination Architectures with Thiazole-and Oxazole-Spaced Carboxylates." (Di Credico, B.; Reginato, G.; Rossin, A.; Gonsalvi, L.; Peruzzini, M.).

Ringraziamenti

L'ultima pagina di questa tesi è dedicata a tutte le persone che, in modi diversi, hanno condiviso con me i tre anni di Dottorato.

Vorrei innanzitutto esprimere la mia gratitudine e riconoscenza al Dr. Maurizio Peruzzini, che ha reso possibile questo lavoro di ricerca, ringraziandolo per il supporto professionale e umano, e per la disponibilità e la fiducia dimostratemi. Un ringraziamento speciale per i continui incoraggiamenti, consigli e apprezzamenti va alla Dr. Gianna Reginato, con la quale condivido la mia crescita professionale da sei lunghi anni, durante i quali Gianna è diventata soprattutto un'amica. I miei più sinceri ringraziamenti al Dr. Andrea Rossin, con il quale ho lavorato a stretto contatto durante l'attività di laboratorio. Grazie alla competenza di Andrea è stato possibile ottenere gran parte dei risultati descritti in questa tesi. Ringrazio inoltre per il contributo dato al lavoro sperimentale e alla stesura di questa tesi il Dr. Luca Gonsalvi.

Sono grata a tutte le persone (ricercatori, assegnisti e borsisti, tecnici e amministrativi) che lavorano presso l'Istituto ICCOM-CNR di Firenze, presso cui ho svolto l'attività di ricerca qui descritta, e in modo particolare a coloro che mi sono stati vicini nel lavoro e nella vita privata: Valentina, Antonella, Andrea e Carlo.

Infine, grazie alla mia famiglia, Tommaso, Elvira, Angela, Piero, le mie nonne, e alle mie amiche di sempre, Elena e Simona. Grazie soprattutto ai miei genitori, a quali dedico questa tesi dottorale, per il sostegno economico, ma più di ogni altra cosa per l'aiuto tacito o esplicito che è venuto dal loro cuore.

Si ringrazia l'Ente Cassa di Risparmio di Firenze per il supporto finanziario attraverso il progetto *motu proprio* Firenze Hydrolab (<http://www.iccom.cnr.it/hydrolab/>).